Development and Application of Cryo-Cell – UV-Laser Ablation Mass Spectrometry (UV-LA-ICPMS) to Greenland Ice Cores: Implications for Abrupt Climate Change and Ice Physics

Damiano Della Lunga

Supervised by

Wolfgang Müller

A thesis submitted for the degree of

Doctor of Philosophy

May 2015

Department of Earth Sciences

Royal Holloway University of London

Egham, United Kingdom

Declaration of Authorship

I, Damiano Della Lunga, hereby declare that this thesis work is entirely my own, as well as all the manuscripts and results presented, apart from data, figures and contributions by other authors which are acknowledged in the text.

Signed: 

Date:

Acknowledgements

I would like to express my gratitude to all the friends and colleagues that helped me throughout the years of my PhD, even if it is difficult here to mention everyone that contributed to the success of the project.

Firstly, I would like to thank my supervisor, Wolfgang Müller, for his patience and kindness which made this PhD a very pleasant experience.

A sincere thank goes to Jerry Morris, whose help during these three years has been invaluable and contributed significantly to the development of the methodology. I would like to thank Sune Olander Rasmussen and Anders Svensson together with Paul Travis Vallelonga and Jorgen Peder Steffensen from Niels Bohr Institute (Copenaghen), which inspired most of the work and contributed with helpful discussions, comments and suggestions throughout the entire PhD project. I also would like to thank Royal Holloway University of London (RHUL) for supporting my PhD project through the RHUL scholarship and travel grants.

I owe my deepest gratitude to my family, my mother Lisetta, my brother Diego and my sister Rebecca together with my uncle Fabio, whose continuous support allowed me to purse my studies abroad, even when we have been trough difficult times. You all showed patience, endurance and strength that I will bear as an example in the future. A friendly thank also to the other little members of my family, Elvish and Cash, which provide always good time and memorable moments.

These years in Egham would have not been the same without a legendary group of friends, “The Zorras”: the craziest, weirdest and greatest bunch of people you can hope to meet. I’d like to thank here Miguelito, Oris, Seb, Eldy, Ivan, Jorge[1], Rebecca, Arnaud, Laura, Marianne, Elena, Sammia, Basim, Viola, Jorge[2], Francisco, Erwan, George, Sila, Maxim, Camilla, Max, Aldo, Lorenzo, and Kat. A special thank to the italian crew, Gio , Silvia, Serena and Giulia, and to my ‘lovely’ housemates Albert ‘El chocho’ de Monserrat, ‘Naughty-Naughty’ Ben and again Serenita, ‘la Zazzerona’ and Milly.

Abstract

Ice cores from Greenland preserve a continuous ~125 kyrs record of climate change at very high resolution. The most remarkable of these changes are Dansgaard-Oeschger (DO) cycles, which are characterized by very rapid Greenland temperature shifts of 5-16°C recorded in $\delta^{18}O$ and reflected in many other proxies such as dust (Ca, Al, Fe) and sea salt (Na, Mg). DO events also are recorded in other northern and southern hemisphere archives such as speleothems and thus show the large-scale extent of these climate variations.

By applying cryo-cell UV-LA-ICPMS (Ultra-Violet Laser-Ablation Inductively-Coupled-Plasma-Mass-Spectrometry) directly to frozen NGRIP ice samples, we investigated elemental proxies of dust and sea salt at an unprecedented spatial resolution of ≤200 µm while maintaining ppb detection limits. For the investigated DO event 22 (87.6-84.7 ka), we thus achieve approximately bi-monthly time resolution. Using a series of suitably homogenous reference ice standards specifically prepared during this project, fully quantitative external concentration calibration is achieved.

This high resolution dataset for the main GS22 transitions as well the GS21 precursor shows (1) the phasing of dust, sea salt and temperature proxies, where dust precedes temperature change by three to ten years, (2) the ~ten-fold change in dust concentrations within one year at the GS21.2 and GI21 warming events, (3) a transient phase from interstadial to stadial lasting several decades and characterized by high amplitude oscillations before the onset of the cold/warm phase (‘flickering of climate signal’), (4) the confirmation that dust and sea salt proxies vary significantly even during minor precursor climatic events, and (5) the quantification of rapid changes in dust provenance as deduced from elemental ratio signatures. We also investigated the role of soluble and insoluble impurities during ice grain growth and recrystallization, and show that impurities distribute preferentially on grain boundaries for relatively low concentration ice but not for ‘dirtier’ ice. This difference is interpreted to be related to the size of impurities. While in clear ice impurities are mostly mobile soluble micro-inclusions with sub-micron dimensions that are easily harvested by moving boundaries, in impurities-enriched layers (cloudy-bands) large insoluble particles prevail, reducing the mobility of grain boundaries.

Table of Contents

List of Acronyms

AABW	Antarctic Bottom Water
ACC	Abrupt Climate Change
AI	Aerosol Index
AIM	Antarctic Isotopic Maxima
AMOC	Atlantic Meridional Overturning Circulation
AO	Arctic Oscillations
AWI	Alfred Wegener Institute
B-A	Bølling- Allerød
CB	Cloudy Bands
CFA	Continuous Flow Analysis
CIC	Centre for Ice and Climate
D-O	Dansgaard-Oeschger events
EASM	East Asian Summer Monsoon
ECM	Electrical Conductivity Measurements
EDS	Energy Dispersive Spectroscopy
EGIG	Expédition Glaciologique Internationale au Groenland
EIS	European Ice Sheet
EPF	Expeditions Polaire Francaises
EPICA-DML	European Project for Ice Coring in Antarctica – Dronning Maud Land
EPICA-Dome C	European Project for Ice Coring in Antarctica – Dome C
ESF	European Science Foundation
FFT	Fast Fourier Transform
GB	Grain Boundaries
GBM	Grain Boundary Mobility
GCM	Global Circulation Models
GI	Greenland Interstadial

GISP	Greenland Ice Sheet Program
GRIP	Greenland Ice Core Project
GS	Greenland Stadial
HDPE	High-density polyethylene
INTIMATE	Integrating Ice Cores, Marine and Terrestrial records
IRD	Ice Rafted Detritus
ITCZ	Inter Tropical Convergence Zone
LGM	Last Glacial Maximum
LIS	Laurentide Ice Sheet
LN	Liquid Nitrogen
MIS	Marine Isotope Stage
NADW	North Atlantic Deep Water
NAO	North Atlantic Oscillations
NBI	Niels Bohr Institute
NEEM	North Greenland Eemian Ice Drilling
NGRIP	NorthGreenland Ice Core Project
nssCa	Non sea salt Calcium
PTFE	Polytetrafluoroethylene
RHUL	Royal Holloway University of London
SEM	Scanning Electron Microscope
SIPRE	Snow, Ice, and Permafrost Research Establishment
SR	Stochastic Resonance
ssMg	Sea salt Magnesium
SST	Sea Surface Temperature
THC	Thermohaline Circulation
UV-LA-ICPMS	Ultra-violet Laser Ablation Inductively Coupled Plasma Mass Spectrometry
WBC	Western Boundary Current
YD	Younger Dryas

1) **Introduction**

Among the many natural archives that contain information about the climate of the late Pleistocene, ice cores are one of the most reliable, since they have the highest resolution and continuity (Alley, 2000).

In particular, ice cores from Greenland have a higher time resolution than ice cores from elsewhere, and can extend back to ~120-130ka[1] (Dansgaard et al., 1993), i.e., just reaching the last interglacial. In contrast, lower accumulation rate ice cores from Antarctica reach ~800 ka, thus including several glacial cycles (Jouzel et al., 2007). Within the last glacial period, several abrupt climatic changes occurred, marked by a rapid temperature variation over Greenland between 5 and 16 °C and followed by a more gradual cooling (Huber et al., 2006). These oscillations, called Dansgaard-Oeschger events (see Chapter 2), occurred 25 times during the last glacial and lasted between one and three millennia on average. The temperature shift is accompanied by a change in the quantity of dust supplied to Greenland by atmospheric transport, increasing significantly during cold periods. This can be inferred from several proxy measurements in ice which, among others, include Ca, Al and Fe for dust and Na and *sea-salt*-Mg (ssMg) for sea salt.

The acquisition of profiles of dust and sea salt concentration in ice cores across climatic changes is routinely carried out by Continuous Flow Analysis (CFA), which utilizes different techniques such as ion chromatography on liquid fractions of ice produced by a melting-head. The resolution achievable with this technique in routine analysis is around 10 mm (Bigler et al., 2011), and thus enough to well resolve seasonal cycles in shallow ice; however, below a certain depth (~ 2600 m at NGRIP) annual layer thickness approach the CFA resolution limit so that identification of seasonal cycles becomes more challenging. This is particularly relevant in DO warming transitions where dust proxies show abrupt changes at the onset of interstadial condition and vice versa. In this case the drop or rise of concentration can occur in as short as few years (Steffensen et al., 2008). Therefore, to elucidate the

[1]Thorough the whole thesis, the terminology ‘a’, ‘ka’, ‘Ma’ has been used for exact times in the past and ‘yrs’, ‘kyrs’ ‘Myrs’ for time intervals, as suggested in Aubry et al. (2009).

correct timing and phasing of dust proxies in comparison with other proxies (e.g. temperature and moisture), the need for higher sub-annual resolution analysis across DO events has been long established (Thomas et al., 2009). A precise location of soluble and insoluble impurities in ice at a millimetric scale is also crucial in understanding the observed grain size reduction occurring at the onset of stadial conditions and also in correspondence of dusty layers (cloudy bands). In fact, many studies suggest that the location of impurities can halt grain growth and recrystallization by reducing the grain boundaries mobility.

1.1 - Objectives

The goals of this PhD include:

- Developing and improving the methodology and the equipment to routinely perform ice core analysis by Laser Ablation (LA)-ICPMS. At the time when this PhD project started in September 2011, no other laboratory in the world was doing LA-ICPMS on ice cores utilizing a 193 nm laser wavelength and/or a two-volume laser-ablation cell (a situation that 3.5 yrs later has not substantially changed). Since this is a pioneering study, particular interest has been given to the methodological development.
- Analysing NGRIP ice corresponding to DO events 22 (87.60-84.76 ka; Rasmussen et al., 2014), with emphasis on transitions and internal oscillations of the climate signal. The sequence, phasing and abruptness of dust and sea salt variations (Mg, Ca, Al, Fe proxies) has been analysed by UVLA-ICPMS at a resolution of approximately 200 µm. This constituted the main application of this PhD project.
- Improving the annual layer counting for deep ice by providing sub-millimetre resolution, which also allows elucidating the seasonality of proxies.
- Investigating the location of impurities concerning their partitioning between grain boundaries and interiors and their relationship with recrystallizing ice with 1D profiles as well as 2D and 3D maps of

elements. Diffusion of soluble impurities has also been quantified based on the data acquired.

This PhD project was conducted in partnership with the Niels Bohr Institute, Centre for Ice and Climate at University of Copenhagen, Denmark, which provided the ice core samples from the NGRIP site (North Greenland Ice Core Project) and helped with discussion throughout. Early discussions with Alfred Wegener Institute for Polar and Marine research of Bremerhaven, in Germany, also helped to develop the methodology and standard preparation.

In the next section the research hypothesis is described followed by a brief history of ice core science, as derived from Greenland drilling projects. Chapter two focuses on Pleistocene Climate variations and abrupt climatic changes such as D-O events, while Chapter three illustrates the methodology development. Results are described in chapters 4-7 in the form of manuscripts and finally a critical evaluation is given in Chapter 8.

1.2 - Research hypotheses

Several research hypotheses have driven this PhD project and are summarized in the following statements:

1. UV-LA-ICPMS at a wavelength of 193 nm provides an optimal balance between material removal, ablation uniformity and low-ppb sensitivity, when compared to other LA-ICPMS ice core techniques (Reinhardt et al., 2001, 2003; Sneed et al., 2015).
2. Routine UV-LA-ICPMS analysis of ice cores can be achieved using liquid-nitrogen cooled equipment to enable sample holding, loading, smoothing and contamination removal, without a cold-room environment.
3. Calibration of the analyses can be achieved by preparing inhouse ice standards made from international aqueous solutions, in order to establish a transfer function from LA-ICPMS intensities to element concentrations (ppb).
4. Profiling and mapping element concentrations as proxies for soluble and insoluble impurities across ice grains reveals the preferential distribution

of particles between grain interiors and boundaries in different section of ice.

5. Differently from insoluble particles, soluble impurities may undergo sub-centimetre diffusion in deep ice that can be quantified.
6. UV-LA-ICPMS reveals seasonal variability of elemental proxies for dust and sea salt, such as Ca, Al, Fe, Na and Mg in deep glacial stadial/interstadial ice.
7. Dust and sea salt proxies abruptly change in concentrations across stadial/interstadial warming transitions over a time scale of just few years, in contrast with interstadial/stadial transitions that appear more gradual.
8. Elemental ratios such as Ca/Al, Fe/Al and Mg/Al can be used to track possible Greenland dust sources and their variations across stadial/interstadial transitions and vice versa.

1.3 - Ice Core Science

The scientific interest in polar regions started in the mid-19th century and rose mostly during the first decade of 20th century, when expeditions towards the poles became more feasible.

1.3.1 - Greenland Ice Core Projects

Outside Antarctica, half of the remaining fresh water on Earth resides in the Greenland Ice Sheet (Dansgaard, 2004) which covers more than 2 million km^2 and measures 2500 km north-south and 750 km west-east, reaching an altitude of 3250 m a.s.l. near the Summit base (Fig. 1.1) and a maximum thickness of 3367 m (Bamber et al., 2001).

In contrast to the Laurentide ice sheet (LIS) and the European Ice Sheets (EIS) of the last glacial period most of the Greenland Ice Sheet survived the warm interglacial because of its elevation above the sea level and the uninterrupted supply of precipitation from the Atlantic caused by a low-pressure zone moving across the island (Raynaud et al., 1997).

During the winters of 1912 and 1913 the meteorologist Alfred Wegener and Danish officer J.P. Koch were the first to ever drill Greenland ice to a depth of 25 m in order to measure the temperature during winter at various depths. In 1929-1930 Wegener led another expedition to Greenland to conduct a twelve month survey of the Arctic weather. Establishing a permanent station at Eismitte (Fig. 1.1) they developed a method to measure annual accumulation of snow and also calculate ice thickness and ice sheet drifting (Ahlman 1933, 1934; Sverdrup 1935).

German glaciologist Ernest Sorge was the first to continuously study the near surface snow/firn strata in the 25 m deep pit at Station Eismitte. Measuring frozen precipitation in a rain gauge, he calculated annual snow accumulation cycles for near surface ice layers (Sorge 1933, 1935).

Figure 1.1: Map of Greenland showing the most important ice drilling sites with indication of the years of activity of each site given in brackets. (modified from Dansgaard 2004).

In 1950-1951 the French ethnologist Paul Emile Victor led the *Expeditions Polaires Francaises* (EPF) which bored two holes into the ice at Camp VI and

Station Central (Fig. 1.1), to depths of 126 and 150 m. These two projects reached only a fraction of the depth expected, and could not recover complete ice cores from the holes. Despite this, the members of the EPF provided some interesting studies on ice physical properties (Péguy, 1951).

The fundamental idea of using ice cores to study past climate was first considered by the Danish physicist Willi Dansgaard in the early 1950s. In 1952, he had discovered that the amount of heavy oxygen isotopes in precipitation correlated with the temperature at the location where the precipitation was formed.

The variation of oxygen isotopes in precipitation is formalized using the so-called δ–value:

$$\delta^{18}O\ (‰) = \left[\frac{\left(\frac{^{18}O}{^{16}O}\right)_{SAMPLE} - \left(\frac{^{18}O}{^{16}O}\right)_{STANDARD}}{\left(\frac{^{18}O}{^{16}O}\right)_{STANDARD}}\right] \cdot 10^3$$

Water molecules can be built up as $H_2{}^{16}O$ or $H_2{}^{18}O$. The first one has a vapor pressure 10‰ higher than the second one, which means that H_2O^{16} has 10‰ higher tendency to evaporate from a water surface and 10‰ lower tendency to condensate from water vapour compared to H_2O^{18}. The $\delta^{18}O$ in water is constant in all the oceans and is taken as standard value (Standard Mean Ocean Water), with $\delta^{18}O_{SMOW}$ = 0 ‰. Hence, water evaporated from an ocean surface has a $\delta^{18}O$ of -10‰ at 25 °C. Conversely, when this vapor condenses, its $\delta^{18}O$ value returns to 0‰ for the initial drops.

Dansgaard demonstrated (1954) that the $\delta^{18}O$ value of precipitation decreases by 0.7 ‰ per °C. For instance, when a frontal system develops, the first rain forms at the highest and thus coldest part of the precipitating front cloud, and therefore the $\delta^{18}O$ value is low. As time goes on, the rain forms at steadily decreasing altitudes and so the $\delta^{18}O$ value increases because temperature increases.

Being a function of temperature, the $\delta^{18}O$ value changes with altitude but also latitude. Over polar regions the water vapour is isotopically depleted with present $\delta^{18}O$ values around -30‰. During the past, however, the high-latitude regions experienced warmings and coolings, altering the $\delta^{18}O$ value in precipitation. Realizing that the oxygen isotope technique could be used to derive information on past climate conditions from layers of old precipitation stored in ice caps, Willi Dansgaard made the following statement in 1954:

"In certain areas on the Greenland Ice Cap is a distinct layer formation caused by melting in the summer season. On the supposition that the character of the circulatory processes, in all essentials, have not varied over a long period of time, the above, in the opinion of this author, offers the possibility of measuring the amount of the heavy oxygen isotope in these layers of ice to determine climatic changes over a period of time of several hundred years of the past."

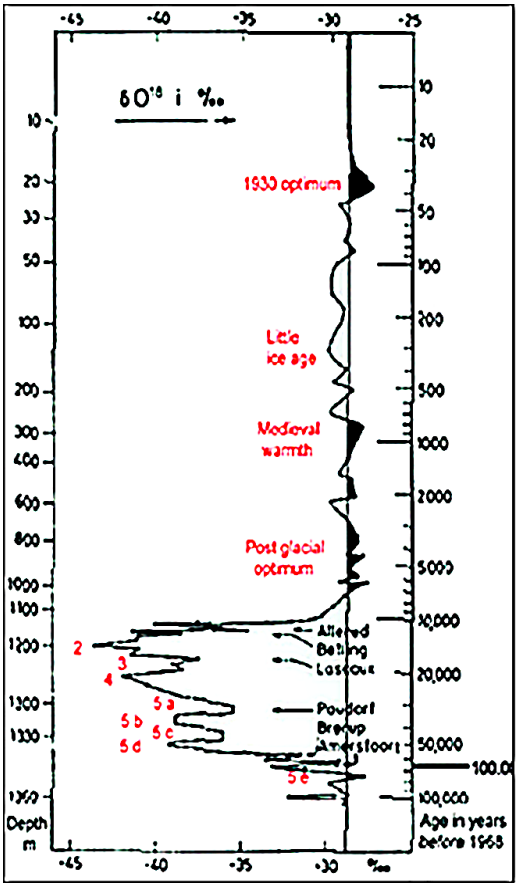

Figure 1.2: The graph shows the amount of heavy isotopes (given as $\delta^{18}O$ value) as a function of depth and age along the 1390 meter long ice core [from Dansgaard, 1969].

Few years later (1956 and 1957), the US Army Snow, Ice, and Permafrost Research Establishment (SIPRE), which was formed in 1949, recovered successfully deep polar ice cores from Site 2 in Greenland (Fig. 1.1). Samples of snow/ice for oxygen isotope analysis were collected in several 4 m deep pits. The $\delta^{18}O$ data collected from the upper snow/ice layers of some pit walls were strongly reflecting a seasonality pattern, with minima in winter and maxima in summer (Benson, 1962). Beetween 1957 and 1960 Willi Dansgaard analyzed samples from the Greenland Ice Sheet

collected during the 'Bubble' expedition (1958) and the EGIG expedition (*Expédition Glaciologique Internationale au Groenland,* 1959-1967). All of his measurements confirmed that the amount of heavy oxygen isotopes in precipitation correlated with temperature. But these measurements were taken only from the first meters of ice, reflecting thus the temperatures of just the last few decades. The oxygen isotope analysis from five sites in mid Greenland showed how the temperature changed during the 20th century, with values higher by 2-3 °C from the '20s to the '50s, after which temperature dropped by approximately 0.4 °C (Dahl-Jensen et al., 1998). Another significant contribution of the EGIG regarded the speed of the ice sheet movements. Dating the CO_2 in bubbles via radiocarbon dating established the age of the icebergs (Scholander et al., 1961). The $\delta^{18}O$ values was then use to infer at which altitude of the ice cap that iceberg was formed, and therefore how far inland it was coming from (Dansgaard et al., 1960).
However, in order to investigate the temperatures of the past glacial-interglacial transition back to 120 ka ago, the ice sheet had to be drilled more deeply. But the cost of building drilling facilities in Greenland was still too high at the time to be taken in serious consideration.

In 1959, at the height of the *Cold War*, the U.S. Army decided to build a network of mobile nuclear missile launch sites under the Greenland ice sheet, at *Camp Century* in northwest Greenland (Fig. 1.1). A total of 21 tunnels were built with an overall length of about 6 km (Clark, 1965). It was discovered then that the ice was moving much more intensively than had been anticipated which would have destroyed the tunnels and launch stations in about two years. The facility was evacuated in 1965 and closed in 1966. Nevertheless, the project generated valuable scientific information and provided scientists with some of the first ice cores (Dansgaard, 2004).

In 1966, the 1390 m Camp Century ice core was drilled, yielding a low time resolution temperature record extending far enough into the past to show that the Greenland ice sheet did not completely melt during the last interglacial.

The results were shown in a graph in which the variations of $\delta^{18}O$ were plotted against depth, and thus time (Fig. 1.2; Dansgaard et al., 1969).

The deepest part of the record, at 1350 m of depth approximately (Fig. 1.2), shows a peak indicating a temperature higher than modern times. This period has been interpreted as the preceding interglacial period, the Eemian, already well known at that time from pollen studies (Frey, 1962).

According to Fig.1.2, the last glaciation lasted from 70 to 10 ka, and it was followed by a warming period from 10 ka, when the Holocene starts. High temperatures were reached until 3 ka, during the post glacial optimum, and then decreased and rose again in medieval times (medieval warmth). After that, a cold period, called “Little Ice Age”, was characterized by lower temperatures by a few degrees Celsius.

Low time resolution, uncertainties about the dating of the core, and poor-understood ice flow limited the scientific value of the core (Dansgaard 2004). However, it demonstrated the potential of ice cores for climate research, thus enabling future projects to proceed.

In 1970, scientists discussed the feasibility of conducting a dedicated ice core drilling investigation over the entire Greenland Ice Sheet. The result of this discussion was the birth of the Greenland Ice Sheet Program (GISP), a collaboration between U.S.A., Switzerland and Denmark.

1.3.1.1 - Greenland Ice Sheet Program (GISP)

The perspectives for ice core drilling were tested at the American radar station Dye 3 in the southern part of Greenland in 1971 and again in 1973, obtaining two cores of 372 m and 390 m respectively (Langway and Shoji, 1985). In these cores 740 seasonal $\delta^{18}O$ cycles were identified. Other cores were drilled at Milcent in 1973 (398 m) and Crete in 1974 (405 m), in the general vicinity of the station Eismitte (Fig. 1.1). In August 1981 the drilling at Dye 3 reached the bedrock at 2038 m depth. This core covered continuosly the last 90 kyrs. Continuous profile of $\delta^{18}O$, electric conductivity and dust

concentration were obtained. Furthermore, cosmogenic $^{36}Cl/^{10}Be$ ratio measurements were carried out as a new dating method (Beer et al., 1987). Nevertheless, this well-dated record at Dye-3 could not reproduce the $\delta^{18}O$ record of Camp Century for the last few thousand years.

The drilling at Dye 3 was not immediately followed by deep drilling in central Greenland as it was planned at first, when contentions between Americans and Europeans arose (Jouzel, 2011).

It was just a few years later, between 1989 and 1993, that the GISP2, the Greenland Ice Sheet Project 2, developed by U.S., drilled through the ice in the centre of Greenland. The bedrock was reached in July 1993 at a depth of 3053 m.

In parallel, a collaboration between the University of Bern, the Centre for Ice and Climate at the University of Copenhagen, and the French Laboratoire de Glaciologique et Physique de l'Enviroment at the University of Grenoble, produced the recovery of a 300m core ("Eurocore"), drilled in 1986 at Summit.

In 1987, the European Science Foundation (ESF) decided to support a large-scale project which included the contributions of eight European countries: Denmark, Switzerland, Belgium, France, Germany, Great Britain, Iceland and Italy. This project drilled in parallel with the GISP2. The selected location was Summit, in central Greenland, just 30 km away from the GISP2 site. The project was called Greenland Ice Core Project (GRIP).

1.3.1.2 - Greenland Ice Core Project (GRIP)

The Greenland Ice Core Project drilled successfully the Greenland ice sheet at Summit. The project started in 1989 and reached the bedrock in the summer of 1992 at a depth of 3029 m (Johnsen et al., 1992). The core provided many data including dust, $\delta^{18}O$, visual stratigraphy, radioactive elements, aerosols, physics of the ice, biogenic species (Dansgaard, 2004).

The $\delta^{18}O$ and temperature profile along the whole core length (Fig. 1.3) confirmed most of the previous findings. The ice core reached more than 130 ka back in time well into the second last glaciation and also the end of the last interglacial, but at a certain depth, corresponding to an age of 105 ka, the ice layers began to be disturbed (Johnsen et al., 1992).

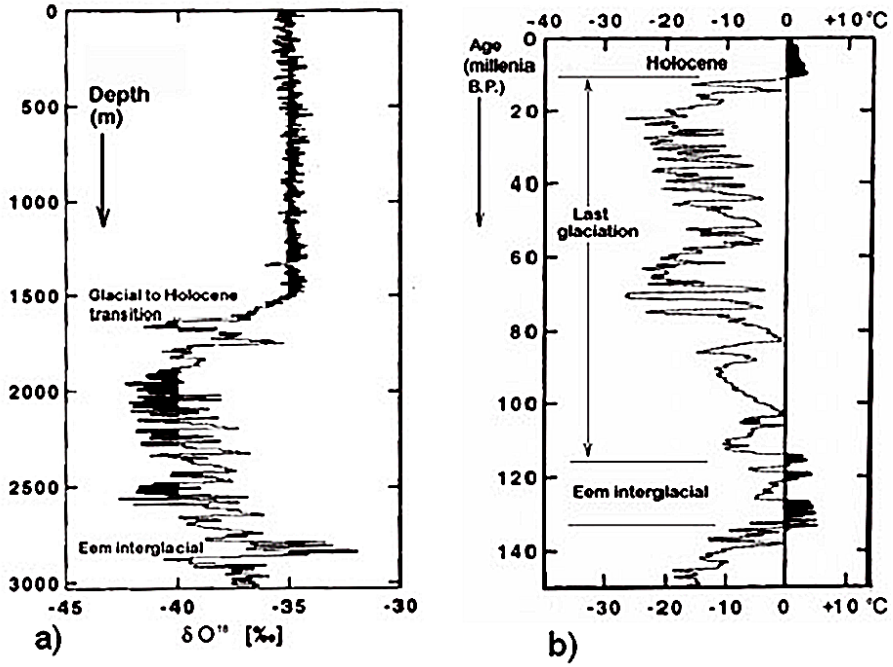

Figure 1.2: a) $\delta^{18}O$ profile along the GRIP ice core. The record from 1500 to 2750 m depth reflects the glacial climate before the Holocene starts. b) Calculated Greenland temperature: deviations from present values through the last 150 kyrs (from Dansgaard, 2004).

The glaciation recorded in GRIP lasted from 117 to 11.5 ka, and carried evidence of abrupt climate changes, sharper than in Europe and Antarctica. From ~22 ka to 70 ka, the climate was extremely cold, with temperatures up to 25°C lower than today (Fig. 1.3) (Johnsen et al., 1992).

The $\delta^{18}O$ profile shows that during the Holocene (from 11.5 ka) the climate was stable with temperatures that culminated around 9 ka, when the climate was approximately 4 °C warmer than today. Nevertheless, within this stable period, the $\delta^{18}O$ profile shows a rapid cooling period from 8.25 to 8.00 ka (the '8.2 ka event'; Thomas et al., 2007).

The Eemian interglacial was then defined between 131 ka to 117 ka and at least 5 stadials were identified, the temperature oscillating by 5 °C between each one, even though the layers sequence was strongly disturbed in the deepest 10% of the core (Johnsen et al., 1995). In this period the sea level was 6-8 m higher than today, and Europe was chacarcterized by sub-tropical fauna (Stirling et al., 1998).

In 1993, the results of the drilling at GISP2 were published (Grootes et al., 1993; Alley et al., 1993). The comparison of the $\delta^{18}O$ profile of the deepest part of the GRIP and GISP2 record is shown in Figure 1.4.

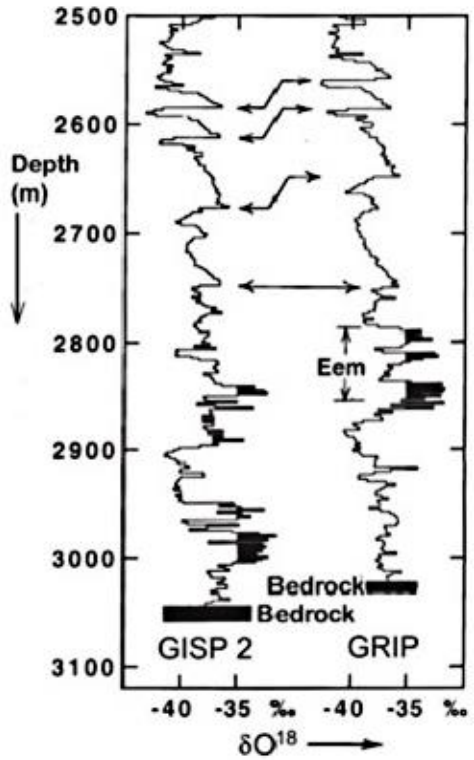

Figure 1.3: $\delta^{18}O$ profile of the deepest parts of GISP2 (left) and GRIP ice core (right). The two profiles are very similar down to a depth of 2750 m, where they start to be different because of ice layer disturbances.

The GRIP and GISP2 records are identical along 90% of the depth of the cores and differ just in the last 10% (Fig. 1.4). It is now generally accepted that the order of the ice layers in the GISP2 record is more disturbed than the one of the GRIP (Johnsen et al., 2001).

A correct understanding of the climate dynamics during the last interglacial, the Eemian, could help elucidating what might happen at the end of our own interglaciation, and therefore has been always a primary target of ice core drilling.

Since both the GRIP and GISP2 couldn't obtain a reliable $\delta^{18}O$ profile for the Eemian, due to disturbed ice layers, the challenge for scientists was to find a place in the Greenland ice sheet where there was old enough undisturbed ice. An apparently favourable location were identified 320 km NNW of Summit, where in October 1995 the North Greenland Ice Core Project (NGRIP) was started.

1.3.1.3 - North Greenland Ice Core Project

The North GReenland Ice core Project (NGRIP) was founded by a consortium with Denmark (main contributor), Germany, Belgium, France, U.K., Iceland, Japan, Sweden, Switzerland and U.S.A. (Dansgaard, 2004).

In 1996, drilling started but got stuck in 1997 at a depth of 1370m. Drilling started again in 1999 but got stuck several times in 2000 and 2001 at various depths (Dansgaard, 2004).

Bedrock was reached in July 2003 at a depth of 3085m, making the NGRIP the longest ice core ever drilled in Greenland. Many sets of data were obtained at a resolution of 1 cm: concentrations of ammonium, sodium, calcium, hydrogen, peroxide, nitrate, sulfate and dust. Also 3500 filters and approximately 60,000 ice sample were collected for tephra analysis and $\delta^{18}O$ measurements respectively, as well as many other proxies (Anderssen et al., 2004).

Nevertheless, it was clear during the drilling already that the annual layer thickness did not decrease downward as fast as expected, implying that the core would not reach as far back in time as predicted. However the $\delta^{18}O$ values in the deepest part of the core were 2‰ higher than those typical of

the warmest part of the present interglacial, meaning that the NGRIP core reached the previous interglacial, the Eemian, but did not penetrate it fully.

The comparison between $\delta^{18}O$ of plantonic foraminifera in the ocean core MD95-2042 and $\delta^{18}O$ of NGRIP core suggested that the Greenland record was preserved at very high resolution (Fig. 1.5), although several assumptions were necessary to allow comparison. According to the ocean record, the Eemian lasted from 127 to 116 ka. In this case the deepest 25 m of the NGRIP core represent the last local maximum in the Eemian, i.e. the Marine Isotope stage 5e (Goñi et al., 2000).

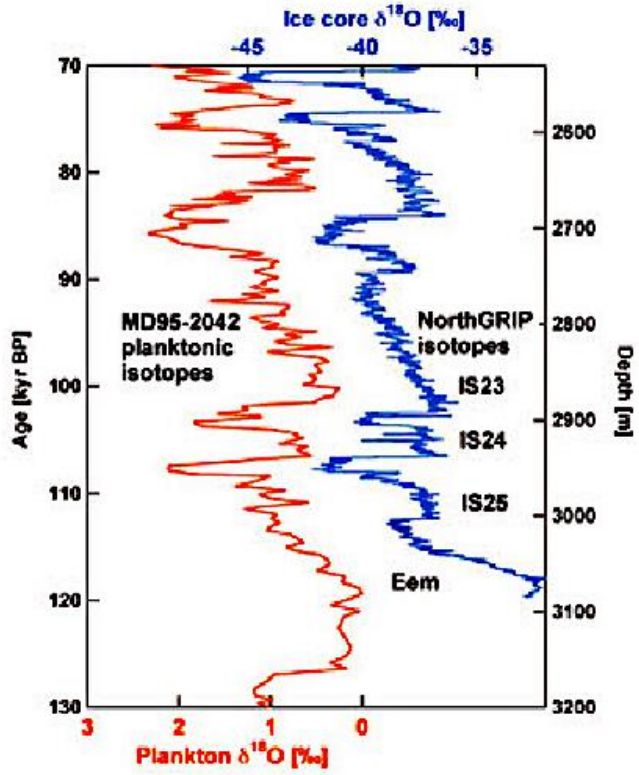

Figure 1.4: The NorthGRIP profile (in blue) of the last 550 m compared with a radiometrically dated profile (in red) of plantonic foraminifera in an ocean sediment core (MD95-2042) situated in the Northwest Atlantic Ocean (from Goñi et al., 2000).

The challenge to obtain undisturbed ice layers of the complete Eemian was not achieved in any of the ice core projects in Greenland (Camp Century, DYE-3/GISP, GRIP, GISP2, or NGRIP) (Dansgaard, 2004).

During the Eemian, Greenland temperatures were about 3-5 °C higher than present, making the Eemian a useful analogue to for future climate, which due to global warming is projected to warm by 2-4°C per century (Dansgaard, 2004). Understanding how the Eemian climate evolved would improve our ability to make projections for how our current climate may evolve in the future.

In order to do that, an international ice core research project was developed to retrieve an ice core from North-West Greenland, reaching back through the previous interglacial (Buchardt and Dahl-Jensen, 2008). The project has been called North Greenland Eemian Ice Drilling – NEEM.

1.3.1.4 - North Greenland Eemian Ice Drilling – NEEM

During the International Polar Year 2007-2008, NEEM was developed. The site is located 150 km ESE of Camp Century. Radar soundings revealed that undisturbed layers from the Eemian could be retrivied at this site (Blake et al., 2009), where the ice is thick enough, the bedrock is flat and the accumulation rate is high.

The project, involving 14 different countries (Belgium, Canada, China, Denmark, France, Germany, Iceland, Japan, Korea, The Netherlands, Sweden, Switzerland, UK and U.S.A.), started in 2007, when two tracked vehicles dragged equipment from the previous drill site, NGRIP, to the NEEM drill site. The camp was built in 2008, when the drilling started, and in July 2010 the bedrock was reached at a depth of 2537m.

The main areas of study are: isotope ratios of the ice for reconstructing temperatures, impurities in the ice layers, gas bubbles trapped in snow crystals, crystal structure of ice, temperature of the bore hole, content of biological material (Dahl-Jensen et al., 2013). However, undisturbed Eemian ice was not retrieved as the stratigraphy below ~2200 m appears to be corrupted (Rasmussen et al., 2013).

2) Pleistocene climate variations

Since the recognition in the mid-nineteenth century that glaciers had been considerably more extensive than at present (Agassiz and Bettannier, 1840), the Quaternary has been synonymous with glaciation of the mid/high-latitudes. The Pleistocene represents the first epoch of the Quaternary period and differs from the preceding Pliocene period mainly because its climate has varied remarkably in time and space perhaps following oceanic heat transport reorganization in relation to the closure of the Panama strait and the Indonesian seaway (Schneider and Schmittner, 2006). In the Cenozoic, we know that several ice caps formed: in Eastern Antarctica in the Oligocene; in Alaska, Greenland, Iceland and Patagonia in the Miocene and in the Alps and Andes during the Pliocene (Alley et al., 2005). Today, evidence from land and ocean demonstrates that glaciations in the Pleistocene characterizes particularly the last 1-0.8 Myrs rather than punctuating the Quaternary period which spans from 2.588 Ma (±.005) to the present day (Ehlers and Gibbard, 2003). In fact, the early Pleistocene (2.6–0.8 Ma) was characterized by climatic fluctuations dominated by the 41 kyrs precession cycle, during which relatively few cold periods were sufficiently cold and long to allow the development of substantial ice sheets (Ehlers and Gibbard, 2003). Only 14 of the 41 cold stages of that period currently show evidence of major glaciation. They include the Plio-Pleistocene boundary events Marine Isotope Stage (MIS) 104, 100, and 98, together with Early Pleistocene MIS 82, 78, 68, 60, 58, 54, 52, 36, 34, 30, and 26 which reach $\delta^{18}O$ of 4.6–5 ‰ in ocean sediments (Ehlers and Gibbard, 2007). Transition in dominant orbital cyclicity to the 100 kyrs cycle began approximately 1.2 Ma and was fully established by about 800 ka (“middle Pleistocene transition”), allowing cold periods (glacials) to be regularly cold and long enough to develop ice-sheet on continents outside the polar regions (Ehlers and Gibbard, 2004). However, it is during MIS 22 (870–880 ka) that the first of the “major” cold events reached critical values of $\delta^{18}O$ in ocean sediments microfossils of roughly 5.5 ‰ or above, which indicates substantial growth of ice volumes that typify glaciations of the later Pleistocene (e.g., MIS 16, 12, 10, 6, 4–2; Ehlers and Gibbard, 2004). Potentially therefore, it is likely that

there were a minimum of 20 periods during which extensive glaciation could have developed during the last 2.6 Myrs, with the most extensive being limited to the last 900 kyrs (Ehlers and Gibbard, 2007). These climate variations have been identified over the years from several proxies in different archives, such as oxygen isotopes measurements ($^{18}O/^{16}O$) on benthic and planktonic microfossils (mainly foraminifera), speleothems and ice cores, allowing palaeo-temperature reconstruction. A brief selection of ice core proxies include nitrogen isotopes, used to infer past nutrient consumption through analysis of sediments and diatoms (Huber et al., 2006), ^{13}C in fossils shell, utilized to reveal patterns of productivity in the ocean (Schulte and Muller, 2001), Mg/Ca ratios fixed in the shell during life, used to quantify sea surface temperature (Dwyer and Chandler, 2009, Evans and Muller, 2012) as well as alkenone from fossil phytonplankton in sediments which provides information about temperature and carbon dioxide levels in the past (Kim et al., 2012). Finally, environmental information is retrieved from various sediments and fossil record of flora and fauna from peat, lakes, caves allowing reconstruction of ecology and climate (Voelker et al., 2002).

Ice cores from polar regions have been extremely important in unraveling climatic oscillations clearly showing that Earth experienced eight different glacial cycles during the last 800 kyrs (Jouzel et al., 2007). This was inferred mainly from $\delta^{18}O_{ice}$ and δD in Antarctic ice as well as grain radius, dust concentration, dielectric profile, electrical conductivity and analyses of the entrapped air. (e.g. CO_2, CH_4, and N_2O). Particular interest has been raised analyzing the last glacial cycle which started approximately 130-120 ka ago and terminated roughly 10 ka ago with the onset of the current interglacial, the Holocene. This period is recorded at high resolution in the Antarctic and especially in Greenland ice cores, showing that, beside the major glacial cycle, the entire time interval is punctuated by at least 25 climatic oscillations that happened in few millennia only (Daansgard et al., 1993). The oscillations are called Dansgaard-Oeschger events.

2.1 - Phenomenology of Dansgaard-Oescher events

Dansgaard-Oeschger events, named after two climate scientists, Willi Dansgaard and Hans Oeschger (D-O events; Bond et al, 1993), are a collection of 25 sudden climatic changes observed over the last 120 kyrs (Fig. 2.1). During these events, the temperature generally increased by 5-16 °C over periods ranging from 10 to 50 yrs (Dansgaard et al., 1993).

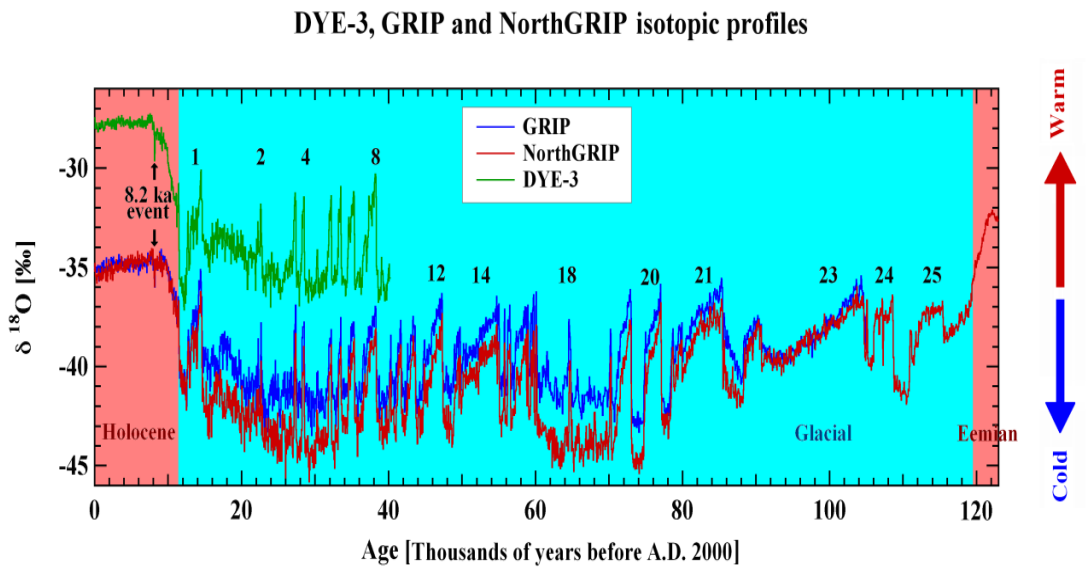

Figure 2.1: Profiles of $\delta^{18}O$ (proxy for temperature) from the DYE-3, GRIP and NGRIP ice cores. The most prominent Dansgaard-Oeschger events during the glacial period are numbered [from Johnsen et al., 2001]

Related to some of the coldest intervals between D-O events were six to eleven distinctive events, discovered by the paleoclimatologist Hartmut Heinrich, that are recorded in North Atlantic marine sediments as layers with a large amount of coarse-grained sediments transported as ice-rafted debris (Fig. 2.2) (Heinrich, 1988; Hemming 2004).

The most recent D-O event was the Bølling-Allerød/Younger Dryas (around 14.7-11.5 ka; Broecker et al., 1988; Baldini et al., 2015). Although evidence shows that D-O events have not occurred during interglacials (Adkins et al., 1997), understanding their dynamics and causes will allow us to model more accurately how the Earth might respond at the termination of the interstadial we are currently living in, the Holocene.

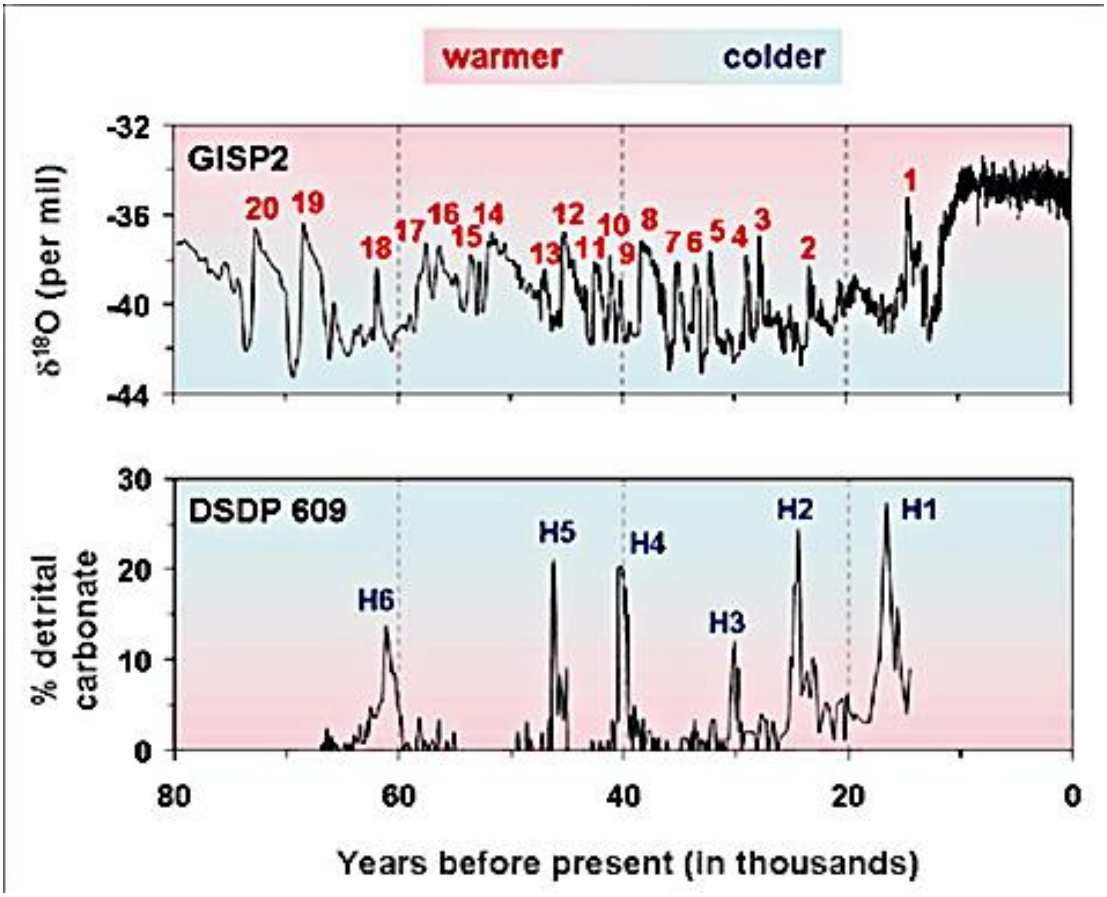

Figure 2.2: (Above) The $\delta^{18}O$ record from the GISP2 ice core in Greenland, showing 20 of the 25 observed Dansgaard-Oeschger events during the last glacial period (Grootes et al., 1993). (Below) A record of ice-rafted material during Heinrich events from a deep-sea core in the North Atlantic (Bond and Lotti, 1995).

Dansgaard and his colleague Oeschger discovered that rapid changes in the Earth's climate have occurred much more often than previously recognized. As a result, countless studies have tried to understand the root causes of these events (Bond et al., 2001; Andrews and Barber, 2002; Stocker and Johnsen, 2003, Braun et al., 2005; Kageyama and Paillard, 2005; Ditlevsen et al., 2007, Petersen et al, 2013; Dokken et al., 2013; Zhang et al., 2014). While the exact cause is unknown, a number of hypotheses exist.

The record of D-O cycles has been labelled by dividing each cycle into a warm and a cold phase, where the warm phases are named Greenland interstadials (GI) and the cold phases are named Greenland stadials (GS) (Björk et al., 1998; Rasmussen et al., 2014). Each GI/GS is associated with a number (1, 2, 3. . .) and each numbered GI/GS is then subdivided by alphabetic letters (a, b, c. . .), which can be divided further by numbers

associated with warm and cold phases. This numbering system allows the incorporation of data from new sites if additional variations or oscillations are found within a specific GI/GS. For example, GI-1 contains three warm periods, where the two oldest are the Allerød and Bølling events. GS-1 is also called Younger Dryas (YD), from the name of the alpine-tundra wildflower *Dryas octopetala*, whose pollen is particularly abundant in sediments of this period (Alley, 2000b). Older Dryas (GI-1d), however, is the cold spell between the before-mentioned Allerød (GI-1c) and Bølling (GI-1e) (Rasmussen et al., 2014).

D-O events seem to occur in 1,470 year cycles (Bond et al., 1993). Nevertheless, while they generally occur every 1,470 years, some D-O events are 'missed' and the next does not appear in ice core records for another ~1,500, ~3,000, or even ~4,500 years (multiples of 1,470) (Rahmstorf, 2003). While this semi-irregular pattern suggests D-O events are influenced by a cyclical event, a precise cause has yet to be determined (Braun et al., 2005).

A D-O event starts with an abrupt jump from a period of extreme cold to relatively warm conditions which usually last for a few centuries to thousand years (Huber et al., 2006). But while Greenland is in a cold D-O phase, Antarctica experiences a slow warming until the temperature drops again, in correspondence of a warming in Greenland (Blunier and Brook, 2001; EPICA community members, 2006; Barker et al., 2009; Petersen et al., 2013). This antiphase relationship between the two polar regions is still not completely understood (Stocker and Johnsen, 2003, see chapter 2.2).

During the cold phase of a D-O cycle, there is a large increase in deposition of dust and sea salt in Greenland ice (Thomas et al., 2009). Sea salt concentrations are thought to be influenced by the sea ice position and wind speed in the potential source region and by the transport to the ice sheet region (Abram et al., 2013). During cold periods in fact, the atmospheric circulation is subjected to changes that lead to higher dust load which is attributed to higher aridity in the source region and higher storminess (McGee 2010; Sun et al., 2012; Mayewski et al., 2014). During this colder

climate, there is an increase of the speed of the wind, which lashes vigorously at the sea surface producing droplets that then outburst and leave sea-salt aerosol. The aerosol is then transported north to the ice sheet region. These changes in atmospheric circulation seems to take place at a hemispheric scale (Thomas et al., 2009).

Besides $\delta^{18}O$ and the analogue δD, which are proxies of temperature, and *deuterium excess* (d= $\delta D - 8\delta^{18}O$), which is a proxy of moisture of the source region (Pfahl and Sodemann, 2014), sea salt concentration and dust content are very important monitors of the abrupt transition of D-O events, since they have both seasonal and long-period variability (Abram et al., 2013).

In 2009, Thomas et al. performed a conventional high-resolution (2 mm) study of D-O event 8 (around 38 ka), pointing out that continental ions such as Ca^{2+}, Al^{3+} and Fe^{2+} appear to be the first to change preceding the other proxies by three-ten years, followed by snow accumulation rate, moisture source conditions and finally temperature. This scheme lead again to the hypothesis that atmosperic and oceanic change inside and outside the North Atlantic originates the D-O transitions. With relevance for the present project Thomas et al (2009) said:

"*Because Greenland ice cores contain signatures that are representative of different parts of the northern hemisphere climate system[....]well-resolved records from Greenland ice cores are a highly suitable piece of evidence for such comparison* (between North and South hemisphere climate sensitivity, ed)*[....]*

Finally, [...] it would be desirable to carry out similar studies on other Greenland interstadials, in order to establish a more general climatology of such transitions."

Evidence of D-O events has been observed primarily in Greenland ice cores, firstly in the $\delta^{18}O$ record from the Camp Century ice core, then in the $\delta^{18}O$ record of the Dye 3 ice core and finally confirmed when the two Summit drillings, GRIP (Dansgaard et al., 1993) and GISP2 (Grootes et al., 1993), were finished. At Summit, where horizontal movement is slow, the changes in

the oxygen isotope record should not, for most of the record, originate from internal folding of the ice layers due to ice movement over rough bedrock. Therefore, they must be a signal of actual climate changes occurring over most of Greenland. At first, the signal was circumspectly attributed to climatic changes in the Greenland/North Atlantic region (Bond et al., 1993; Hendy and Kennet, 2000). Later, the area was enlarged to include Europe when evidence of D-O cycles was found in Europe (Thouveny et al., 1994; Allen and Huntley, 2000, Spötl and Mangini 2002). The area influenced by the D-O cycles was later further enlarged to include most of the Northern Hemisphere and even across the Equator (Voelker et al., 2002).

During the last 10-15 yrs, evidence of D-O cycles has also been found throughout the world, from the Caribbean to the Arabian Sea in both Northern and Southern Hemisphere (Schulte & Muller, 2001; Spotl and Mangini, 2002; Burns et al., 2003; Schmidt et al., 2006; Fleitmann et al., 2007; Itambi et al., 2009; Lachniet et al., 2009) (Fig. 2.3).

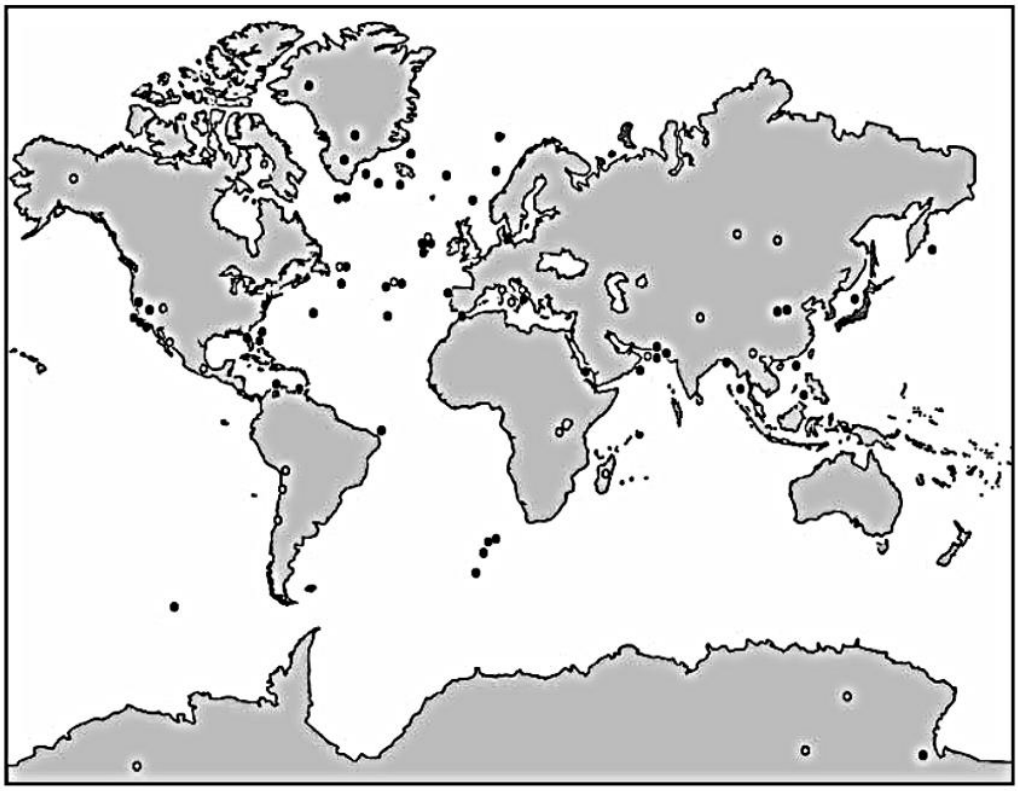

Figure 2.3: Global spatial distribution of sites where impacts of Dansgaard-Oeschger cycles have been recorded in paleorecords. Black dots indicate sites with a clear D-O type oscillation, open circles show sites where no or unclear D-O cycles have been found (after Voelker et al., 2002).

2.1.1 - The trigger of Dansgaard-Oeschger events/cycles

Many studies suggest that ocean heat transport - rather that atmospheric heat transport - is likely the primary cause of rapid climatic changes such as DO events, since ocean currents carry more heat during the same amount of time at low latitudes compared to atmospheric air masses (Broecker, 1997; Boyle, 2000; Rahmstorf 2003; Schmidt et al., 2006, Zickfeld et al. 2007, Li et al., 2010; Thornalley et al., 2013). The evolution of a D-O event begins with a temperature change (warming or cooling) in the northern hemisphere, as evidenced by comparison between Antarctic and Greenland ice cores (WAIS Divide Project Members, 2015). This temperature change would then spread throughout the north hemisphere, and finally, the southern hemisphere would show a lagged response. Such a delay strongly suggests that ocean heat transport is the cause, as an atmosphere-driven event would see global temperatures change much more rapidly (Landais et al., 2015).

A slowing of the global thermohaline circulation is one of the most widely accepted hypotheses. During the past 120 kyrs, ice sheets covered large expanses of Earth's surface. At times, these ice sheets would inject freshwater into the ocean by melting or depositing icebergs directly into the ocean. It has been suggested that these injections of freshwater coming from the ice sheets sufficiently diluted the surface ocean to slow the thermohaline circulation (THC) (Broecker, 2009). Since the THC plays an important role in transporting heat poleward, a slowing of the overturning circulation would cause the North Atlantic to cool. Later, as the addition of freshwater decreased, ocean salinity increased and climate conditions recovered.

There is still disagreement over what exactly causes this change in heat transport (Zickfeld et al., 2007). Some have argued that the Atlantic THC changes in strength throughout the cycle of D-O events (Boyle, 2000, Kissel et al, 2008); possibly associated with changes in ocean convection properties during D-O abrupt shifts (Dokken & Jansen, 1999).

Marginal changes in solar energy output and other climate forcings ('tipping points'; Lenton et al, 2008), which would in turn affect other Earth processes such as THC, have also been hypothesized as triggers of Abrupt Climate

Changes (ACC), defined as “transition of the climate system to a new state at a rate determined by the climate system itself and faster than the cause, after the system is forced to cross some threshold” (Lenton et al., 2008). The 1470 year cycle, however, does not align with the short-term solar cycles of 87 and 210 years. To get around this, some hypothesize that the solar cycle may cause a chain reaction that could at times have a noticeable effect on climate (Bond et al., 2001). In the latter paper it was proposed that surface winds and surface ocean hydrography in the subpolar North Atlantic have been influenced by variations in solar output, inferred by changes in the production rates of the cosmogenic nuclides carbon-14 and beryllium-10, as direct proxies of solar activity, matching centennial to millennial time scale changes in proxies of drift ice measured in deep-sea sediment cores (Bond et al., 2001).

The amplifying mechanism, therefore, may have been solar-triggered reductions in North Atlantic thermohaline overturning, especially if accompanied by increased sea-ice fluxes into the Nordic Seas. Indeed, during the late 1960s to late 1970s an increase in windblown Arctic drift ice through the Fram Strait between Greenland and Svalbard Islands resulted in a surface water freshening of 0.4-0.6 salinity units in the Nordic Seas and subpolar North Atlantic coined ‘the Great Salinity Anomaly’ (Belkin et al., 1998), falling within the range of salinity decreases implied by planktonic $\delta^{18}O$ measurements of the eastern North Atlantic (Bond et al., 2001).

Braun et al. (2005) identified also a solar origin for the 1470-years glacial D-O cycle. They developed a numerical model that shows rapid climate shifts similar to the Dansgaard–Oeschger events with a spacing of 1470 years, when forced by periodic freshwater input into the North Atlantic Ocean in cycles of 87 and 210 years. They attributed the robust 1470-year response time to the superposition of the two shorter cycles, together with strongly nonlinear dynamics and the long characteristic timescale of the thermohaline circulation. For Holocene conditions, similar events do not occur.

The D-O events seen in the Greenland ice core records have Antarctic counterparts called Antarctic Isotopic Maxima (AIM; EPICA community

members, 2004). The shape is, however, different and the phase is shifted. Stocker and Johnsen (2003) proposed a simple model for the dynamics in which North Atlantic temperature changes are associated with those in the South Atlantic. These changes are of the same magnitude but of opposite sign, which is why the model is called "the seesaw". The temperature of the Southern Ocean, by which Antarctic temperatures are influenced, then drifts toward this South Atlantic temperature (Barker et al., 2009) (Fig. 2.7).

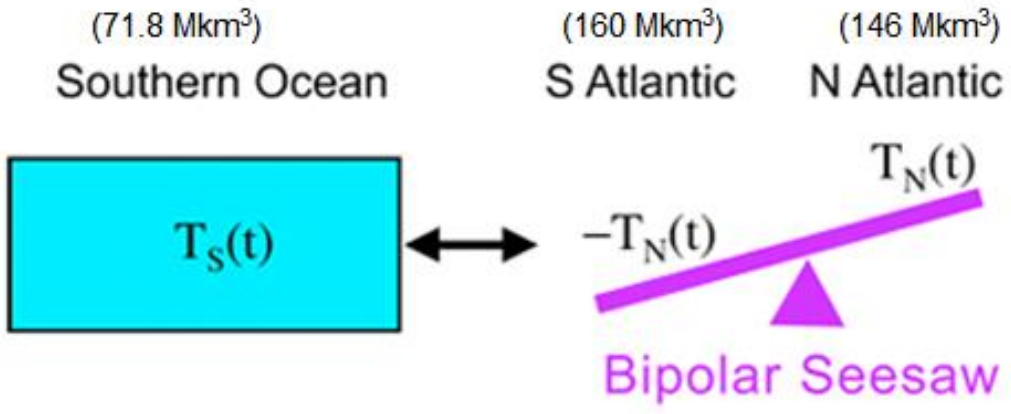

Figure2.7: Schematics of the bipolar seesaw. North Atlantic temperature changes are mirrored by equal amplitude South Atlantic changes of opposite sign. Southern Ocean temperatures are equilibrated with South Atlantic temperature. In brackets the size of the water reservoirs of each component (modified from Stocker and Johnsen, 2003).

The response of the Southern Ocean is slow compared to the Atlantic temperature seesaw, being a greater heat capacitor compared to the Atlantic and strongly separeted from the remaining global circulation system. In its cleanest form, and without any other climate processes at work, the model would produce a step-shaped Northern Atlantic climate curve (black) and a slower Southern Ocean response (green curve) (Fig. 2.8).

The modelled curves resemble the observed records from Greenland mimicking North Atlantic temperatures and Antarctica representing Southern Ocean and Antarctic temperatures (Wunsch, 2003). This simple seesaw model can to a large extent account for both the phase change and the shape of the events.

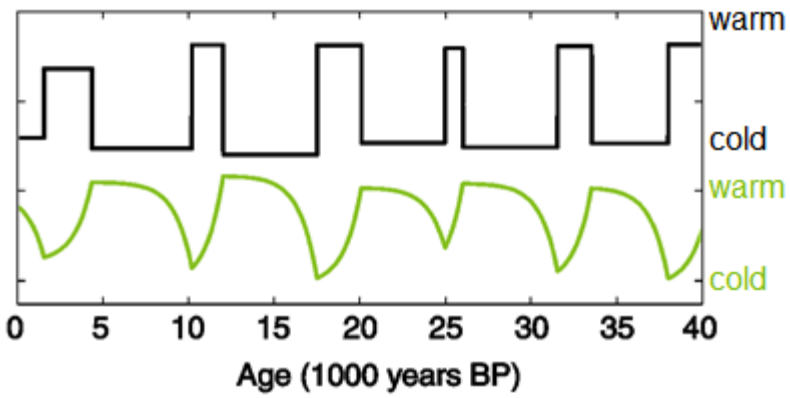

Figure 2.8: Theoretical bipolar seesaw climate curve of the North Atlantic (black) and Southern Ocean (green). The Southern climate warms when Greenland is cold and vice versa. On the y axis T or a proxy of temperature is assumed (Seidov, 2005).

The distinction of in-phase versus antiphase in the context of millennial climate change is challenging and requires that the common time scale of palaeoclimatic records be known with a resolution better than 500 years or less, irrespective of whether the time scale is absolute or relative (Stocker and Mysak, 1992). Nevertheless, current palaeoclimatic evidence suggest that abrupt climate changes were not contemporaneuos in the two hemispheres (Landais et al., 2015, WAIS divide project members, 2015). In fact, data show that, on average, abrupt Greenland warming leads the corresponding Antarctic cooling onset by 218 ± 92 years (2σ) for Dansgaard–Oeschger events, including the Bølling event. Greenland cooling then leads the corresponding onset of Antarctic warming by 208 ± 96 years. Considering the short timescale, it is likely that the abrupt climatic signal propagates to the Southern Hemisphere high latitudes by oceanic rather than atmospheric processes. (Capron et al., 2010; Landais et al., 2015, WAIS divide project members, 2015). This is also supported by a analysis of a pollen record from New Zealand (Singer et al, 1998).

Numerous modeling studies (Crowley et al., 1992; Blunier et al., 1998; Wunsch, 2003) have shown that changes in the meridional heat transport in the Atlantic Ocean, caused by sudden changes of the Atlantic's thermohaline circulation, are resulting in antiphase behavior of north and south. A sudden increase of the northward meridional heat flux draws more heat from the

south and leads to a warming in the north that is synchronous with a cooling in the south (Rintoul et al., 1991). It has been shown that the stability of this circulation is limited (Manabe et al, 1997) and that changes in the surface salinity can trigger major reorganizations of this circulation. More importantly, simulations demonstrate that the amplitudes and rapidity of events compare well with the paleoclimatic record (Mikolajewicz et al., 1997).

Another plausible mechanisms capable of explaining the recurrent climatic changes that occurred on Earth during the Quaternary era is *stochastic resonance*.

Stochastic resonance (SR) was first proposed to explain the 100 kyrs periodicity of glacial cycles by Benzi et al., (1981). However, this original idea has not been supported by subsequent evidence. Meanwhile, the concept of stochastic resonance has found numerous applications in physics, chemistry, the biomedical sciences, etc. In an analysis of the Greenland ice core record Ganopolski et al (2002) found that the statistical properties of abrupt warmings such as DO events are consistent with stochastic resonance, but inconsistent with the more straightforward stochastic mechanisms such as a simple white-noise response. Various ocean circulation models support the hypothesis that even small freshwater forcing can abruptly switch the North Atlantic deep water (NADW) between different equilibrium states (Ganopolski, 2002; Lenton et al., 2008). These models exhibit hysteresis behavior, whereby the system flips rapidly from strong to weak/no overturning, or vice versa, after crossing some surface salinity threshold. Furthermore, the overturning can be bistable, meaning that it can exist in either state for a given range of freshwater forcing. Glacial boundary conditions may narrow the hysteresis loop, such that a smaller range of salinity forcing is required to cause abrupt switches (Hawkins et al., 2011).

Periodic or quasi-periodic salinity “triggers” may result from internal ice sheet dynamics (iceberg calving) (Schmittner et al., 2002) or possibly solar variations. When combined with white noise salinity variability (natural long-time variation of salinity), the required magnitude of salinity forcing is further reduced, giving the stochastic resonance (Alley et al., 2001). Similarly

Ganopolski and Rahmstorf (2001) modelled a reduction and subsequent resumption of the AMOC imposing a sinusoidal freshwater input flux with period 1470 yrs but the rate of overturning required by the model was unrealistically high (~50 Sv).

However, Winton (1993) showed that a rapid shift towards higher values of overturning rate of the AMOC could be produced on a millennial scale without the need of a periodicity. Nevertheless, all these hypotheses predicted a magnitude of the warming which was substantially less than the one reconstructed for Greenland during D-O events (Huber et al., 2006).

Another complementary mechanism for triggering D-O warmings involves seasonal variations in sea ice cover (Li et al., 2005): Removing winter sea ice cover over a large part of the North Atlantic results in an increase of 5-7 °C over Greenland, consistent with the lower end of D-O warm phases inferred from $\delta^{18}O$ and $\delta^{15}N$ of gases trapped in the ice (Huber et al., 2006). Therefore, a reduction of sea ice, perhaps induced by wind stress or heat transport variations, could account for the rapid warming onset of a D-O event (Li et al, 2010), but cannot explain the gradual cooling of the warm phase and the sustained stadial part which typically lasts hundreds of years, even if some studies suggest that the sea ice loss could promote a reorganization of the water column allowing heat release and gradual cooling (Dokken et al., 2013).

The role of seasonality switches dominated by wintertime plunges of Greenland temperature has been highlighted by Denton et al. (2005). The authors suggest that, during the last glaciation, the climate system of the northern hemisphere was very close to a winter threshold possibly related to AMOC bimodal state. The non-linear variation of climate forcings such as sea-ice extent could cause winter climate to cross this threshold repeatedly with consequent change in seasonality that might have amplified the signal of abrupt climate changes in the northern hemisphere.

Petersen et al. (2013) hypothesize an similar mechanism for a D-O cycle: In stadial conditions sea ice over the North Atlantic expands; local albedo and insulating effect of the ice causes the temperatures to decrease and to

remain low as long as an ice shelf is present. A modest weakening of the AMOC would then cause the subsurfaces water to warm facilitating the collapse of the ice shelf. The only ocean cover present would then be sea ice and floating icebergs which could easily melt as a consequence of changes in wind stress or heat transport, resulting in an increase of the freshwater input and the open ocean area and a further weakening of the AMOC. This can explain the abrupt warming that starts a D-O event. Increase of precipitation over Greenland would then induce a positive mass balance during the interstadial phase, helping the ice sheet to grow and the Greenland temperature to slowly decrease. Once the ice shelf would reach a critical size, it would cause the sea ice to rapidly expand through positive albedo feedbacks, driving the climate back into stadial conditions.

Zhang et al. (2014) simulated an abrupt transition from weak to strong AMOC mode resulting from a gradual variations in the height of the North Hemisphere Ice Sheet (or gradual CO_2 change) triggering a non-linear response of the glacial ocean. This would be induced by a change in the sea ice coverage and the subpolar and subtropical gyre systems in the North Atlantic, both of which can occur in response to a change in the westerlies wind stress which would shift northwards after the increase of the height of the LIS. This is consistent with other recent simulations (Gong et al.,2015) showing that an increase in the surface wind stress curl over the North Atlantic ocean is positively correlated to higher topographies of the LIS, resulting in an intensification of the subtropical and subpolar gyres and the western boundary currents (WBCs).

Recently, Roberts et al., (2014) suggested that any cooling corresponding to Heinrich events is also a result of the non-linear combination of both freshwater and togographic forcing of the LIS producing a weakening of the THC without a complete cessation of the AMOC. Indeed, recent studies using the $^{231}Pa/^{230}Th$ and $^{143}Nd/^{144}Nd$ proxies (Böhm et al. 2015) suggested that AMOC persisted strongly during most of the last glaciation, showing only few possible periods of complete shutdown. Indeed many studies suggest that AMOC shifts from on to off mode cannot account solely for the many D-O events that puncuated the last 120 kyrs (Rahmstorf 2002; Zickfeld et al.,

2007), even if evidence of a pronounced shift in the circulation regime of NADW at the onset of glacial conditions of DO events exists (Thornalley et al., 2013).

Böhm et al. (2015) also showed that AMOC minima better coincide with Heinrich events than with D-O cycles. The link between these two North Atlantic climatic phenomena has been drawn recently also by Menviel et al (2014). In their simulation, a continuum between Heinrich events and D-O events exists: Ice calving, induced by an instability of the North Hemisphere Ice Sheet, is responsible for Heinrich events and for the input of freshwater into the ocean. However, Barker et al. (2015) showed a systematic delay between pronounced surface cooling and the arrival of ice-rafted detritus (IRD), demonstrating that iceberg discharge represents a consequence of the cooling rather than a cause, providing even so a positive feedback for enhancing stadial conditions. The consequent weaking of the AMOC would reduce the transport of heat northwards leading to a strong cooling in the North Hemisphere which is more pronounced at high latitudes due to albedo feedbacks. Such temperature changes would induce a strong gradient over the north hemisphere and therefore a strengthening of the North Easterlies trade winds with conquent shift of the Polar Front and the ITCZ southwards, resulting in more dry and arid conditions over the entire North Atlantic. The latter can be observed in stadial conditions in many ice cores proxies. As proposed by Petersen et al. (2013), a new mass balance of the ice sheets would reduce the freshwater input, increase the salinity of the ocean water and strengthen the AMOC again, initiating a new stadial/interstadial transition.

It is clear from this review that many different explanations exist regarding the mechanisms responsible for millenial and sub-millennial climate variability in the past glacial period, although the general consensus focus on changes in the AMOC as a possible trigger.

Recently, a 800 kyrs synthetic record of Greenland climate variability has been reconstructed from Antarctic temperature records of the last 8 glacial cycles (Barker et al., 2011). The similarity between the Greenland synthetic

and the Greenland ice core record for the first 120 kyrs represents solid evidence to extend the Greenland temperature reconstruction further back in time, showing that millennial time scale variability and abrupt climate oscillations possibly occurred in Greenland throughout the last 800 kyrs. Barker et al (2011) suggest that the bipolar seesaw played an active role in the mechanisms of deglaciation, in combination with albedo feebacks and a change in the insolation forcing, with a super-critical size of continental ice sheet as a precondition. It is possible, therefore, that the observed late Pleistocene variability might be the result of an interaction between millennial and orbital variations, modulated by the bipolar seesaw. Again Barker et al. (2014) suggest that sudden changes in the ocean/atmosphere circulation patterns, triggered by a change in orbital configurations, such as a decrease in 65° N summer insolation cooling the NADW coupled with a decrease in obliquity facilitating sea ice formation in the Southern Ocean, lead the climate system above a threshold across which ocean circulation enters its glacial mode.

However, a recent review of the bipolar seesaw model (Landais et al., 2015) suggests that Greenland temperature could be decoupled from AMOC and low latitude atmospheric circulation changes during long stadials, while Antarctica show fast teleconnection between temperature and atmospheric circulation at the same time, thus challenging Greenland temperature reconstruction based on Antarctic records (Barker et al., 2011).

In conclusion, the bipolar seesaw might not represent the complexity of the climate processes involved in DO events, but remains the most comprehensive model to assess rapid climatic changes that are punctuating the last glacial cycle.

2.3 - The global cycle of sea salt and dust inferred from Greenland ice cores

Dust and sea salt records in North Greenland ice cores show prominent variations in concentrations between seasons, both for present day

conditions and glacial periods. At the present day, the largest portion of dust and sea salt is deposited during the winter-spring season, with sea salt usually peaking slightly before dust (Ruth et al., 2002).

On longer time-scales, the supply of dust and sea salt to the polar regions is strongly related to climate, because the ice cores record remarkable variations in the impurities amount that correlate strongly with isotopic variations such as $\delta^{18}O$ (Dansgaard et al., 1984, Petit et al., 1990; Thomas et al., 2009). For example, during the Last Glacial Maximum (LGM), dust concentrations were up to 100 times higher than at present day, and sea salt up to ten times higher (Steffensen, 1997, Ruth et al., 2003). The high amount of dust during the LGM has been associated with a combination of different factors, such as globally more arid condition and a more intense wind circulation in the source regions (De Angelis et al., 1997, Ruth et al., 2003), together with a southward movement of the polar front (De Angelis et al., 1997) and an extension of the source areas since the sea level was up to 120 m lower than present day.

The global dust cycle represents an important factor to be considered in climate model predictions. Satellite observations can reproduce the large-scale patterns of dust for the present day (Derbyshire, 2003; Tegen, 2003), but for the past glacial period, polar ice cores provide extremely important information because they provide both dust and sea salt records, so that the climatic influences on these two different particulate aereosol species can be simultaneously investigated. Aerosol dust are better characterized than sea salt aerosols since its record is available from many locations world-wide and also because its coupling with the climate system is more clearly defined (Kohfeld & Harrison, 2001). In fact, dust aerosols play an important role in the global radiative balance, on atmospheric chemistry and biogeochemical cycles (Derbyshire, 2003; Tegen, 2003). Its importance lies also in the fact that rapid climate changes, such as D-O events or glacial/interglacial transitions, in general occur more abruptly in dust records than in other proxies, including isotope records (Dansgaard et al., 1989; Fuhrer et al., 1999, Thomas et al., 2009).

2.3.1 - Atmospheric dust

Mineral dust particles with grain size less than 5 μm are loaded into the atmosphere by strong surface winds, globally amounting over 10^{11} kg yr^{-1} (Prospero et al., 1983).

The geographical variation of dust sources reveal that most of the sources are located in the northern hemisphere, between North Africa, Middle East and Central Asia (Prospero et al., 2002) (Fig. 2.9).

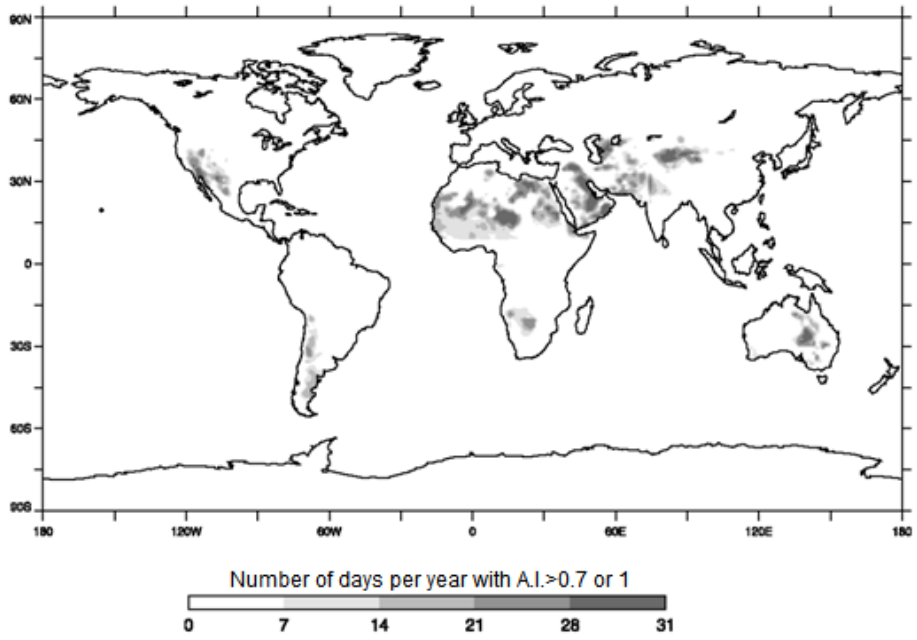

Figure 2.9: Global distribution of dust sources detected by 'Total Ozone Mapping Spectrometer' (TOMS), on the Nimbus 7 satellite measuring backscattered UV radiance, indicated as Aerosol Index (A.I.) (Prospero et al., 2002).

Winds pick up aerosol dust and deposit it mostly down-wind near source areas, but part of the dust may be lifted up to into the mid and upper troposphere and long-range transported over thousands of km by high altitude winds, as far as to polar regions like Greenland and Antarctica. Although the physical proccesses governing dust mobilization and transport are well understood, modellers have experienced problems in reproducing ice core levels of dust and sea salt concentrations from the last glaciation based on present day knowledge of atmospheric circulation. (Reader & McFarlane, 2003; Werner et al., 2002). Early studies explained this with an expansion in the source areas by desertification or exposure of continental

shelves (Grousset et al., 1992; De Angelis et al., 1992). Later it has been suggested that dynamical factors like stronger circulation (Werner et al., 2002) and low precipitation (Yung et al., 1996, Fischer et al., 2007) increased the long-transport capability of atmosphere and the dust lifetime, which makes it easier for particles to be deposited in the remote polar regions. The most important source region for dust, inferred by isotopic composition of Sr and Nd together with mineral characteristics, are located in the Asian deserts (Svensson et al., 2000), and mainly from the Taklamakan desert north of the Tibetan Plateau (Bory et al., 2003a).

The dust in the Greenland ice cores is characterized by particles that have dimensions of about 2 μm in diameter (Svensson et al., 2000). Such fine particles are mobilized in the source region by a process called ‘saltation’, when larger particles, in the range of 60-100 μm, are carried by surface winds and successively impact finer ones, lifting them high enough to be sustained and transported by winds (Pye, 1995).

A limiting effect on dust emissions is provided by soil moisture, which tends to bind particles together, making the surface more resistant to mechanical erosion. The presence of vegetation across a potential dust source area can also act as a control for emissions. Plants act as a protective cover and inhibit wind erosion by decreasing the amount of wind that reaches the soil surface (Field et al., 2010). However, moisture also induces chemical and physical weathering, which, by the action of water, tend to make the particles finer and therefore more likely to be mobilized. Furthermore, water leaches salts from rocks and, during dry seasons, these salts can form a resistant crust over the soil surface, enhancing the dust availability. This explain why semi-arid areas, like alluvial fans or lake shorelines are greater sources of dust than hyper-arid areas (Arnold et al., 1998), as shown by satellite observations (Prospero et al., 2002). Processes like glacial crushing and grinding also produce silt-sized particles (Pye, 1995). Preferential reservoirs of these particles are topographic lows, where dust accumulates and forms source areas.

2.3.2 - East Asian dust sources

Globally, the major dust sources at present are the North African and Middle Eastern deserts, but, as mentioned in the previous section, the large desert areas in Central Asia play a predominant role as sources of Greenland dust, despite the fact that these areas are located far away from the major Quaternary ice sheets (Derbyshire, 2003). A large amount of dust from Chinese deserts is stored in Chinese loess deposits, which provide very important information for a better understanding of processes influencing the global dust fluxes and thus Greenland dust supply, and therefore have been carefully investigated (Zhang et al., 1999; Porter, 2001). Their importance resides in the fact that they are exclusively produced during glaciations and typically from the Quaternary period, since they are supposedely formed by sub-glacial grinding and subsequentely mobilized to glaciofluvial outwash plains (Muhs et al., 2013).

The wind systems in Eastern Asia are quite complex and have strong seasonality. During winter, a high pressure system over Siberia is formed, caused by the convergence of summer air flows being cooled over interior northeast Asia as days shorten. In the process of the Siberian High's formation, the upper-level jet is transferred across northern Eurasia by adiabatic cooling and descending advection. This creates the Asian winter monsoon, with cold and dry westerly and northwesterly winds (Dykoski et al., 2005). During summer, low pressure is formed over the southern asian continent due to radiative heating of air masses that transfer moist and warm marine air from the Pacific and the Indian ocean, towards China and Tibet. These areas north of the Tibetan Plateau and in northern China are currently arid areas, while areas in eastern China are relatively wet. However, during glacial times the water balance was much different due to changes in the strength of the monsoon and in the precipitation/evaporation balance, so that during LGM times freshwater lakes occupied what is now in some cases a salt lake or playa (Zhang et al., 2002).

During the Asian winter monsoon, dust is mobilized by westerly winds in the lower troposphere, and primarily deposited down-wind onto Chinese loess

deposits. However, during the spring season, desert dust storms occur and particles are transported towards remote regions such as polar areas (Zhang et al., 1999). The spring peak observed in ice core dust is very likely associated to this phenomenon that affects western China (De Angelis et al., 1997; Bory et al., 2003a), whereas deserts located in the inner Mongolia are likely to contribute to the year-round background of Greenland dust (Bory et al., 2003b). These storms are generated by strong winds from the confluence of cold air from the north and the warm air further south, where arid conditions exists during the spring season. The dust storms last three months from March to May, with a major occurence during April, when dust uplifted to the mid-troposphere is transported northwards (Sun et al., 2001). The highest frequency of dust storms is observed in the Gobi desert (Sun et al., 2001), but satellite measurements show strong seasonal activity from February to September in the Tarim basin (Prospero et al., 2002), which is surrounded by the Tian Shan to the north, the Tibetan Plateau to the south and the Pamir in the west and is largely occupied by the Taklamakan desert, where climate is extremely dry because air must cross high mountains to reach the desert and in so doing loses much of the moisture it carries. This results in a particularly strong and unique air dynamic: In summer, northerly and northwesterly winds prevail and meet in the central part of the Taklamakan desert to form a complex circulation system clearly reflected in the sand dunes of the desert, which, in this part, are up to 200 m high. In spring, when the surface land becomes warm, ascending currents start to form, and northwesterly winds dominate. This produces many storms able to fill the atmosphere with dust up to an altitude of more than 5 km (Bory et al., 2003a,b). Winds from other directions also raise clouds of dust into the air, covering the Taklamakan with a shroud for almost the entire year. For comparison, dust plumes created by storms in the Gobi desert do not reach more than 3 km in altitude (Bory et al., 2003a), therefore, the Taklamakan dust is much more likely to be long-range transported as far as Greenland.

Polar jet streams are responsible for this long-range transport and consist of very high altitude (7-12 km) winds near 60˚N that originate from strong temperature gradients between cold and dry polar air masses and warm and

moist air masses from lower latitudes. Around 30˚N, a weaker subtropical jet stream is flowing at even higher altitudes (10-16 km). These major jet streams are mostly westerly winds with a general shape that can be interrupted, split into two parts, flow in opposite directions or create loops (Baldwin et al., 2007). Together they form a global meandering wave where each meander is a “Rossby wave” and can penetrate consistently south into mid-tropical latitudes associated with the westerlies and with a high energy meteorological surface dynamic.

The jet stream patterns produce geographical locations where dust aerosol can be uplifted and transported more easily over long ditances (Schiemann et al., 2009). These locations are favourable positions where dust storms are created, and they strongly depend on jet stream seasonality, which is represented mainly by a southward shift of the polar front and the jet stream itself during winter (Schiemann et al., 2009).

Transport pathways of dust from China have been followed by satellites: Plumes formed in the Gobi and Taklamakan area are transported by the westerlies across the Pacific Ocean, and can reach the coast of North America in one week (Husar et al., 2001). These have been found to be the general transport patterns dust plumes, with a seasonal variation that brings higher dust concentrations between February and June (Propsero et al., 1990). In cases when the Rossby waves are particularly pronounced the jet stream seems to affect the climate over Greenland in various ways, such as producing heat domes and unusual melting over the ice sheet (Hanna et al., 2012). Variations in the circulation of the jet streams are likely related to atmospheric oscillation at various levels. A good example is the NAO (North Atlantic Oscillation) index, which by definition has a value that can be either positive or negative. In winters where NAO is positive, the Icelandic low pressure and the Azores high pressure are prominent, which drives a very strong westerly circulation that prevents cold Arctic air plunging southward and creating storms. In winters where NAO is negative, the low pressure zone over Iceland and the high pressure zone over the Azores are weakened, together with the westerly circulation. This allows Arctic air to move south and collide with tropical warm air, generating cyclones and

storms. The origin of the oscillation between positive and negative NAO is not well understood yet, and it varies from a few months to more than one year. This effect is superimposed on seasonal atmospheric changes described above (monsoons), producing a highly variable circulation that can account for the short scale variability observed in dust concentration of Greenland ice cores.

2.3.3 - Sea salt aerosol

Sea salt is produced either from evaporation of sea spray by bubble bursting or during wave breaking induced by wind (Wolff et al., 2003). Sea salt global emission (measured on <5 µm particles) is comparable to that of dust, again in the order of 10^{11} kg yr^{-1} (Prospero et al., 1983). Salt brines formed on top of sea ice during its formation have been established to be an additional source of sea salt aerosol for both coastal and inland areas in Antarctica (Rankin et al., 2002; Wolff et al., 2003) and Greenland (Rankin et al., 2004). However, until now, the respective contribution to the sea salt record in ice cores from sea ice brines and from the open ocean has not been quantified, so that the main source of sea salt aerosol is still thought to be bubble bursting and wave breaking in the open ocean triggered by storminess (Fenger et al., 2013).

Large scale transport properties of sea salt generated over open ocean are at present-day very similar to that for mineral dust, where conditions for uplift and long-range transport are related to wind patterns in the troposphere. Both the North Pacific and North Atlantic are the main sources of sea salt aerosol recorded in Greenland ice cores, with a distinct signature peak of ionic species during wintertime. This is compatible with the surface and upper-level wind speed measured over open ocean which, during winter, are on average 15 ms^{-1} and 50 ms^{-1} respectively, whereas during summer are <10 ms^{-1} and <20 ms^{-1} respectively (Risien and Chelton, 2006).

2.3.4 - Atmospheric circulation during the last glaciation

During the last glacial period Earth's atmospheric conditions were markedly different, since large continental ice sheets and mountain glaciers increased albedo and influenced pressure and temperature of the troposphere (Löfverström et al., 2014). Furthermore, the sea level during the LGM was <130 m lower than present day allowing continent to be exposed to weathering and providing space for ice shelves to grow (Yokoyama et al., 2000). This effect enhanced the climatic variability between polar regions and tropical-equatorial regions, strongly increasing the gradient of pressure and temperature of the atmosphere emphasized also by the presence of the LIS (Calvo et al., 2001). As a consequence, atmospheric circulation, and particularly jet streams, experienced a strong modification if we compared them to the present day.

Over the last 30 years many Global Circulation Models (GCM) have been developed to constrain ocean-atmosphere circulation during glacial periods (a partial list includes Manabe and Broccoli, 1985; Kutzbach & Guetter, 1986; COHMAP, 1988; Kageyama et al., 1999; Hewitt et al., 2003; Pollard, 2010; Yanase & Abe-Ouchi, 2010). Most of these models contain a sea level pressure field that, during the last glacial period, featured large high-pressure areas over the Laurentide ice sheet in winter and over the Scandinavian ice sheet in summer; so that storms were moving across the Laurentide ice sheet towards the Scandinavian ice sheet and the Arctic in summer, providing precipitation for snow cover in Greenland. The high pressure zones were generated by cooling over the ice sheet, a function of altitude. The higher the ice sheet, the thinner the atmosphere above and hence the more depleted in greenhouses gases that reduce outward radiative fluxes (Gong et al., 2015). In this scenario, the air over the ice sheets was significantly cooler and therefore generated a high pressure nucleus. This cold air was additionally maintained by the albedo of the ice sheet, which reflected a significant percentage of incoming solar radiation. Winds around these zones provided a greater westerly circulation over the Arctic than currently exists and weaker westerly winds more to the south, helping the eastern part on North America to have a more continental climate (Kutzbach & Guetter,

1986). In more sophisticated models (Rind, 1987; Feltzer et al., 1996, Peltier and Vettoretti, 2014) strong katabatic winds came off the Laurentide ice sheet. Storm systems and baroclinicity also experienced strong shifts in location, since the presence of the ice cap created a pronounced temperature gradient over North America which induced the formation of storms in mid-latitude regions on land. This situation extended also to the eastern North Atlantic, producing storms that crossed North America all the way to western Europe (Kageyama et al., 1999). The stronger latitudinal temperature gradient also intensified the jet stream in its subtropical positions, crossing the Pacific Ocean and the Eastern North Atlantic to Southern Europe. The low-pressure systems were displaced southwards from their current location, and the storms followed this modified path to the north of the ice sheets, along coastal Alaska and into the Arctic, increasing also their frequency and intensity (Bromwich et al., 2004). At high altitudes, the location of the Rossby wave troughs, which are currently over eastern North America, eastern Asia and eastern Europe in winter, appeared to experience no major changes (Feltzer et al., 1996); however, the southward shift of the jet stream, was followed in some models (Bromwich et al., 2004) by a ‘split-jet’ around the Laurentide Ice Sheet, bringing Pacific air over the Arctic. With cooling undoubtedly affecting the entire troposphere, in polar regions, the maximum temperature shift was reached just above ice sheets (Rind et al., 2001). The resulting increased temperature gradients at low altitudes, and the decreased temperature gradient at high altitudes, would have likely enhanced the west-winds in low-to middle troposphere and east-winds in the upper troposphere. In the North Atlantic, the southward shift of the storm pathway resulted in a generally more negative North Atlantic Oscillation phase, although in some models the north split of the jet stream maintained a strong positive NAO circulation. The Arctic equivalent of the NAO, the Arctic Oscillation (AO), was supposedly maximized at the surface, with strong positive values, which decrease to negative values with altitude in the troposphere (Bromwich et al., 2004).

3) Methodology

This section illustrates the development of the cryo-cell UV-LA-ICPMS procedures to perform ice core analysis, briefly describing both the equipment and the strategies utilized during this PhD project. Details of LA system and operational conditions are given in Della Lunga et al. (2014).

UV-laser ablation of frozen ice cores at Royal Holloway University of London utilizes a custom-built sample holder made of anodized aluminium specifically developed by Laurin Technic (Australia) to work with a two-volume LA cell (Müller et al., 2011). Its temperature is kept below -20°C using water-cooled peltier elements. This holder replaces the other conventional sample holders of the RESOlution M-50 excimer laser ablation system, with a wavelength of 193 nm (Müller et al, 2009). The LA system is coupled with an Agilent 7500cs ICPMS operated in collision/reaction mode. The sample holder can host at the same time three strips of ice 5 cm long, 1.2 cm thick and 1.3 cm wide. The strips are held in position by teflon-coated Cu-Be springs.

The temperature suggested for storing ice cores safely for long periods is around -25 °C (U.S National Ice Core Laboratory). At this temperature or at lower temperatures, microcracks, contamination of fossil air with modern air and recrystallation of ice is avoided (National Research Council, 2002).

In order to store and handle ice core samples directly at Royal Holloway University of London, our laboratory has been equipped with:

- A *Tefcold* freezer, with operating temperature kept at -37 °C (Fig. 3.1)
- Infrared thermometer *RayTemp 8 thermometer kit*, with a range of measurable temperatures from -60 to 500°C.
- A *Dilvac Dewar Flask SS/222*, with a capacity of 2 l and holding time of 48h, for the liquid nitrogen (LN) supply.
- A custom-made cold portable device utilized for sample handling and surface-cleaning when samples are removed from the freezer.

Figure 3.1: Tefcold freezer in the Laser Ablation Laboratory at Royal Holloway University of London. Operating temperature range from -36 to -38 °C. The freezer has been plugged into an Uninterrupted Power Supply (UPS) socket.

To handle ice cores in the ultra-clean (US10-100) laboratory at RHUL with an average temperature of +18 °C several possibilities were considered: Following the sketch in Fig. 3.2, polycarbonate pipes cut longitudinally in half were used for holding liquid nitrogen. The liquid nitrogen reservoir should have been cooling the entire box well below -20 °C, including an upper work-surface. However, tests made showed that polycarbonate, especially where welded, cracks when it has to hold LN for more than few minutes, which was not foreseen from material information (www.goodfellow.com/ pdf/1175_1111-010.pdf).

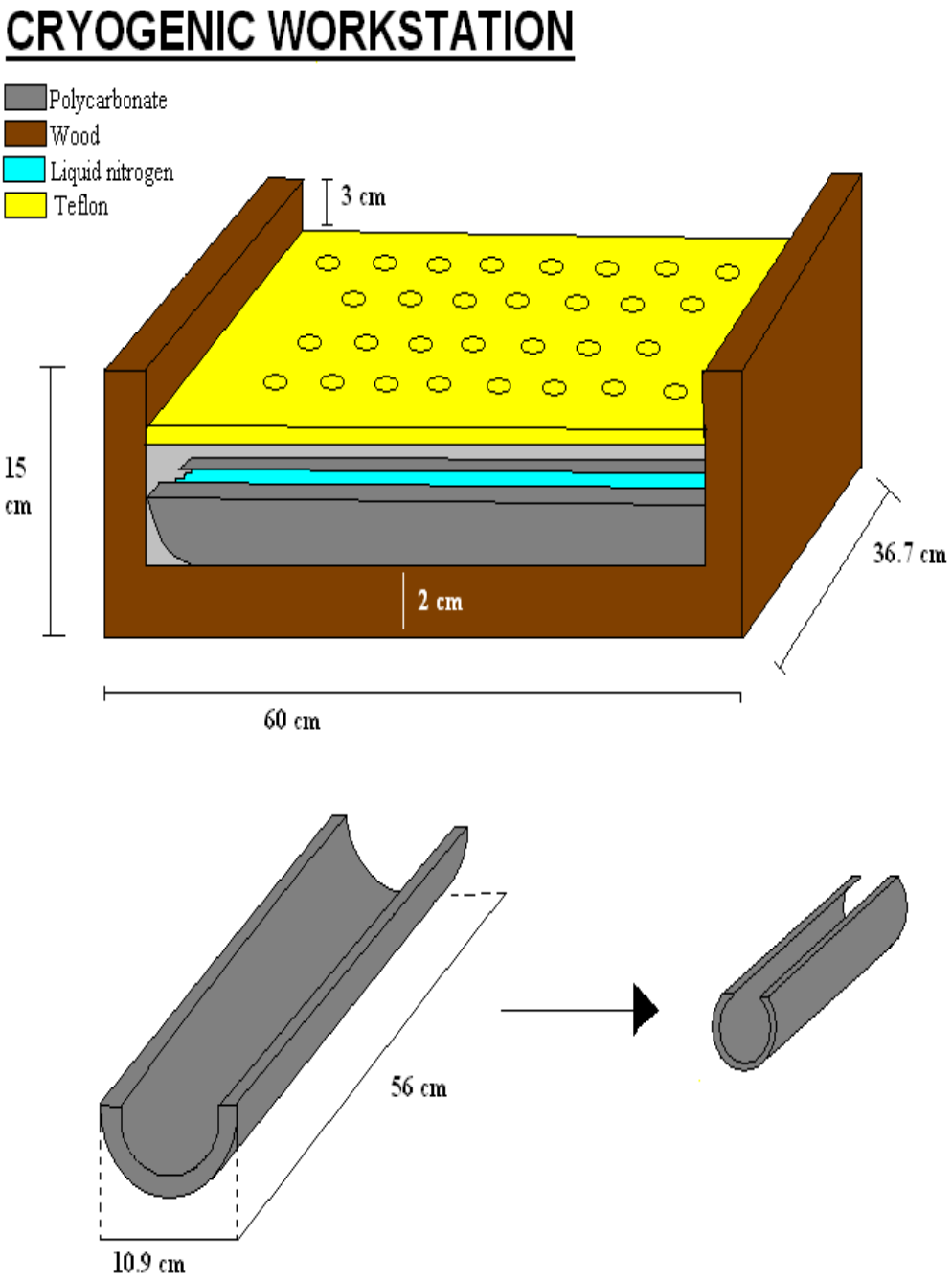

Figure 3.2: Sketch of the cryogenic workstation initially designed to locally produce a clean surface at sub-zero temperatures. The polycarbonate pipes were cut in two different ways, as shown in the figure above, in order to hold LN. The ice sample should lie on the top of the PTFE surface, which is kept cold by the LN reservoir underneath. Holes in the worksurface facilitate heat exchange.

Endcaps were firstly welded at either end of the polycarbonate pipes, which were then cut half way (Fig. 3.3).

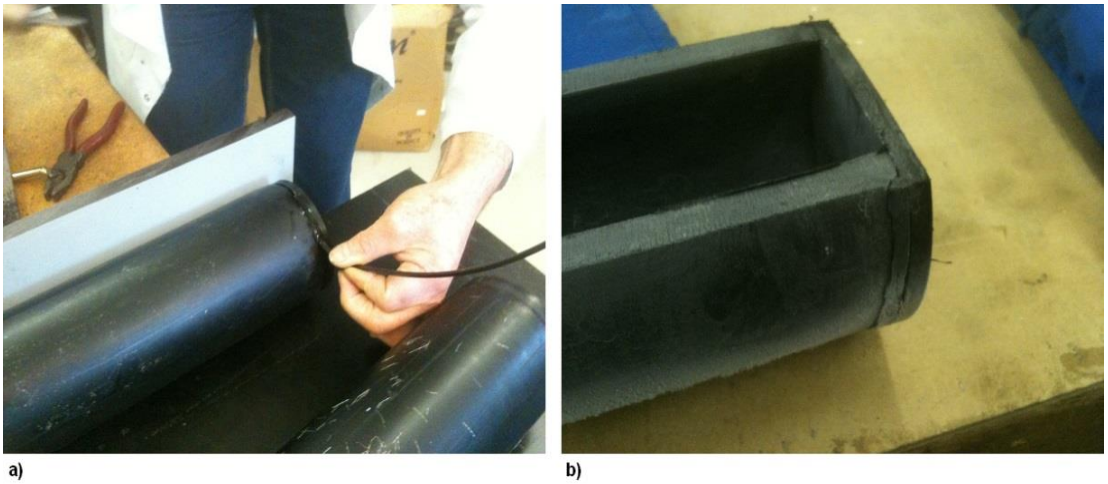

Figure 3.3: a) Endcaps were welded at either end of the pipes. b) The pipes were then cut longitudinally approximately half way (Fig. 3.2)

The pipes were then reinforced with transversal barriers, as in Fig. 3.4, and then filled with liquid nitrogen.

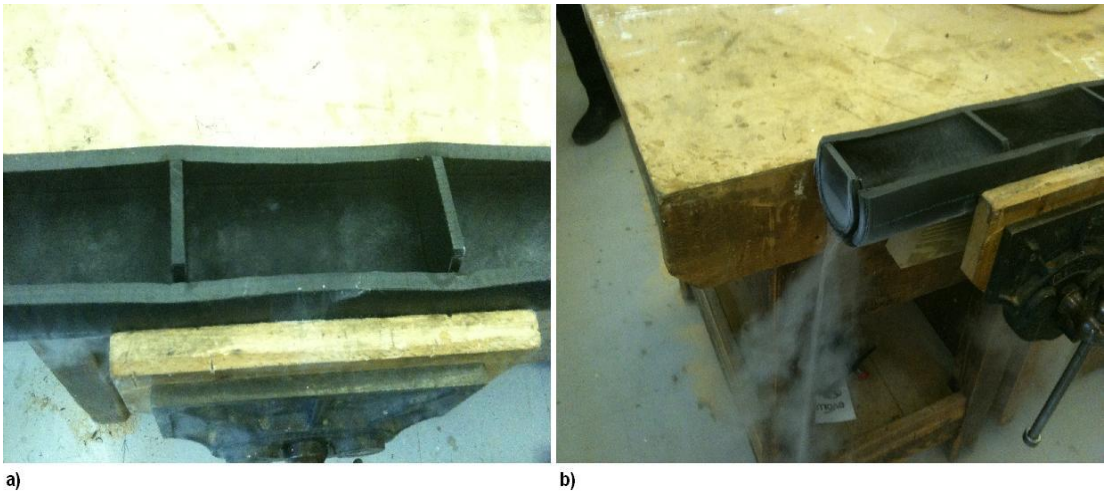

Figure 3.4: a) Polycarbonate pipe reinforced with 2 transversal barriers. b) Failure of the polycarbonate pipe where welded, approximately 5 min after being filled with LN.

When filled with liquid nitrogen the pipe started to shrink partially, and eventually it failed (Fig. 3.4b), after approximately 5 minutes.

Another attempt was made cutting a pipe as shown in Fig. 3.2, on the right. This shape was chosen to prevent evaporation of LN in order to prolongate the cooling capability, but once filled with LN the wall of the pipe shrunk too much to mechanically resist, and again it failed.

To hold liquid nitrogen for long enough, another material was tested, namely high density polyethylene (HDPE).

A PTFE worksurface was designed to be combined with a *Sanyo Coolbox BCS-130,* made of high-density polyethylene (HDPE), capable of holding 0.6 l of LN (Fig. 3.5).

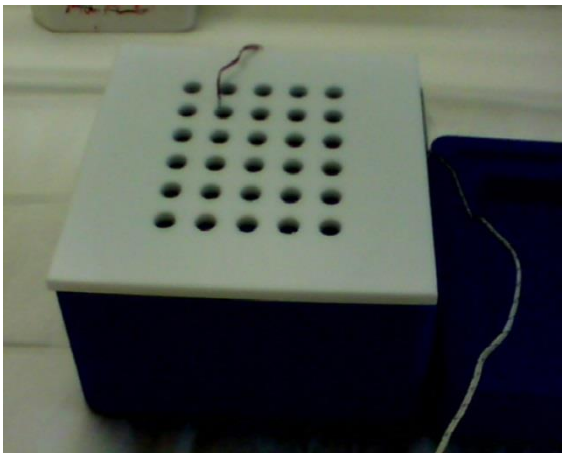

Figure 3.5:The purple box is a *Sanyo Coolbox BCS-130,* made of high-density polyethylene (HDPE). A custom-built PTFE worksurface with 0.8 cm holes was designed to reside on top of the coolbox.

Temperature tests made with the coolbox are illustrated in Fig. 3.6.

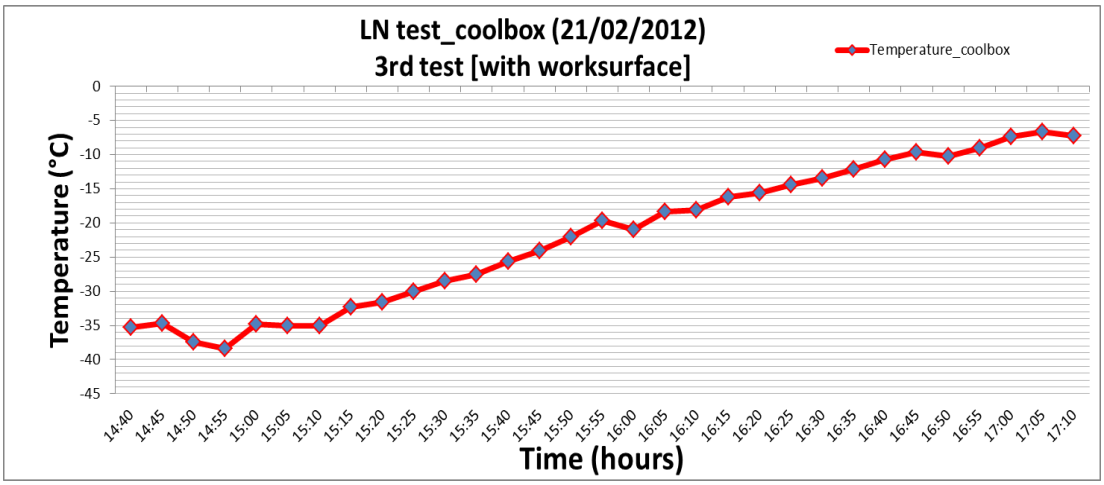

Figure 3.6: Test of the modified Sanyo Coolbox BCS-130. The temperature on the top of the worksurface was checked every 5 minutes with a thermocouple (as shown in Fig. 3.5). The graph shows that, once the coolbox volume is filled with LN the worksurface stays below 0°C for more than 2 hours. The temperature of -20°C is reached after more than 1 hour. Therefore, the operating time window for handling ice without contamination, is recommend to be 1 hour after the LN refill.

The graph above illustrates that the coolbox can be used easily to handle ice samples long enough without compromising them. A copy of the coolbox with larger capacity (2 l) has been subsequently made in HDPE at RHUL. The coolbox was used to perform ice cleaning via a custom-built PTFE vice featuring a metal-free blade (Della Lunga et al., 2014) and ice standard preparation inside class-10 clean hood.

3.1 - Ice Standard Preparation

Quantitative determination with LA-ICPMS requires calibration with a matrix-matched standard or an internal standard combined with an external standard with no matrix corrections. Previous LA-ICPMS ice core works (Reinhardt el al. 2003) utilized m/z=17 (^{16}OH) as internal standard and shock-frozen layers of reference water solutions as matrix-matched external standard. Owing to the UV-LA-ICPMS small sample consumption, however, m/z=17 was not resolvable in our case since it's often below ICPMS background level and also because it presents interferences by other oxygen isotopes.

Ice standards can be easily prepared by freezing a solution with known concentration of elements. However, this method produces frequently inhomogeneous ice standards, because elements tend to redistribute inside the ice if the freezing is not fast enough. We designed three PTFE moulds to create ice standards fitting the dimension of the sample holder. Further description of equipment is given in Della Lunga et al. (2014).

In order to produce homogeneous ice standards with <20 % varying concentrations over hundreds of µm a stepped procedure has been followed:

- A solution of 25 ppm of Na and Ca, 5 ppm of K and Mg, and 1 ppm of trace elements has been diluted 10 times (1 ml of solution and 9 of deionized H_2O).
- The solution was pipetted into three different PTFE moulds that had been carefully cleaned with HNO_3 and HCl using a 1000 µl *Eppendorf*

pipette. The solution was poured in steps of different quantities (see Fig. 3.7 and 3.8)

Four standards were thus obtained:

- Standard #1: 8 steps of 500 µl (4 ml in total)
- Standard #2: 6 steps of 750 µl (4.5 ml in total)
- Standard #3: 25 steps of 100 µl (2.5 ml in total)
- Standard #4: 1 step of 5 ml (5 ml in total)

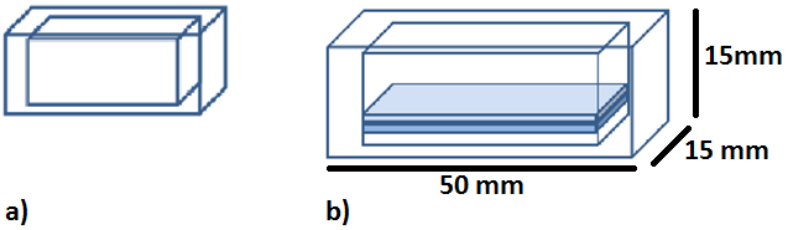

Figure 3.7:Sketch illustrating the standard preparation. a): Sketch of the PTFE mould, showing the outer case and the inner volume. b): Sketch of the PTFE mould filled with three layers of solution which represent three different steps. Every layer was subjected to shock freezing before being covered by the next layer. Ideally the positioning of the layers should resemble the sketch on the right, with flat horizontal layers.

Figure 3.8: Ice Standard preparation. Two different teflon moulds were dipped inside the HDPE coolbox lid. The standard solution was poured in different steps inside the moulds. As soon as the solution was poured shock freezing took place. This procedure avoids redistribution of elements in the ice caused by the process of freezing. The less the quantity of solution is poured in every step, the faster the freezing it is, and thus the less inhomogeneous the ice standard it is. However, PTFE surface do not allow a sufficient spreading of liquid and thus results in inhomogeneity. The temperature of the mould was constantly monitored. On average: -13.2 °C on the outer side, -101.7 °C on the bottom of the mould.

Most of the standard produced resulted in unsatisfactory homogeneity both laterally and vertically, shown by laser tracks and spots, respectively. An example of data acquired for standard 2 is illustrated in Fig. 3.9.

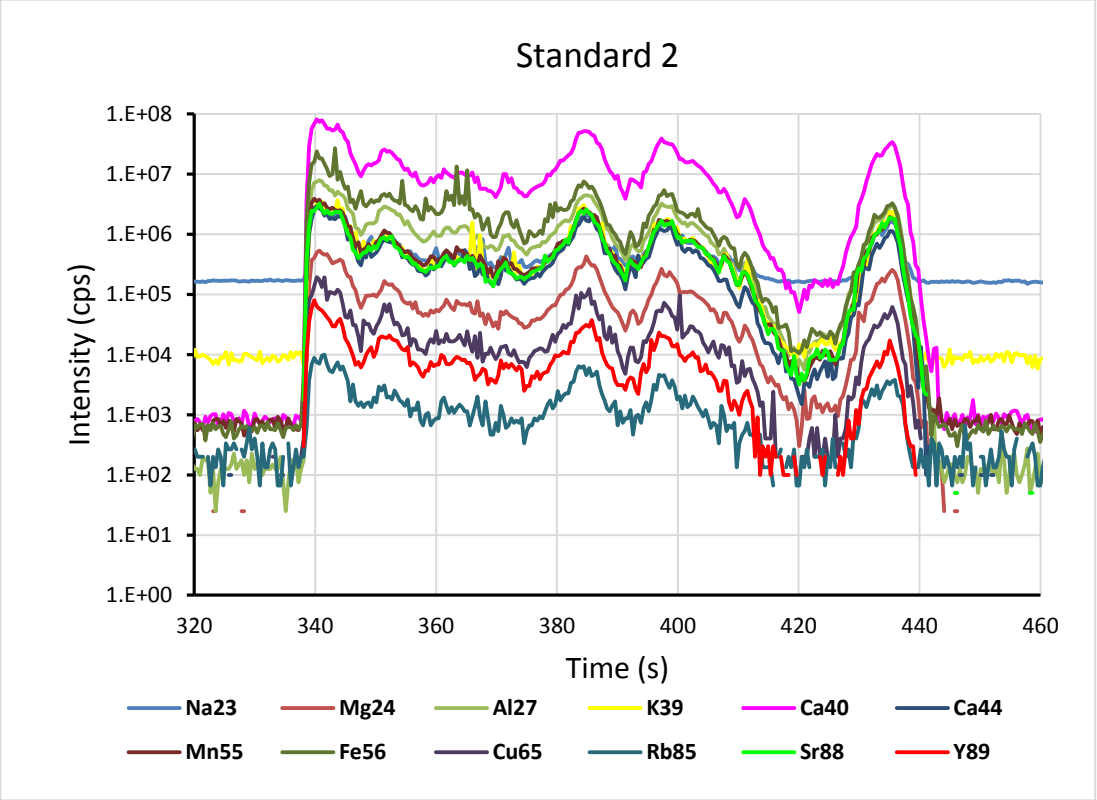

Figure 3.9: UV-LA-ICPMS data for a single spot drilled in standard #2. Spot size: 280 µm, repetition rate: 20 Hz, crater depth: approx 100 µm. Inhomogeneity of up to three orders of magnitude in the standard is clearly visible as the laser drills the ice surface.

Better results were achieved using a different ice standard mould (Fig. 3.10a). In this case a round PTFE cylinder was cut to fit a pyrex borosilicate petri dish. The cylinder features an inner opening of 45 x 10 x 10 mm. The standard solution can be pipetted into this rectangular slit and is nearly-instantaneously frozen as it comes in contact with the glass of the petri dish. The higher wettability of pyrex allows the solution to spread before freezing, producing a more uniform layer and homogenous content of impurities (Fig. 3.10b).

Relative standard deviation for data shown in Fig. 3.10b range between 18 and 25 % for all elements.

A further improvement in developing a technique to create homogeneous ice standard is described in chapter 5 (Della Lunga et al., 2015a, planned submission).

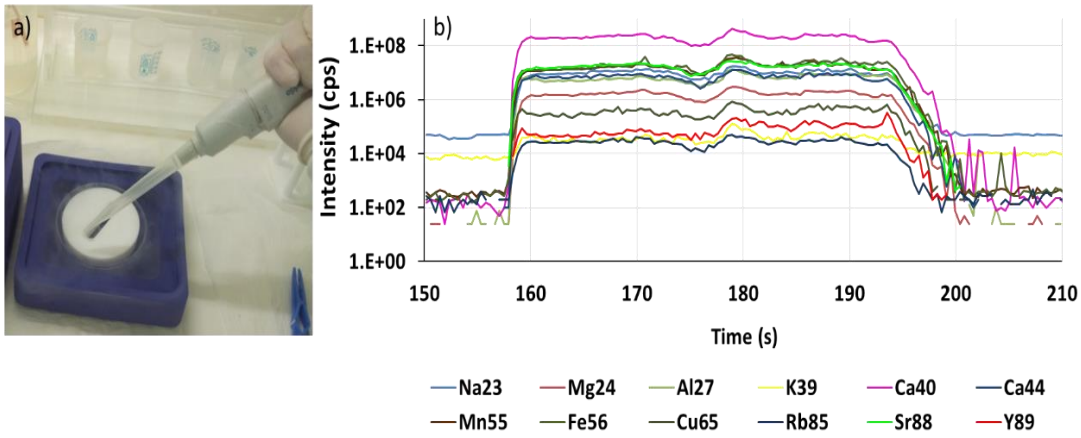

Figure 3.10: a) Alternative setup for ice standard preparation: the purple HDPE container is filled with liquid nitrogen where a petri dish is dipped together with a PTFE mould. The standard solution is pipetted into the internal opening of the mould and frozen in uniform layers. This procedure is repeated several times to produce a layered ice volume as in Fig. 3.7. b) UV-LA-ICPMS data for a 3 mm track in an ice standard prepared as described in (a). Spot size: 280 µm, repetition rate: 20 Hz, crater depth: approx 20 µm.

3.2 – Cleaning and smoothing procedures

The labware material included mainly pyrex borosilicate glass and teflon (PTFE). Cleaning was carried out routinely using the following procedures:

1. For PTFE:
    - Wiping the inside of the PTFE material with a sponge or kimwipe soaked in detergent bath solution and acetone.
    - 3 cycles of 15 min of ultrasonic bath in deionized water at 25 °C.
    - 2-4 hours of ~6M HCl bath at 75 °C.
    - 6-10 hours of ~7M HNO_3 bath at 90 °C.
    - Boiling in $H_2O_{deionized}$ at 100 °C for 2-4 hours.
    - Rinsing with ultra-pure deionized water (18 MΩ·cm) for 3-4 times.
2. For glassware:

- Brushing with wooden or plastic handles or sterile cotton swabs.
- 3 cycles of 15 min of ultrasonic bath in deionized water at 25 °C.
- Soaking for several hours in acidified water (a 1% solution of HCl or HNO_3).
- Rinsing with ultra-pure deionized water (18 MΩ·cm) 3-4 times.

Cleaning and surface smoothing of ice samples has been conducted using a custom-built PTFE vice (for details see Della Lunga et al., 2014). This procedure allows to reduce surface roughness, to improve ablation performances, to remove possible contamination from sample cutting, and to improve the visualization of the grain boundary network on the ice surface. The benefits can be seen in the figure below (Fig. 3.11).

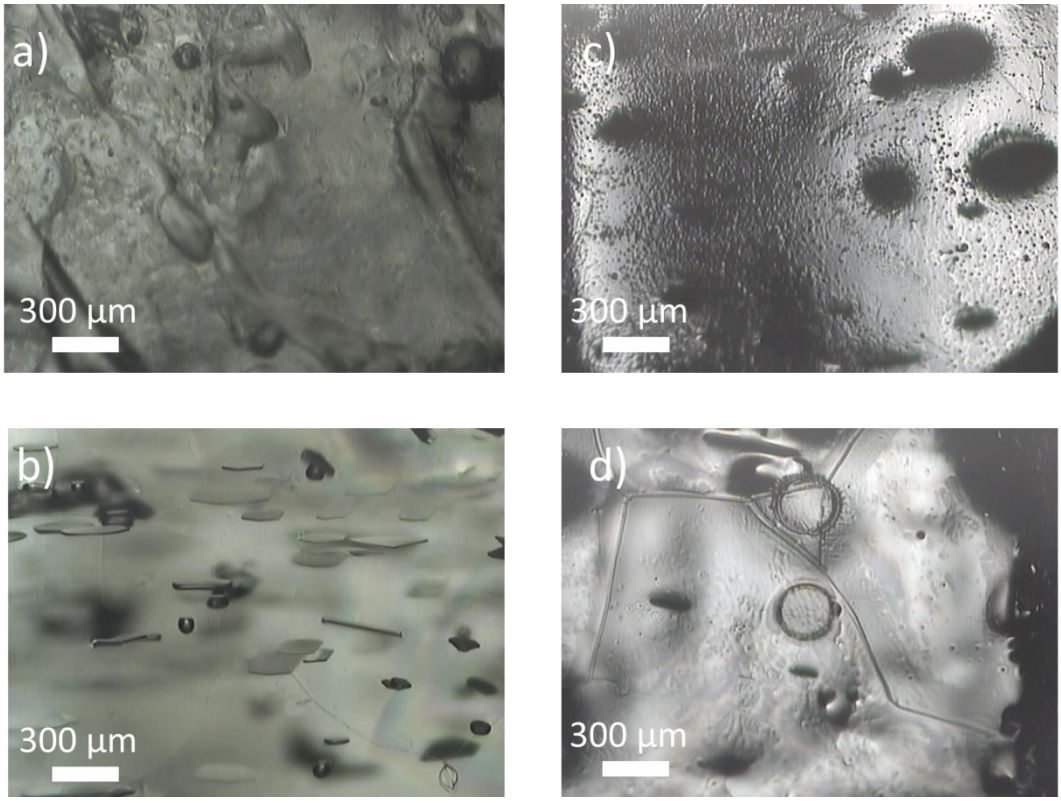

Figure 3.11: a) Unsmoothed ice surface in transmitted light. b) Ice surface seen in (a) after smoothing, transmitted light. The grain boundary network can be observed as well as air bubbles (black spots) and air hydrate and clathrates (rhomboid shapes). c) Unsmoothed ice surface in reflective light. d) Ice surface seen in (c) after smoothing, reflective light. Laser craters (280 µm) can be observed.

3.3 - Optical properties of ice

Optical properties of water and ice are mainly described by the refractive index, a dimensionless number that indicates how light, or any other radiation, propagates through a medium. It is defined as:

$$n = \frac{c}{v}$$

where *c* is the speed of light in vacuum and *v* the speed of light in the substance. For water *n* is 1.332986 at 20 ˚C, whereas for ice it is slightly lower: 1.31 at 0 ˚C (Warren and Brandt, 2008). In general, the index of refraction is a complex number with both a real and an imaginary part, where the latter represents the strength of absorption loss at a particular wavelength.

The measured intensity I of transmitted light through a layer of material with thickness x is related to the incident intensity I_0 according to the inverse exponential power law that is usually referred to as Beer–Lambert law (Warren and Brandt, 2008):

$$I = I_0 e^{-\alpha x}$$

where *x* denotes the path length and α is the absorption coefficient, also defined as:

$$\alpha = \frac{4\pi m_i}{\lambda}$$

where m_i (also called 'extinction coefficient') is the imaginary part of the refractive index *n* and λ is the wavelength (Warren and Brandt, 2008).

Absorption coefficients for water and ice are almost identical, as shown in the Figure 3.12.

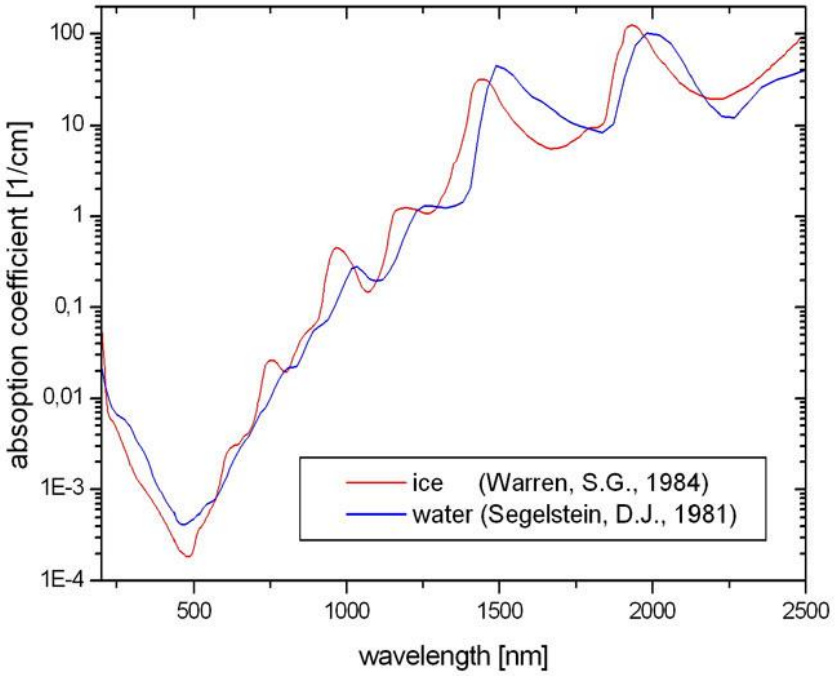

Figure 3.12: Absorption coefficient of ice (red line) and water (blue line) across UV, visible and near infrared wavelength range (Warren and Brandt, 2008).

The spectra show strong absorption for the near infrared, progressively decreasing towards visible wavelengths. Then, at shorter wavelengths the absorption has a minimum in the region of the visible (blue) and near ultraviolet. Further down, in the region of the UVC, ice shows a rapid increase from about 200 nm going to shorter wavelengths (Fig. 3.12 and 3.13).

We derived the laser crater depth carrying out several visual comparisons at different repetition rate and time of ablation, estimating a value of ~ 0.1 μm of depth ablated per pulse (Müller et al., 2011).

We thus calculated the volume of ablation according to the formulation:

$$V \approx \pi r x s^2$$

where *s* is the spot size, x is the depth ablated per pulse and r is the roughness coefficient (for ice we used a range of 0.90-0.95).

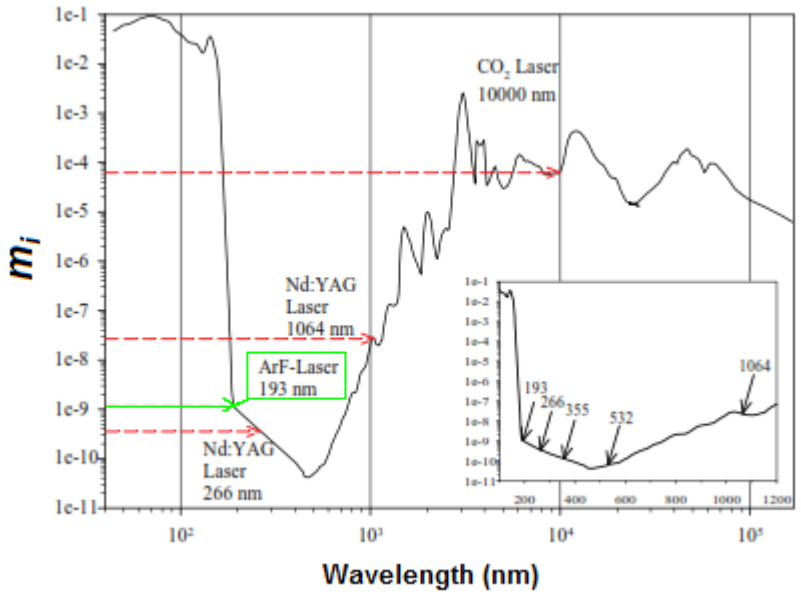

Figure 3.13: Imaginary part of refractive index coefficient for ice at different wavelengths. In red are indicated the absorption coefficient for the most utilized wavelength in LA-ICPMS works. (from Wilhelms-Dick, 2008).

Considering a spot size of 280 µm we obtain a quantity of 22 ng of ice ablated per pulse. This is consistent with theoretical calculation based on previous formulation assuming values of $1.640 \cdot 10^{-8}$ and 1.4042 for m_i and m_{re} respectively at 193 nm (Warren, 1984), associated to a laser fluence of 3-4 J/cm^2.

Absorption increases going to shorter wavelengths up to 160 nm, where there is a very sharp absorption edge. This represents a photon energy of 7.8 eV, which is the minimum required to excite transitions between the electronic energy levels in ice. For photons of energy larger than this and up to the soft X-rays, ice is almost completely opaque. Therefore laser ablation of ice at wavelengths smaller than 160 nm is very impractical and results in significant heat release that reduces the quality of the ablation process. We conclude that UV-LA-ICPMS at 193 nm represents a good compromise between ablation uniformity and material removal, improving performances of the other laboratories that currently (May 2015) utilize LA-ICPMS on ice cores at 213 nm (Sneed et al., 2015) and 1064 nm (Reinhardt et al., 2001, 2003, Wilhelm-Dick, 2008).

Chapter 4

Citation: Della Lunga, D., Müller, W., Rasmussen, S. O. & Svensson, A. S. (2014). Location of cation impurities in NGRIP deep ice revealed by cryo-cell UV-laser-ablation ICPMS. *Journal of Glaciology*, **60** (223), 970-988.

This manuscript was published in the *Journal of Glaciology* on the 1st of November 2014. It includes a description of the equipment, the methodology and the operating conditions utilized for the entire PhD project. The results contained in this manuscript represent the main contribution of the present PhD project to Ice Physics.

Author contributions: DDL developed the research in discussion with WM, SOR and ASS, performed the analyses and wrote the manuscript. WM helped design the analytical procedure and edited the manuscript together with SOR and ASS.

Location of cation impurities in NGRIP deep ice revealed by cryo-cell UV-laser-ablation ICPMS

Damiano DELLA LUNGA,[1] Wolfgang MÜLLER,[1] Sune Olander RASMUSSEN,[2] Anders SVENSSON[2]

[1]*Department of Earth Sciences, Royal Holloway University of London, Egham, Surrey, UK*
E-mail: damiano.dellalunga.2011@live.rhul.ac.uk
[2]*Centre for Ice and Climate, Niels Bohr Institute, University of Copenhagen, Copenhagen, Denmark*

ABSTRACT. In polar ice sheets, the average grain size varies with depth. Ice grain size increases due to several factors including ice temperature and impurity content, which in turn varies with climate. The effect of impurities on grain growth is thought to be crucial but has never been observed experimentally. Using a methodology recently developed at Royal Holloway University of London, in situ chemical analysis of frozen ice at sub-ppm concentrations with unprecedented spatial resolution (~150 μm) is achievable using ultraviolet laser ablation inductively coupled plasma mass spectrometry (UV-LA-ICPMS) featuring a two-volume cryo-LA-cell. Following surface cleaning with a custom-built vice equipped with a ceramic blade, NGRIP ice slabs (~86 ka before AD 2000) have been analysed using a series of one-dimensional profiles and two-dimensional maps of laser spots at a resolution of 200–300 μm. Results demonstrate that cation impurities are not uniformly distributed in ice layers and show significant variations in concentration on a sub-millimetre scale. Furthermore, a different pattern of elemental distribution between clear ice and layers enriched in impurities (cloudy bands) has been identified: while concentration differences for cloudy bands are not resolvable between boundaries and inner grain domains, within clear ice, grain boundaries and junctions are significantly (up to 100 times) impurity-enriched relative to corresponding grain interiors.

KEYWORDS: crystal growth, glaciological instruments and methods, ice chemistry, ice core, ice crystal studies

INTRODUCTION

Ice cores from ice sheets are a valuable archive of palaeoclimatic information. Traditionally, most of the information about past climate comes from water isotopes, air bubbles trapped in the ice and chemical analyses. Changes in grain size appear to be associated with climatic events, which were early on observed at the transition between the Holocene and the Last Glacial Maximum (LGM) in the Dome C ice core from Antarctica (Duval and Lorius, 1980). Since then, this generally sharp grain-size decrease has also been observed for termination I and II in the EPICA Dome C core from Antarctica (Durand and others, 2006), the Greenland Ice Sheet 2 (GISP2) ice core (Gow and others, 1997), the Greenland Ice Core Project (GRIP) ice core (Thorsteinsson and others, 1995, 1997) and the NorthGRIP (NGRIP) ice core (Wang and others, 2002). The relationship between grain size and climatic changes may be assigned to ice microstructure dynamics (Durand and others, 2006), which include migration of grain boundaries by soluble impurities (Alley and Woods, 1996), pinning by insoluble microparticles (Jun and others, 1998) or a conditioning of surface temperature at the moment of deposition (Petit and others, 1987). Since many ice-core parameters (e.g. water isotope record, impurity concentration and dust particle concentration) show abrupt changes at climatic transitions, it is difficult to establish what governs the observed grain-size changes across such transitions.

The objective of this paper is to assess the influence of impurities on ice grain growth and/or recrystallization through the identification of the location of cation impurities and the distribution of these between inner parts of grains and grain boundaries. In fact, the location of impurities in the ice lattice of the large ice sheets is still a matter of debate and, although it is generally assumed that trace constituents tend not to be confined uniquely to grain boundaries, this assumption has never been confirmed beyond doubt in experiments (Ohno and others, 2005). To confirm or disprove this assumption – using an in situ technique with sub-ppm detection limits such as ultraviolet laser ablation inductively coupled plasma mass spectrometry (UV-LA-ICPMS) directly in frozen ice cores – is the main aim of the present work.

Grain growth is generally assumed to be slowed by the interaction of grain boundaries with microparticles and impurities (Alley and others, 1986). Microparticles such as dust are generally micrometer-sized and thus much larger than ionic impurities which may diffuse and possibly move into the ice lattice, whereas dust cannot. In a so-called 'low-velocity regime', the force that drives the migration of grain boundaries is not large enough to force apart microparticles or impurities, which therefore tend to lie on grain boundaries (Alley and others, 1986). In contrast, in a 'high-velocity regime', the grain boundaries migrate more rapidly than the extrinsic material (particles or impurities) which will lie in the inner part of the ice grain more frequently compared to the low-velocity regime (Alley and others, 1986). It is generally assumed that polar ice is in a low-velocity regime compared to soluble particles, and in a high-velocity regime compared to microparticles and dust (Alley and others, 1986). Impurity records can be applied for the identification of annual layers in ice cores, since seasonally varying impurity compositions can often be observed, which for

Holocene ice in Greenland include a sea-salt peak (Na, Mg) in late winter, followed by a dust peak (Ca, Al, Fe) in spring and enhanced $[SO_4]^{2-}$, $[NO_3]^-$ and $[NH_4]^+$ during summer (Rasmussen and others, 2006). During glacial periods, however, all impurity peaks may coincide (Andersen and others, 2006).

The impurity content is therefore crucial in order to reconstruct the climate variability at high resolution. Moreover, the location and distribution of these soluble and insoluble impurities inside grains of deep ice cores provide important information about the occurrence of ice recrystallization, grain growth and deformation at various depths.

In this paper, we present the first attempt to analyse chemically at the sub-ppm level the nature, location and distribution of microparticles and impurities within two different domains of glacial ice samples directly in the frozen state with sub-millimetre resolution via cryo-cell UV-LA-ICPMS (Müller and others, 2011), with a specific focus on areas with either high amounts of impurities or areas with a strong concentration gradient.

The investigated samples are taken at depths of ~2700 m from the NGRIP ice core (NorthGRIP Members, 2004) where the ice has an age of ~86 ka b2k (thousand years before AD 2000).

IMPURITIES IN ICE

Snow falling over Greenland generally contains low amounts of impurities, since most of them have been removed already by precipitation or fallout during transport from the sources to the pole. Nevertheless, ~80% of all precipitation over the poles nucleates on dust or aerosol particles (Barnes and Wolff, 2004). Furthermore, the majority of the impurities are attached or embedded in snowflakes, but not necessarily as a nucleus (Fischer and others, 2007).

Impurities include dust particles, acids and ash from volcanoes, sodium and chloride ions (indicators of sea-ice extension), ammonium (related to forest wildfires), and lead, sulphate and nitrate from human pollution. All are indicators of past climate or environment. Their distribution plays a crucial role in determining most of the physical properties of ice and has implications for the mobility of chemical species after deposition, as well as conductivity, via the interaction between different components trapped in ice (Rempel and others, 2001, 2002).

Ice-core impurities can be divided into soluble and insoluble fractions. The soluble impurities include chemical compounds of marine, terrestrial and biogenic origin such as Na^+, K^+, NH^+, Mg^{2+}, Ca^{2+}, NO^{3-}, $SO_4{}^{2-}$ and Cl^- (Legrand and Delmas, 1988). The insoluble impurities include microparticles of terrestrial origin that are often referred to as 'dust' (e.g. Steffensen, 1997).

Polar ice continually recrystallizes even at constant temperature and under zero stress/strain conditions (Faria and others, 2014). The analysis of grain size and *c*-axis orientation vs depth in Antarctic cores (e.g. the Byrd deep ice core) suggested that three main recrystallization regimes affect the microstructural evolution of ice grains (Stephenson, 1967; Gow, 1969; Alley and others, 1986, Durand and others, 2006). According to these authors, for the uppermost ~400–700 m of the ice, grains linearly increase their average size in a process called 'normal grain growth'. Below this depth the increasing strain in the ice sheet was thought to occur via rotation recrystallization, a process that involves the rotations of subgrains and the migration of subgrain boundaries across regions with lattice curvature, eventually outlining a new boundary between two different grains. In the very deep part of the ice sheet (bottom ~150 m), 'migration recrystallization' might take place, when entirely new grains are formed and boundaries migrate very fast. This so-called 'tripartite paradigm' has recently been challenged (Kipfstuhl and others, 2006, 2009) through a detailed microstructure study of Antarctic ice and firn at EPICA Dome C and EPICA-DML. At these two sites the authors found evidence of migration and rotation recrystallization at very shallow depths, where these mechanisms appear to be dominant. Computer simulation and laboratory experiments on normal grain growth have also raised doubts about the tripartite paradigm, showing that shallow polar ice cores are characterized by microstructures affected by processes other than normal grain growth, i.e. dynamic recrystallization (Faria and others, 2014).

In general, it is assumed that ice grain growth is influenced by impurities and the relation describing grain boundary velocity v can be written as (Alley and others, 1986)

$$v = \mu P \tag{1}$$

where μ is the grain mobility and P is the driving force for grain boundary migration, which, for normal grain growth, can be defined as (Alley and others, 1986)

$$P = \frac{2\gamma}{R'} \tag{2}$$

where γ is the surface tension and R' is the radius of curvature of a spherically curved section of grain boundary that migrates.

Alley and others (1986) derived the following relationship for the grain boundary drag effect of microparticles:

$$\frac{P_\mathrm{p}}{P_\mathrm{i}} = \frac{9V_\mathrm{p}R}{4r_\mathrm{p}} \tag{3}$$

where P_p is the drag force due to microparticles, P_i is the intrinsic driving force for grain growth, V_p is the volume fraction of particles, R is the average grain radius and r_p is the particle radius. The model predicts an increased drag effect $P_\mathrm{p}/P_\mathrm{i}$ with higher volume concentrations and small particle size, and with larger grain sizes. However, the growth rate reduction calculated from Eqn (3) for termination I and II in GRIP ice has been found to be far too low to be responsible for the observed grain-size reduction (Thorsteinsson and others, 1995). Weiss and others (2002) also found, in the EPICA Dome C core, that high soluble impurity content does not necessarily imply a slowing-down of grain growth kinetics, whereas the pinning of grain boundaries by dust particles could explain, in some cases, the change of the ice microstructure.

Guillope and Poirier (1979) had previously considered two possible avenues for grain boundary migration when impurities are present: (1) slow migration of the boundary when it is unable to break away from the impurities and must drag them along with it as it migrates, and (2) fast migration of the boundary, when the driving force for migration is sufficient to overcome impurity drag, and the boundary can break away from the pinning effect of the impurities. Factors that can trigger the sudden jump to fast migration include higher temperature and higher misorientation across a boundary, both increasing the grain boundary mobility.

The identification of the dominant mechanism of grain growth and recrystallization in polar ice has been discussed over many years. Although some models (Durand and others, 2006, 2009), taking into account recrystallization processes and effects of impurities, were able to reproduce the grain-size variations for the first ~2000 m of core (EPICA Dome C), below this depth the observed grain size was greater than the model predicts, meaning that the modelled pinning effect was too strong. A better reproduction of the evolution of grain size with depth in EPICA Dome C has been achieved implementing a thermally activated unpinning effect (Durand and others, 2009), which, however, cannot describe accurately the amplitude of decreases in grain size during climatic transitions below 2200 m depth. This might be due to the establishment of equilibrium between the unpinning effect induced by temperature on particles, and the pinning effect that can act again on the same particles through the effect of grain growth (Durand and others, 2009).

From the brief overview above, it is clear that the location and distribution of soluble and insoluble impurities in ice, and especially in deep ice cores, is still largely unclear, as is the effect of microparticles on grain-size variation.

Several in situ analyses of impurities in polycrystalline ice have been carried out in the past: Mulvaney and others (1988) used cryo-SEM and X-ray analysis of Antarctic samples to detect sulphur (reported detection limit 490 ppm; Mulvaney and others, 1988), whose contribution was thought to be entirely from sulphuric acid. Sulphur was found to be located preferentially at triple junctions, as confirmed by other studies on Antarctic samples with Raman spectroscopy, but also in liquid veins (Fukazawa and others, 1998). On the other hand, Cullen and Baker (2000, 2001) observed that the majority of impurities in the GISP2 core and in the Antarctic Byrd core are not trapped in two-grain boundaries or triple junctions. Using scanning electron microscope (SEM)/energy-dispersive spectroscopy (EDS) microscopy, Baker and Cullen (2003) observed filaments in grain boundaries, and impurity spots in grain interiors. They concluded that, although the filaments are an artefact produced by the sample sublimation, they demonstrate the presence of impurities segregated along boundaries. They also concluded that impurity spots in grain interiors reside there and are not transported during specimen preparation or observation. In the less recrystallized Holocene ice, Barnes and Wolff (2004) performed SEM X-ray analysis on ice from four different polar sites, concluding that impurities are present in a wide range of locations, which include triple junctions, grain boundaries, lattice and vapour/solid interfaces (estimated detection limit 2–5 ppm for S, Na, Mg and Cl; Barnes and Wolff, 2004). Iizuka and others (2004) performed ion chromatography at 2 mm resolution on Holocene ice at Dome Fuji, concluding that coexistence of specific cation–anion pairs could lead to different distributions of soluble impurities in the ice microstructure. In fact, Na^+ was found to be related to Cl^- (mainly from sea-salt input) with no preferential distribution between boundaries and interiors, whereas Mg^+ largely coexisted with SO_4^{2-}, which has been observed preferentially at triple junctions (Mulvaney and others, 1988; Fukazawa and others, 1998). However, Ohno and others (2005) analysed ice from Dome Fuji, for a range of Holocene depths using micro-Raman spectroscopy, concluding that most sulphate and soluble impurities were trapped in inclusions within the grains as sulphate salts, which are not affected by alteration or diffusion after deposition, thus preserving the climate-related signal. According to Durand and others (2006) the grain-size decreases associated with glacial periods in EPICA Dome C are mainly the result of pinning by dust particles located along grain boundaries. X-ray tomography of LGM samples of the same core showed that the largest dust particles were concentrated along grain boundaries (Durand and others, 2006). This conclusion has recently been taken as evidence for the faster densification observed in impurity-rich layers of polar firn (Hörhold and others, 2012). Obbard and Baker (2007) used ion chromatography and SEM microscopy–X-ray spectroscopy to determine the type and location of impurities over a range of depths along the entire Vostok ice core. They concluded that the high dust content, while positively correlated with small grain size, was not the cause of it, and the large particles observed were always within the grain interiors and never on boundaries. However, they observed the occurrence of high concentrations of Ca^+ along boundaries in glacial ice, and concluded that over a certain critical concentration Ca^+ decreased grain boundary mobility, leading to an abnormally small grain size. These findings agree with Iizuka and others (2008), who performed ion chromatography and Raman spectroscopy on Dome Fuji and GRIP samples over a wide range of depths to determine the relationship between ion balance and the chemical compound of salt inclusions, showing that most of the impurities were not aligned on grain boundaries. Using micro-Raman spectroscopy and energy-dispersive X-ray spectroscopy, Sakurai and others (2009, 2010) determined that micro-inclusions tend to group together in small clusters, rather than being evenly distributed in the ice grains. However, the distribution of these clusters was not influenced by grain boundaries.

Reinhardt and others (2001, 2003) applied infrared (IR)-LA-ICPMS to deep GRIP and NGRIP samples to demonstrate the positive linear relationship between the concentration of elements such as Na, Mg, Al, Fe and particle concentration (measured by laser scattering), concluding that elements were bonding to particulate matter (reported detection limit 0.1–1 $\mu g\,kg^{-1}$; resolution 4 mm; Reinhardt and others, 2003).

RECRYSTALLIZATION AND INTEGRITY OF NGRIP CORE

The stratigraphy of the NGRIP ice core (NorthGRIP Members, 2004) is generally regarded as remarkably well preserved (Svensson and others, 2005). It is visible to the naked eye throughout the last glacial period, with high dust concentrations and many bright layers (so-called cloudy bands) which occur during the coldest events. The horizontal layering is recognizable by cloudy bands formed by particle-enriched layers alternating with clear ice layers. In general, the cloudy bands are characterized by small ice grain sizes whereas the clear ice contains crystals up to a factor of 10 larger (Svensson and others, 2005).

Down to 2600 m depth the horizontal layering is highly regular and undisturbed. Below this depth, cloudy bands develop mm-sized undulations, together with layers inclined up to 15°. However, it is just below 2800 m that the visual stratigraphy becomes more uncertain, since the record is penetrating into climatically and physically warmer ice, due to heat flux from the bedrock.

Inclined, folded and wavy strata are known to affect dielectric profiling (DEP) and continuous flow analysis (CFA), because they mix the signal that is a result of an average over a cross section of the core (Faria and others, 2010). The problem is especially important in the case of CFA since the rate of melting of an ice-core slab is sometimes not constant and the continuous collection of meltwater by the melting head and the distribution through capillaries to the sensors are occasionally discontinuous, introducing other small alterations to the climate signal (Faria and others, 2010). Due to a much smaller sampling area and sub-mm acquisition, UV-LA-ICPMS is not affected by these problems and facilitates chemical detection of different layers even when the layer thickness approaches the physical limit of CFA resolution (up to ~10 mm; Bigler and others, 2011), as in the case of our samples whose reported layer thickness is ~12 mm (Vallelonga and others, 2012).

Among the processes mentioned in the previous section for ice recrystallization, normal grain growth and rotation recrystallization do not affect the palaeoclimatic signature or the impurity distribution except at a mm scale (Duval and others, 2012). According to Faria and others (2010), there is hardly any interaction between visible micro-inclusions and grain boundaries down to 2500 m depth at EPICA-DML, whereas the deeper ice seems to 'harvest' micro-inclusions. The cause of this phenomenon is still a matter of research, and it may be related to changes in the internal structure of grain boundaries in response to a temperature increase (Azuma and others, 2012). It has been proposed that the activation energy for grain boundary diffusion may be larger than that for lattice diffusion, suggesting that grain boundaries could be either in solid amorphous state or have a quasi-liquid structure, where water molecules are jammed (Faria and others, 2014). This would significantly affect the grain boundary energetics and therefore the regime of interactions between grain boundaries and impurities.

After comparing the visual stratigraphy profiles of EDML (Fig. 1a, from Faria and others, 2010) and NGRIP (Fig. 1b, from Svensson and others, 2005) we conclude that the original stratigraphy is well preserved at the NGRIP site at the studied depths of 2695–2720 m, and dynamic recrystallization, if present, has a negligible effect on the impurities redistribution. Moreover, although some mm-sized deformation is occasionally evident (Fig. 1b), the observable deformation is probably related to the large-scale dynamics of the ice sheet, which will not significantly affect the relative position of impurities in the ice, so that our samples have essentially preserved the conditions at the time of the closure of the system (i.e. firn–ice transition at ~100 m depth).

MATERIALS AND METHODS

Samples from the NGRIP ice core were cut at the ice repository at the Centre for Ice and Climate, Niels Bohr Institute, Copenhagen. The cryo-cell sample holder is able to hold, simultaneously, up to three ice volumes (50 mm length × 11 mm width × 11 mm depth). For this study, five ice strips of such dimensions from NGRIP, labelled as 4899_A7, 4899_B8, 4900_A5, 4946_B4 and 4882_B5 from depth intervals 2694.1–2694.15 m, 2694.025–2694.075 m, 2694.75–2694.8 m, 2720.075–2720.075 m and 2684.825–2684.875 m respectively, were chosen, representing an age range of ~84.4–87.8 ka b2k. All samples correspond to a few years each, given the layer thickness of ~12 mm

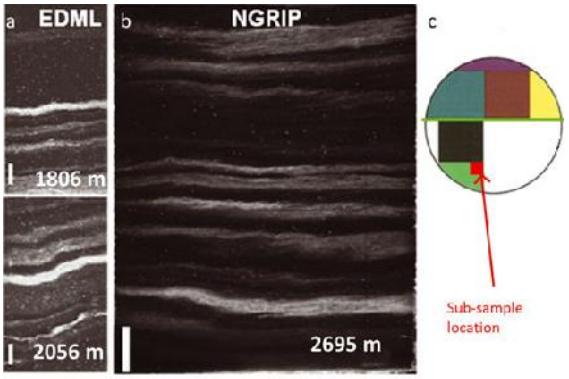

Fig. 1. Visual stratigraphy comparison between (a) EPICA-DML, from Faria and others (2010), and (b) NGRIP, from Svensson and others (2005). The methodology used to acquire these pictures is described in detail by Svensson and others (2005). Depth (m) is indicated at the bottom right. All scale bars are 1 cm. The occurrence of wavy layers and mm-scale folds that takes place between 1800 and 2050 m at EDML is less pronounced at NGRIP, which is well preserved at the depth shown (~2700 m) and below. (c) Sketch of the NGRIP cross section with subsamples utilized for the present study, indicated by a red arrow. The green line represents the cut surface analysed for visual stratigraphy as in Svensson and others (2005).

(Vallelonga and others, 2012), and overall cover the ending, beginning and middle part of Greenland Stadial 22 (i.e. the 'cold' part of Dansgaard–Oeschger event 22), whose duration exceeds 3000 years (Vallelonga and others, 2012).

A careful spatial referencing of the samples with images of the core, taken by Svensson and others (2005), was carried out to provide a mm-to-mm match between scan pictures and acquisition grids of laser spots via UV-LA-ICPMS. Knowing the exact depth interval of the sample and the subsample location, the corresponding section of the core scan was located by counting pixels on the image of the corresponding NGRIP bag.

Cleaning of the ice surface was conducted using a ceramic Y-doped ZrO_2 blade (American Cutting Edge, USA), mounted on a custom-built PTFE vice that allows surface smoothing and ice scratching in steps of <0.5 mm in order to remove contamination from cutting (Fig. 2c). The blade was analysed by LA-ICPMS to quantify the presence of metals and to assess eventual contamination of ice; its composition is 96.9% Zr, ~3% Y, <0.1% Al, <10 ppm of Fe, Cu, Mg, Ca. Approximately 2 mm of ice were removed from all surfaces about to be analysed, which correspond to the upward-facing surface of the section of NGRIP ice core utilized. A sketch of the cross section of the NGRIP core with an indication of the section utilized for the present study is provided in Figure 1c.

The methodology used for these analyses is modified here from Müller and others (2009, 2011). The RESOlution M-50 excimer (ArF, 193 nm) laser system (prototype) at Royal Holloway University of London (RHUL) is coupled with an Agilent 7500cs ICPMS operated in collision/reaction cell mode (Fig. 2a). A unique, specifically designed cryo-sample holder (Laurin Technic, Australia) made of anodized aluminium capable of keeping up to three strips of 50 mm long ice core (<12 mm thick, <13 mm wide) below –15°C is compatible with the Laurin two-volume LA cell (Fig. 2d).

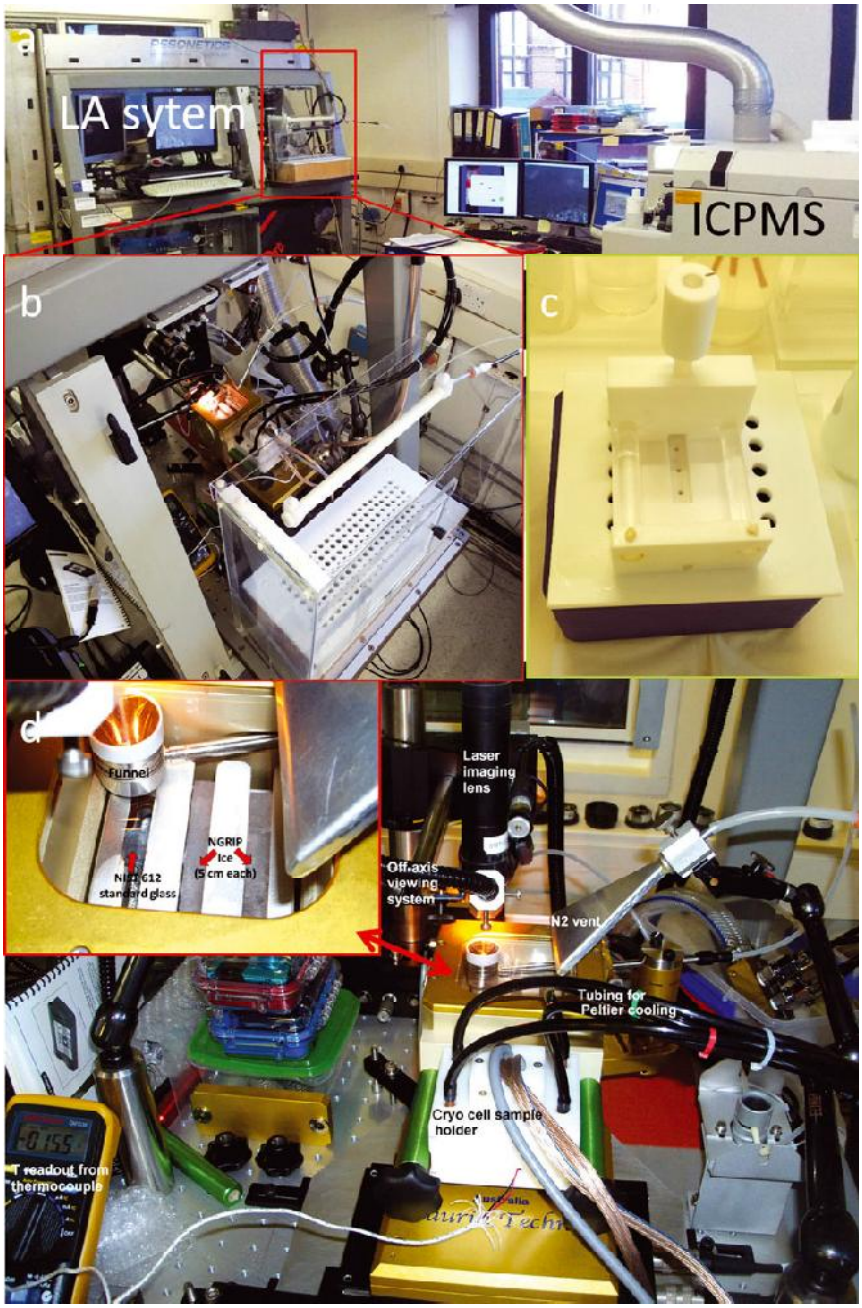

Fig. 2. Photographs of the UV-LA-ICPMS system when operating for ice analysis. (a) The laser-ablation system (left) is coupled with an Agilent 7500cs quadrupole ICPMS (right). The red inset (b) shows a close-up of the work surface in front of the LA cell, which comprises a polyurethane cool box covered with a clear plastic hood. This represents the sample-loading area. The cool box is filled with liquid N_2 which cools the air above, and N_2 blown in from the top of the hood (white PTFE cylinder) preserves a dry atmosphere in the loading area and prevents frosting of samples during loading procedures. (c) Custom-built PTFE vice for ice scraping, in a clean laboratory (class 100) workstation. The purple reservoir contains liquid N_2, which is used to cool the overlying PTFE lid and vice. (d) Close-up of the LA-cryo-cell.

PTFE-coated Cu-Be springs are used to lift the ice volumes against the reference surface of each slot, so that the ice is held in position firmly and evenly. The cool side of a Peltier element, powered by a low-voltage power supply, is used to cool the cell, while the warm side of the same Peltier element is cooled in turn by filtered cooling water.

The laser beam passes through a motorized aperture mask wheel with 12 round apertures allowing selection of circular spot sizes between 7 and 300 µm, or via a variable rotating rectangular aperture; a demagnified image of the chosen aperture size is imaged and focused onto the sample surface. Large spot sizes, typically between 280 and

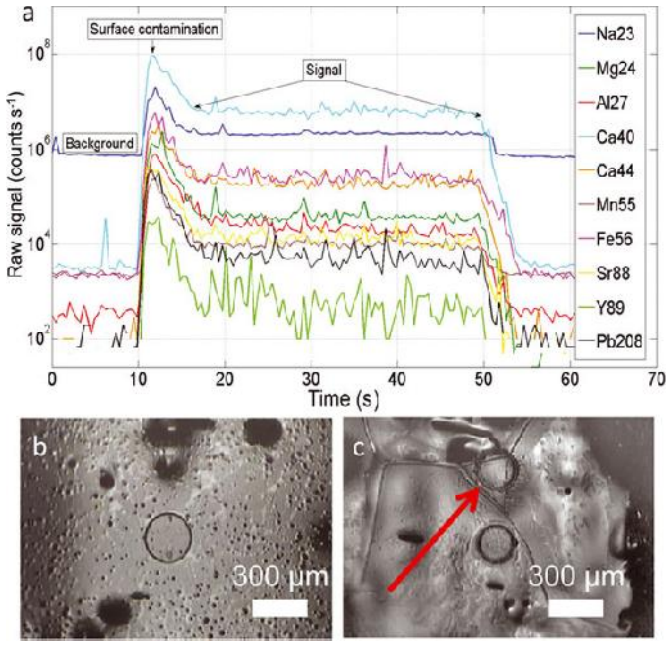

Fig. 3. (a) Raw intensities of a single spot drilling, seen in (b) (laser spot 280 µm). Ablation time 40 s + 20 s background. The data reduction includes subtraction of background and removal of surface contamination. (b) Laser crater, 280 µm, 20 Hz. (c) Laser craters at 280 µm, 20 Hz: the crater shape is not affected by drilling on boundaries or triple junctions, as indicated by the arrow.

128 µm, are needed to detect concentrations of major cations in Greenland ice, which are at sub-ppm level.

The absorption coefficient of ice shows a sharp increase from 250 nm to 175 nm of ~10 orders of magnitude (Warren and Brandt, 2008), with ice at 193 nm having a relatively low absorption coefficient of ~0.1 cm^{-1}. At a wavelength of 193 nm we estimate a removal of ~0.1–0.15 µm of ice per laser pulse at fluences (laser energy per unit area on the work material) of ~3 J cm^{-2} (Müller and others, 2011), 5000 times less than the ~30 µm removed per pulse by IR-LA on ice, which uses much higher laser energies (Reinhardt and others, 2001). Lower fluences, which are kept constant by preventing frosting over the cell window from air humidity with a small N_2 vent, provide a more controlled ablation and create craters of smooth circular shape (Fig. 3b and c).

A custom-built cryo-worksurface (~45 cm × ~20 cm) can be attached to the LA system to help with sample loading; a polyurethane cool box (~40 cm × ~16 cm) is filled with liquid nitrogen and covered with a PTFE lid (Fig. 2a and b). A regular grid of 0.8 cm holes in the lid allows the liquid nitrogen to cool air above the PTFE surface down to –20°C for >1 hour. This permits the safe handling of ice samples in the vicinity of the cell and facilitates loading procedures. Nitrogen is blown over the top of the lid and the whole cool box is covered by a clear plastic hood that keeps a cold, clean and dry atmosphere around the holder during the loading procedures, preventing frosting-over of samples and allowing the user to access the inside via plastic flaps from the sides of the hood (Fig. 2b).

A He flow (850 mL min^{-1}) inside the LA cell carries ablated particles to the ICPMS and is mixed downstream with 650–700 mL min^{-1} of Ar. H_2 (8 mL min^{-1}) was also added downstream to enhance the sensitivity of low-mass elements. The Agilent 7500 ICPMS has been fitted with a cs-lens that allows better low-mass enhanced tuning, and it was operated in collision/reaction cell mode. Plasma-based interferences such as ^{40}Ar and $^{40}Ar^{16}O$ are removed inside the collision cell by adding 4.5 mL min^{-1} of H_2, allowing measurements of mass 40 and 56 (Ca and Fe respectively) at the lowest ppb concentration levels, since ^{40}Ar and $^{40}Ar^{16}O$ undergo charge transfer reaction inside the cell (McCurdy and Woods, 2004). KED lens tuning between OctP, QP bias and QP focus has been set (Table 1). Typical limits of detection (LODs) for Na, Mg, Al, Ca and Fe, measured using NIST 612 standard glass, are 100, 0.8, 20, 8.6 and 8.0 ppb respectively, using a 280 µm spot size at 20 Hz repetition rate. Possible hydride formation was quantified on NIST 612 with ice present in the LA cell using three monitor masses at 233, 239 and 210, i.e. ^{232}ThH, ^{238}UH and ^{209}BiH, and resulted in hydride/element formation values <0.5%, with ThO/Th at ~0.2% and $^{232}Th/^{238}U$ >90%.

As shown in Table 1, the following mass/charge ratios were acquired: 23(Na), 24(Mg), 27(Al), 34(S), 39(K), 40(Ca), 44(Ca), 55(Mn), 56(Fe), 65(Cu), 85(Rb), 88(Sr), 89(Y), 138(Ba), 139(La), 140(Ce), 141(Pr), 147(Sm), 153(Eu), 157(Gd), 172(Yb), 208(Pb). Among these, only the following usually show resolvable signal/background ratio and will be displayed as results: 23(Na), 24(Mg), 27(Al), 40(Ca), 56(Fe), 88(Sr), 208(Pb). Mass 39(K), despite resolvable signal/background ratio, has a potentially significant contribution from ^{38}ArH; therefore it will not be displayed in the results. Data acquisition was performed both as chains-of-spots and continuous tracks of different spot size. All the spot chains were carried out at 20 Hz, with laser fluence of ~3 J cm^{-2} for 40 s (800 pulses), plus 20 s of background. This produces a crater depth of ~100 µm. Continuous tracks were acquired at 20 Hz repetition rate and 0.8 mm min^{-1} speed. To remove the surface contamination, each laser track was pre-ablated at 25 Hz at a speed of 3 mm min^{-1}.

Table 1. Operating conditions of cryo-cell UV laser ablation ICPMS

ICPMS: Agilent 7500cs	
RF power	1190–1300 W (optimized daily)
Carrier gas flow	650–700 mL min^{-1} (optimized daily)
Coolant gas flow	15 L min^{-1}
Auxiliary gas flow	1 L min^{-1}
Dwell time/mass	40 ms: ^{24}Mg, ^{27}Al, ^{40}Ca, ^{55}Mn, ^{56}Fe 20 ms: ^{23}Na, ^{88}Sr 15 ms: ^{85}Rb, ^{208}Pb 10 ms: ^{34}S, ^{44}Ca, ^{89}Y, ^{138}Ba, ^{139}La, ^{140}Ce, ^{141}Pr, ^{147}Sm, ^{153}Eu, ^{157}Gd, ^{172}Yb 5 ms: ^{39}K, ^{65}Cu
Collision/reaction cell gas	H_2 (99.9999%), 4.5 mL min^{-1}
Monitored masses (m/z)	23, 24, 27, 34, 39, 40, 44, 55, 56, 65, 85, 88, 89, 138, 139, 140, 141, 147, 153, 157, 172, 208
Sampler, skimmer cones	Ni
Extraction lenses	cs (tuning optimized for low masses)
OctP bias	–25 V
QP bias	–20 V
QP focus	–9 V
Hydride/element formation	<0.5%
^{232}Th/^{238}U	>90%
ThO/Th (248/232)	<0.5%, typically 0.2%
Laser-ablation system RESOlution M-50	
Laser and wavelength	193 nm excimer (CompexPro 110)
Energy density (fluence) on target	3 J cm^{-2}
He gas flow	850–900 mL min^{-1} (optimized daily)
H_2 carrier gas flow addiction	8–9 mL min^{-1} (optimized daily)
Laser repetition rate	20 Hz
Laser spot size (circular)	128, 164, 280 m
Laser acquisition mode	Chain-of-spots and tracks at 150, 200, 300 m spacing
Ar, H_2 carrier gas	Admixed downstream of LA cell
Signal smoothing	'Squid' included
Cryo-cell sample holder	
Cooling mechanism	Two Peltier elements
Sample holder temperature	–16°C (with He)
Holder material	Anodized aluminium

Results are shown in net intensities, namely background corrected counts per second, so conversion into concentrations will not be displayed, similar to data from XRF core scanners (Weltje and Tjallingii, 2008). This is due to the lack of homogeneous (<5%) external ice standard and due to the impossibility of finding an internal standard. Some external standards prepared at RHUL by building a volume of ice, adding frozen-shock layers of water with known concentration of elements, proved to be inhomogeneous (Müller and others, 2011). Internal standardization using ^{17}(OH) is impossible because ICPMS background for mass 17 is too high. The feasibility of using mass 34 ($^{16}O^{18}O$) as internal standard is currently under evaluation.

Elemental ratios are quantifiable assuming that ablation differences between NIST612 and particles in ice are insignificant. These ratios have been calculated according to Longerich and others (1996):

$$\frac{C_x}{C_y} = \frac{I_{x\_\text{sample}}}{I_{y\_\text{sample}}} \frac{I_{y\_\text{std}}}{C_{y\_\text{std}}} \frac{C_{x\_\text{std}}}{I_{x\_\text{std}}} \quad (4)$$

where $C_{x,y}$ are the concentrations of elements (ppm) in the sample or standard (NIST 612, from Jochum and others, 2011) and $I_{x,y}$ the net intensities (i.e. background-corrected) of elements x and y in the sample and the standard. Instrumental drift was monitored by analysing NIST 612 at regularly spaced intervals and corrected daily, linearly normalizing the intensity according to

$$I_{\text{sensitivity normalized}} = I_{\text{measured}} \cdot f_N \quad (5)$$

f_N is the normalizing factor and is equal to $\frac{I_{\text{average per ppm}}}{I_{\text{measured per ppm}}}$. $I_{\text{average per ppm}}$ is the ratio between intensity of element x and concentration of element x averaged over all the ablations of NIST612 during one acquisition campaign, and $I_{\text{measured per ppm}}$ is the ratio between intensity of element x and concentration of element x of the NIST612 acquisition closest to the sample acquisition.

Intensities of isotopes acquired as one-dimensional (1-D) profiles and two-dimensional (2-D) maps were recalculated as elemental intensities based on their relative isotopic abundance taken from Henderson and Henderson (2009). Images of the surface of the samples were obtained with the viewing system of the laser after the surface was smoothed with the ZrO_2 blade, and show boundaries of mm-sized grains in fine detail, allowing deliberate acquisition of data along profiles that cross grain boundaries and triple junctions. The drilling of a single spot (Fig. 3a) shows a transient peak 10–20 times higher than the actual signal, interpreted as surface contamination and followed by a gentle decrease typical of spot drilling. During data reduction, a baseline was fitted interpolating the background intervals between spot acquisitions. The baseline was subtracted from the signal, and surface contamination removed by cutting out the first 10 s of every spot acquisition. A regression line was then fitted to the remaining net signal (30 s), and the y-intercept at $t = 0$ of every line was assumed as the value representative of each spot drilled, allowing error calculation as $\pm 2\sigma$. The values were then corrected for instrumental drift according to Eqn (7), and the intensity maps of analytes were interpolated from the values obtained in this manner. Due to the relatively high Na background (Fig. 3a), the Na signal was carefully hand-picked from sections where it was resolvable.

RESULTS

Data were acquired both as 1-D profiles and 2-D maps on five 50 mm ice strips, which were carefully surface-cleaned in order to avoid contamination by using the custom-built PTFE vice equipped with a ZrO_2 blade. Results are displayed in Figures 5–19 and Table 2.

A total of 25 1-D profiles were acquired over areas of clear ice, and another 25 were acquired on adjacent cloudy bands in the five samples analysed. Of these 50 profiles a representative selection of 22 is shown in results. Cloudy bands form when the transport and deposition of impurities increase due to seasonal events such as atmospheric storms (Svensson and others, 2005). The more particles are present, the more the layers will appear bright in the scan images due to light scattering. For the same reasons, clear ice appears dark because it does not contain high amounts of impurities. The profiles were acquired both as chains-of-spots and tracks of 128 µm size over cloudy bands and of 164 or 280 µm size over clear ice. Cloudy bands and clear ice were identified in the ice sample combining scan images of the core for the selected interval taken by Svensson and others (2005) with images acquired in transmitted and reflected light with the laser camera, which show a fairly good

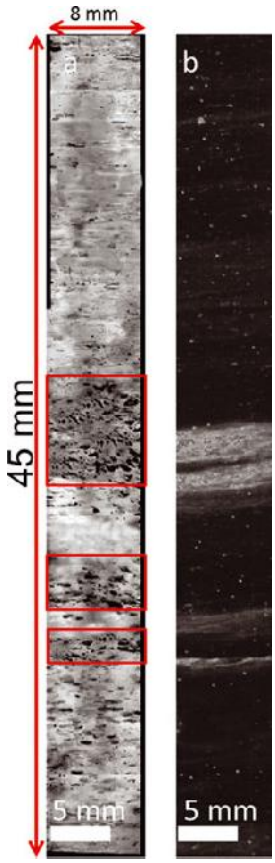

Fig. 4. (a) Transmitted-light image of an entire NGRIP subsample (4882_B5) taken with the camera of the laser ablation system. Cloudy bands are highlighted in the red boxes. (b) Corresponding zoom-in of the scanned image of the sample (Svensson and others, 2005) showing similar variation of cloudy bands and clear ice. The discrepancy is attributable to the parallax error that exists between the two surfaces shown in (a) and (b), which are parallel but a few cm apart (Fig. 1c).

correspondence (Fig. 4). The profiles shown were deliberately acquired both across and along grain boundaries (Figs 5–15). On average, in *clear* ice the intensities span five to six orders of magnitude and the variability of each element ranges over two orders of magnitude. Ca is usually the highest analyte, followed by Na, Al, Fe, Mg, Sr and Pb. Owing to the elevated level of impurities, the smaller spot size utilized for *cloudy* bands allows them to be analysed at higher spatial resolution. Intensities of elements, despite the smaller spot size resulting in an approximately fivefold signal drop between 280 and 128 μm, are comparable with those acquired for clear ice. For most elements the cloudy-band data show continuous profiles with no significant peaks corresponding clearly to grain boundaries. On the other hand, in clear ice, most of the intensity peaks are visibly related to ablation over grain boundaries. In the five samples analysed, this pattern is undoubtedly identified in 17 of the 25 profiles acquired on clear ice. The other eight do not present such an unequivocal correlation between grain boundaries and intensity. In the case of cloudy bands, 20 of the 25 profiles show no increase in intensities of elements along boundaries, while the other 5 reveal slight increases of intensities of one or more elements. In the 50 profiles analysed, the average grain-size differences between cloudy bands and clear ice are not very large but amount to ~20%, with grains measuring on average 2.5 and 3.2 mm respectively (at the longest axis of the grains). All the images of ice surfaces shown in Figures 5–19 were obtained with the camera attached to the viewing system of the laser-ablation system in either reflective or transmitted light illumination, to better highlight grain boundaries. Black dashed lines were drawn along the grain boundaries wherever they were not evident. Figures 5–9 show compositional data of both chains-of-spots and tracks of regular and irregular shape, in many cases parallel to each other, acquired on identified cloudy bands, deliberately intercepting several grain boundaries at various angles.

The elemental intensities in cloudy bands are overall relatively flat, with no significant oscillations (Figs 6 and 9), or present some intra-profile variability (Figs 5, 7 and 8), but all the local peaks in such profiles correspond to locations in the interior of grains and not to grain boundaries. The inter-elemental variability in cloudy bands is not pronounced, with the exception of a few Fe and Al peaks (Fig. 6b spot No. 9; Fig. 7a spot No. 6). An interesting example is shown in Figure 7a, spot No. 6, where ablation across a boundary corresponds to a decrease in intensity of one order of magnitude for all the elements except Fe, which by contrast increases by two orders of magnitude. This might be due to the presence of an iron-rich particle that was situated on the boundary.

In clear ice, the compositional profiles show peaks where the highest intensities clearly correspond to boundaries and triple junctions (Figs 10–15). In most cases, the intensity of the peaks exceeds one order of magnitude relative to the adjacent spots. Interestingly, a junction area where four grains are connected corresponds to a much broader peak compared to simple grain contacts, and thus likely corresponds to a larger area of enriched impurities (Fig. 10b, spots 12–14). The intra-element variability in clear ice is greater compared to cloudy bands, but inter-elemental differentiation is negligible. However, also in this case, a few minor exceptions are present (Fig. 10b, spot No. 9; Fig. 12a, spot No. 14), and some elements show different trends or amplitude of increase/decrease between each other.

Table 2. Comparison between Ca/Al and Fe/Al ratios from different sources of dust (modified from Lee and others, 2010). The values obtained in this work show affinity with a mix of dust from east Asian deserts such as the Taklamakan and Gobi

	Non-East Asian	Gobi	Taklamakan	Upper crust	China loess	Present study
Ca/Al	1.5	1.6	2.6	0.37–0.47	1.08	2.1 ± 0.4 (2s.e.)
Fe/Al	0.7	1.3	2	0.42–0.57	0.5	1.5 ± 0.3 (2s.e.)

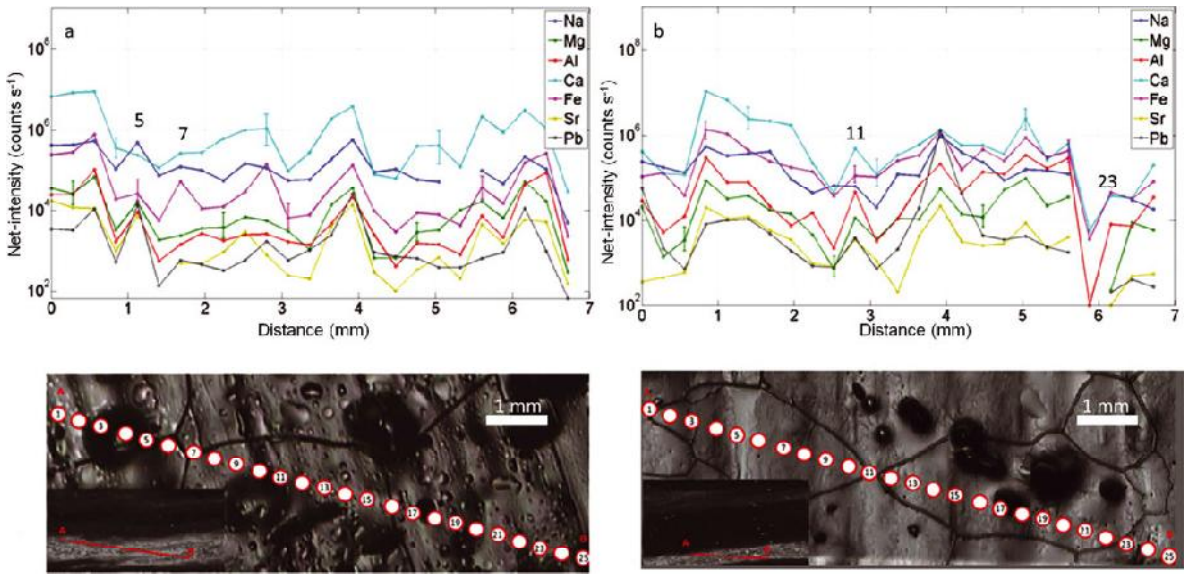

Fig. 5. (a, b) Cloudy band areas of NGRIP sample 4900_A5 (2694.75–2694.8 m). Chain of 25 spots with diameter of 128 μm at 150 μm spacing along two profiles of ~6.5 mm from A to B (see insets in the bottom left). No correlation between intensities and grain boundaries is observed for cloudy bands. Representative 2σ error bars are shown for Na, Mg and Ca.

A comparison between profiles acquired along grain boundaries in cloudy bands and clear ice is shown in Figure 15. In the first case (Fig. 15a), the elemental intensities are similar to those of the rest of the profiles acquired in cloudy bands. In contrast, in clear ice the data are up to one order of magnitude higher than average values (note the *y*-axis scale up to 10^{10}), with local peaks that correspond to triple junctions.

Compositional data of Na, Mg, Al, Ca and Fe from a 2-D grid of spots (9×35 spots with 280 μm diameter) over a 27×6 mm surface of ice from NGRIP at ~2695 m depth (sample 4899_A7) are shown in Figure 16. Sr and Pb could

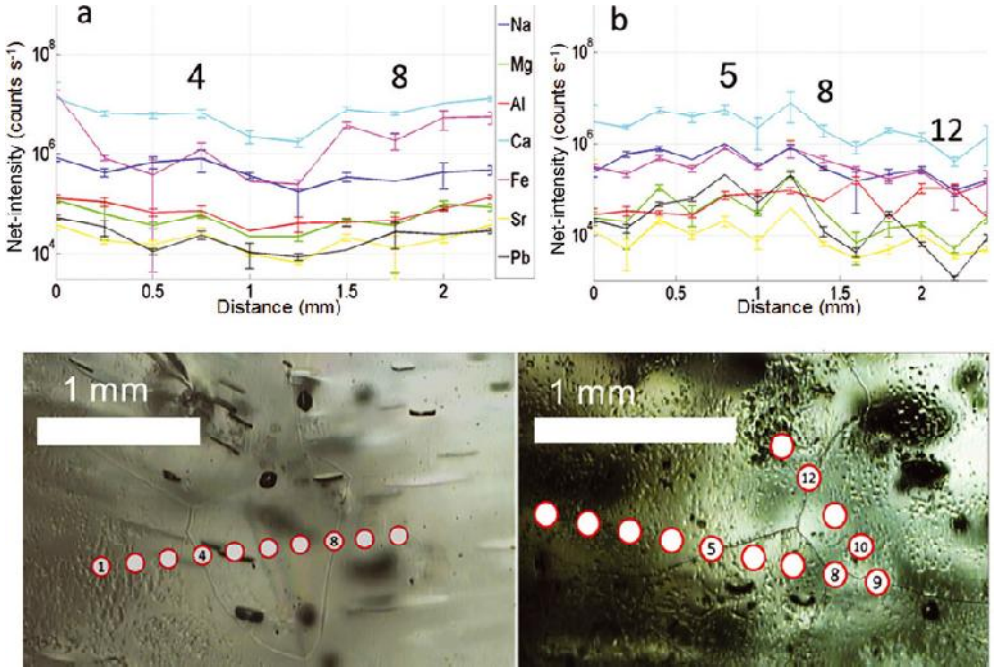

Fig. 6. (a, b) Profiles acquired in cloudy band areas of NGRIP sample 4946_B4 (2720.075–2720.125 m). Chain of 10 and 13 spots respectively, diameter 128 μm, spacing 150 μm; 2σ error bars are shown. No correlation between intensities and grain boundaries is observed.

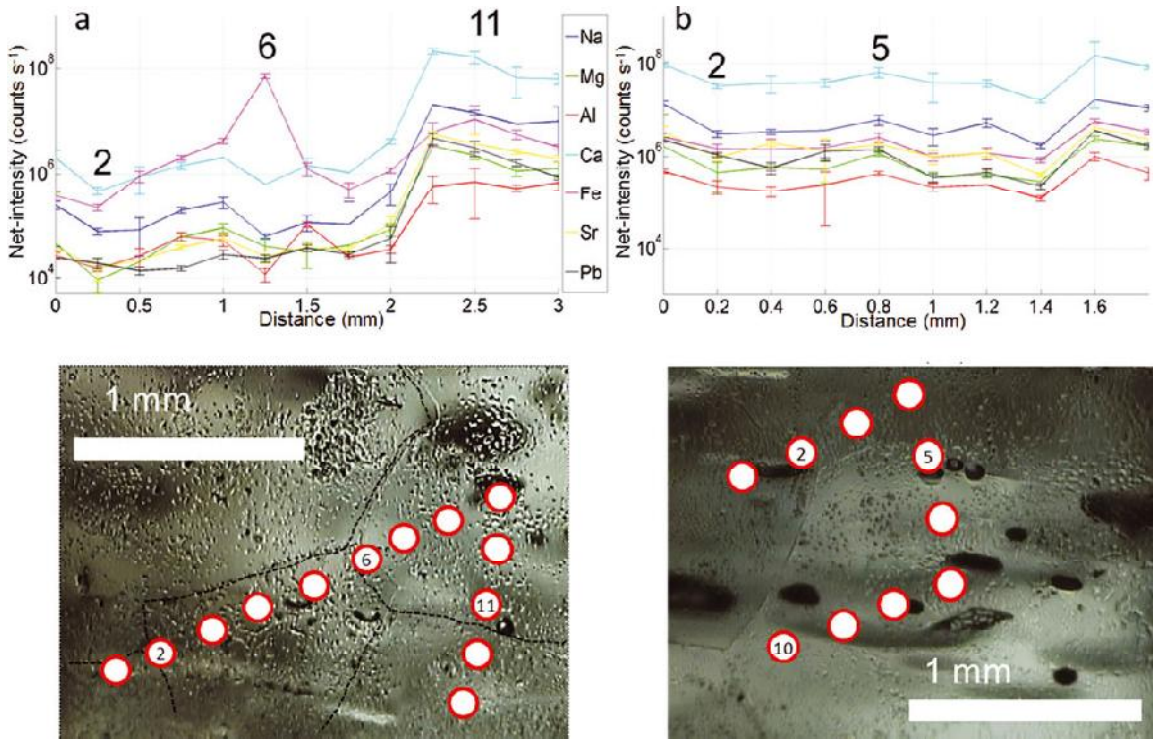

Fig. 7. (a, b) Profiles acquired in cloudy band areas of NGRIP sample 4882_B5 (2684.825–2684.875 m). Chain of 13 and 10 spots respectively, diameter 128 µm, spacing 150 µm; 2σ error bars are shown. No correlation between intensities and grain boundaries is observed. Spot No. 6 in (a) shows a Fe peak which could be a contribution from ablation of an iron-rich particle.

not be sufficiently resolved in this case. The maps show a strong small-scale variability (up to 10^5 counts s^{-1} in 1 mm), higher intensities within cloudy bands, and a general patchy behaviour where areas of extreme values tend to occur within grain interiors rather than near boundaries. The highest-intensity elements are again Ca and Al followed by Fe, Na and Mg. From the bottom to the top of every map we can distinguish two alternations of bands of low/high intensities whose inclination varies from 30° to 60° from the horizontal axis, dipping to the right, plus another band of low intensities on the top. This alternation is best visible for Na and Fe, but is less clear for Ca, Al and Mg. The scan image shown in Figure 16b again presents two alternations of bright layers and clear ice which broadly appear to correlate to the intensity bands, although the lower bright layers in Figure 16b are not well defined. A direct correlation is also made difficult by the fact that the surface scanned for visual stratigraphy (Svensson and others 2005) and the surface analysed by UV-LA-ICPMS are not the same. In fact, as shown in Figure 1c, the sample surface and the scanned surface are few cm apart, although they represent exactly the same depth. As the layers are wavy at this depth, small variations between the two surfaces are to be expected (parallax effect). However, the most intense zone of the elemental maps of Na, Fe and partially Al, Ca and Mg match the brightest cloudy bands in Figure 16b (tilted by ~25°). The different elements show their highest intensities in various areas of the map, with Ca, Al and Mg, yet contrasting peaks from the top to the bottom of the map. These peaks are generally not related to grain boundaries. Figure 16a shows that the grain sizes range between <1 mm (at the top and bottom of the section) and several millimetres (middle part of the section).

A second 2-D grid of 27 × 13 spots (164 µm spot size, 200 µm spacing) from an undeformed cloudy band was mapped for Na, Mg, Al, Ca, Fe, Sr and Pb (Figs 17–19) from a depth of 2694.75–2694.8 m (sample 4900_A5). Overall, Ca shows the highest intensities, followed by, Fe and Al and in turn by Na and Mg. Sr and Pb have intensities at least two orders of magnitude smaller than the other elements. All the maps confirm the tendency of elements to concentrate in patches with an internal variability that covers six orders of magnitude for Al, Ca and Fe and from five to three orders for the others. All the elements seem to have similar distributions, having higher intensities in the top part, and lower in the bottom part, with differences in some cases (cf. symmetric behaviour of Al and Fe compared to Ca in the top part). The image obtained with the laser camera (Fig. 17) shows a noticeable variation of grain size, going from mm-sized grains in the bottom left part of the map to hundreds-of-micron-sized grains in the right middle part of the map. Mg intensities are relatively homogeneous throughout the section, with maxima at the top and minima at the bottom. The same behaviour is presented by Ca and Sr, despite the upper section of the map showing decreasing intensities from left to right. A different pattern is presented by Al and Fe, where the variability between the upper and the lower part of the map is more accentuated and the upper part of the section shows decreasing intensities from right to left, opposite to Ca. Na has generally low intensities except in the uppermost part of the map, where it creates a sub-mm layer of high intensities that contrasts remarkably with the

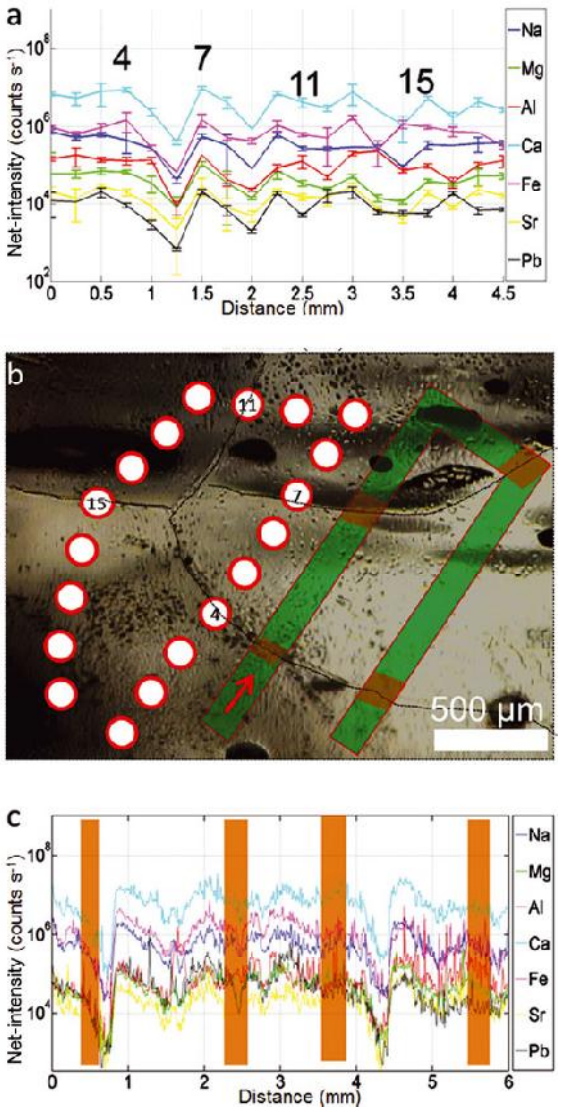

Fig. 8. Comparative, parallel profiles across several ice grains – acquired both as chain-of-spots and continuous track – in a cloudy band of NGRIP sample 4899_B8 (2694.025–2694.075 m). (a) Net-intensities of selected elements along a chain of 19 spots (128 µm diameter, 150 µm spacing) with 2σ error bars. Grain boundaries are marked by spot numbers. (b) Image of the surface of the ice sample, with indications of the chain-of-spots and track visible in (a) and (c). The red arrow indicates start and direction of the track. (c) Net-intensities of selected elements along the continuous track alongside the chain-of-spots in (a) (pre-cleaning with 164 µm, 25 Hz, 50 µm s^{-1}; acquisition with 128 µm, 20 Hz, 13.3 µm s^{-1}), where grain boundaries are indicated by shading. No correlation between intensities and grain boundaries is observed.

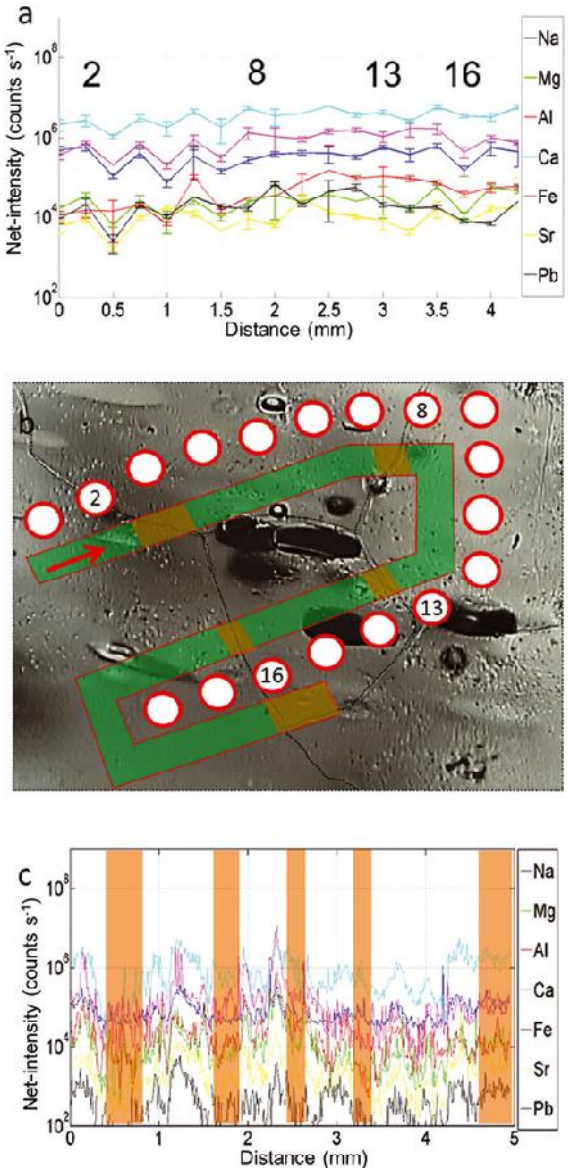

Fig. 9. Same as Figure 8, but for NGRIP sample 4946_B4 (2720.075–2720.125 m) and with 18 spots.

rest of the map but perfectly matches a layer of clearer ice, visible in the scan image (Fig. 18a). Sr shows similarities with the maps of Ca and Mg, but its intensities are at least two orders of magnitude lower and fairly homogeneously distributed throughout the map. Pb, in contrast, has a stronger internal variability and even lower intensities. Elemental maps show a variability of intensities which cannot be ascribed to grain boundaries, since, for most of the elements, highest and lowest peaks appear within the grain interiors.

In order to compare results from this cloudy band with various crustal sources, Ca/Al and Fe/Al ratios were calculated (quantified relative to NIST612) and are shown in Figure 19c and d. The maps have values that range between 0 and 14, and overall values of 2.1 ± 0.4 (2× standard error) (2s.e.) and 1.5 ± 0.3 (2s.e.) respectively. The bottom half of each map is very similar, whereas the upper half shows different patterns when comparing Ca/Al and Fe/Al. In fact, zones of high Ca/Al values almost perfectly match those with low Fe/Al ratios and vice versa. The average values of both Ca/Al and Fe/Al ratios of the sections compare well with values from Asian deserts (Table 2), which are known to be the predominant source of Greenland dust during the last glacial period (Svensson and others, 2000).

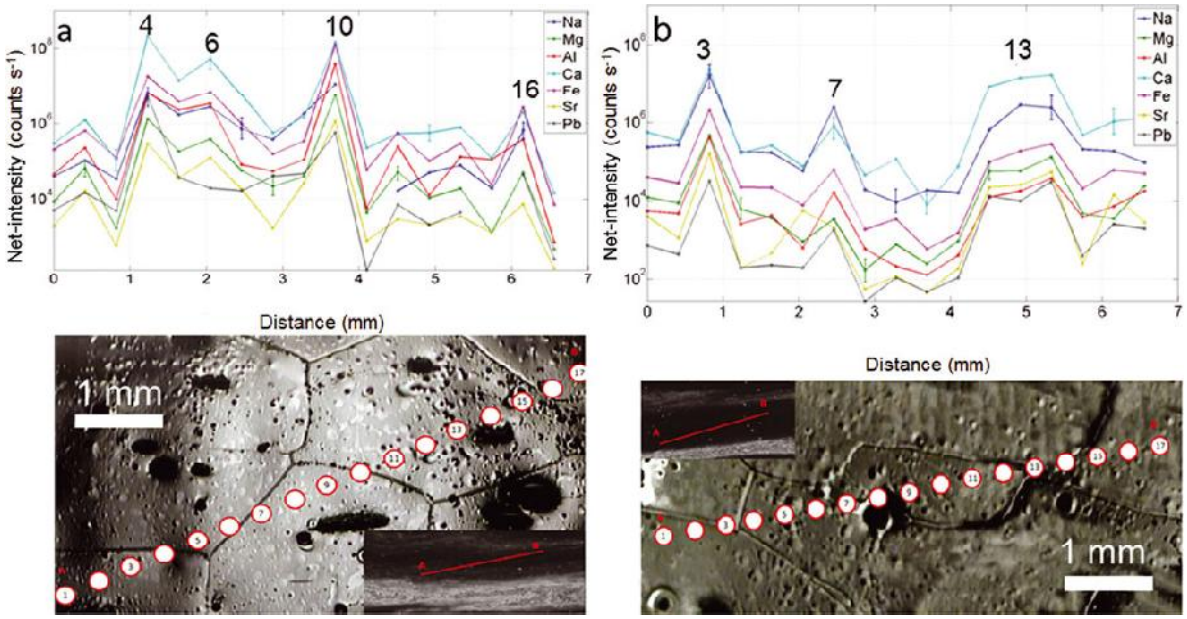

Fig. 10. (a, b) Profiles acquired over clear ice on NGRIP sample 4900_A5 (2694.75–2694.8 m). Two chains of 17 spots with diameter of 280 μm at 300 μm spacing were acquired along the profiles of ~6.5 mm from A to B (see insets in the bottom right and upper left corner respectively). A strong correlation between intensities and grain boundaries is observed. Representative 2σ error bars are shown for elements Mg, Ca and Fe.

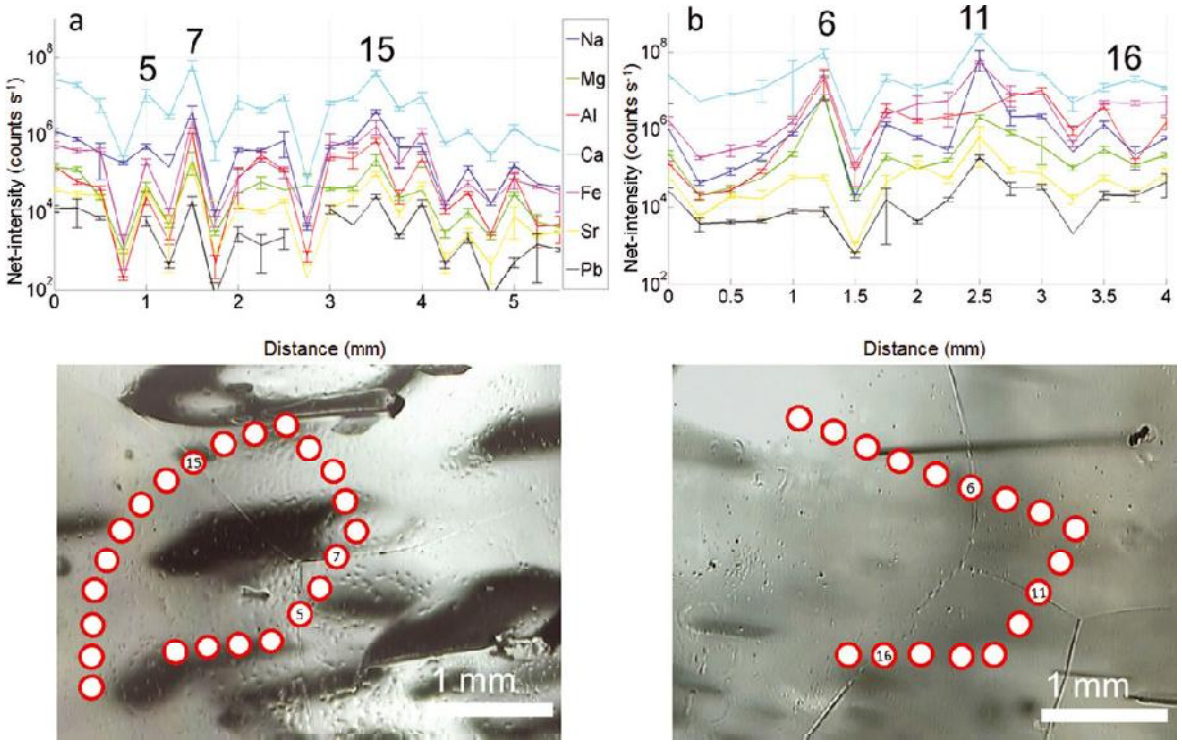

Fig. 11. (a, b) Profiles acquired in clear ice areas of NGRIP sample 4946_B4 (2720.075–2720.125 m). Chain of 23 and 17 spots respectively, diameter 164 μm, spacing 200 μm; 2σ error bars are shown. Good correlation between intensities and grain boundaries is observed.

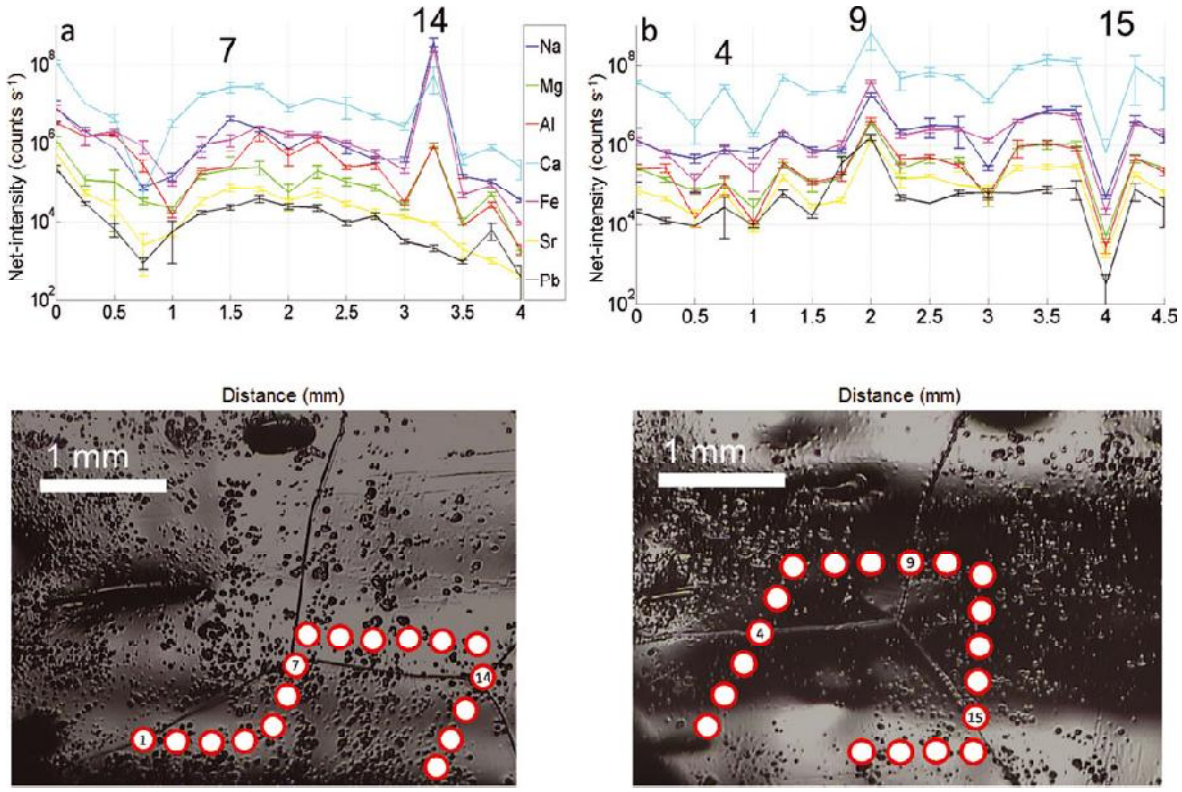

Fig. 12. (a, b) Profiles acquired in clear ice areas of NGRIP sample 4882_B5 (2684.825–2684.875 m). Chain of 17 and 19 spots respectively, diameter 164 μm, spacing 200 μm; 2σ error bars are shown. Good correlation between intensities and grain boundaries is observed.

DISCUSSION

Visual comparison between scanned images from NGRIP (Svensson and others, 2005) and other ice-core records shows that NGRIP is rather well preserved, the integrity of the original horizontal layering being preserved down to >2750 m depth. Millimetre-scale folds are observed only from a depth of ~2700 m downwards (Fig. 1) with tilting of the layers (Fig. 16b) up to 30°. Nevertheless, the layering is always resolvable and preserved and no folding is observed in the samples investigated herein. Smoothing of the ice surfaces with a ceramic ZrO_2 blade, mounted on a custom-built PTFE vice, makes the grain boundaries easily identifiable with the viewing system of the laser ablation system, and also removes sample contamination from cutting.

Deep UV laser ablation of ice is a controlled process and yields smooth intensities over the duration of an analysis. Moreover, it generates circular craters both in the middle of ice grains (Fig. 3b) and along boundaries as well as triple junctions (Fig. 3c). Analyte background/signal ratios proved to be resolvable using spot sizes of 280, 212, 164 and 128 μm, achieving the best compromise between high spatial resolutions for spot sizes of 164 or 128 μm at 20 Hz repetition rates.

The profiles acquired over cloudy bands (Figs 5–9) and over clear ice (Figs 10–14) show that the former are characterized by approximately fivefold increases in elemental intensities compared to the latter, which is consistent with cloudy bands being layers enriched in impurities (Svensson and others, 2005). This also matches with visual comparisons between clear ice and cloudy bands on scan images. The profiles for clear ice reveal that significantly higher elemental concentrations occur at grain boundaries or triple junctions, relative to the inner parts of the grains, which in many cases are slightly larger than in cloudy bands. However, in cloudy bands all the elements show generally similar patterns, though sometimes a few elements (especially Fe and Al) have significant anticorrelation that might be related to horizontal or vertical variations of the composition and concentration of the impurities. In clear ice, Na has a much stronger variability and intensity, sometimes even higher than that of Ca, whereas in cloudy bands the variability decreases. This reflects the seasonality peak of Na that appears in winter, which usually corresponds to clear ice. As a sea-salt proxy, Mg shows lower intensities in clear ice compared to cloudy bands, opposite to Na. Contribution to Mg abundance from dust in such cases is probably larger than the sea-salt peak contribution, which marks the difference between clear ice (winter) and cloudy bands (spring).

The profiles over cloudy bands were taken from the layers immediately below the clear ice sections analysed. In these cases, no clear relationships between the intensities observed and grain boundaries are noticed. The observed compositional variability is not related to differences due to preferential distribution of impurities between boundaries and grains, since both the highest peaks and the lowest dips are found within the ice grains. Compared to clear ice, intensities of elements on boundaries are generally lower,

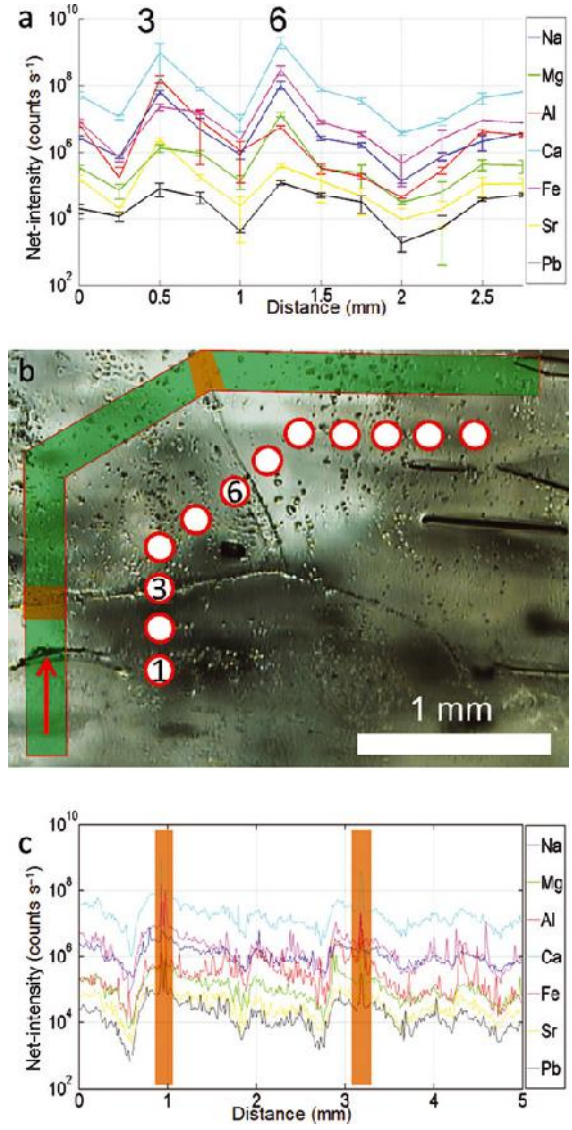

Fig. 13. Comparative, parallel profiles across several ice grains – acquired both as chain-of-spots and continuous track – in a cloudy band of NGRIP sample 4899_A7 (2694.1–2694.15 m). (a) Net-intensities of selected elements along a chain of 12 spots (164 µm diameter, 200 µm spacing) with error bars (2σ). Grain boundaries are marked by spot numbers. (b) Image of the surface of the ice sample, with indications of the chain-of-spots and track visible in (a) and (c). The red arrow indicates start and direction of the track. (c) Net intensities of selected elements along the continuous track alongside the chain-of-spots in (a) (pre-cleaning with 196 µm, 25 Hz, 50 µm s^{-1}; acquisition with 164 µm, 20 Hz, 13.3 µm s^{-1}), where grain boundaries are indicated by shading. A good correlation between intensities and grain boundaries is observed.

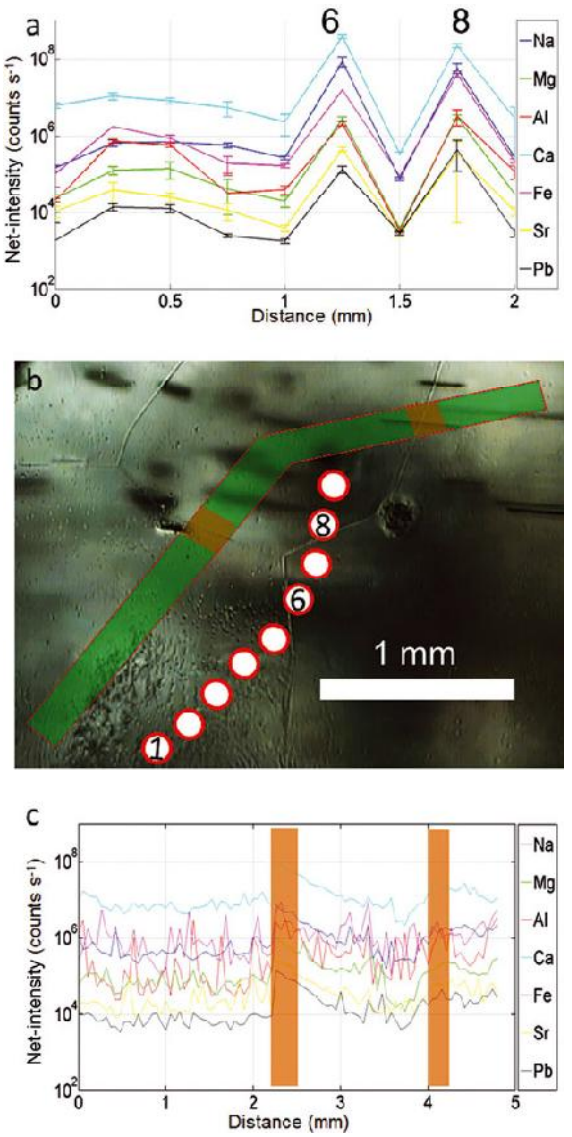

Fig. 14. Same as Figure 13, but for NGRIP sample 4882_B5 (2684.825–2684.875 m) and with nine spots.

and this pattern is almost identical for every element. In some cases (Fig. 7a, spot No. 6), a dip in intensity of one order of magnitude for all the elements corresponds to a rise in intensity of Fe of two orders of magnitude. This effect shows the possibility of having microparticles of different nature on a very fine scale, which may be located on both boundaries and grain interiors.

Elemental maps reveal sub-mm variability of concentrations, having maxima in correspondence to cloudy bands (Fig. 16), although elemental concentration does not exactly match the distribution of impurities inferred from the scan images, not least because the two surfaces do not exactly correspond, as images were taken from the centre whereas the analysed samples are from outer core ice. The overall distribution of impurities is not confined to grain boundaries, suggesting that it is not influenced by eventual grain boundary migration.

The 27 mm section represented in Figure 16 seems to be compatible with a 2 year cycle, given the layer thickness at this depth for the NGRIP core (~12 mm). The cycle is well represented in all elemental maps, having two alternations of low/high concentration from the bottom upwards, plus another low-concentration zone at the very top, although

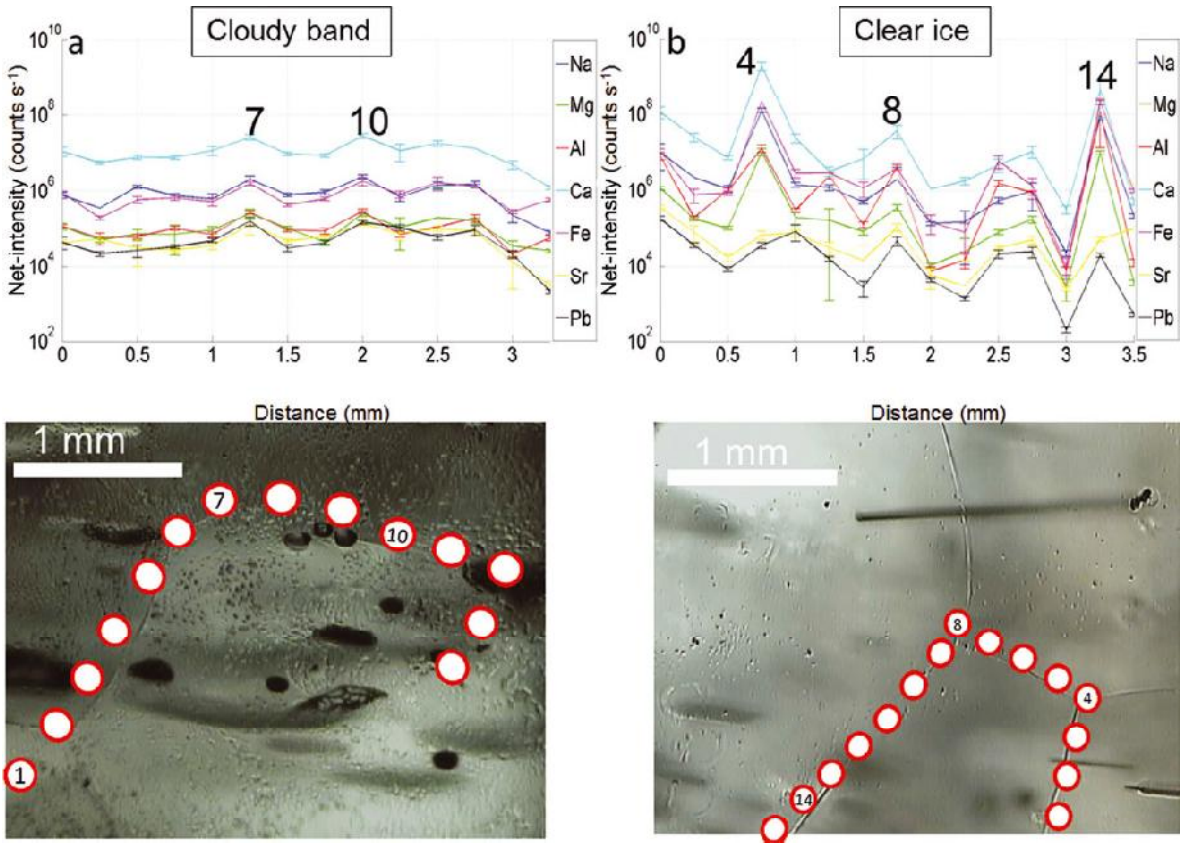

Fig. 15. Comparison of two chains-of-spots acquired along grain boundaries in cloudy bands (a) and clear ice (b) in NGRIP sample 4899_B8 (2694.025–2694.075 m). (a) Chain of 14 spots, size 128 μm, spacing 150 μm. Intensity values are comparable with those acquired in grain interiors in Figures 5–10. (b) Chain of 15 spots, size 164 μm, spacing 200 μm. Intensity values are higher than those acquired in grain interiors in Figures 11–14 (note the *y*-axis scale up to 10^{10}), with peaks that correspond to triple junctions. (Intensities with 164 μm spots are nominally ~1.7× higher than those at 128 μm.)

the inclination of the layering in the elemental maps is greater than is observed in the scan image (30–60° and ~30° respectively).

Figures 17–19 show elemental mapping across a cloudy band at ~2695 m depth. Concentrations of elements are high enough to also access elements like Sr and Pb, with the exception of Na, which shows relatively low concentration in the middle part, having higher concentration where the ice is clearer at the top. All the elements present similar maps showing that, within cloudy bands, elements do not lie preferentially on grain boundaries, even in areas where grain sizes are considerably smaller. Most of the variability within the band can be ascribed to different grains or different domains, which naturally can incorporate different amounts of impurities that seem to be evenly distributed within the grains.

The Ca/Al ratio (Fig. 19) is more variable than the Fe/Al ratio, and also tends to differ between neighbouring grains, with values varying between 0 and 15. This might represent a different input of particles, which even at the mm scale could distribute differently from grain to grain. Ca/Al ratios and Fe/Al obtained in this analysis (Table 2) are at least three times higher than the representative values of upper crust, and most probably result from a mix of dust from different sources located near some of the major Asian deserts such as the Gobi and Taklamakan. A clear component derived from Chinese loess could not be identified in this case.

The distribution of impurities observed in the samples suggests that at this depth of the NGRIP ice core grain boundaries do not always have high concentrations of soluble impurities, as was observed by Barnes and Wolff (2004) for Holocene ice and by Cullen and Baker (2000, 2001) for GISP2 and Byrd records. In fact, impurities tend to distribute themselves evenly between boundaries and bulk nuclei, as confirmed by profiles acquired over different cloudy bands and different core depths (Figs 5–9). When impurities are not abundant, as in clear ice, the data suggest that they tend to be allocated on boundaries and even more on junctions between grains.

From Eqn (3) we know that the smaller amount of impurities present in clear ice compared to cloudy bands should decrease the pinning effect and produce a more homogeneous distribution of impurities between boundaries and grain interiors. However, our data suggest that, in cloudy bands, the mobility of the grains is high enough to make the boundaries break away from impurities, which therefore can be homogeneously distributed between

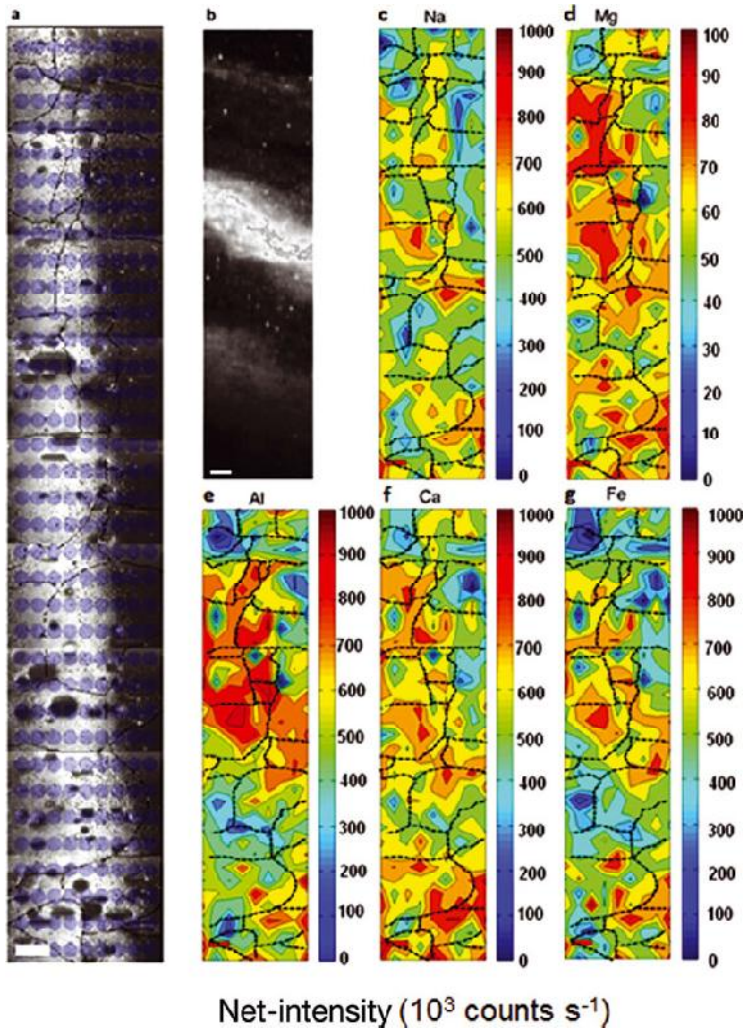

Fig. 16. (a) Picture of ice surface analysed as 2-D grid with the corresponding laser spots (9 × 35 spots, 280 μm size, 300 μm spacing; sample A7). (b) Scan image of the small section of the core analysed (27 mm × 6 mm). (c–g) Major elements indicative of dust (Al, Ca, Fe) and sea salt (Na, Mg) are shown; scale bar is 1 mm. High intensities of elements (Al, Ca, Fe) match the cloudy band (shown in (b)) reasonably well. There is no clear correspondence of high intensities and grain boundaries, but elements seem rather to distribute differently from one grain to another, having extreme values in the interior parts of the grains and not near boundaries. The grain boundary net (dashed black line) is overlapped to the graphs. Depth interval is 2694.7–2694.65 m.

boundaries and interiors. In clear ice, the force that drags boundaries of ice grains is not large enough to make the boundaries break away from the impurities, resulting in resolvable differences between grain boundaries and interiors of grains in terms of intensities. This may suggest that impurities in cloudy bands have a greater size than in clear ice, possibly originating from dust input, whereas in clear ice impurities may predominantly be in the form of soluble particles. This would increase the drag effect (again according to Eqn (3)) in clear ice and decrease it in cloudy bands. Further investigations of this effect in ice from various depths will be necessary to fully understand the distribution of impurities between grain boundaries and grain interiors.

The correlation between the layering visible on scan images and the impurity distribution is fairly well preserved, especially in elements like Na and Fe, whereas for Mg, Al and Ca the high-intensity zones sometimes exceed the corresponding area identifiable as a bright layer on the scan image.

CONCLUSIONS

The application of UV-laser ablation ICPMS analysis on ice cores allows mapping of impurities at a resolution well below 1 mm, namely <150–300 μm. All the elements show a signal/background ratio sufficient to resolve intensities at different spot sizes, although Na is challenging in clear ice. The vertical section analysed (Fig. 16) shows two complete seasonal cycles with a layering tilted by ~30°. This is mimicked well by Fe and Na intensity variability across the section.

Soluble and insoluble impurities are evenly distributed between grains and grain domains, and impurities do not

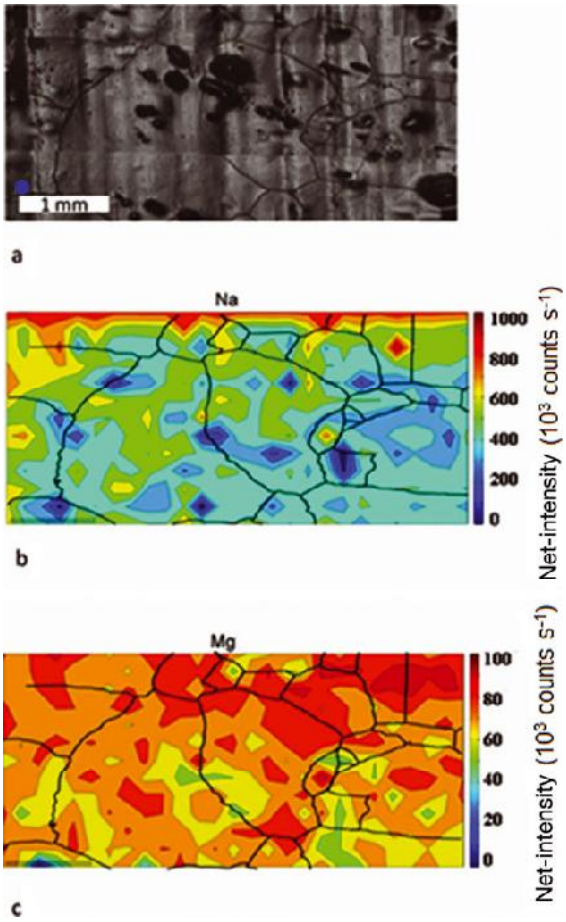

Fig. 17. (a) Image of the section analysed taken with the camera of the laser system. For size comparison a single spot is shown above the scale bar (sample 4900_A5). (b–d) Elemental variability over a 10 mm × 5 mm area of NGRIP sample at depth of 2694.75–2694.8 m; scale bar is 1 mm. Laser spot size is 164 µm, 200 µm spacing, repetition rate 20 Hz. The grain boundary net (black lines) is overlapped to the image.

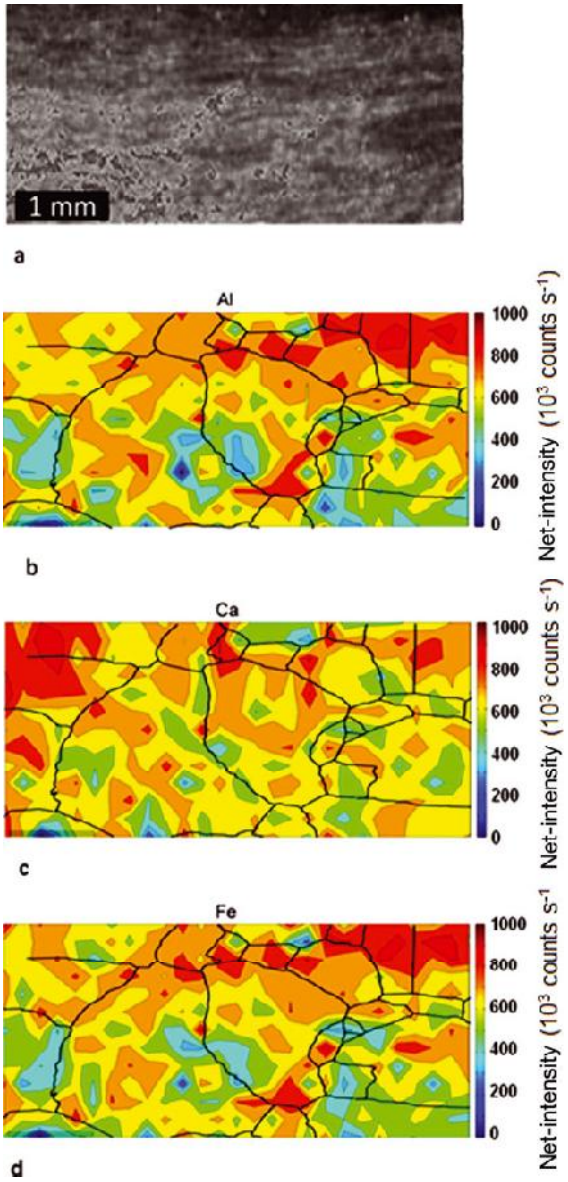

Fig. 18. (a) Crop of the section analysed taken by Svensson and others (2005). (b–d) Elemental variability over a 10 mm × 5 mm area of NGRIP sample 4900_A5 at 2694.75–2694.8 m depth; scale bar is 1 mm. Laser spot size is 164 µm, 200 µm spacing, repetition rate 20 Hz. The grain boundary net (black lines) is overlapped to the image.

always show a clear tendency to distribute themselves along grain boundaries or triple junctions. Also in cases of reduced grain size the highest elemental concentrations can be found within the interiors of grains. However, in some cases, especially for clear ice, a strong relationship between grain boundaries or triple junctions and abundance of impurities is observed. This suggests that the harvesting of micro-inclusions acts differently in cloudy bands and clear ice, possibly because of a difference in particle size between clear ice and cloudy bands. However, further studies of the distribution of impurities between boundaries and grain interiors will be necessary to understand their interaction with grain mobility at various depths.

The comparison between scanned images of the core and LA-ICPMS derived elemental maps shows that Fe is the most reliable proxy for 'second phase particles' (i.e. dust), whereas Na and, to a lesser extent, Mg are the best proxies for soluble impurities (i.e. sea-salt proxies). Our Ca/Al and Fe/Al ratios are consistent with a mix of different dust sources located among the major deserts of East Asia, such as the Gobi and Taklamakan.

ACKNOWLEDGEMENTS

We thank the Scientific Editor John W. Glen, Paul Vallelonga and Martin King for helpful discussions. Reviews by Sergio Faria and an anonymous reviewer helped to significantly improve the manuscript. A special acknowledgement is due to Jerry Morris (workshop), whose continued invaluable help made this work feasible. This work was funded by a RHUL studentship, Department Research Committee fund at

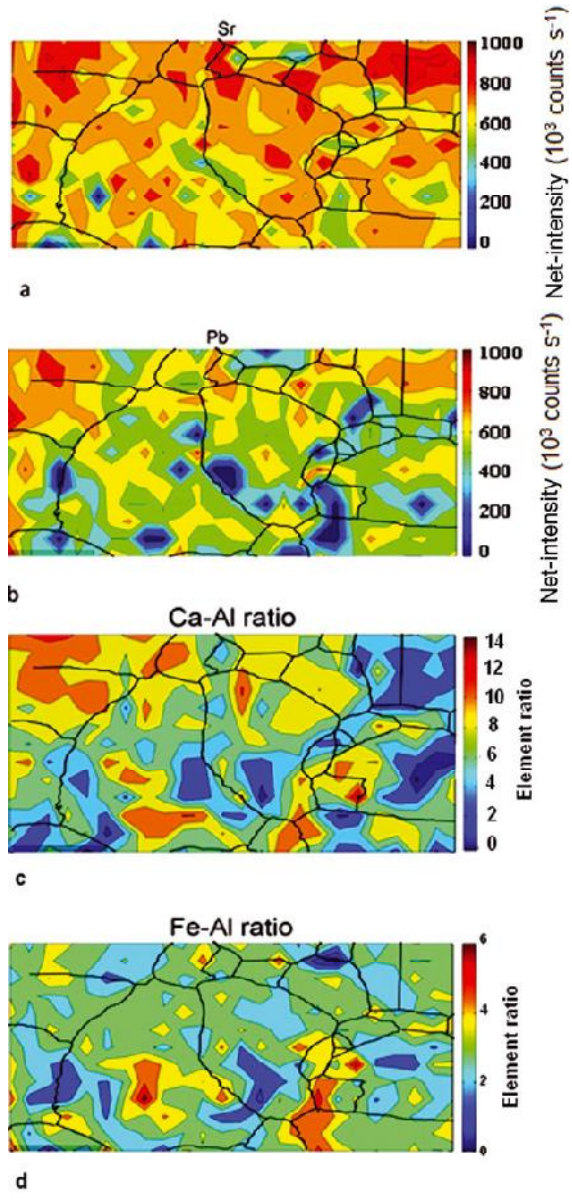

Fig. 19. (a) Sr elemental variability map. (b) Pb elemental variability map. (c) Ca/Al ratio over the section analysed. (d) Fe/Al ratio over the section analysed. The grain boundary net (black lines) is overlapped to the image. Sample 4900_A5, depth interval 2694.75–2694.8 m.

RHUL, and the INTIMATE cost action–STSM fund, all bestowed upon Damiano Della Lunga.

REFERENCES

Alley RB and Woods GA (1996) Impurity influence on normal grain growth in the GISP2 ice core, Greenland. *J. Glaciol.*, **42**(141), 255–260

Alley RB, Perepezko JH and Bentley CR (1986) Grain growth in polar ice: I. Theory. *J. Glaciol.*, **32**(112), 415–424

Andersen KK and 11 others (2006) The Greenland Ice Core Chronology 2005, 15–42 ka. Part 1: constructing the time scale. *Quat. Sci. Rev.*, **25**(23–24), 3246–3257 (doi: 10.1016/j.quascirev.2006.08.002)

Azuma N, Miyakoshi T, Yokoyama S and Takata M (2012) Impeding effect of air bubbles on normal grain growth of ice. *J. Struct. Geol.*, **42**, 184–193 (doi: 10.1016/j.jsg.2012.05.005)

Baker I and Cullen D (2003) SEM/EDS observations of impurities in polar ice: artifacts or not? *J. Glaciol.*, **49**(165), 184–190 (doi: 10.3189/172756503781830773)

Barnes PRF and Wolff EW (2004) Distribution of soluble impurities in cold glacial ice. *J. Glaciol.*, **50**(170), 311–324 (doi: 10.3189/172756504781829918)

Bigler M, Svensson A, Kettner E, Vallelonga P, Nielsen ME and Steffensen JP (2011) Optimization of high-resolution continuous flow analysis for transient climate signals in ice cores. *Environ. Sci. Technol.*, **45**(10), 4483–4489 (doi: 10.1021/es200118j)

Cullen D and Baker I (2000) Correspondence. The chemistry of grain boundaries in Greenland ice. *J. Glaciol.*, **46**(155), 703–706 (doi: 10.3189/172756500781832783)

Cullen D and Baker I (2001) Observation of impurities in ice. *Microsc. Res. Tech.*, **55**(3), 198–207 (doi: 10.1002/jemt.10000)

Dahl-Jensen D and 8 others (2002) The NorthGRIP deep drilling programme. *Ann. Glaciol.*, **35**, 1–4 (doi: 10.3189/172756402781817275)

Durand G and 10 others (2006) Effect of impurities on grain growth in cold ice sheets. *J. Geophys. Res.*, **111**(F1), F01015 (doi: 10.1029/2005JF000320)

Durand G and 7 others (2009) Evolution of the texture along the EPICA Dome C ice core. In Hondoh T ed. *Physics of ice core records II*. (Supplement issue of Low Temperature Science 68) Institute of Low Temperature Science, Hokkaido University, Hokkaido, 91–106

Duval P and Lorius C (1980) Crystal size and climatic record down to the last ice age from Antarctic ice. *Earth Planet. Sci. Lett.*, **48**(1), 59–64 (doi: 10.1016/0012-821X(80)90170-3)

Duval P, Louchet F, Weiss J and Montagnat M (2012) On the role of long-range internal stresses on grain nucleation during dynamic discontinuous recrystallization. *Mater. Sci. Eng. A*, **546**, 207–211 (doi: 10.1016/j.msea.2012.03.052)

Faria SH, Freitag J and Kipfstuhl S (2010) Polar ice structure and the integrity of ice-core paleoclimate records. *Quat. Sci. Rev.*, **29**(1–2), 338–351 (doi: 10.1016/j.quascirev.2009.10.016)

Faria SH, Weikusat I and Azuma N (2014) The microstructure of polar ice. Part II: state of the art. *J. Struct. Geol.*, **61**, 21–49 (doi: 10.1016/j.jsg.2013.11.003)

Fischer H, Siggaard-Andersen M-L, Ruth U, Röthlisberger R and Wolff E (2007) Glacial/interglacial changes in mineral dust and sea-salt records in polar ice cores: sources, transport, and deposition. *Rev. Geophys.*, **45**(RG10), RG1002 (doi: 10.1029/2005RG000192)

Fukazawa H, Sugiyama K, Mae S, Narita H and Hondoh T (1998) Acid ions at triple junction of Antarctic ice observed by Raman scattering. *Geophys. Res. Lett.*, **25**(15), 2845–2848 (doi: 10.1029/98GL02178)

Gow AJ (1969) On the rates of growth of grains and crystals in South Polar firn. *J. Glaciol.*, **8**(53), 241–252

Gow AJ and 6 others (1997) Physical and structural properties of the Greenland Ice Sheet Project 2 ice cores: a review. *J. Geophys. Res.*, **102**(C12), 26 559–26 575 (doi: 10.1029/97JC00165)

Guillope M and Poirier JP (1979) Dynamic recrystallization during creep of single-crystalline halite: an experimental study. *J. Geophys. Res.*, **84**(B10), 5557–5567 (doi: 10.1029/JB084iB10p05557)

Henderson P and Henderson GM (2009) *The Cambridge handbook of earth science data*. Cambridge University Press, Cambridge

Hörhold MW, Laepple T, Freitag J, Bigler M, Fischer H and Kipfstuhl S (2012) On the impact of impurities on the densification of polar firn. *Earth Planet. Sci. Lett.*, **325–326**, 93–99 (doi: 10.1016/j.epsl.2011.12.022)

Iizuka Y, Takata M, Hondoh T and Fujii Y (2004) High-time-resolution profiles of soluble ions in the last glacial period of a

Dome Fuji (Antarctica) deep ice core. *Ann. Glaciol.*, **39**, 452–456 (doi: 10.3189/172756404781814302)

Iizuka Y and 6 others (2008) A relationship between ion balance and the chemical compounds of salt inclusions found in the Greenland Ice Core Project and Dome Fuji ice cores. *J. Geophys. Res.*, **113**(D7), D07303 (doi: 10.1029/2007JD009018)

Jochum KP and 11 others (2011) Determination of reference values for NIST SRM 610–617 glasses following ISO guidelines. *Geostan. Geoanal. Res.*, **35**(4), 397–429 (doi: 10.1111/j.1751-908X.2011.00120.x)

Kipfstuhl S and 6 others (2006) Microstructure mapping: a new method for imaging deformation-induced microstructural features of ice on the grain scale. *J. Glaciol.*, **52**(178), 398–406 (doi: 10.3189/172756506781828647)

Kipfstuhl S and 8 others (2009) Evidence of dynamic recrystallization in polar firn. *J. Geophys. Res.*, **114**(B5), B05204 (doi: 10.1029/2008JB005583)

Lee YC, Yang X and Wenig M (2010) Transport of dusts from East Asian and non-East Asian sources to Hong Kong during dust storm related events 1996–2007. *Atmos. Environ.*, **44**(30), 3728–3738 (doi: 10.1016/j.atmosenv.2010.03.034)

Legrand MR and Delmas RJ (1988) Soluble impurities in four Antarctic ice cores over the last 30 000 years. *Ann. Glaciol.*, **10**, 116–120

Li J, Jacka TH and Morgan V (1998) Crystal-size and microparticle record in the ice core from Dome Summit South, Law Dome, East Antarctica. *Ann. Glaciol.*, **27**, 343–348

Longerich HP, Jackson SE and Günther D (1996) Inter-laboratory note. Laser ablation inductively coupled plasma mass spectrometric transient signal data acquisition and analyte concentration calculation. *J. Analy. Atom. Spectrom.*, **11**(9), 899–904 (doi: 10.1039/JA9961100899)

McCurdy E and Woods G (2004) The application of collision/reaction cell inductively coupled plasma mass spectrometry to multi-element analysis in variable sample matrices, using He as a non-reactive cell gas. *J. Analy. Atom. Spectrom.*, **19**(5), 607–615 (doi: 10.1039/B312250F)

Müller W, Shelley M, Miller P and Broude S (2009) Initial performance metrics of a new custom-designed ArF excimer LA-ICPMS system coupled to a two-volume laser-ablation cell. *J. Analy. Atom. Spectrom.*, **24**(2), 209–214 (doi: 10.1039/B805995K)

Müller W, Shelley JMG and Rasmussen SO (2011) Direct chemical analysis of frozen ice cores by UV-laser ablation ICPMS. *J. Analy. Atom. Spectrom.*, **26**(12), 2391–2395 (doi: 10.1039/C1JA10242G)

Mulvaney R, Wolff EW and Oates K (1988) Sulphuric acid at grain boundaries in Antarctic ice. *Nature*, **331**(6153), 247–249 (doi: 10.1038/331247a0)

North Greenland Ice Core Project (NorthGRIP) Members (2004) High-resolution record of Northern Hemisphere climate extending into the last interglacial period. *Nature*, **431**(7005), 147–151 (doi: 10.1038/nature02805)

Obbard R and Baker I (2007) The microstructure of meteoric ice from Vostok, Antarctica. *J. Glaciol.*, **53**(180), 41–62 (doi: 10.3189/172756507781833901)

Ohno H, Igarashi A and Hondoh T (2005) Salt inclusions in polar ice core, location and chemical form of water-soluble impurities. *Earth Planet. Sci. Lett.*, **232**(1–2), 171–178 (doi: 10.1016/j.epsl.2005.01.001)

Petit JR, Duval P and Lorius C (1987) Long-term climatic changes indicated by crystal growth in polar ice. *Nature*, **326**(6108), 62–64 (doi: 10.1038/326062a0)

Rasmussen SO and 15 others (2006) A new Greenland ice core chronology for the last glacial termination. *J. Geophys. Res.*, **111**(D6), D06102 (doi: 10.1029/2005JD006079)

Reinhardt H and 6 others (2001) Laser ablation inductively coupled plasma mass spectrometry: a new tool for trace element analysis in ice cores. *Fresenius' J. Anal. Chem.*, **370**(5), 629–636 (doi: 10.1007/s002160100853)

Reinhardt H, Kriews M, Miller H, Lüdke C, Hoffmann E and Skole J (2003) Application of LA–ICP–MS in polar ice core studies. *Anal. Bioanal. Chem.*, **375**(8), 1265–1275 (doi: 10.1007/s00216-003-1793-5)

Rempel AW, Waddington ED, Wettlaufer JS and Worster MG (2001) Possible displacement of the climate signal in ancient ice by premelting and anomalous diffusion. *Nature*, **411**(6837), 568–571 (doi: 10.1038/35079043)

Rempel AW, Wettlaufer JS and Waddington ED (2002) Anomalous diffusion of multiple impurity species: predicted implications for the ice core climate records. *J. Geophys. Res.*, **107**(B12), 2330 (10.1029/2002JB001857)

Sakurai T and 6 others (2009) Direct observation of salts as micro-inclusions in the Greenland GRIP ice core. *J. Glaciol.*, **55**(193), 777–783 (doi: 10.3189/002214309790152483)

Sakurai T, Ohno H, Horikawa S, Iizuka Y, Uchida T and Hondoh T (2010) A technique for measuring microparticles in polar ice using micro-Raman spectroscopy. *Int. J. Spectrosc.*, **2010**, 384956 (doi: 10.1155/2010/384956)

Steffensen JP (1997) The size distribution of microparticles from selected segments of the GRIP ice core representing different climatic periods. *J. Geophys. Res.*, **102**(C12), 26 755–26 763

Stephenson PJ (1967) Some considerations of snow metamorphism in the Antarctic ice sheet in the light of ice crystal studies. In Oura H ed. *Physics of snow and ice*. Hokkaido University, Institute of Low Temperature Science, Sapporo, 725–740

Svensson A, Biscaye PE and Grousset FE (2000) Characterization of late glacial continental dust in the Greenland Ice Core Project ice core. *J. Geophys. Res.*, **105**(D4), 4637–4656 (doi: 10.1029/1999JD901093)

Svensson A and 7 others (2005) Visual stratigraphy of the North Greenland Ice Core Project (NorthGRIP) ice core during the last glacial period. *J. Geophys. Res.*, **110**(D2), D02108 (doi: 10.1029/2004JD005134)

Thorsteinsson T, Kipfstuhl J, Eicken H, Johnsen SJ and Fuhrer K (1995) Crystal size variations in Eemian-age ice from the GRIP ice core, central Greenland. *Earth Planet. Sci. Lett.*, **131**(3–4), 381–394 (doi: 10.1016/0012-821X(95)00031-7)

Thorsteinsson T, Kipfstuhl J and Miller H (1997) Textures and fabrics in the GRIP ice core. *J. Geophys. Res.*, **102**(C12), 26 583–26 599 (doi: 10.1029/97JC00161)

Vallelonga P and 12 others (2012) Duration of Greenland Stadial 22 and ice-gas Δage from counting of annual layers in Greenland NGRIP ice core. *Climate Past*, **8**(6), 1839–1847 (doi: 10.5194/cp-8-1839-2012)

Wang Y, Thorsteinsson T, Kipfstuhl J, Miller H, Dahl-Jensen D and Shoji H (2002) A vertical girdle fabric in the NorthGRIP deep ice core, North Greenland. *Ann. Glaciol.*, **35**, 515–520 (doi: 10.3189/172756402781817301)

Warren SG and Brandt RE (2008) Optical constants of ice from the ultraviolet to the microwave: a revised compilation. *J. Geophys. Res.*, **113**(D14), D14220 (doi: 10.1029/2007JD009744)

Weiss J, Vidot J, Gay M, Arnaud L, Duval P and Petit JR (2002) Dome Concordia ice microstructure: impurities effect on grain growth. *Ann. Glaciol.*, **35**, 552–558 (doi: 10.3189/172756402781816573)

Weltje GJ and Tjallingii R (2008) Calibration of XRF core scanners for quantitative geochemical logging of sediment cores: theory and application. *Earth Planet. Sci. Lett.*, **274**(3–4), 423–438 (doi: 10.1016/j.epsl.2008.07.054)

MS received 16 October 2013 and accepted in revised form 5 July 2014

Chapter 5

Citation: Della Lunga, D., Müller W., Rasmussen S. O., Svensson A. S. & Vallelonga P. T. (2015a). Calibrated cryo-cell UV-LA-ICPMS elemental concentrations in NGRIP ice reveal abrupt, sub-annual shift in dust across glacial stadial precursor event GI-21.2. Planned submission to *Journal of Quaternary Science*.

This manuscript is in preparation. Together with Chapter 4 it forms the methodology of this thesis, including the calibration strategies utilized for the quantification of elemental concentrations.

Author contributions: DDL designed the research and the calibration method together with WM, performed the analysis and interpreted the data. WM, SOR, ASS and PTV edited the manuscript.

Calibrated cryo-cell UV-LA-ICPMS elemental concentrations in NGRIP ice reveal abrupt, sub-annual shift in dust across glacial stadial precursor event GI-21.2.

Damiano Della Lunga[1], Wolfgang Müller[1], Sune Olander Rasmussen[2], Anders Svensson[2], Paul Vallelonga[2]

[1] Department of Earth Sciences, Royal Holloway University of London,

Egham TW20 0EX, United Kingdom.

[2], Centre for Ice and Climate - Niels Bohr Institute, University of Copenhagen, 2100 Copenhagen Ø, Denmark.

Correspondence to: D. Della Lunga

(damiano.dellalunga.2011@live.rhul.ac.uk)

Abstract

Several abrupt switches from periods of extreme cold (Greenland stadials, GS) to relatively warmer conditions (Greenland interstadials, GI) called Dansgaard-Oeschger events are recorded in Greenland ice cores. The onset and termination of these events can occur over just a few years, but their dynamics are not well understood, nor is the phasing of the corresponding proxies.

Using cryo-cell UV-laser ablation inductively-coupled-plasma mass spectrometry (UV-LA-ICPMS), we analysed 260 cm NGRIP ice (~200 years; depth range: 2691.15-2688.55 m) across the GI-21 precursor event (GI-21.2). GI-21.2 is marked by a 3-4 ‰ increase in the $\delta^{18}O$ values that occurred approximately 250 years before the major GI-21 warming (GI-21.1). We report concentrations of major elements indicative of dust and/or sea salt

(Fe, Al, nssCa, ssMg, Na) at a spatial resolution of ~200 µm, while maintaining detection limits in the low-ppb range, thus achieving sub-annual time resolution. We present an improved external calibration and quantification procedure using a set of five ice standards, specifically made from aqueous (international) standard solutions.

Our results show that proxies react in as short a time as only one year at the onset of the GI-21 precursor warming, with a sudden drop in concentration, and more gradually at the termination of the GI-21 precursor warming, when concentrations come back to typical GS-22 values through several small jumps. We suggest that the GI-21.2 event might be related to a change at the Asian dust source from dry to wet conditions which reduced uplift and residence time of particles in the atmosphere.

Introduction

Dansgaard-Oeschger (D-O) events are abrupt climatic changes from periods of extreme cold (called Greenland stadials GS) to relatively warm conditions (Greenland interstadials GI). These events occurred during the last 120 kyrs and were first identified in Greenland ice cores mainly as $\delta^{18}O$ oscillations but also in several other proxies such as dust and sea salt content (and relative proxies; Dansgaard et al., 1993). Each of these cycles lasted from a few centuries to thousands of years, with a temperature increase of 5 to 16 °C over Greenland during the warming period (Severinghaus and Brook, 1999; Huber et al., 2006). Evidence of D-O events is also found in different environmental archives in both Northern and Southern hemispheres (Voelker, 2002). In ocean sediment cores, D-O cycles can be identified in different climate proxies, such as the abundance of *Neogloboquadrina pachyderma* (sin) in the sub-polar North Atlantic, which is a cold water species of foraminifera and therefore decreases in abundance to almost 0% during the warm phases (Broecker et al., 1992). Speleothems across Europe and Asia also record shifts in $\delta^{18}O$ corresponding to D-O events, confirming

that these oscillations happened at least at a hemispheric scale (Spötl and Mangini, 2002, Clement and Peterson 2008).

During stadial periods deposition of dust and sea salt in Greenland ice significantly increases. Sea salt aerosols in ice cores are present with several species (e.g. Na^+, Cl^- and Mg^{2+}) as major impurities. The source of these particles derives from bubble bursting over open ocean water, where winds lash vigorously the sea surface. The aerosols are then transported and deposited on the ice cap. This phenomenon is emphasized during long cold periods but also within a year, having a peak in wintertime (Wolff et al., 2003). This is because storminess over the ocean enhances the transport of sea salt species inland during winter and glacial periods, although this effect has to counter the typical increase of sea ice extent during winter that makes it more difficult for sea salt aerosols to reach a particular site, since they have to travel further (Petit et al*.,* 1999). Another effect contributes to the above mechanism, which is thought to be the primary reason for sea salt enrichment in ice during cooling events. When sea ice is formed, highly saline brine and fragile frost flowers form on top of the frozen surface. This brine represents a further source of aerosol, carried again by the wind towards the inland (Wolff et al, 2003).

Studies suggest that during the glacial period the increased storminess and surface wind speed, the reduced atmospheric and soil moisture leads to sharp increases also of dust transport over polar areas (Yung et al., 1996; Kreutz, 2013). The source of Greenland dust includes high-elevation sites and high latitude steppe in Asia (Mahowald et al*.*, 1999), whose areas widely spread during cold, more arid, periods. The phasing of proxies has always been a key aim of high-resolution investigations of Greenland ice cores to determine a correct time scale for variations of parameters such as $\delta^{18}O$, deuterium excess, precipitation (layer thickness), input of Asian dust (Ca mainly), sea salt (Na) as well as gas concentrations (e.g. Wolff et al., 2010). Therefore, dust records in polar ice cores as inferred from non-sea salt fraction of several species (e.g. Ca^{2+}, Mg^{2+}, Al^{3+}, K^+, Fe^{2+}), which is largely the result of carbonate and silicate mineral weathering (Lewis and Schwartz.,

2004), can be used to reconstruct changes of past climatic conditions, temperature and atmospheric circulation.

Impurities in ice are measured routinely by Continuous Flow Analysis (CFA), melting a section of the ice cores at a constant speed and collecting the liquid water to measure different proxies such as Na^+, NH_4^+, dust and conductivity through several detectors at a resolution of ~ 10 mm (Bigler et al., 2011).

The trigger of these DO abrupt changes remains a matter of debate (for summary see Petersen et al., 2013 and Barker et al., 2015). Current thinking is mainly focused around two different ideas. One relates to multiple states of the ocean's thermohaline circulation which seems to be the prominent mechanism that drives climate changes in model simulations (Randall et al., 2007; Zhang et al., 2014), while the other one focuses on the dynamics of the tropical atmosphere-ocean system (Clement et al., 2001). A promising approach, as suggested by W. S. Broecker (2003), is to "*search for and study precursory events*" which were firstly identified by Johnsen et al. (1992) and Dansgaard et al. (1993). Recent work (Capron et al., 2010) investigated minor D-O 'side' events and identified (i) short-lived and abrupt warming events preceding some GIs (precursor-type events) and (ii) abrupt warming events at the end of some GIs (rebound-type events). A good example is GI-21.2, which, in the NGRIP isotopic profile, represents a $\delta^{18}O$ oscillation of ~4 ‰ lasting more than 100 yrs before the onset of GI-21.1. The occurrence of this particular precursor event was also confirmed by $\delta^{18}O$ variations measured in GRIP and GISP2 cores (Seierstad et al., 2014) and by their detection in high-resolution records of $\delta^{15}N$ data and CH_4 (Johnsen et al., 1992; Grootes and Stuiver, 1997; Grachev et al., 2009). Evidence of GI-21.2 has also been found in Northern Alps Speleothems (NALPS) $\delta^{18}O$ records, where an increase of 1.7 ‰ and a subsequent rapid decrease of 2.2 ‰ preceding GI-21.1 has been identified around an age of 85.36 ka lasting for 190 yrs from 85.44 to 85.25 ka (Boch et al., 2011). Moreover, total reflectance measurements of high-resolution laminated sediments from the Cariaco basin (Venezuela) identified GI-21 and GI-23 precursor-type events

demonstrating their large-scale climatic footprints and the recording sensitivity of these tropical archives (Deplazes et al., 2013).

In summary, precursor-type events have been detected in $\delta^{18}O$ from ice cores and speleothems and total reflectance of sediments (Capron et. al, 2010; Boch et al., 2011; Deplazes et al., 2013), but in other records their occurrence is ambiguous. The aim of the present study is to assess the sensitivity and the correct phasing of dust/sea salt proxies as Fe, Al, Ca, Mg, and Na at a resolution of ~200 µm (i.e. nominally approximately bimonthly) in response to fast and abrupt warming/cooling events such as precursor-type events. In order to achieve this, we investigated the so called GI-21 precursor (GI21.2), a minor warming event marked by shift of ±4 ‰ in the $\delta^{18}O$ values, taking place and a few decades before the onset of GI-21.1 (Fig. 1). We also present an updated fully quantitative calibration for the elements under investigation, following Della Lunga et al. (2014) and Müller et al. (2011).

Methods and Calibration

NGRIP ice core samples were prepared at the Centre for Ice and Climate, Niels Bohr Institute, Copenhagen. They were cut to fit the laser ablation cryo-cell sample holder, which is able to simultaneously hold three ice strips of dimensions 50 x 11 x 11 mm (see Della Lunga et al., 2014). For this study a section of 260 cm of NGRIP ice from the depth interval 2688.55-2691.15 m was selected. This section corresponds to more than two hundred years, given the layer thickness of ~10 mm (Vallelonga et al., 2012). This section contains GI-21.2, the so-called GI-21 precursor representing an age range of 85.06 – 84.96 ka (Rasmussen et al., 2014).

The analytical methodology of cryo-cell UV-LA-ICPMS used for these analyses follows Müller et al. (2009, 2011) and especially Della Lunga et al. (2014) and only a brief summary will be given here. Cleaning of the ice surface has been conducted using a ceramic ‘major-elements free’ Y-doped ZrO_2 blade (American Cutting Edge, U.S.A.), mounted on a custom-built, acid-cleaned PTFE vice that allows ice scratching in steps of less than 0.5

mm and surface smoothing in order to remove contamination from cutting. Approximately 2 mm of ice were removed from all the surfaces about to be analysed. We utilized the upward-facing surface of the NGRIP ice core as described in Della Lunga et al. (2014). Handling and smoothing procedures were conducted always under a clean hood utilizing laboratory gloves in an ultra-clean laboratory (US 10-100, ISO4-5).

The adopted methodology includes the acquisitions of the following mass/charge ratios: 23(Na), 24(Mg), 27(Al), 34(S), 39(K), 40(Ca), 44(Ca), 55(Mn), 56(Fe), 65(Cu), 85(Rb), 88(Sr), 89(Y), 138(Ba), 139(La), 140(Ce), 141(Pr), 147(Sm), 153(Eu), 157(Gd), 172(Yb), 208(Pb), with dwell times ranging from 5 to 40 ms (see Della Lunga et al., 2014). Among these, only the following usually show resolvable signal/background ratio and will be displayed as results: 23(Na), 24(Mg), 27(Al), 39(K), 40(Ca), 56(Fe). However, mass 39(K), despite resolvable signal/background ratio, suffers from potentially significant interference of ^{38}ArH, and therefore will not be considered further. Rare Earth Elements were monitored as indicator of further possible contamination due to smoothing and were not the main target of this study.

Intensities of isotopes acquired have been recalculated as elemental intensities based on their relative isotopic abundance taken from Berglund and Wieser (2011).

Correction for instrumental drift has been carried out as follows:

$$I_i^{Sa} = \frac{I_i^{raw}}{\left(\frac{t-t_0}{2}\right)\sum_{i=1}^{k}\frac{1}{k}[m_{std}]} \quad \text{(eq.1)}$$

where I_i^{Sa} is the intensity of element i in the sample and surrounding background corrected for instrumental drift, I_i^{raw} is the raw intensity of element i in the sample, t indicates the time (in s) between the analysis and the start t_0, and m_{std} represents the slope of the regression line obtained correlating NIST 612 standard data acquired during a single ICPMS run executed during a day of analysis where *k* ICPMS runs are performed (Fig. 2).

Each element has been calibrated using a set of four ice standards out of a total of five (SLRS-5, SLRS-5_10, ICP-20, NIST 1648a and Water Low) made in our laboratory from four different standard solutions at different concentrations (in 2% HNO_3) and different dilutions (Table 1). This external calibration assumes overall comparable ablation characteristics of NGRIP ice and ice standards, which in view of their similar matrix are a satisfactory assumption. Furthermore, using m/z=17 (OH) as an internal standard following Reinhardt et al. (2003), is not feasible because the significantly lower sample consumption of UV-LA relative to IR-LA (Müller et al., 2011) does not result in a background-resolved ICPMS signal at m/z=17.

Ice standards were made in a laminar-flow clean hood located in an ultra-clean laboratory (US 10-100, ISO4-5) at RHUL, using an acid-cleaned custom-made PTFE mould shown in Fig. 3a,b. The mould features two inner volumes, namely one round pool where liquid nitrogen can be used to cool the mould and the innermost volume that uses a polished Pyrex borosilicate slide as bottom surface that can be removed to extract the ice. The procedure to produce homogenous ice standards is as follows:

i) A polyurethane box is filled with 0.5 l of liquid nitrogen (LN) (Fig. 3b)
ii) 1 ml of standard solution already prepared (for concentrations see Table 1) is pipetted into the inner volume of the mould, to create a ~2 mm liquid layer residing on the glass (Fig 3a).
iii) The entire mould is dipped into the liquid nitrogen, which causes near-instantaneous shock-freezing of the liquid contained in the inner volume (Fig 3b). The procedure indicated in ii) and iii) is then repeated 5 times to create ~10 mm volume of ice built up by shock-frozen layers of standard solution.

This procedure allows the standard solution to freeze to ice in well-developed layers and ensures acceptable homogeneity of elements in the ice volume at relative standard deviations (RSD) of ~10-15 % within a single analysis (Fig. 4), improving what achieved in other UV-LA-ICPMS ice core works (Sneed et al., 2015). A standard suspension of NIST1648a has been prepared by

carefully weighing 4.92 mg of 'Urban dust' NIST1648 reference material which was subsequently diluted in 100 ml of ultrapure (18 MΩ-cm) water and 2 ml of HNO_3. The solution then was homogenised through 3 cycles of 5 min of mechanical vibration of the container, before being frozen as described in i), ii) and iii). Given the NIST1648a average particle size of 5 - 10 μm and the 90% percentile of 30 μm, we assume a homogeneous distribution of particles at the scale of the acquisition spot size utilized (212 μm).

Ice blanks were also produced following the procedure described above by shock-freezing of ultrapure (18 MΩ-cm) water; an example of UV-LA data is shown in Fig. 5.

For each element, the equation of the linear regression fitting the four standards selected has been utilized to convert intensities into concentration (ppb) (Fig. 3).

Analyses were carried out using laser tracks which had been preceded by three laser cleaning passages at 25 Hz with a spot size of 280 μm and a speed of 8 mm/min. This was done to remove residual contamination and surface effects. Data were subsequently acquired at 20 Hz, 212 μm spot size, 3 mm/min speed and laser fluence of ~3.5 J/cm^2. This gives a resolution of approximately 200 μm and a cumulative trench depth of ~20 μm (estimated by visual imaging and a typical ablation rate per pulse of 0.10 μm; Müller et al., 2011). Every acquisition run starts and ends with a NIST612 and ICP-20/SLRS-5/NIST 1648a track and comprises two parallel longitudinal tracks, to assess reproducibility (three cleaning + one acquisition tracks) along the long axis of each 5 cm sample. The instrumental drift corrected intensities were then averaged between the two tracks and used for calibration.

Since Ca and Mg have contributions from both dust (*nss*) and sea salt (*ss*), their concentrations have been recalculated according to Kreutz (2013), assuming that all Na has a sea salt origin:

$$nssCa^{2+} = Ca^{2+} - Na^{+} \cdot R_m \quad \text{(eq. 2)}$$

$$ssMg^{2+} = Mg^{2+} - \frac{nssCa^{2+}}{R_c} \quad \text{(eq. 3)}$$

where R_m and R_c are the ratios of Ca^{2+}/Na^{+} (0.038) and Ca^{2+}/Mg^{2+} (1.44) in marine aerosol and average crust respectively. Sea salt magnesium is usually around 20% of non-sea salt magnesium.

Limit of detection were calculated as follows:

$$LOD_i^{Sa} = \left(\frac{c_i^{std}}{I_i^{std} - I_i^{bkg}}\right) 3\sigma_i^{bkg} \quad \text{(eq. 4)}$$

where c_i^{std} is the concentration (in ppb) of the element *i* in the standard, σ_i^{bkg} is the standard deviation of the background for an element *i*, I_i^{std} is the averaged intensity of the element *i* in the sample and I_i^{bkg} is the averaged intensity of background of element *i*. The values obtained for this study are listed in Table 1. The Na LOD value is higher due to typical elevated (LA-ICPMS) sodium background, exaggerated by using routinely NIST61x glasses (14±0.1 % m/m Na_2O; Jochum et al., 2011) for other LA work. Uncertainties have been estimated using the following equation:

$$\sigma_{tot} = \sqrt{\left(\sigma_{nist\_std}\right)^2 + \left(\sigma_{ice\_std}\right)^2 + (\sigma_{id})^2 + \left(\sigma_{ice\_calib}\right)^2} \quad \text{(eq. 5)}$$

where σ_{nist_std} and σ_{ice_std} represent the relative standard error of the signal acquired during a single run for NIST 612 and the selected ice standard respectively, while σ_{id} and σ_{ice_calib} represent the standard errors related to the instrumental drift correction and the calibration and are typical for each element. These values are shown in Fig. 6. The total uncertainty σ_{tot} is on average about ±16%, σ_{ice_std} contributing for 90% of this value.

Results

Standardization

Results are displayed in Figures 2-10 and listed in Table 1. Figure 2 shows the ICPMS instrumental drift (~5-8%/h) typically observed during an ~100 min long data acquisition 'run' comprised of standards, cleaning and data acquisition, with NIST 612 intensities slightly decreasing with time. This

observed drift of NIST612 standard glass is used to correct that of ice samples and standards. Figure 4 presents a comparison between LA-ICPMS data from NIST 612 and data from one of the ice standards prepared for this study (ICP-20), showing that ice standards are sufficiently homogeneous both intra-analysis and inter-analysis (RSD values of ±10-15%), especially considering the large concentration contrasts observed in ice (see below). Ablation of ice blanks (Fig. 5) shows that intensities of all the analysed elements drop to ICPMS-background levels after two laser cleaning passages. Obtained calibration curves for Na, Mg, Al, Ca, and Fe are shown in Fig.6. For each element a linear relationship between net intensities and concentrations in the ice (ppb) has been found, with R^2 values ranging from 0.87 to 0.99 for Mg and Na respectively.

GI-21 precursor (GI-21.2)

Results of Na, ssMg, Al, nssCa, Fe measurements across 260 cm of NGRIP ice (2691.15 - 2688.55 m) corresponding to GS21.2 and GI-21.2 are displayed in Figs. 7-11. For each millimetre of ice analysed, we obtain 40 analytical data points. The resolvable spatial resolution is ~200 µm given the interplay between spot size, stage speed, ICPMS dwell time and laser repetition rate, making down-sampling in the form of a moving average necessary. The matching $\delta^{18}O$ profile (Vallelonga et al., 2012) at 5 cm resolution shows a ~4 ‰ shift to more positive values between 2690.70 and 2690.40 m depth, indicating the GI-21.2 rapid warming event, after which $\delta^{18}O$ gradually comes back to pre-warming values (Figs. 1 and 7). The element profiles acquired via UV-LA-ICPMS show a slightly different pattern (Fig 7). The drop in concentrations (when viewed from greater to shallower depths) appears within the first 15 cm of our profile for all of the elements (depth range 2691.15 - 2691.00 m). For the key dust proxies nssCa and Fe, the drop in concentration is even sharper and can be located within a depth range of 10 mm (2691.09-2691.08 m), corresponding to a time span of just a single year. The concentration of nssCa, for instance, drops ~tenfold from 200±50 to 30±15 ppb over the distance of 10 mm, matched by that of Fe at

the same location, whose concentration drops from 40±10 ppb to 3±1 ppb. Towards shallower depths, most of the elements show after some characteristic variations a further decrease in concentrations up to a depth of 2690.60 m that corresponds to the peak of the warming phase. At these depths concentrations often fall below LODs, having the lowest values of the entire section. However, the minima are not perfectly synchronized among all the elements, since some proxies show them earlier, as ssMg and Al (at depth 2690.80 m approximately), whereas some others show it later around a depth of 2690.60 m (Na, nssCa). In some other elements, like Fe, a clear minimum is not identifiable.

Furthermore, elemental minima are not where most of the $\delta^{18}O$ shift occurs, instead they appear to coincide with a strong $\delta^{18}O$ jump of 1.5‰ around a depth of 2690.70m, while the $\delta^{18}O$ maximum at ~2690.35m already sees rather dusty conditions.

From depth 2690.20 m onwards $\delta^{18}O$ gently decrease from approximately -37.5 ‰ to -41‰, representing the cooling phase. In this part, elemental concentrations increase gradually and the patterns present a higher degree of variability. Overall, the record can be divided in four intervals labelled as 'section 1,2,3 and 4' in Fig.7: The deepest 40 cm (2691.15-2690.75 m, green bar) show a decrease in concentrations of least one order of magnitude for every element, made by small sequential decreases following a major one situated at 2691.08 m. From depth 2690.75 to depth 2690.60 m concentrations reach a minimum for each element, often below LODs (section 2, purple bar). Most of the elements concentrations rise again of one order of magnitude at depth 2690.60 m, stabilizing at these levels until a depth of 2689.00 m. At this section 3 (blue bar), elements show pronounced recurring short-term variability at multiannual time scale with more than tenfold concentrations variation, with for instance nssCa and Fe showing possible antiphase behaviour. The last 45 cm (depth 2689.00-2988.55 m, orange bar) indicate a further increase in all concentrations towards higher values, which is especially sharp at 2688.95 m, and concentrations finally reach similar values to the profile start at ~2691.15 m. Figures 8 and 9 show

in detail two of the major jumps in concentrations across the entire section and correspond to the first and the last part of the above mentioned sections 1 & 4, respectively. They illustrate particularly well the abruptness of the concentration changes observed.

The data variability is particularly high during the cooling phase (Fig. 10), where oscillation in concentrations can reach more than an order of magnitude in a short time scale (1-2 years). Interesting features are also observable at depth 2690.15 m and 2689.60 m. In the first case most of the elements and nssCa in particular, shows a local minimum that is possibly anti-correlated to Fe, which shows a local peak. In the second case we can observe a rapid rise and subsequent drop in Al concentrations with a small flat plateau in between. This pattern, however, differs from what can be observed for other elements at the same depth.

LA-ICPMS-CFA data comparison

For comparison, our UV-LA data have been plotted together with previously published CFA results from the same NGRIP depths (Vallelonga et al., 2012). The profiles of $\delta^{18}O$, NH_4, CFA-Na, CFA-dust and conductivity have a resolution of 5, 0.35, 0.35, 0.1, 0.1 cm respectively. The two datasets show some similarities: between a depth of 2691.10 and 2691.00 m NH_4, Na and conductivity profiles present a significant peak and subsequent drop, similarly to what observed for our elemental proxies, marking GI-21.2 starting point, which, however, occur earlier in our LA-ICPMS profiles. Furthermore, minima for the entire section are located at a depth of 2690.75 m in both datasets. Also, both datasets agree in the shallowest part of the section, showing an increase towards higher concentrations around a depth of 2689.10 m.

However, UV-LA-ICPMS data show several differences compared to CFA: firstly, elemental concentrations increase distinctly already at a depth of 2690.60 m, secondly, no abrupt drop of CFA concentration is observed at 2691.10 and data show a significant rise in concentration only at a depth of 2690.10 m. Comparing the Na record between CFA and LA-ICPMS for the section 2688.55-2689.00 m (where LA-ICPMS Na is resolvable) yields

367 average values of 60 and 84 ppb respectively. This represents a difference of
368 ~27% between the two datasets. However, this is strongly influenced by a
369 few factors, such as the elevated UV-LA-ICPMS LOD for Na (which
370 decreases the number of low value data points) and probably by volume
371 effects. In fact, we estimated that every LA-ICPMS data point corresponds to
372 ~120 ng of ablated ice (based on scanning speed and ice crater depth)
373 whereas CFA sampling resolution is about 2.3 g (Vallelonga et al., 2012) for
374 each data point. This introduces a sampling volume mismatch between the
375 two datasets that can also be influenced by surface effects and especially by
376 the wavy nature of layers at this scale and depth. Furthermore, the CFA data
377 presented here refer to measurements of insoluble dust of size > 1 μm and
378 therefore do not account for ionic impurities (Vallelonga et al., 2012).
379 Figure 10 shows a tentative annual layer counting based on both CFA and
380 LA-ICPMS data. The difference in resolution between the two datasets can
381 be observed. Comparing the various signals we identified 15 ± 4 annual layer
382 in a section of 15 cm, for an annual layer thickness between 8 and 10 mm,
383 which is compatible with what has previously been observed (Vallelonga et
384 al., 2012).
385

386 ## Discussion

387 Our fully quantitative calibration of UV-LA-ICPMS net count rates (see Della
388 Lunga et al., 2014) is presented here for the first time. We have succeeded in
389 producing suitably homogeneous ice standards (±10-15% RSD, Fig. 5) from
390 four different solutions at known concentration of elements and one frozen
391 suspension at different dilution. This represents an improvement to what has
392 been previously achieved in ice standard preparation (Wilhelm-Dick, 2008;
393 Reinhardt et al., 2003, Sneed et al., 2015). The correlation between the
394 elemental concentrations in the standards and the resulting signals from LA-
395 ICPMS (in counts per second, cps) is remarkable and follows the expected
396 linear relationship (Fig. 3), with R^2 values ranging from 0.87 (Mg) and 0.99
397 (Na).

The removal of contamination is ensured not only by surface-smoothing executed via a 'major-element free' ZrO_2 blade (Della Lunga et al., 2014), but also by laser cleaning performed three times before each acquisition. Its effectiveness can be demonstrated using ice blanks (Fig. 6). The overall uncertainties estimation derived from analysis and calibration gives an average value of ±16%, which has to be considered acceptable for ice core analysis where elemental concentrations are typically in the lowest ppb range and variability usually covers more than one order of magnitude.

Fig. 7 shows remarkably strong variations of concentrations of all the elements, confirming that sea salt (Na, ssMg) and dust proxies (Al, nssCa, Fe) do react to natural abrupt climate change (ACC) events at time scales shorter than the duration of a D-O event itself. The pattern of all the elements presents a sudden drop within the first 15 cm (Fig. 8), to reach a minimum with values of few ppb or even ppt (below LOD) (Fig. 7). Concentrations then rise suddenly again and show much more pronounced oscillations, with a further increase to higher values towards the end of the section, where concentrations return to the same order of magnitude of the ones characterising the deepest part.

The slightly different pattern between $\delta^{18}O$ and elemental proxies has to be expected as the resolution of the two records is different, namely 5 cm and ~200 µm respectively. The diffusion length at this depth in the NGRIP ice core has been estimated to be much less than 1 cm (Gkinis et al., 2014), therefore oxygen isotopes undergo diffusion at much smaller scales than visible in the $\delta^{18}O$ signal.

CFA analysis on the same section show similar features to what we observe in UV-LA data, especially regarding starting/ending points of GI21.2, which occur at approximately the same depth in both cases. However, elemental proxies (Fig. 7) show much clearer features in terms of abruptness and amplitude of oscillations compared to CFA data, and a more pronounced variability at cm-scale (Fig 8 and 9) that is often related to sub-annual

variations, observable in Fig. 10 where annual layer has been assigned comparing both CFA and LA-ICPMS data.

In fact, our data suggest that dust and sea salt proxies undergo extremely abrupt variations during small climate events, presenting most of the drop/rise in phase with the earliest signal of $\delta^{18}O$ rise/drop (Fig. 8 and 9) and certainly before its major jumps. This has been previously observed in other studies which show that dust and deuterium excess undergo the most rapid changes, with sudden variation both at warming and cooling transitions, within 1 to 3 years' time (Fuhrer et al., 1999; Masson-Delmotte et al., 2005). This is the case for GI1/YD (Steffensen et al., 2008) and has been related to changes in the moisture source as well as the storm patterns at high latitudes in the North Hemisphere.

For the start of YD it has been noticed that the ramp that identifies the decrease in dust appears earlier than the changes in $\delta^{18}O$ (Steffensen et al., 2008). This has been also observed for GI8 (Thomas et al., 2009). Such phasing has been suggested to be indicative of variations that start at low latitude and lead to a change in atmospheric circulation at an early stage, followed by a slightly later change in temperature and climate over Greenland (Wolff et al., 2010).

Our data suggest that nssCa and Fe are more suitable than others elements like Al as proxies for dust, since they react more abruptly to warming and cooling events.

Na and ssMg present a very high degree of similarity and react to minor warming/cooling event like GI21.2 with amplitude and abruptness similar to dust proxies. Our results also show that the warming phase induces a drop in dust proxies (nssCa and Fe) before the $\delta^{18}O$ starts to rise, and the rapidity of this change is remarkable (1 year, Fig. 8). As previously observed by Fuhrer et al. (1999) in the GRIP record for GI3, the variations of particularly nssCa occur in discrete steps lasting between 2 and 3 years for warming phases and up to 150 years for the cooling phase which takes place more slowly but still in distinct steps (Fig. 9). Any mechanism responsible for these changes

must be capable of producing a series of extremely abrupt shifts, and must be able to switch on and off very quickly.

D-O cycles have often been related to changes in the Atlantic Meridional Overturning Circulation (AMOC) with its key role in transporting heat from low to high latitudes and in ocean CO_2 storage. A weakening of the AMOC, which is classically explained by freshwater forcing (Clark et al., 2002; Stocker et al., 2013), would reduce the northwards heat transport, causing a cooling which also would benefit from positive feedbacks of reduced evaporation that maintains the low salinity and alteration of atmospheric waves due to reduced oceanic circulation (Toom et al., 2012). Freshwater input could be explained by ice-sheet-size controlling iceberg discharges according to a binge/purge mechanism and also by sea ice coverage reduction, classically hypothesized to explain Heinrich events (MacAyeal, 1993). Zhang et al. (2014) modelled that a sea ice extent variation can be triggered by an increase of the height of the Northern Hemisphere Ice Sheet or a raise in CO_2, which shifts the northern westerlies northwards together with the tropical rain-belt and creates a positive atmosphere-sea-ice-ocean feedback. A larger ice-sheet would be also easier to destabilize at relatively short-term timescales causing the AMOC to switch on and off alternatively. However, evidence suggests that GI-21 occurs during a period of relative ice sheet minima (Bintanja et al., 2005). Furthermore, isotopic analysis of $^{231}Pa/^{230}Th$ demonstrates that AMOC persisted strongly through all the last glaciation with only few weakening events, although $^{231}Pa/^{230}Th$ ratios might suffer of fractionation driven by opal (Böhm et al., 2015). However, for the reasons mentioned above, we rule out the possibility that precursor events like GI21.2 have as a first cause an interruption of the thermohaline circulation by a reduction of the AMOC, which is unlikely to operate at such short time-scale.

A more plausible explanation for precursor-type events derives from the fact that smaller ice sheets are more affected by local radiative perturbation (Capron et al., 2010). During GI-21, summertime insolation at 65° N is at a maximum (Laskar et al., 2004), which could have shifted the atmospheric

patterns towards monsoon-type circulations, as observed in Clemens et al. (1996) and Wang et al. (2001).

Therefore, a reorganization of atmospheric circulation at mid-high latitudes in the Northern Hemisphere during these rapid warming/cooling episodes could enhance mobilization at the dust sources (Asian deserts), as proposed by Fuhrer et al. (1999), and an increase in residence time of particles could account for most of the drop in concentration of proxies observable for GI21.2. GCM simulations (Kutzbach et al., 1993) showed that during the LGM, storms strengthen their intensity and changed their trajectory moving further north and changing the pressure regime over central Asia. Even a very small increase in maximum wind speed during episodic storms could have overtaken the threshold value for mobilization of particle of a certain size (Gillette and Passi, 1988). The first signs of the rapid warming would therefore decrease nssCa concentrations as a result of the wetter conditions at the Asian dust-source areas, where dust uplift was reduced by humidity and washout was increased by precipitation. The change in moisture at the dust source seems to agree also with the early occurrence of deuterium excess changes observed by Steffensen et al. (2008) for GS1, GI1a and GS2.

Summary and Conclusions

Using cryo-cell UV-LA-ICPMS we obtained 260 cm of dust (nssCa, Fe, Al) and sea salt (Na, ssMg) profiles within NGRIP ice covering GI21.2 (GI21-precursor) at a resolution of ~200 µm, which nominally represents approximately two months at roughly 85 ka ago. Quantification of LA-ICPMS signals was possible using a set of five external ice standards produced at Royal Holloway University of London, which proved to be homogeneous at ~15% level. Our results show that dust proxies (especially nssCa and Fe) react earlier than $\delta^{18}O$ by 1-2 years, showing abrupt drops or rises in reaction to warmings or coolings. The drop in concentration during the warming event is more abrupt than the following rise that corresponds to the subsequent

cooling event, but in both cases concentrations do not rise or fall in a gradual way but in more than one step. During the warming even of GI21.2, the main drop in nssCa and Fe concentrations occurs very rapidly, namely within one year. We suggest that wetter conditions at Asian sources could have lowered dust uplift and increase the washout during GI21.2 warm period, when atmospheric circulation over Asian deserts was weaker. This would have resulted in a reduction of transport and therefore a decrease in the dust and sea salt supply to Greenland by 1-2 years. At the onset of the following cooling period, the end of the wet conditions together with an increase in wind speed and storminess above a threshold level, allowing uplift of more particles, explains the subsequent rise of concentrations of dust and sea salt to pre-warming levels.

Acknowledgements

This work has been supported by a RHUL studentship granted to Damiano Della Lunga,whereas the analytical costs were co-funded via a research grant from Resonetics LLC & Laurin Technic to Wolfgang Müller. The authors would like to thank Jerry Morris for continuing invaluable technical support at RHUL. Initial discussions with Michael Kriews and Dorothee Wilhelms-Dick helped to improve the methodology of ice standard preparation.

References

Barker, S., Chen, J., Gong, X., Jonkers, L., Knorr, G., & Thornalley, D. (2015). Icebergs not the trigger for North Atlantic cold events. *Nature*, **520**(7547), 333-336.

Berglund, M., and Wieser, M. E. (2011). Isotopic compositions of the elements 2009 (IUPAC Technical Report). *Pure and Applied Chemistry*, **83**(2), 397-410.

Bigler, M., Svensson, A., Kettner, E., Vallelonga, P., Nielsen, M. E., & Steffensen, J. P. (2011). Optimization of high-resolution continuous flow

551 analysis for transient climate signals in ice cores. *Environmental*
552 *science & technology*, **45**(10), 4483-4489.

553 Bintanja, R., van de Wal, R. S., & Oerlemans, J. (2005). Modelled
554 atmospheric temperatures and global sea levels over the past million
555 years. *Nature*, **437**(7055), 125-128.

556 Boch, R., Cheng, H., Spötl, C., Edwards, R. L., Wang, X., and Häuselmann,
557 P. (2011). NALPS: a precisely dated European climate record 120–60
558 ka. *Climate of the Past*, **7**(4), 1247-1259.

559 Böhm, E., Lippold, J., Gutjahr, M., Frank, M., Blaser, P., Antz, B., Fohlmeister
560 J., Frank N., Andersen M. B. & Deininger, M. (2015). Strong and deep
561 Atlantic meridional overturning circulation during the last glacial cycle.
562 *Nature*, **517**(7532), 73-76.

563 Broecker, W., Bond, G., Klas, M., Clark, E., & McManus, J. (1992). Origin of
564 the northern Atlantic's Heinrich events. *Climate Dynamics*, **6**(3-4), 265-
565 273.

566 Broecker, W. S. (2003). Does the trigger for abrupt climate change reside in
567 the ocean or in the atmosphere?. *Science*, **300**(5625), 1519-1522.

568 Capron, E., A. Landais, J. Chappellaz, A. Schilt, D. Buiron, Dahl-Jensen D.,
569 Johnsen S.J., Jouzel J., Lemieux-Dudon B., Loulergue L., Leuenberger
570 M., Masson-Delmotte V., Meyer H., Oerter H., Stenni B. "Millennial and
571 sub-millennial scale climatic variations recorded in polar ice cores over
572 the last glacial period." *Climate of the Past* **6**, 3 (2010): 345-365.

573 Clark, P. U., Pisias, N. G., Stocker, T. F., & Weaver, A. J. (2002). The role of
574 the thermohaline circulation in abrupt climate change. *Nature*, **415**(6874),
575 863-869.

576 Clement, A. C., Cane, M. A., & Seager, R. (2001). An Orbitally Driven
577 Tropical Source for Abrupt Climate Change. *Journal of Climate*, **14**(11),
578 2369-2375.

579 Clement, A. C., & Peterson, L. C. (2008). Mechanisms of abrupt climate
580 change of the last glacial period. *Reviews of Geophysics*, **46**(4).

581 Clemens, S. C., Murray, D. W., & Prell, W. L. (1996). Nonstationary phase of
582 the Plio-Pleistocene Asian monsoon. *Science*, 274(5289), 943-948.

583 Dansgaard, Willi, S. J. Johnsen, H. B. Clausen, D. Dahl-Jensen, N. S.
584 Gundestrup, C. U. Hammer, C. S. Hvidberg, Steffensen J.P.,
585 Svelnbjornsdottir A.E., Jouzel J., Bond G.. (1993): "Evidence for general
586 instability of past climate from a 250-kyr ice-core record." *Nature*, **364**,
587 no. 6434 218-220.
588 Della Lunga, D., Muller, W., Rasmussen, S. O., and Svensson, A. (2014).
589 Location of cation impurities in NGRIP deep ice revealed by cryo-cell
590 UV-laser-ablation ICPMS. *Journal of Glaciology*, **60**(223).
591 Deplazes, G., Lückge, A., Peterson, L. C., Timmermann, A., Hamann, Y.,
592 Hughen, K. A., Röhl U., Laj C., Cane M. A., Sigman D.M., Haug, G. H.
593 (2013). Links between tropical rainfall and North Atlantic climate during
594 the last glacial period. *Nature Geoscience*, **6**(3), 213-217.
595 Fuhrer, K., Wolff, E. W., and Johnsen, S. J. (1999). Timescales for dust
596 variability in the Greenland Ice Core Project (GRIP) ice core in the last
597 100,000 years. *Journal of Geophysical Research: Atmospheres*
598 *(1984–2012)*, **104**(D24), 31043-31052.
599 Gillette, D. A., and Passi, R. (1988). Modeling dust emission caused by wind
600 erosion. *Journal of Geophysical Research: Atmospheres (1984–2012)*,
601 **93**(D11), 14233-14242.
602 Gkinis, V., Simonsen, S. B., Buchardt, S. L., White, J. W. C., & Vinther, B. M.
603 (2014). Water isotope diffusion rates from the NorthGRIP ice core for
604 the last 16,000 years–Glaciological and paleoclimatic implications.
605 *Earth and Planetary Science Letters*, **405**, 132-141.
606 Grachev, A. M., Brook, E. J., Severinghaus, J. P., and Pisias, N. G. (2009).
607 Relative timing and variability of atmospheric methane and GISP2
608 oxygen isotopes between 68 and 86 ka. *Global Biogeochemical*
609 *Cycles*, **23**(2).
610 Grootes, P. M., and Stuiver, M. (1997). Oxygen 18/16 variability in Greenland
611 snow and ice with 10− 3-to 105-year time resolution. *Journal of*
612 *Geophysical Research: Oceans* (1978–2012), **102**(C12), 26455-
613 26470.

614 Huber, C., Leuenberger, M., Spahni, R., Fluckiger, J., Schwander, J.,
615 Stocker, T. F.,Johnsen S., Landais A., Jouzel, J. (2006). Isotope
616 calibrated greenland temperature record over marine isotope stage 3
617 and its relation to CH4. *Earth and Planetary Science Letters,* **243**(3-4),
618 504-519.
619 Jochum, K. P., Weis, U., Stoll, B., Kuzmin, D., Yang, Q., Raczek, I., Jacob
620 D.E., Stracke A., Birbaum K., Frick D. A., Günther D., and Enzweiler, J.
621 (2011). Determination of reference values for NIST SRM 610–617
622 glasses following ISO guidelines. Geostandards and Geoanalytical
623 Research, **35**(4), 397-429.
624 Johnsen, S. J., Clausen, H. B., Dansgaard, W., Fuhrer, K., Gundestrup, N.,
625 Hammer, C. U., Iversen P., Jouzel J., Stauffer B., Steffensen, J. P.
626 (1992). Irregular glacial interstadials recorded in a new Greenland ice
627 core. *Nature*, **359**(6393), 311-313.
628 Kreutz, K.J., and Koffman, B., (2013), Glaciochemistry, in *Encyclopedia of*
629 *Quaternary Science* 2nd edition, S. Elias, ed., Elsevier Publishers, 326-
630 333.
631 Kutzbach, J. E., Guetter, P. J., Behling, P. J., and Selin, R. (1993). Simulated
632 climatic changes: results of the COHMAP climate-model experiments.
633 *Global climates since the last glacial maximum*, 24-93.
634 Laskar, J., Robutel, P., Joutel, F., Gastineau, M., Correia, A. C. M., &
635 Levrard, B. (2004). A long-term numerical solution for the insolation
636 quantities of the Earth. *Astronomy & Astrophysics*, **428**(1), 261-285.
637 Lewis, E. R., & Schwartz, S. E. (2004). Sea salt aerosol production:
638 mechanisms, methods, measurements, and models-A critical review.
639 American Geophysical Union, 2004.
640 MacAyeal, D. R. (1993). Binge/purge oscillations of the Laurentide ice sheet
641 as a cause of the North Atlantic's Heinrich events. *Paleoceanography*,
642 **8**(6), 775-784.
643 Mahowald, N., Kohfeld, K., Hansson, M., Balkanski, Y., Harrison, S. P.,
644 Prentice, I. C., Schulz M., Rodhe, H. (1999). Dust sources and
645 deposition during the last glacial maximum and current climate: A

comparison of model results with paleodata from ice cores and marine sediments. *Journal of Geophysical Research: Atmospheres,* **104**(D13), 15895-15916.

Masson-Delmotte, V., Jouzel J., Landais A., Stievenard M., Johnsen S.J., White J. W. C., Werner M., Sveinbjornsdottir A., Fuhrer K. "GRIP deuterium excess reveals rapid and orbital-scale changes in Greenland moisture origin." *Science* **309**, no. 5731 (2005): 118-121.

Müller, W., Shelley, M., Miller, P., and Broude, S. (2009). Initial performance metrics of a new custom-designed ArF excimer LA-ICPMS system coupled to a two-volume laser-ablation cell. *Journal of Analytical Atomic Spectrometry*, **24**(2), 209-214.

Müller, W., Shelley, J. M. G., and Rasmussen, S. O. (2011). Direct chemical analysis of frozen ice cores by UV-laser ablation ICPMS. *Journal of Analytical Atomic Spectrometry,* **26**(12), 2391-2395.

Petersen, S. V., Schrag, D. P., & Clark, P. U. (2013). A new mechanism for Dansgaard-Oeschger cycles. *Paleoceanography*, **28**(1), 24-30.

Petit, J. R., Jouzel, J., Raynaud, D., Barkov, N. I., Barnola, J. M., Basile, I, M. Bender, J., Chappellaz, M. Davis, G. Delaygue, M. Delmotte, V. M. Kotlyakov, M. Legrand, V. Y. Lipenkov, C. Lorius, L. PÉpin, C. Ritz, E. Saltzman and Stievenard, M. (1999). Climate and atmospheric history of the past 420,000 years from the Vostok ice core, Antarctica. *Nature,* **399**(6735), 429-436.

Randall, D.A., R.A. Wood, S. Bony, R. Colman, T. Fichefet, J. Fyfe, V. Kattsov, A. Pitman, J. Shukla, J. Srinivasan, R.J. Stouffer, A. Sumi and K.E. Taylor, 2007: Cilmate Models and Their Evaluation. In: Climate Change 2007: The Physical Science Basis. Contribution of Working Group I to the Fourth Assessment Report of the Intergovernmental Panel on Climate Change [Solomon, S., D. Qin, M. Manning, Z. Chen, M. Marquis, K.B. Averyt, M.Tignor and H.L. Miller (eds.)]. Cambridge University Press, Cambridge, United Kingdom and New York, NY, USA.

Rasmussen, S. O., Bigler, M., Blockley, S. P., Blunier, T., Buchardt, S. L., Clausen, H. B. and Winstrup, M. (2014). A stratigraphic framework for

678 abrupt climatic changes during the Last Glacial period based on three
679 synchronized Greenland ice-core records: refining and extending the
680 INTIMATE event stratigraphy. *Quaternary Science Reviews*. volume **106**,
681 14–28.
682 Reinhardt, H., Kriews, M., Miller, H., Lüdke, C., Hoffmann, E., & Skole, J.
683 (2003). Application of LA–ICP–MS in polar ice core studies. *Analytical*
684 *and bioanalytical chemistry*, **375**(8), 1265-1275.
685 Seierstad, I. K., Abbott, P. M., Bigler, M., Blunier, T., Bourne, A. J., Brook, E.,
686 Buchardt S. L., Buizert C., Clausen H. B., Cook E., Dahl-Jensen D.,.
687 Davies S. M., Guillevic M., Johnsen S. J., Pedersen D. S., Popp T. J,
688 Rasmussen S. O., Severinghaus J. P., Svensson A. & Vinther, B. M.
689 (2014). Consistently dated records from the Greenland GRIP, GISP2 and
690 NGRIP ice cores for the past 104 ka reveal regional millennial-scale δ 18
691 O gradients with possible Heinrich event imprint. *Quaternary Science*
692 *Reviews*, **106**, 29-46.
693 Severinghaus, J. P., and Brook, E. J. (1999). Abrupt climate change at the
694 end of the last glacial period inferred from trapped air in polar ice.
695 *Science,* **286**(5441), 930-934.
696 Sneed, S. B., Mayewki, P. A., Sayre, W., Handley, M. J., Kurbatov, A. V.,
697 Taylor, K. C., Bohleber P., Wagenbach D., Erhardt T., Spaulding, N. E.
698 (2015). Instruments and Methods New LA-ICP-MS cryocell and
699 calibration technique for sub-millimeter analysis of ice cores. *Journal of*
700 *Glaciology*, **61**(226), 233.
701 Spötl, C., & Mangini, A. (2002). Stalagmite from the Austrian Alps reveals
702 Dansgaard–Oeschger events during isotope stage 3: Implications for the
703 absolute chronology of Greenland ice cores. *Earth and Planetary*
704 *Science Letters*, **203**(1), 507-518.
705 Steffensen, J. P., Andersen, K. K., Bigler, M., Clausen, H. B., Dahl-Jensen,
706 D., Fischer, H., Goto-Azuma K., Hansson M., Johnsen S. J., Jouzel J.,
707 Masson-Delmotte V., Popp T.,. Rasmussen S. O, R. Röthlisberger R.,
708 Ruth U., Stauffer B., Siggaard-Andersen M. L., Sveinbjörnsdóttir Á. E.,
709 Svensson A.,. White, J. W. C. (2008). High-resolution Greenland ice core

710 data show abrupt climate change happens in few years. *Science,*
711 **321**(5889), 680-684.
712 Stocker, T.F., D. Qin, G.-K. Plattner, L.V. Alexander, S.K. Allen, N.L. Bindoff,
713 F.-M. Bréon, J.A. Church, U. Cubasch, S. Emori, P. Forster, P.
714 Friedlingstein, N. Gillett, J.M. Gregory, D.L. Hartmann, E. Jansen, B.
715 Kirtman, R. Knutti, K. Krishna Kumar, P. Lemke, J. Marotzke, V. Masson-
716 Delmotte, G.A. Meehl, I.I. Mokhov, S. Piao, V. Ramaswamy, D. Randall,
717 M. Rhein, M. Rojas, C. Sabine, D. Shindell, L.D. Talley, D.G. Vaughan
718 and S.-P. Xie, 2013: Technical Summary. In: Climate Change 2013: The
719 Physical Science Basis. Contribution of Working Group I to the Fifth
720 Assessment Report of the Intergovernmental Panel on Climate Change
721 [Stocker, T.F., D. Qin, G.-K. Plattner, M. Tignor, S.K. Allen, J. Boschung,
722 A. Nauels, Y. Xia, V. Bex and P.M. Midgley (eds.)]. Cambridge University
723 Press, Cambridge, United Kingdom and New York, NY, USA, pp. 33–
724 115,
725 Svensson, A., Nielsen, S. W., Kipfstuhl, S., Johnsen, S. J., Steffensen, J. P.,
726 Bigler, M., Ruth, U., Rothlisberger, R. (2005). Visual stratigraphy of the
727 north Greenland ice core project (NorthGRIP) ice core during the last
728 glacial period. *Journal of Geophysical Research-Atmospheres,***110**(D2),
729 D02108.
730 Thomas, E. R., Wolff, E. W., Mulvaney, R., Johnsen, S. J., Steffensen, J. P.,
731 and Arrowsmith, C. (2009). Anatomy of a Dansgaard-Oeschger warming
732 transition: High-resolution analysis of the north Greenland ice core
733 project ice core. *Journal of Geophysical Research-Atmospheres,* **114**,
734 D08102.
735 Toom, M. D., Dijkstra, H. A., Cimatoribus, A. A., & Drijfhout, S. S. (2012).
736 Effect of atmospheric feedbacks on the stability of the Atlantic meridional
737 overturning circulation. *Journal of climate*, **25**(12), 4081-4096.
738 Vallelonga, P., Bertagna, G., Blunier, T., Kjaer, H. A., Popp, T. J.,
739 Rasmussen, S. O., Stowasser C., Svensson A. S., Winstrup M.,
740 Kipfstuhl, S. (2012). Duration of Greenland stadial 22 and ice-gas

741 Δage from counting of annual layers in Greenland NGRIP ice core.
742 *Climate of the Past Discussions*, **8**(4), 2583-2605.

743 Voelker, A. H. (2002). Global distribution of centennial-scale records for
744 Marine Isotope Stage (MIS) 3: a database. *Quaternary Science*
745 *Reviews*, **21**(10), 1185-1212.

746 Wang, Y. J., Cheng, H., Edwards, R. L., An, Z. S., Wu, J. Y., Shen, C. C., &
747 Dorale, J. A. (2001). A high-resolution absolute-dated late Pleistocene
748 monsoon record from Hulu Cave, China. *Science*, **294**(5550), 2345-
749 2348.

750 Wilhelm-Dick, D. (2008). Enhanced analysis of stratified climate archives
751 through upgrade of Laser Ablation Inductively Coupled Plasma
752 Quadrupole to Time of Flight Mass Spectrometry? (Doctoral
753 dissertation, Berlin, Univ., Diss.).

754 Wolff, E. W., Rankin, A. M., and Röthlisberger, R. (2003). An ice core
755 indicator of Antarctic sea ice production?. *Geophysical Research*
756 *Letters*, **30**(22).

757 Wolff, E. W., Chappellaz, J., Blunier, T., Rasmussen, S. O., and Svensson,
758 A. (2010). Millennial-scale variability during the last glacial: The ice
759 core record. *Quaternary Science Reviews*, **29**(21), 2828-2838.

760 Yung, Y. L., Lee, T., Wang, C. H., & Shieh, Y. T. (1996). Dust: A diagnostic of
761 the hydrologic cycle during the Last Glacial Maximum. *Science*,
762 **271**(5251), 962-963.

763 Zhang, X., Lohmann, G., Knorr, G., & Purcell, C. (2014). Abrupt glacial
764 climate shifts controlled by ice sheet changes. *Nature*. **512**, 290–294.
765

Figures

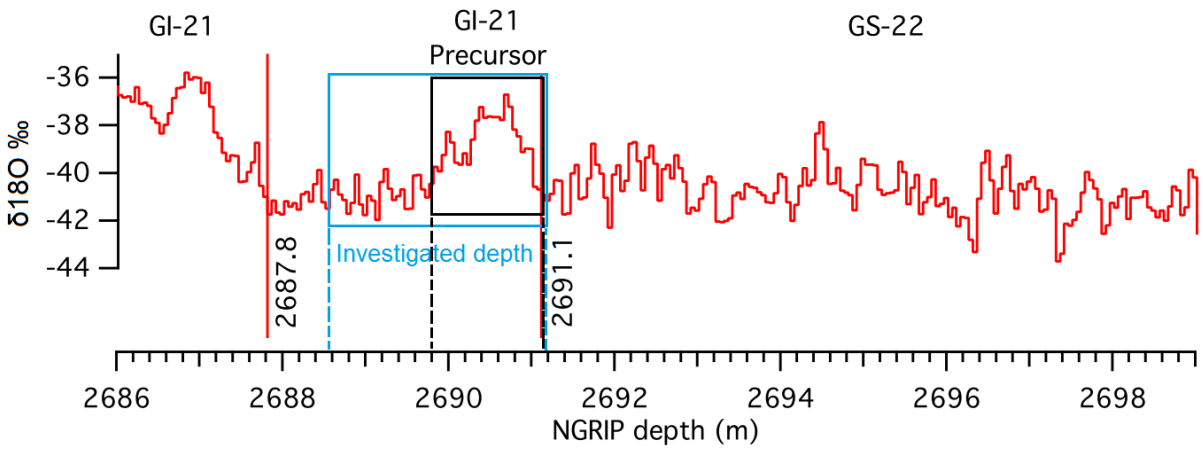

Figure 1: $\delta^{18}O$ profile across the younger part of GS22 (modified from Vallelonga et al., 2012). The black rectangle highlights the GI-21 precursor, or GI-21.2, as defined in Rasmussen et al., (2014). The blue box shows the corresponding section of ice core analysed for this study.

774 **Table 1: Concentration of elements under investigation for aqueous reference**
775 **materials used for ice standard preparation: SLRS-5-"River water reference material**
776 **for trace metals" (National Research Council of Canada, diluted 10 times [SLRS-5_10]**
777 **when not specified), Water low (RHUL internal standard), 90243 Multielement standard**
778 **solution 1 for ICP (Sigma Aldrich, diluted 20 times), and NIST SRM 1648 Urban**
779 **Particulate reference material (in suspension, see text for details).**

Element	Concentration (ppb)	Concentration (ppb)	Concentration (ppb)	Concentration (ppb)	LODs (ppb)
Standard name	SLRS-5_10	ICP-20	Water Low	NIST1648a	
Al	4.95 ± 0.5 49.5 ± 4.8 (SLRS-5)	2525±2.5	9.8±0.1	1683±16	2.5
Fe	9.12 ± 0.58 91 ±6 (SLRS-5)	505±0.5	9.8±0.1	1924±20	2.9
Ca	1050.0 ± 40 10510±380 (SLRS-5)	505±0.5	48.9±0.3	3126±15	1.8
Mg	254 ± 16 2541±155 (SLRS-5)	505±0.5	48.9±0.3	394±5	2.8
Na	538 ± 10 5380±105 (SLRS-5)	2525±2.5	244±1.5	209±4	78

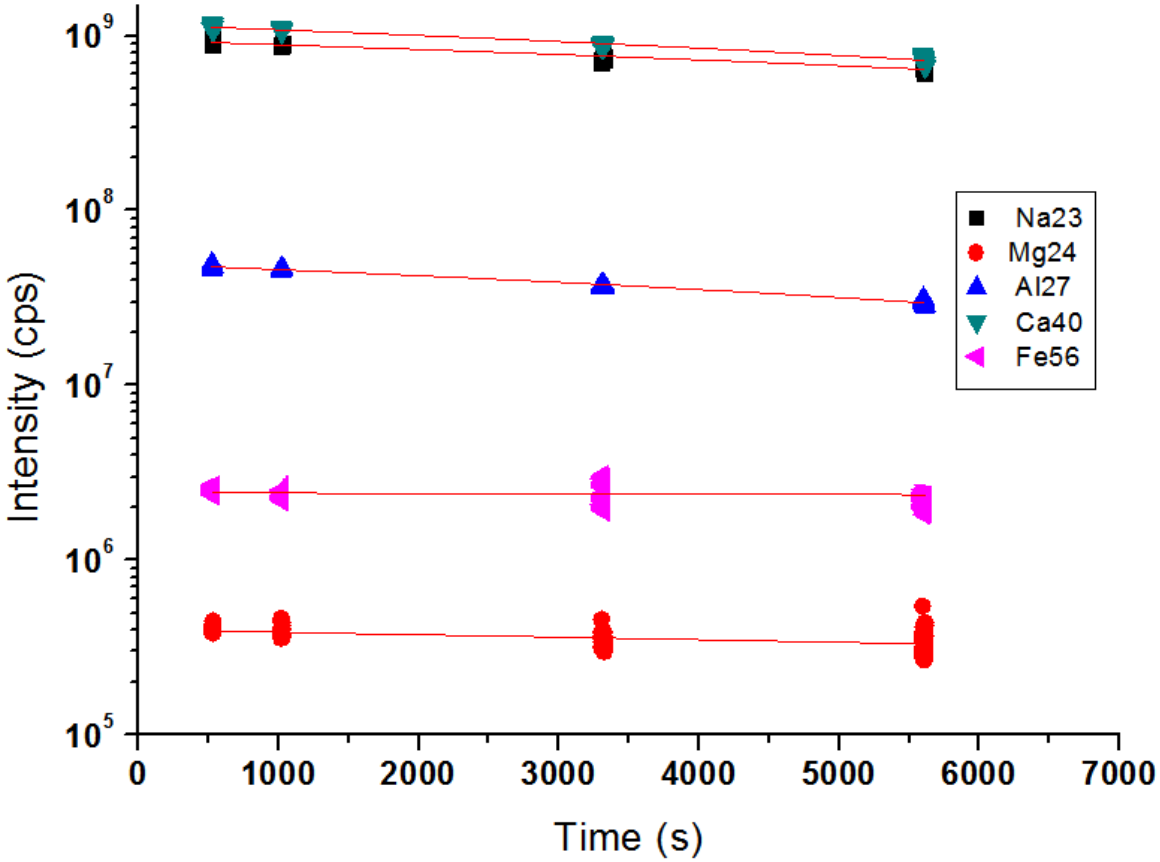

Figure 2: ICPMS instrumental drift correction. The data points represent NIST612 values acquired in between the ice samples during a single run. Sensitivity typically slightly decreases during the analysis and the slope of each element's regression line has been utilized to correct instrumental drift according to eq.1 (See text for details).

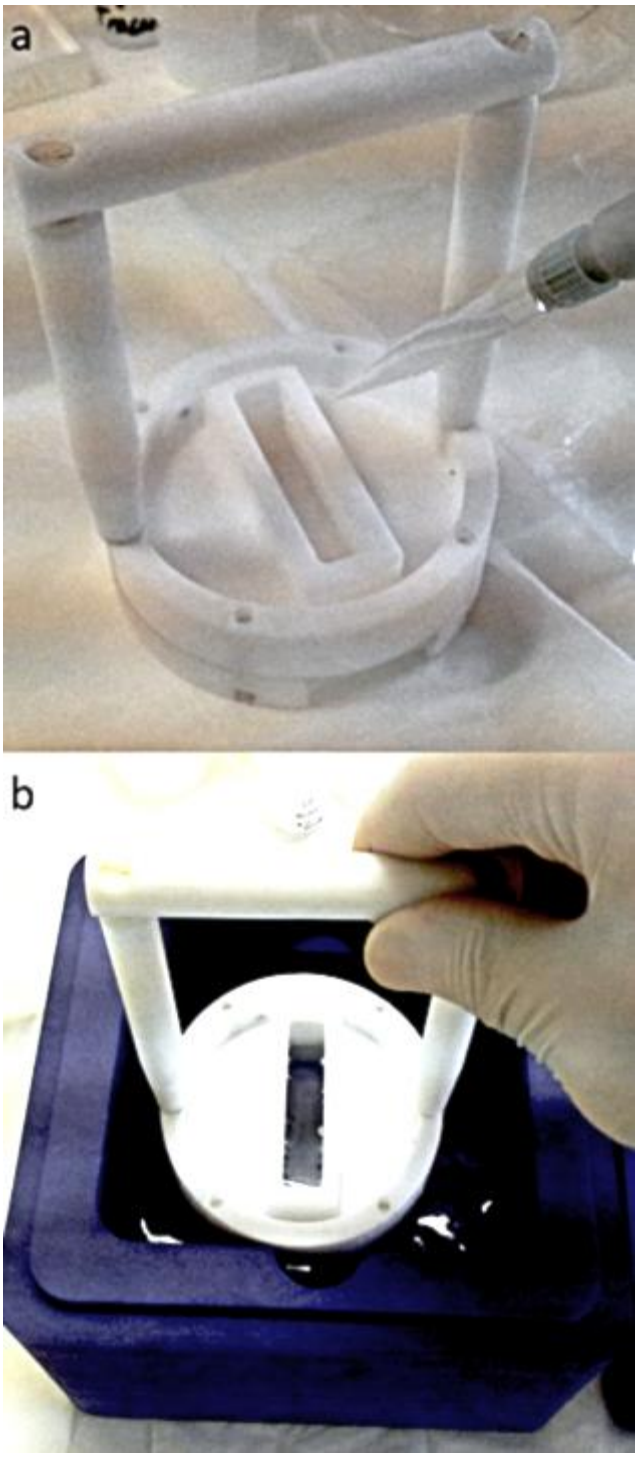

785

786 **Figure 3: Ice standard preparation. a) 1 ml of aqueous standard solution is pipetted**
787 **into the inner volume of a PTFE mould featuring a removable glass surface at the**
788 **bottom to allow the solution to spread uniformly creating a thin layer of water. b) The**
789 **mould is dipped into liquid nitrogen to instantaneously shock-freeze the solution. This**
790 **procedure is repeated five times to build up an ice volume by shock-freezing layer by**
791 **layer of 5 ml total volume resulting in an ice volume approximately 45x10x10 mm.**
792 **Each ice standard was then surface-cleaned via PTFE vice (see text) before analysis.**

793

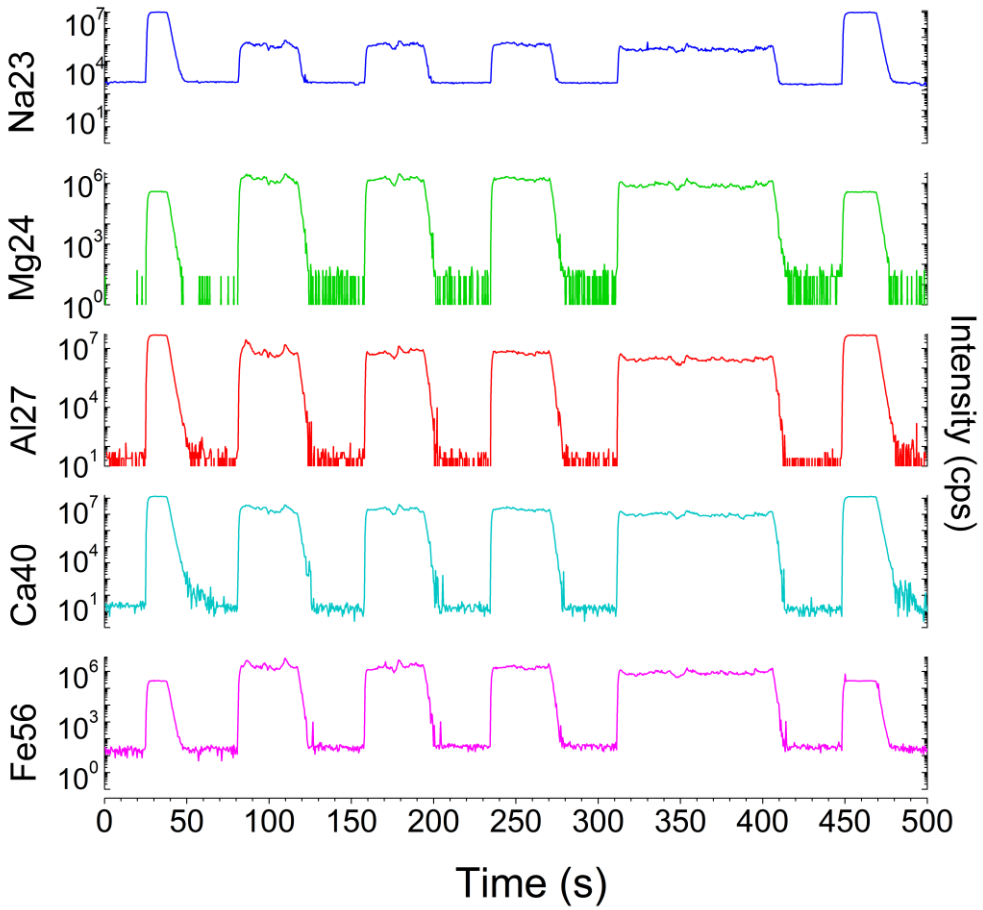

Figure 4: Example of raw intensity data of NIST612 compared to one of the ice standards prepared for this study (ICP-20). This ice standard appears rather homogeneous with typical RSD values (calculated just in the post-cleaning acquisition tracks) between ± 10 and 15 %.

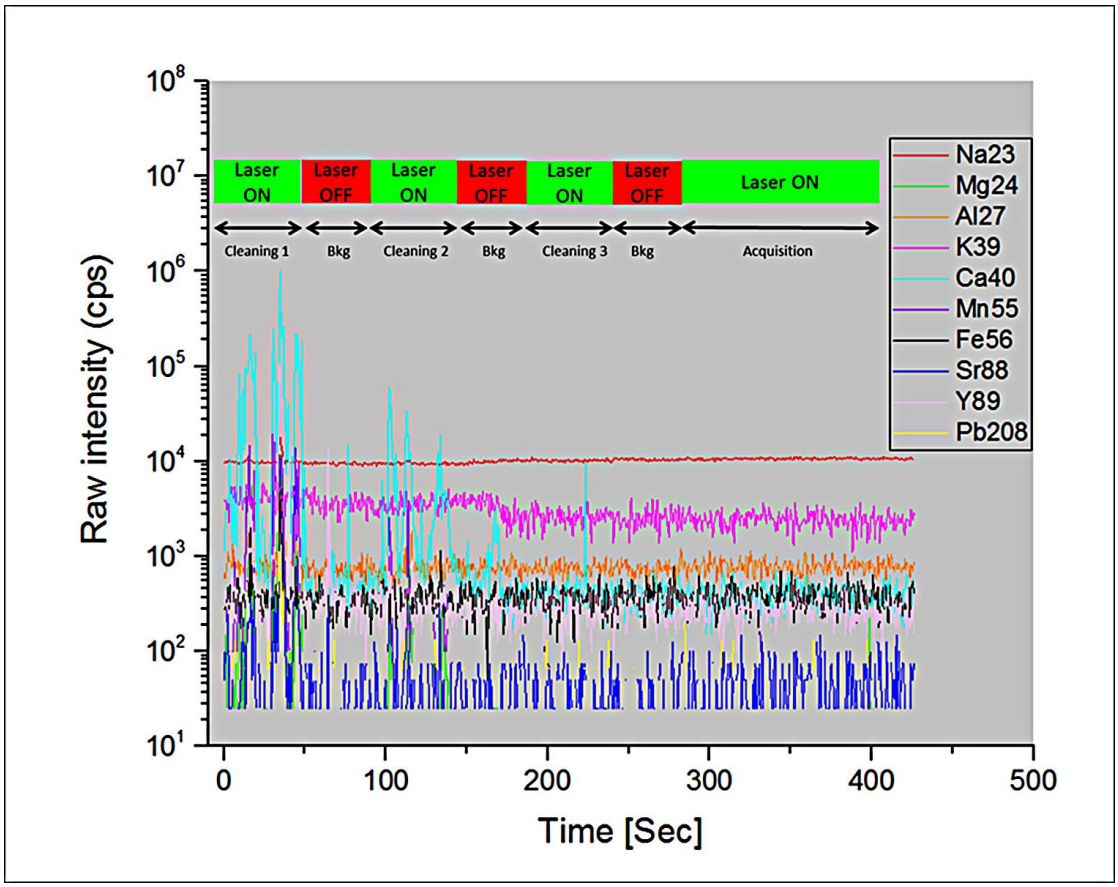

Figure 5: UV-LA-ICPMS analysis of an ice blank. The analysis includes three passages of the laser with 280 µm spot size, 25 Hz repetition rate and 8 mm/min speed, while the last acquisition track has been performed with 212 µm spot size, 20 Hz repetition rate and 3 mm/min speed where no analytes are above ICPMS background anymore. Analytes are most abundant isotopes for each element.

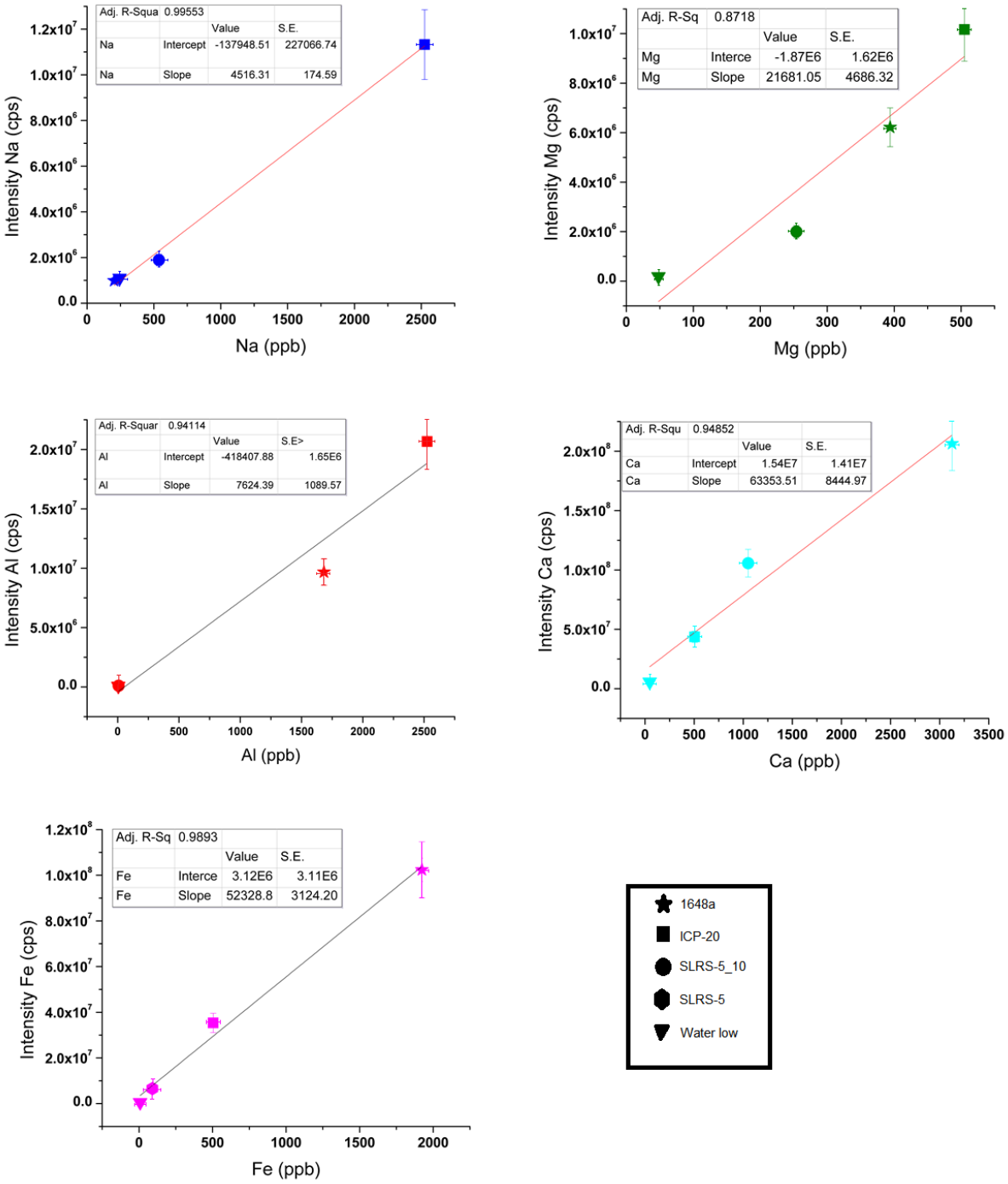

Figure 6: Calibration graphs for elements under investigation. Error bars are 2 standard error (S.E.).

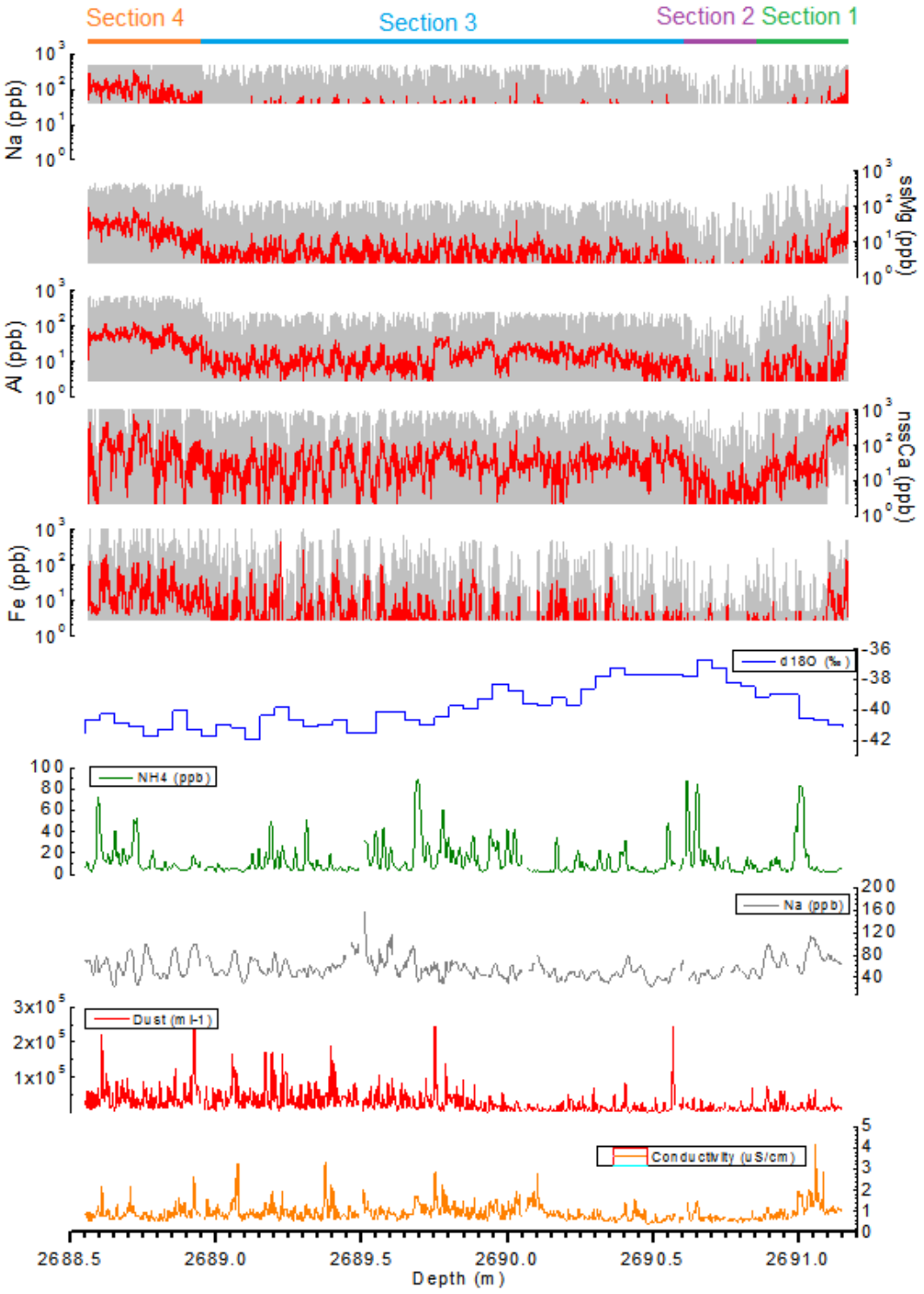

Figure 7: UV-LA-ICPMS element concentration profiles of Na, Mg, Al, Ca, and Fe and corresponding $\delta^{18}O$, NH_4, Na, CFA-dust and conductivity profiles at 5, 0.35, 0.35, 0.1, 0.1 cm resolution respectively (from Vallelonga et al., 2012) across 260 cm of NGRIP ice core that contains the GI21 precursor (GI21.2); depth interval 2691.15-2689.55, #bags 4893-4891. Laser spot: 280 µm, scanning speed: 3 mm/min, rep rate: 20 Hz, laser fluence 3.5 J/cm^2. The grey lines are individual LA-ICPMS data points; red lines represent adjacent-element moving average (period 100). See text for details. Data were cut-off at corresponding LOD (see table 1).

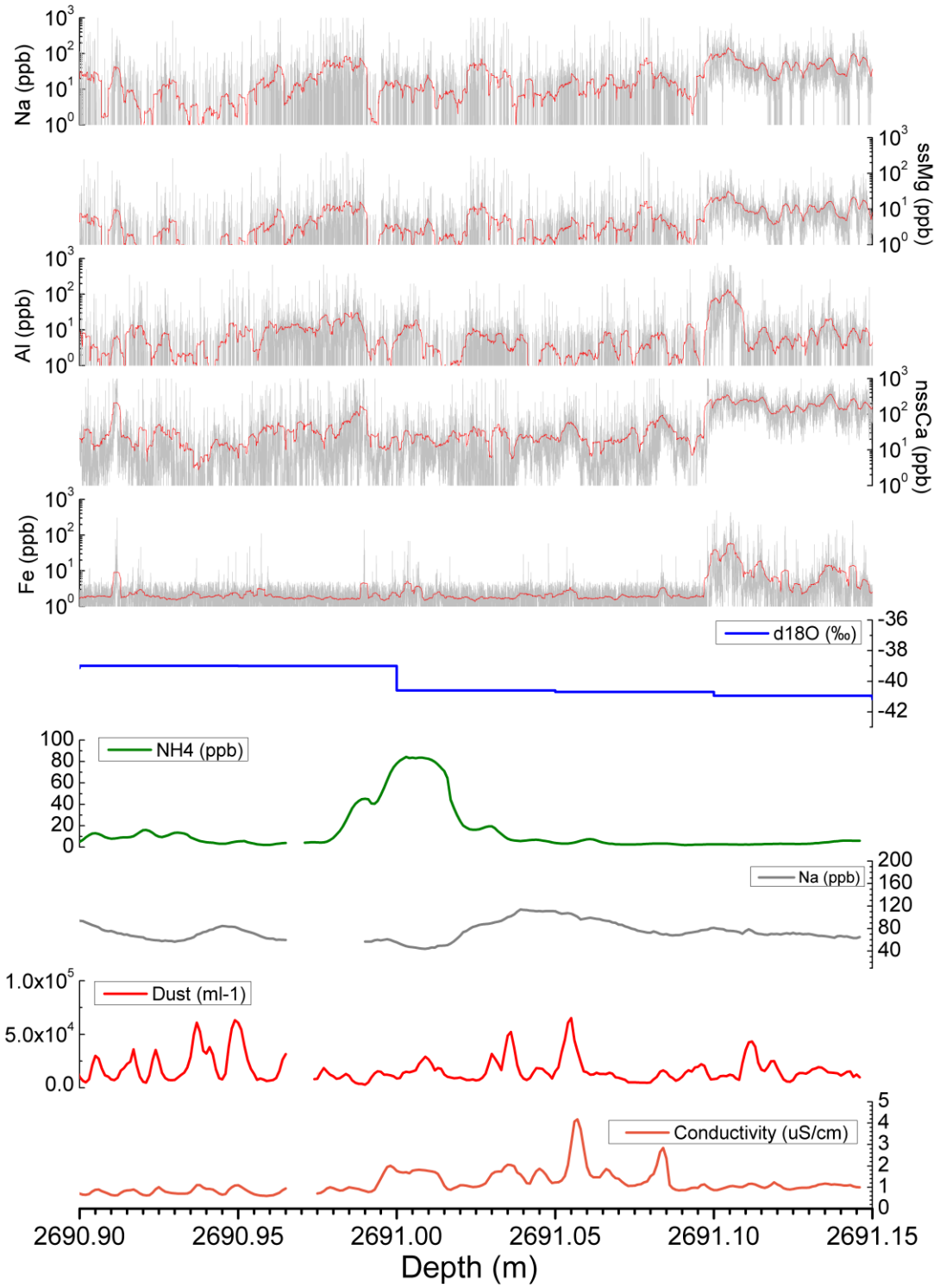

Figure 8: Zoomed-in initial 25 cm of the GI21.2 section analysed for the most significant elements. The concentrations of all elements drop by at least one order of magnitude or more around depth 2691.10 m. The drop occurs within the space of 1 cm, which represent roughly a year at this depth. . Data were cut-off at corresponding LOD (see table 1). $\delta^{18}O$, NH_4, Na, CFA-dust and conductivity profiles at 5, 0.35, 0.35, 0.1, 0.1 cm resolution respectively are from Vallelonga et al., 2012.

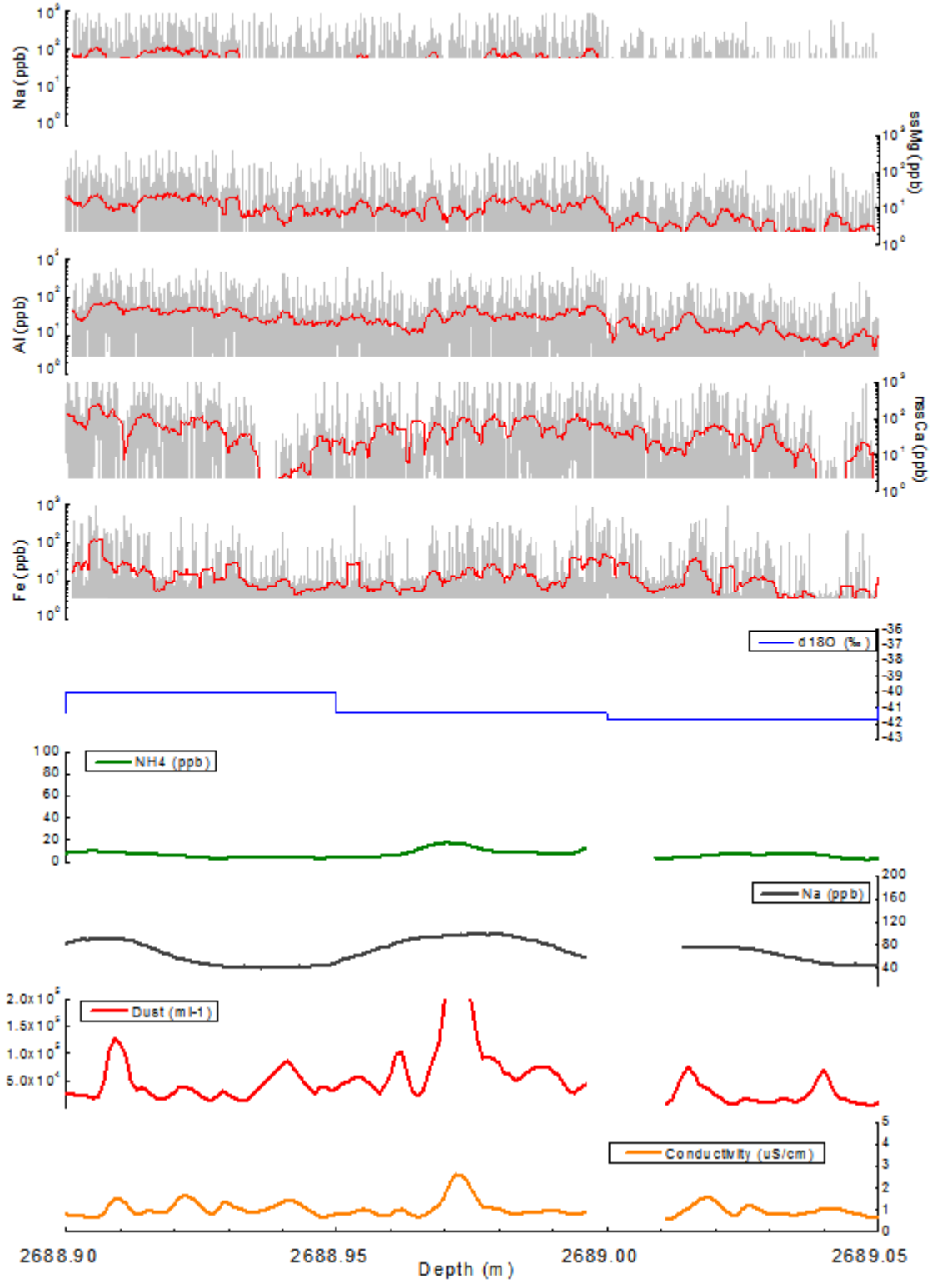

824
825 **Figure 9: Zoomed-in 15 cm of the cooling transition from GI21.2 to GS22 for the most**
826 **significant elements. All concentrations rise significantly but a clear transition peak is**
827 **missing. The rise is more gradual compared with the transition from GS22 to GI21.2,**
828 **and seems to occur in more than one step. Data were cut-off at corresponding LODs**
829 **(see table 1). $\delta^{18}O$, NH_4, Na, CFA-dust and conductivity profiles at 5, 0.35, 0.35, 0.1, 0.1**
830 **cm resolution respectively are from Vallelonga et al., 2012.**

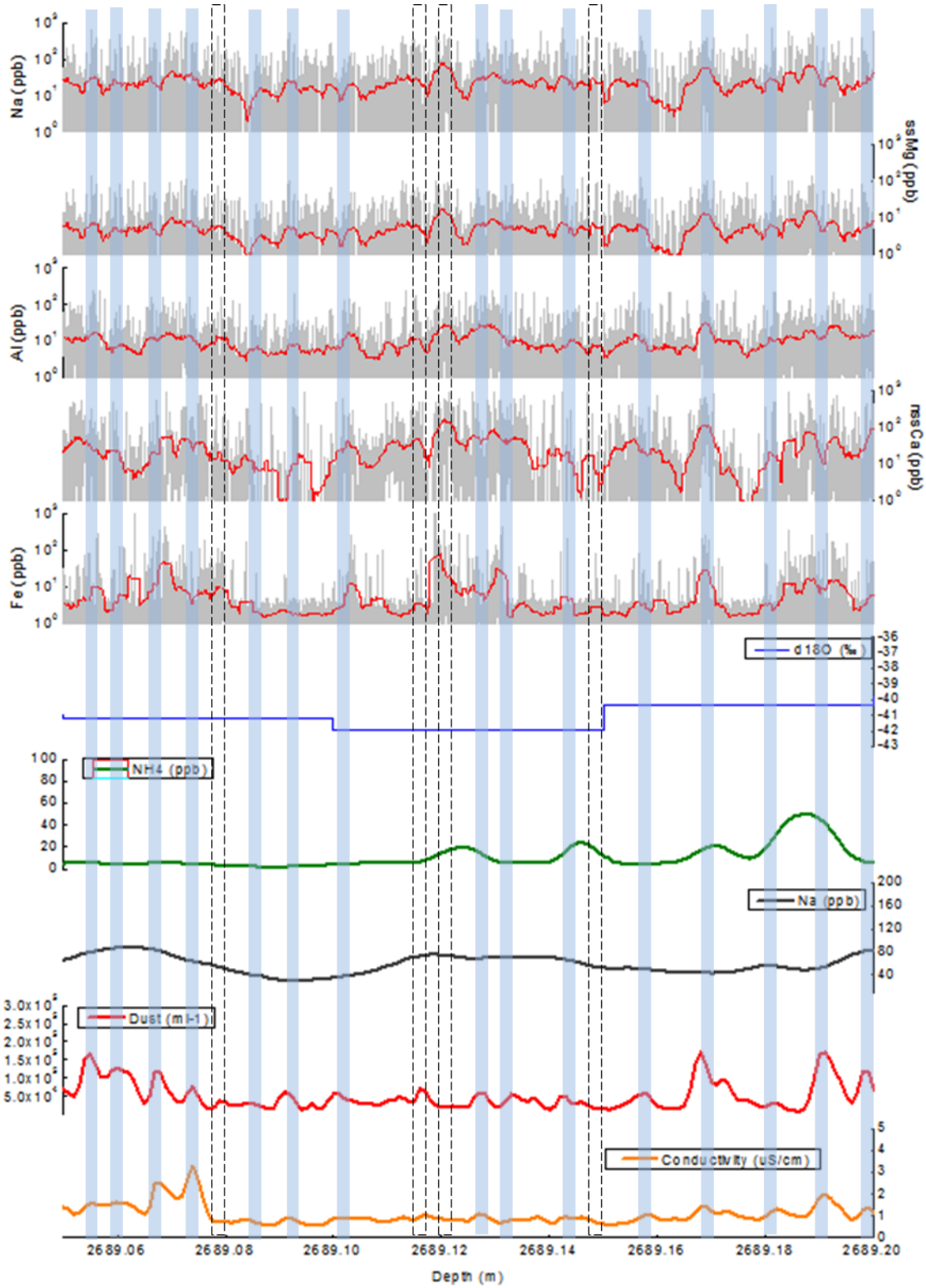

Figure 10: Zoomed-in 15 cm of the cooling transition from GI21.2 to GS22 for the most significant elements. Variability in this section is high, especially for element like Ca and Fe, with oscillations of more than a order of magnitude. Blue bars are annual layer counting based on both UV-LA and CFA data. 15 ±4 annual layers were identified, for an annual layer thickness of 8-10 mm, compatible with what previously published (Vallelonga et al., 2012). $\delta^{18}O$, NH_4, Na, CFA-dust and conductivity profiles at 5, 0.35, 0.35, 0.1, 0.1 cm resolution respectively are from Vallelonga et al., 2012.

Chapter 6

Citation: Della Lunga, D., Müller W., Rasmussen S. O. & Svensson A. S. (2015b). 3-D mapping of cation impurities in deep NGRIP ice. Planned submission to *The Cryosphere*.

This manuscript is in preparation. Together with Chapter 4 it represents our UV-LA-ICPMS investigations regarding ice physics.

Author contributions: DDL designed the research and the analytical procedure in discussion with WM, SOR and ASS, wrote the Matlab reduction code, interpreted the data and wrote the manuscript. WM edited the manuscript.

3-D mapping of cation impurities in deep NGRIP ice

D. Della Lunga[1], W. Müller[1], S. O. Rasmussen[2], A. Svensson[2]

[1] Department of Earth Sciences, Royal Holloway University of London, Egham Hill, Egham TW20 0EX, United Kingdom.

[2] Centre for Ice and Climate - Niels Bohr Institute, University of Copenhagen, Juliane Maries Vej 30, 2100 Copenhagen Ø, Demark.

Correspondence to: D. Della Lunga

(damiano.dellalunga.2011@live.rhul.ac.uk)

Abstract

We analysed major cation concentrations (Na, Mg, Al, Ca, Fe) in a small cuboid of deep NGRIP ice of dimensions 45 x 10 x 10 mm, from a depth interval of 2717.155-2717.200 m (NGRIP ice core), performing 2D mapping on its six external surfaces and two cross sections (deliberately selected to intercept a zone of 'clear ice' and a 'cloudy band'). Acquisition was carried out via cryo –cell UV-LA-ICPMS, performed using 9 laser tracks at 212 µm spot size and 300 µm spacing on each surface. Calibrated concentration data were interpolated, allowing a 3D reconstruction of the location of ionic impurities within the volume, with particular emphasis on the relationship between impurities and grain boundaries in both clear ice and cloudy bands. The sample represents roughly 3-4 years of accumulation, given the layer thickness of approximately 12 mm at this depth. Results show that the distribution of elements in the volume is compatible with three different yearly cycles with high concentration in spring/summer layers and low concentration in winter layers. However, data suggest that migration of major cations within

the ice lattice takes place and facilitates the homogenization of concentrations in the ice volume at sub-cm scale.

Introduction

Polar ice cores contain impurities as dust particles, deposited from the atmosphere as a result of direct fall (dry deposition) or as nuclei of precipitation (wet deposition), and ionic impurities embedded in the ice lattice. The former are known to have a diameter between 1 and 10 µm (1-2 µm on average for the NGRIP ice core; Ruth et al., 2003) and are transported from distant regions such as Asian deserts to Greenland, where they are incorporated into the snow precipitated (Fisher et al., 2007). During firnification and compaction of ice, dust particles do not move as a result of diffusional recrystallization, thus preserving the original depositional layering to great depths (Svensson et al., 2011). This layering can be observed by visual stratigraphy as an alternation of dark and bright horizons that correspond to areas of low and high concentration of particles, respectively. This is due to scattering collected by a camera above the ice core from light entering the ice at a 45° angle (Svensson et al., 2005). Therefore, transparent ice appears dark in the scan images, whereas 'dirty' ice, full of particles, appears brighter. At NGRIP, horizontal layering is perfectly visible down to depths of approximately 2800 m, where some waving and micro-folds of the layers can be observed (Svensson et al., 2005). However, the alternation of bright and dark layers is still clearly visible at depths of approximately 2900 m, where the layering on such scan images becomes obliterated by recrystallization. On a seasonal scale, bright layers typically represent spring/summer periods when storms carry a higher amount of particles to the ice caps (Fischer et al., 2007). On the other hand, the low concentration of particles or impurities during the winter season is represented by dark layers. On a larger scale, cold climatic periods have on average higher densities of visible layers and thus are more intensely bright, whereas milder periods have proportionally more transparent ice. The bright layers are called *cloudy bands* (Gow and Williamson, 1976; Della Lunga et al., 2014) and range in thickness between 1 and 100 mm and usually have a

grain size that is considerably smaller than the adjacent dark ice (from here on referred as *clear ice*), up to a factor of 10.

The content of impurities also plays a crucial role in microstructural processes such as ice grain growth and recrystallization (Faria et al, 2014; Della Lunga et al., 2014). In fact, for a long time it has been proposed that the abrupt drop in grain size from clear ice to cloudy bands was due to grain boundary pinning by micro-inclusions or impurities (Alley et al., 1986; Weiss et al., 2002; Durand et al., 2006). However, several studies suggest that the smaller grain size within cloudy bands is due to impurity-enhanced ice flow (Faria et al., 2014), which represents an anomalous ice rheology that may make identification of annual layers more difficult and thus also dating of ice cores, since it would facilitate the occurrence of heterogeneous ice deformation such as layer thinning (Gow and Meese, 2007; Durand et al., 2007). Furthermore, with reduced grain size, the network of grain boundaries will be more extensive and therefore smearing of the palaeoclimatic signal by diffusion of impurities through liquid veins on grain boundaries and triple junctions would be also possible. However, these hypotheses have never been corroborated and a general consensus on the microstructural role of impurities has not been reached (Faria et al., 2014). In fact, the occurrence of cloudy bands in glacial ice with high concentrations of dust and other impurities has long been established (e.g., Ram and Koenig, 1997), but the nature of those visible layers in ice is still uncertain as well as how they relate to the various impurities in ice in terms of diffusion (Rempel and Wettlaufer, 2002).

Here we present an attempt at reconstructing the 3D features especially of cloudy bands in a small volume of ice using the cryo-cell UV-LA-ICPMS setup established at Royal Holoway University of London (RHUL; Müller et al., 2011, Della Lunga et al., 2014). By measuring major cations such as Na, Mg, Al, Ca and Fe we aim to answer to the following questions: (i) What is the 3D feature of cloudy bands (i.e. do they keep their horizontal continuity in three dimensions?) (ii) How well is the visual stratigraphy matched by elemental concentrations? (iii) Are soluble particles mobilized? (iv) Can the

small-scale alteration of the layering mislead layer counting based on those proxies? And finally (v) can we better constrain the nature of cloudy bands?

Methodology

The analytical setup is described in detail in Della Lunga et al. (2014) and only a brief summary of relevant details is given here. Sample 4941_A8 represents a small ice cuboid volume with dimensions of 45x10x10 mm from the NGRIP depth interval of 2717.155-2717.200 m (Fig. 1 and 2). Approximately three to four years of the first section of the Greenland Stadial GS22 are represented in this sample, given the layer thickness at this depth of 12 mm on average (Vallelonga et al., 2012). Each surface of the sample has been cleaned and smoothed with a metal-free Y-doped zirconia blade to facilitate ablation and remove surface contamination using a custom-built PTFE vice as described in Della Lunga et al. (2014) (Fig.1).

Acquisition of m/z 23(Na), 24 (Mg), 27 (Al), 40 (Ca), 56 (Fe) compositional data, has been performed via a series of parallel laser tracks with 212 µm spot size, 20 Hz laser repetition rate, 300 µm spacing, 3 mm/min speed and a laser fluence of 3.5 J/cm^2 (Fig. 2). Each laser acquisition has been preceded by three laser cleaning passages at 280 µm spot size, 25 Hz, and 8 mm/min speed to remove further contamination. Data have been corrected for instrumental drift, isotopic abundance, and then calibrated using the same materials and strategies as described in Della Lunga et al. (2015, in preparation). Ca and Mg have not corrected to *not-sea salt* Ca and *sea salt* Mg (Della Lunga et al., 2015 in preparation), but represent instead the total content of elemental Ca and Mg. A series of nine parallel longitudinal laser tracks (Fig. 2) on all six main outer surfaces plus two cross sections has been used to create a 3D array of data. Following data acquisition of all external surfaces, the volume was broken into three pieces and ice was shaved off to expose the two cross sections as indicated in Fig. 2, in order to acquire data on such interior surfaces and thus facilitate better 3D extrapolation.

Smoothing of the data via moving average (period 20) and Interpolation to a 3D graphic has been carried out using a simple custom-developed Matlab code (see Appendix I).

Results

Details of the sample are shown in Fig. 1-2, while all results are displayed as colour-coded concentration maps on the 3D cuboid in Figures 3-7, where the sample is oriented SW-NE (above) and SE-NW (below) from depth 2717.200 to 2717.155 m. Voids in the volume represent areas where no interpolation was possible because signals were below the limit of detection (LOD). On the right side of the figures two XZ cross sections intercepting the y-axis at mm 10 and 35 (as indicated in red in Fig. 1 and 2) are shown. The grain boundary network has been obtained from laser camera pictures as shown in Fig. 1-2 and overlaid in white on the cross sections. Figure 1 shows the sub-sample location relative to the NGRIP ice core cross section (Fig .1a) and the numbering assigned to each surface of the cuboid (Fig. 1b) with corresponding LA camera pictures where grain boundaries net has been highlighted (Fig. 1c).

Figure 2 shows that the two cross sections intercept a zone of clear ice and a cloudy band respectively. The scan image of the surface of the core (surface n°3 of the cuboid, Fig. 1b) has been obtained from Svensson et al. (2005). Laser camera images of these sections (Fig. 2) show a significant difference in grain size: 3-4 mm on average for clear ice and 1-2 mm for cloudy bands (Fig. 2). Laser camera images for each surface (Fig. 1c) also show a considerable reduction of grain size in two areas located at ~5 mm from the top and towards the bottom of the section, confirming that they represent a cloudy band and a clear ice layer respectively.

Na shows concentrations that range from 80 to 200 ppb with maxima concentrated in two areas between ~10 - 20 mm and between ~39 - 45 mm. These elevated concentrations do not form a layer of high concentration throughout, as could be expected in correspondence to the extent of cloudy bands. On the contrary, concentrations are heterogeneous through the entire

volume and layering is very difficult to observe, even if the cloudy band at Ymm 40 conserves a geometry that seem to continue across the edges of the cuboid. In clear ice impurity are generally low and peaks of high concentration are generally small isolated patches.

The differentiation between areas of low and high concentrations of elements is more pronounced for elements such as Mg and especially Al and Fe, where approximately three cycles of low-to-high alternation of concentrations can be identified. However, these bands are not continuous throughout the volume as they appear to show concentration gradients in more than one direction. The layering observable in the scan and LA images (Fig. 1-2) is best reproduced in elements like Al, whereas Ca, present a somewhat more patchy distribution of elevated concentrations dispersed over the volume, rather poorly reproducing the stratigraphy of the ice (Fig. 1-2). Ca and Al show the highest concentration from 50 up to 250 ppb, whereas all the other elements present concentrations in a range between few ppb up to 50 ppb.

The two cross sections show that concentrations in clear ice are significantly lower than in cloudy bands, where impurities are dispersed more compared to clear ice in which they tend to concentrate in single spots. In this case, no clear pattern is observable regarding the location of impurities with respect to grain boundaries or triple junctions in neither cloudy bands nor clear ice, as it was observed in previous works (Della Lunga et al., 2014).

Discussions

Sample 4941_A8 contains three complete cycles of low and high concentrations which likely represent seasonal input of micro-particles into the ice. This can also be observed in the scan image of the corresponding section of the core (Fig. 2) which shows at least three cloudy bands that vary in thickness from 2 to 15 mm. The 3D volumes (Fig. 3-7) similarly show alternation of zones of low and high concentration, although the horizontal layering noticeable in the scan images is not conserved equally well in the distribution of elements. However, the degree of similarity between scan images and 3D volumes varies from element to element: Al seems to best

mimic the clean ice/cloudy bands alternation compared to any other element, similarly to Mg and Fe, whereas Ca, and even more Na present a rather disperse zoning where no clear layering is observable. In general, we can conclude that cloudy bands as observed on scan images do not coincide exactly with the distribution of elements and their continuity is not traceable in three dimensions on a mm scale.

Consequently, it is reasonable to consider whether these elements were deposited as we can observe them in the model or whether they became mobilized during the later depositional and deformational history. Since cloudy bands were first defined (Gow and Williamson, 1976), they have been distinguished from ash layers that are composed primarily of dust with dimensions observable to the naked eye (>30 µm). Cloudy bands do not contain particles visible with the naked eye as more than 90% of their insoluble micro-inclusions range in size between 1 and 5 µm at NGRIP (Ruth et al., 2003). But the impurity content of cloudy bands is not made entirely by micro-sized particles of dust. Soluble micro-particles with dimensions ranging from a fraction of 1 µm to ionic dimensions can form a considerable part of the cation content observed in our UV-LA-ICPMS data. Therefore, we conclude that insoluble micro-sized dust cannot be mobilized, as proposed in the literature (Svensson et al., 2011), whereas ionic impurities and extra-fine micro-inclusion may undergo transport in ice through liquid veins or possibly via solid state diffusion. In this view, differences in how elements conserve any original layering of clean ice/cloudy bands can be explained in terms of solubility coefficient.

However, we can assume that self-diffusion is negligible compared to Fickian diffusion (10^{-11} and 10^{-6} cm^2s^{-1} respectively, see Ramseier, 1967 and Yuan-Hui and Gregory, 1974) and that both soluble and insoluble impurities are deposited together in correspondence to the cloudy bands. Therefore we can formalize the diffusion of species in the possible liquid water veins, deriving it from Fick's laws. If the mass of impurities in an arbitrary volume (V) varies with time, it has to be compensated by advection and diffusion of analogous impurities species across the boundary surface (S) of that volume. Therefore the mass balance can be written as:

$$\frac{\partial}{\partial t}\int_V Cl_i dV = -\oint_S Cl_i v - (D_i \varphi \nabla C_i)\, dS \quad \text{(Eq.1)}$$

(Johnsen et al., 2000)

Where Cl_i and C_i represent the concentration of the species *i* in the liquid and the total volume respectively; v is the ice sheet flow velocity; D_i is the diffusion coefficient and φ the mass fraction of liquid present. The left side of eq. 1 represent the rate of loss of impurities over time through liquid veins in a unit volume V, while the right side represent the compensation flow (hence the negative sign) that allows the conservation of mass. However, it can be demonstrated that advective flux of impurities through liquid veins is negligible compared to Fickian diffusion (Dash et al., 2006). We can therefore ignore v to quantify a measurement of the speed with which impurities move relative to the surrounding ice and simply derive the rate of transport (v_t) of a species *i* from Fick's first law:

$$v_t = -D_i \frac{\nabla C_i}{C_i} \quad \text{(Eq.2)}$$

We can note now that C_i represents the mass of impurities in the total volume V, and therefore is related to the mass of impurities in the liquid fraction by the relationship:

$$Cl_i = \varphi C_i \quad \text{(Eq.3)}$$

Substituting eq.3 into eq.2 we have:

$$v_t = \frac{-D_i \varphi \nabla C_i}{Cl_i} \quad \text{(Eq. 4)}$$

As an example we can now attempt to calculate v_t for Ca^{2+} just in the vertical (y) dimension taking 10^{-6} cm^2/s as D_i at 0 °C (Yuan-Hui and Gregory, 1974) and a value of 32 ppb/cm directly derived from our laser data averaging $\frac{\partial C_i}{\partial x}$ of the 9 parallel laser tracks of Ca^{2+} on surface 3 of the cuboid (see Fig .1 and 2). We can now choose our sample 4941_A8 as an arbitrary volume and integrate the Ca^{2+} profile to find out C_i and therefore Cl_i from eq.3 assuming the liquid fraction as 10^{-6} (Rempel and Wettlaufer 2002). The resultant Cl_i on average turn out to be 97 ppb.

So our calculation gives: $v_t = \frac{10^{-6}\ \frac{cm^2}{s} 10^{-6} \cdot 0.032 \frac{ppm}{cm}}{0.097\ ppm}$ = -3.29·10^{-13} $\frac{cm}{s}$

Considering the age of our sample (86400 ka), roughly 2.7·10^{-12} s have elapsed since deposition. So soluble impurities could have diffused across a distance of:

(3.29·10^{-13} $\frac{cm}{s}$)·(2.7·10^{12} s) = 8.9 mm.

This means that soluble impurities could have moved appreciably across the volume since deposition. However, since this migration is in three dimensions, the effect is compensated by mirrored behaviour of adjacent ice and the net transport of impurities from areas of high concentration to areas of low concentration is practically negligible at the scale of several tens of millimetres. Therefore, liquid vein and diffusional transport can only effect impurity migration at a very small scale (mm) and can affect only soluble impurities, since the average vein radius in polar ice is a few nanometers (Rempel and Wettlaufer, 2002), so that only ionic impurities can be transported.

It is clear then that diffusion cannot alter the seasonal variation of elements except on a millimetre-scale and can be observed only by sub-(10) mm spatial resolution such as given by laser ablation and not via CFAs. Therefore, the palaeoclimatic significance of elemental variation from yearly to centennial timescales is entirely conserved. On the other hand, strategies for UV-LA analysis of ice cores for paleoclimatic reconstruction must comprehend an averaging of the signal between at least two parallel tracks along the samples, to compensate for the small-scale bias LA-ICPMS acquisition can encounter because of diffusion of ionic species.

Conclusions

The major findings can be summarized as follows:

- Cloudy bands contain soluble and insoluble impurities in higher concentrations than the surrounding ice, but the 3D continuity of these

279 layers is not always preserved, so that the layers can present a wavy
280 pattern across the edges of an arbitrary volume.
281 • Visual stratigraphy matches fairly well the distribution of elements in
282 the ice, but a fraction of the impurities seems to have moved from
283 areas of high concentration to areas of low concentration. This can be
284 related to diffusion through liquid veins that, as demonstrated, can
285 transport soluble impurities for small (sub-cm) distances over the
286 course of several thousands of years, whereas µm-sized dust micro-
287 particles cannot be transported.
288 In this view, the difference in what is the observed deviation from
289 original layering as per the visual images and the actual distribution
290 among different elements can be explained in terms of the solubility
291 coefficient in water for each element.
292 However, diffusion seems not to happen along grain boundaries as
293 impurities do not concentrate along them (Fig. 3-7, XZ cross sections).
294 • Since transport of impurities acts only at a sub-cm scale, the
295 palaeoclimatic signal as recorded by CFAs is entirely conserved.
296 However, UV-LA analysis of ice cores must comprehend a strategy for
297 averaging the acquisition of signals with several parallel acquisitions to
298 avoid small-scale bias during acquisition.

299

300 ## Acknowledgements

301 The authors would like to thank Jerry Morris (RHUL) for precious technical
302 support; Paul Vallelonga and Jorgen Peder Steffensen (NBI) for discussion
303 and advice.

304

305 ## References

306 Alley, R. B., Perepezko, H., & Bentley, C. R. (1986). Grain growth in polar
307 ice: 1. Theory. *J. Glaciol,* **32**(1), 1.

308 Dash, J. G., Rempel, A. W., & Wettlaufer, J. S. (2006). The physics of
309 premelted ice and its geophysical consequences. *Reviews of modern*
310 *physics*, **78**(3), 695.

311 Della Lunga, D., Müller, W., Rasmussen, S. O., & Svensson, A. (2014).
312 Location of cation impurities in NGRIP deep ice revealed by cryo-cell
313 UV-laser-ablation ICPMS. *Journal of Glaciology*, **60** (223), 970-988.

314 Della Lunga, D., Müller, W., Rasmussen, S. O., & Svensson, A., Vallelonga
315 P. (2015). A precursor of Dansgaard-Oeschger event 21: ultra-high
316 resolution analysis of elemental concentrations in NGRIP ice cores via
317 UV-LA-ICPMS. Planned submission to *Journal of Quaternary Science*.

318 Durand, G., Weiss, J., Lipenkov, V., Barnola, J. M., Krinner, G., Parrenin, F.,
319 Delmonte B., Ritz C., Duval P., Röthlisberger R. & Bigler, M. (2006).
320 Effect of impurities on grain growth in cold ice sheets. *Journal of*
321 *Geophysical Research: Earth Surface* (2003–2012), **111**(F1).

322 Durand, G., Gillet-Chaulet, F., Svensson, A., Gagliardini, O., Kipfstuhl, S.,
323 Meyssonnier, J., Parrenin F., Duval P. & Dahl-Jensen, D. (2007).
324 Change in ice rheology during climate variations–implications for ice
325 flow modelling and dating of the EPICA Dome C core. Climate of the
326 Past, **3**(1), 155-167.

327 Faria, S. H., Freitag, J., & Kipfstuhl, S. (2010). Polar ice structure and the
328 integrity of ice-core paleoclimate records. *Quaternary Science Reviews*,
329 **29**(1), 338-351.

330 Faria, S. H., Weikusat, I., & Azuma, N. (2014). The microstructure of polar
331 ice. Part II: State of the art. *Journal of Structural Geology*, **61**, 21-49.

332 Fischer, H., Siggaard-Andersen, M. L., Ruth, U., Röthlisberger, R., & Wolff,
333 E. (2007). Glacial/interglacial changes in mineral dust and sea-salt
334 records in polar ice cores: Sources, transport, and deposition. *Reviews*
335 *of Geophysics*, **45**(1).

336 Gow, A. J., & Williamson, T. (1976). Rheological implications of the internal
337 structure and crystal fabrics of the West Antarctic ice sheet as revealed

by deep core drilling at Byrd Station. *Geological Society of America Bulletin*, **87**(12), 1665-1677.

Gow, A. J., & Meese, D. A. (2007). The distribution and timing of tephra deposition at Siple Dome, Antarctica: possible climatic and rheologic implications. *Journal of Glaciology*, **53**(183), 585-596.

Johnsen, S. J., Clausen, H. B., Cuffey, K. M., Hoffmann, G., & Creyts, T. T. (2000). Diffusion of stable isotopes in polar firn and ice: the isotope effect in firn diffusion. *Physics of ice core records*, 121-140.

Müller, W., Shelley, J. M. G., & Rasmussen, S. O. (2011). Direct chemical analysis of frozen ice cores by UV-laser ablation ICPMS. *Journal of Analytical Atomic Spectrometry*, **26**(12), 2391-2395.

Ram, M., and G. Koenig (1997), Continuous dust concentration profile of pre-Holocene ice from the Greenland Ice Sheet Project 2 ice core: Dust stadials, interstadials, and the Eemian, *J. Geophys. Res*., **102**(C12), 26,641–26,648.

Ramseier, R. O. (1967). Self-Diffusion of Tritium in Natural and Synthetic Ice Monocrystals. *Journal of Applied Physics*, **38**(6), 2553-2556.

Rempel, A. W., Wettlaufer, J. S., & Waddington, E. D. (2002). Anomalous diffusion of multiple impurity species: predicted implications for the ice core climate records. *Journal of Geophysical Research: Solid Earth* (1978–2012), **107**(B12), ECV-3.

Ruth, U., Wagenbach, D., Steffensen, J. P., & Bigler, M. (2003). Continuous record of microparticle concentration and size distribution in the central Greenland NGRIP ice core during the last glacial period. *Journal of Geophysical Research: Atmospheres* (1984–2012), **108**(D3).

Svensson, A., Nielsen, S. W., Kipfstuhl, S., Johnsen, S. J., Steffensen, J. P., Bigler, M., Ruth U. & Röthlisberger, R. (2005). Visual stratigraphy of the North Greenland Ice Core Project (NorthGRIP) ice core during the last glacial period. *Journal of Geophysical Research: Atmospheres* (1984–2012), **110**(D2).

Svensson, A., Bigler, M., Kettner, E., Dahl-Jensen, D., Johnsen, S., Kipfstuhl, S., Nielsen M. & Steffensen, J. P. (2011). Annual layering in the NGRIP ice core during the Eemian. *Climate of the Past Discussions*, **7**(1), 749-773.

Vallelonga, P., Bertagna, G., Blunier, T., Kjær, H. A., Popp, T. J., Rasmussen, S. O., Steffensen J. P., Stowasser,C. Svensson A. S., Warming E., Winstrup M., Bigler M. & Kipfstuhl, S. (2012). Duration of Greenland Stadial 22 and ice-gas Δage from counting of annual layers in Greenland NGRIP ice core. *Climate of the Past Discussions*, **8**(4), 2583-2605.

Weiss, J., Vidot, J., Gay, M., Arnaud, L., Duval, P., & Petit, J. R. (2002). Dome Concordia ice microstructure: impurities effect on grain growth. *Annals of Glaciology*, **35**(1), 552-558.

Yuan-Hui, L., & Gregory, S. (1974). Diffusion of ions in sea water and in deep-sea sediments. *Geochimica et cosmochimica acta*, **38**(5), 703-714.

Figures

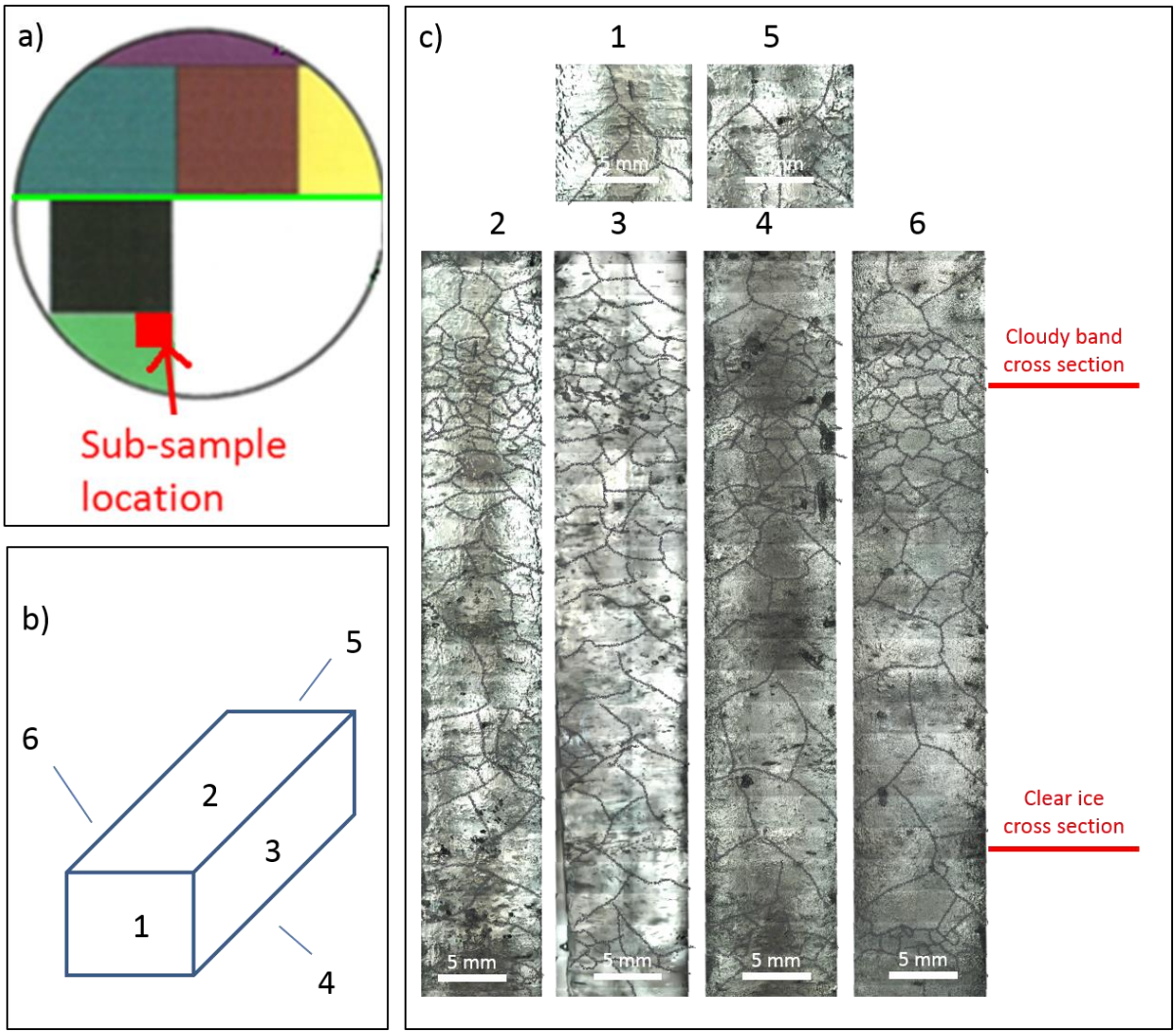

Figure 1: a) Sub-sample location in NGRIP ice core cross section for sample 4941_A8 (2717.200-2717.155 m). b) The surfaces of the cuboid have been numbered form 1 to 6 as in the sketch. c) LA camera images of each sample surface. In red the locations of analysed XZ cross sections are indicated (see Fig. 2).

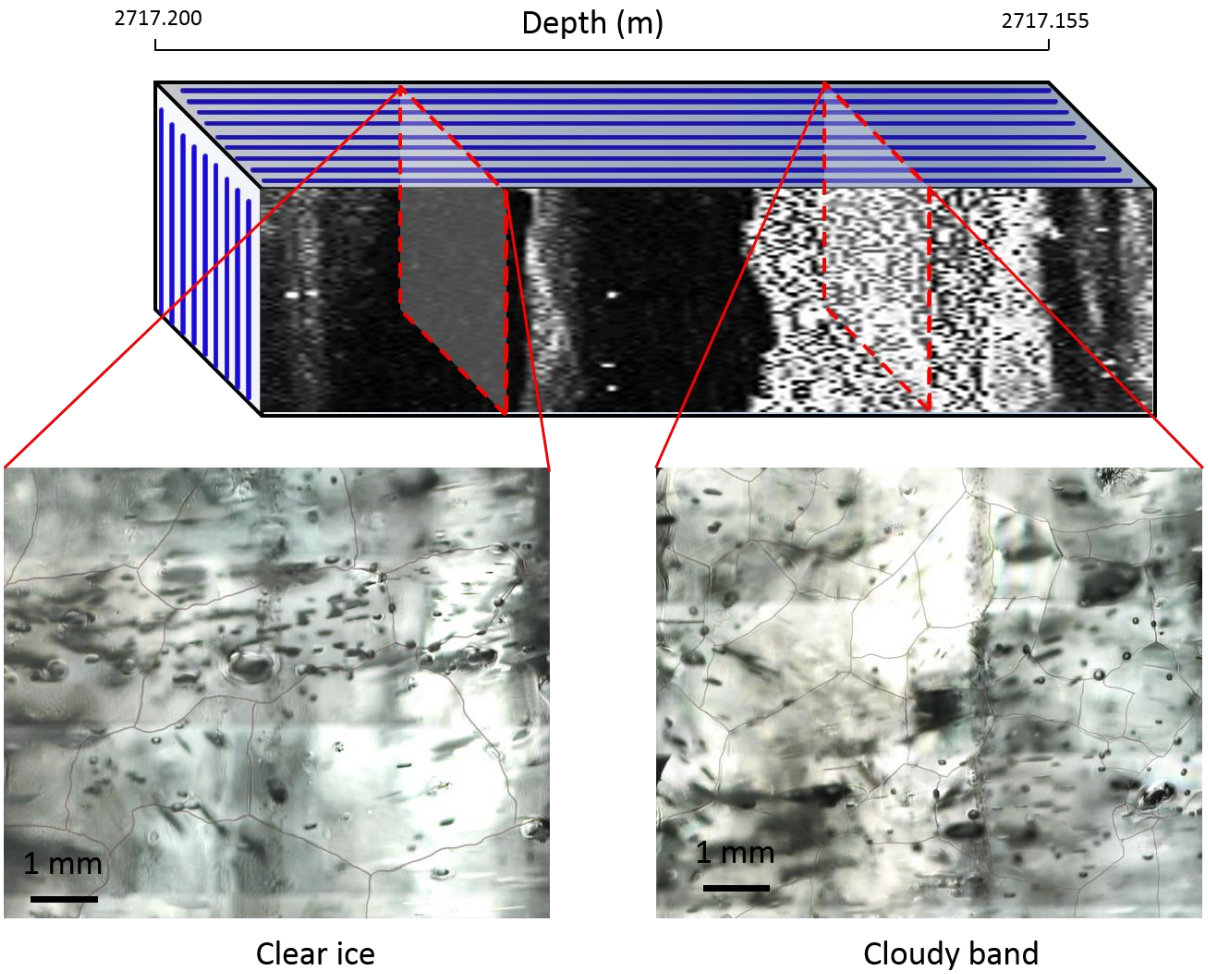

Figure 2: Sketch of the cuboid ice volume selected for analysis. The correct scan image for this depth interval has been overlaid on the corresponding surface of the volume (n° 3 in Fig. 1), to show the presence of cloudy bands. The red planes indicates where the cross section analysed have been taken, with the corresponding images (below) showing the position of grain boundaries in clear ice and cloudy band. Blue tracks represent laser acquisition passage used to create the grid which has been interpolated to create 3D maps. Each surface has been analysed via 9 laser tracks at 212 µm spot size, 300 µm spacing, 3 mm/min speed.

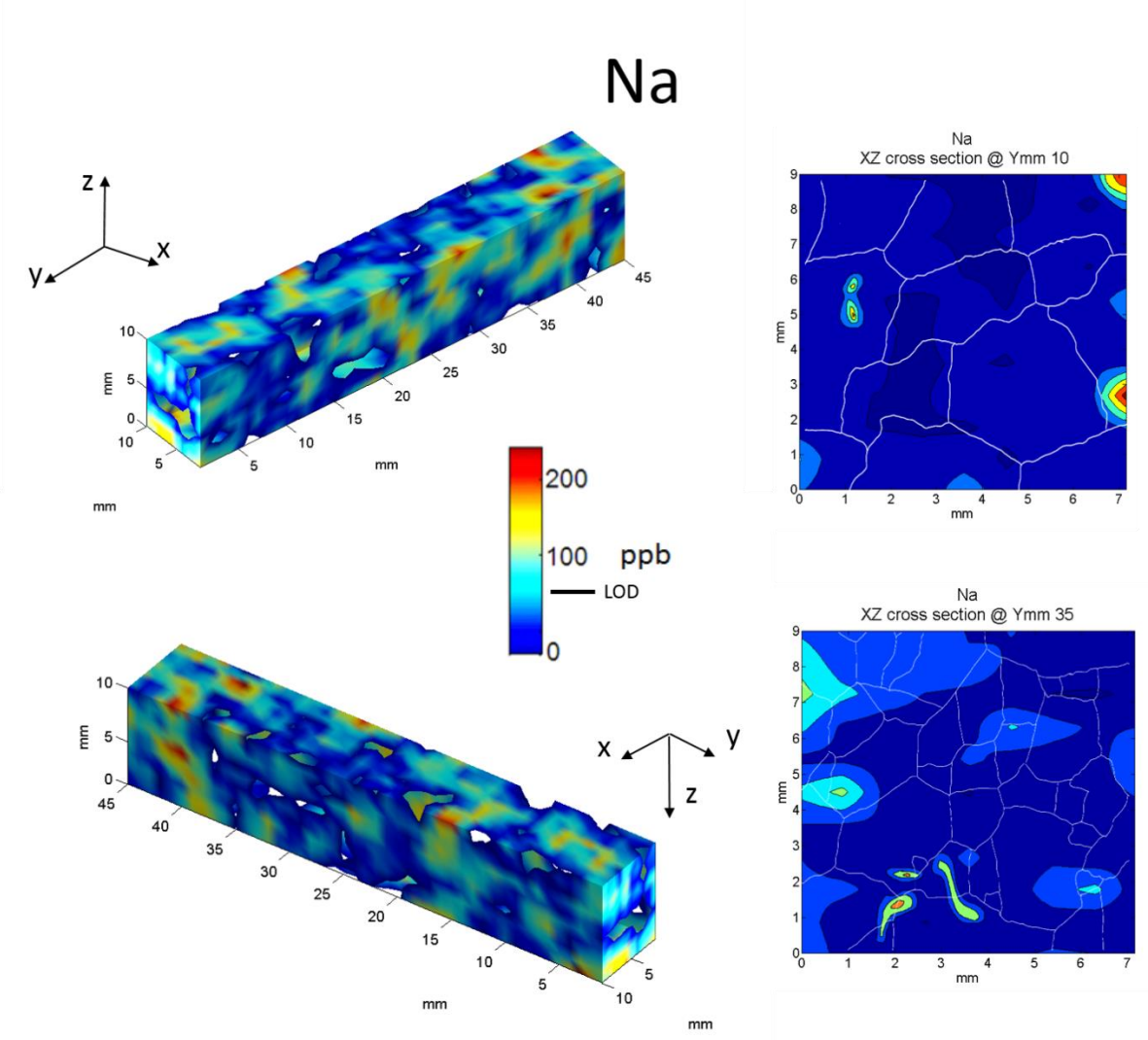

Figure 3-7: 3D visualization of concentration of elements in the sample. XZ Cross section on the right are taken at Ymm 10 and 35; grain boundary net is overlaid in white. Depth range is 2717.200-2717.155 m from Ymm 0 to Ymm 45. The voids in the volume represent parts where interpolation was not possible due to gaps in the data matrix.

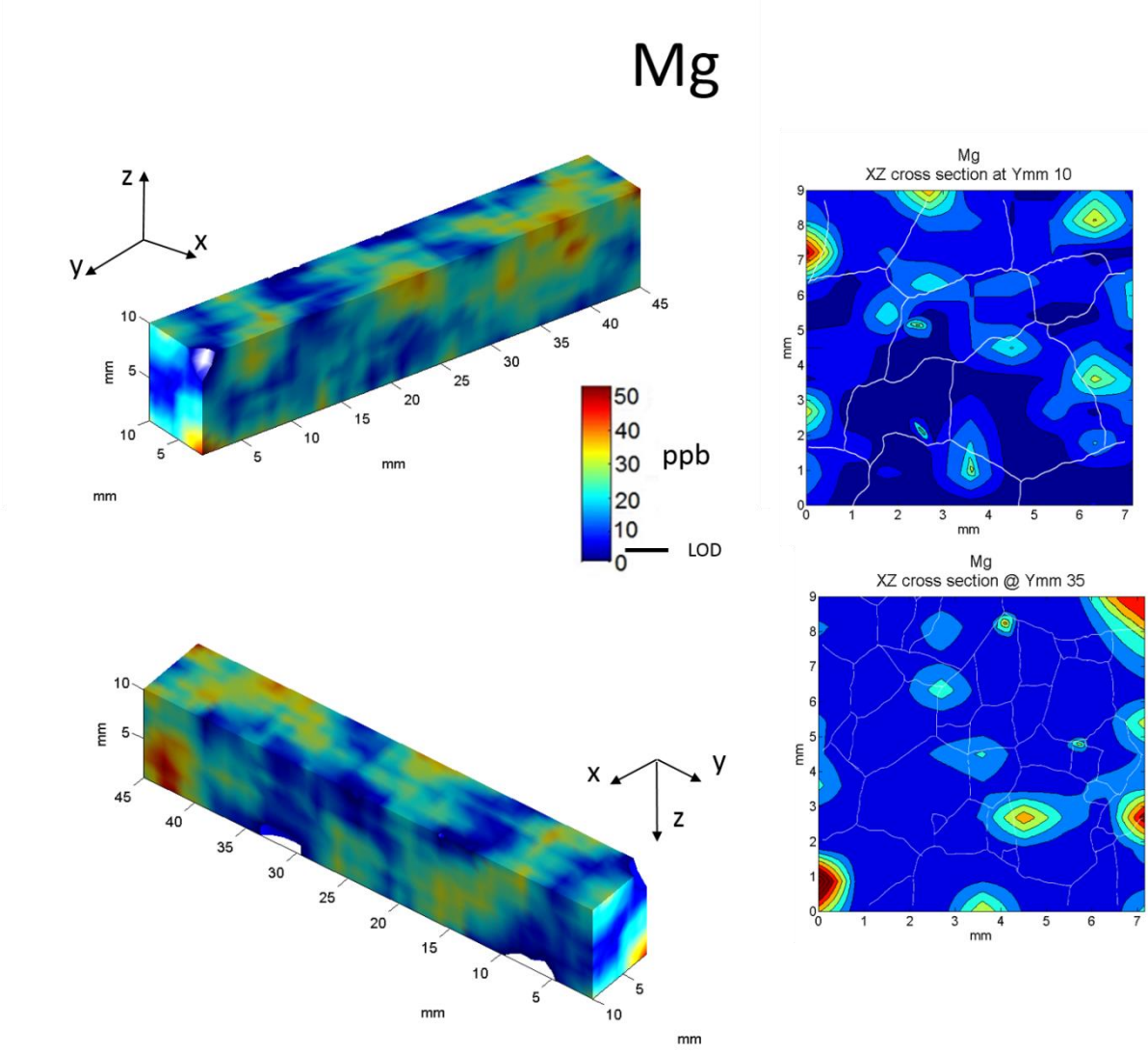

428

429

430

431

432

433

434

435

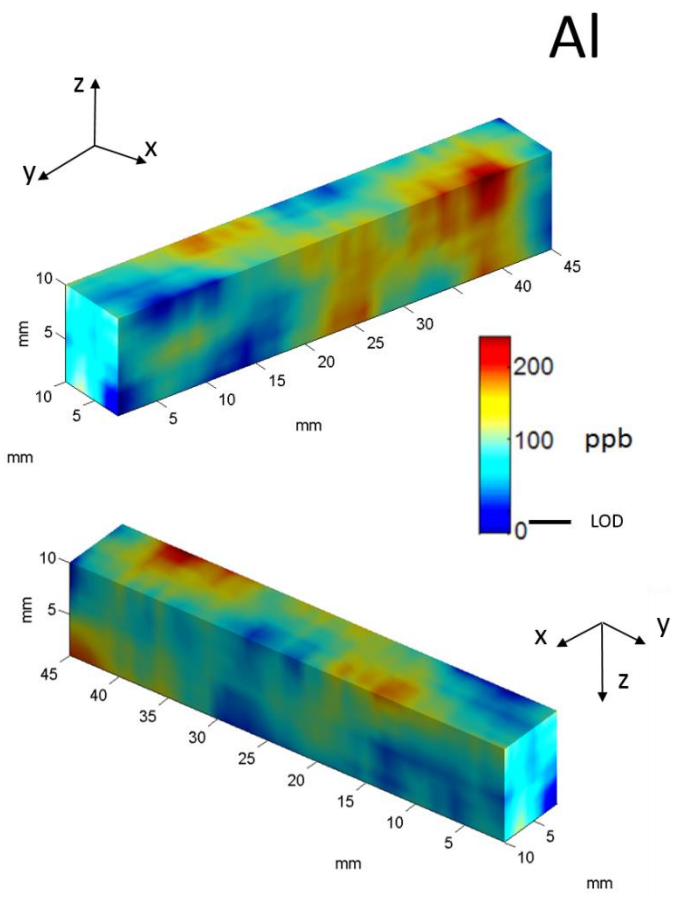

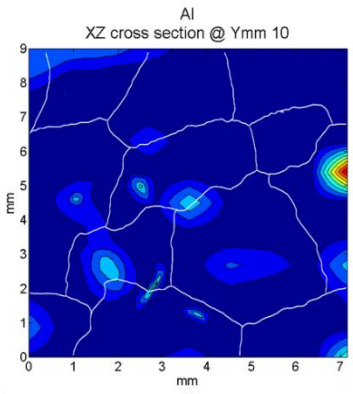

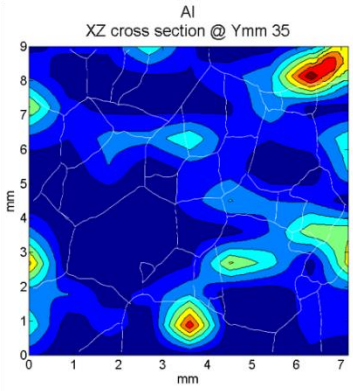

436

437

438

439

440

441

442

443

444

445

446

447

448

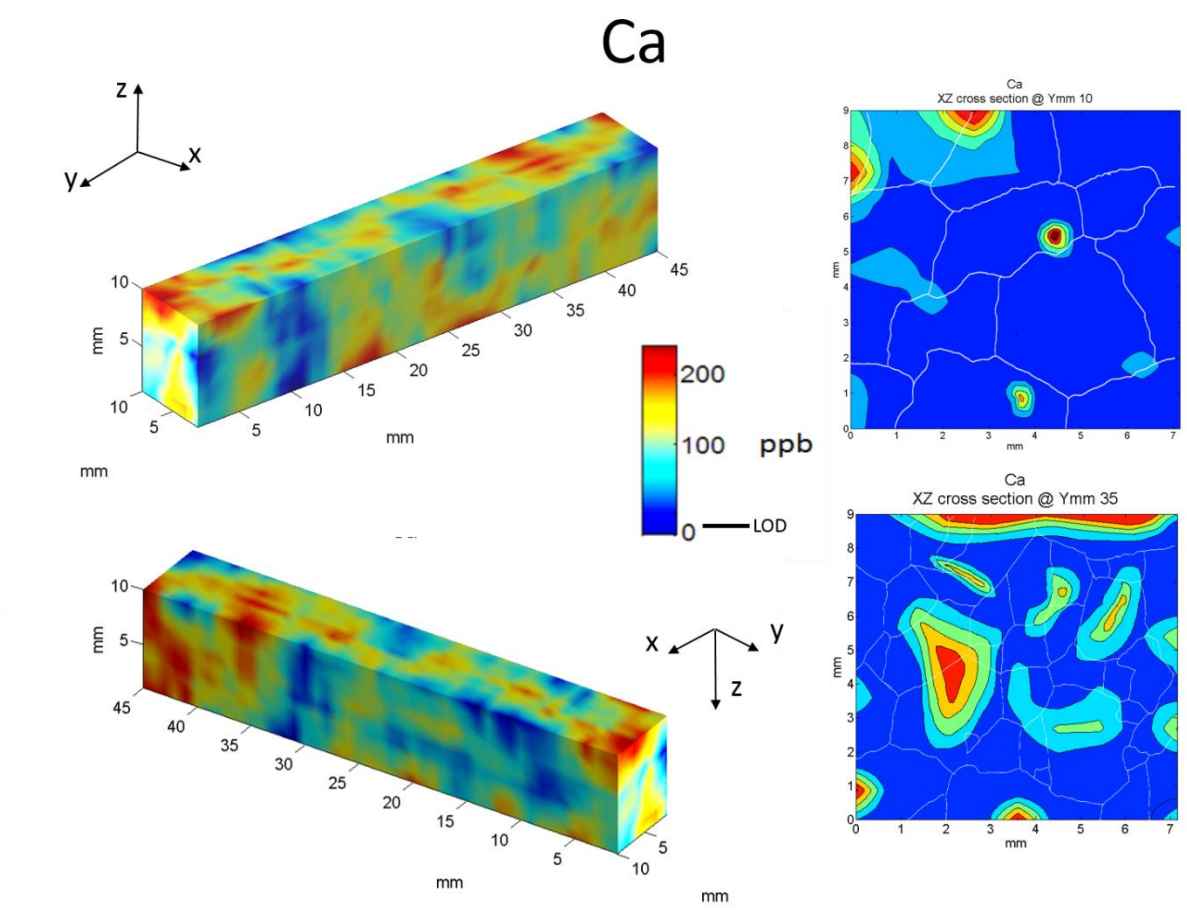
Ca
z
x
y
10
5
mm
10
5
5
10
15
20
25
30
35
40
45
mm
mm
200
100
ppb
0
LOD
10
5
mm
45
40
35
30
25
20
15
10
5
10
mm
x
y
z
mm
Ca
XZ cross section @ Ymm 10
mm
mm
Ca
XZ cross section @ Ymm 35
mm
mm

Fe

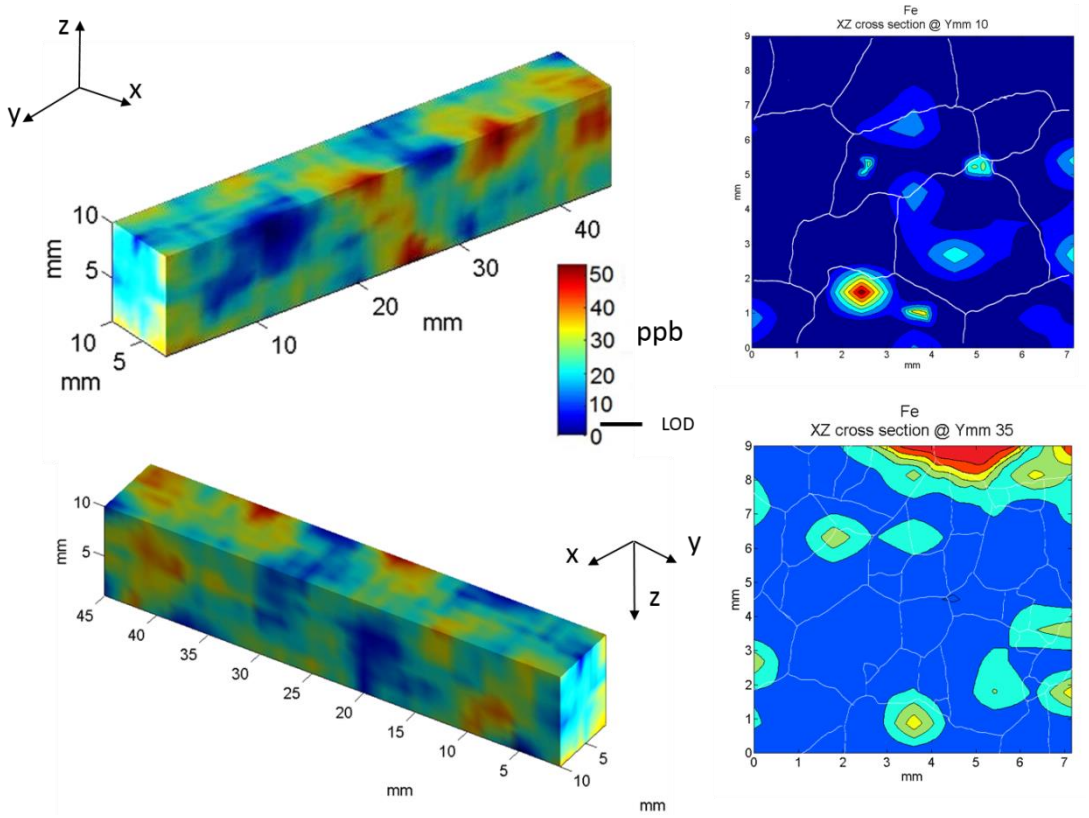

462

463

464

465

466

467

468

469

470

471

472

473

474

Appendix I

Matlab code for 3D interpolation of data:

```
%load the data (example for sodium [Na])%
a=xlsread('3Da.xlsx','Na-surface 1');
b=xlsread('3Da.xlsx','Na-surface 2')
c=xlsread('3Da.xlsx','Na-surface 3')
d=xlsread('3Da.xlsx','Na-surface 4')
e=xlsread('3Da.xlsx','Na-surface 5')
f=xlsread('3Da.xlsx','Na-surface 6')
g=xlsread('3Da.xlsx','Na-cs 10')
h=xlsread('3Da.xlsx','Na-cs 35')
%create the 3D array%
b=a(:,:,size(g));
c=a(1,:,:);
d=a(size(g),:,:);
e=a(:,1,:);
f=a(:,size(g),:);
%insert the two cross sections in the 3D array%
g=a(:(size(g)/45)*10),:);
h=a(:,(size(g)/45)*35),:);
%create the meshgrid for interpolation%
y=a(1,1:end);
x=a(1:end,1);
z=g(1:end,1);
[xq,yq,zq]=meshgrid(x,y,z);
%interpolate data in three dimensions%
data=interp3(a,xq,yq,zq);
%operate a smoothing for the data and set isolines properties%
data = smooth3(data,'box',5);
patch(isocaps(data,.5),...
   'FaceColor','interp','EdgeColor','none');
p1 = patch(isosurface(data,.5),...
   'FaceColor','blue','EdgeColor','none');
isonormals(data,p1)
%visualize the cuboid%
view(3);
axis vis3d tight
camlight left;
colormap jet
lighting gouraud
```

Chapter 7

Citation: Della Lunga, D., Müller W., Rasmussen S. O., Svensson A. S. Vallelonga P. T. & Steffensen J.P. (2015c). High resolution UV-LA-ICPMS analysis of dust and sea salt proxies in deep glacial ice: a complete survey of Greenland Stadial 22 transitions. Planned submission to *Journal of Geophysical Research*.

This manuscript is in preparation. Together with Chapter 5 it contains UV-LA-ICPMS contribution to the investigation of abrupt climate changes during the past glaciation.

Author Contribution: DDL and WM designed the research and analytical procedure in discussion with SOR, ASS, PTV and JPS. DDL performed the analysis, interpreted the data and wrote the manuscript. WM edited the manuscript.

High resolution UV-LA-ICPMS analysis of dust and sea salt proxies in deep glacial ice: a complete survey of Greenland Stadial 22 transitions

Damiano Della Lunga[1], Wolfgang Müller[1], Sune Olander Rasmussen[2], Anders Svensson[2], Paul Vallelonga[2] and Jørgen Peder Steffensen[2]

[1] Department of Earth Sciences, Royal Holloway University of London, Egham TW20 0EX, United Kingdom.

[2], Centre for Ice and Climate - Niels Bohr Institute, University of Copenhagen, 2100 Copenhagen Ø, Demark.

Correspondence to: D. Della Lunga (damiano.dellalunga.2011@live.rhul.ac.uk)

Abstract

Greenland ice cores record seasonal to millennial variability of many elemental species (continental ions: e.g. Ca, Al, Fe) at one the highest resolution observed in natural archives in response to abrupt warming and cooling events (DO events) that punctuated the last glacial phase during the last 120 kyrs. We analysed several species across the two transitions between stadial and interstadial phases characterizing the DO 22 (GS22) via UV-LA-ICPMS at a resolution of ~200 µm. Calibrated concentration show an increase of about one order of magnitude for most of the elements across interstadial/stadial transitions and vice versa, also showing that continental ions often precede the variations in $\delta^{18}O$ and complete the switch from cold to warm conditions five to ten years before temperature. We propose here that atmospheric reorganization is responsible for the major change in

element concentrations through a southward shift of the polar front, leading to a variation in the westerly jet path and strength over East Asia, increasing dust transport to Greenland from different sources. This is confirmed by our Fe/Al and Mg/Al data that demonstrate a two-fold change in dust source between stadial and interstadial conditions, corroborating the idea that atmospheric circulation varies abruptly across warm to cold transitions and vice versa.

Introduction

The climate of the last glacial cycle was characterized by several strong temperature oscillations known as Dansgaard-Oeschger events (Bond et al., 1993; Dansgaard et al., 1993; NGRIP members 2004). All of the 25 DO events identified from ~120 to 11.5 ka started with an abrupt jump from cold conditions (Greenland Stadial, 'GS') to relatively warm conditions (Greenland Interstadials, 'GI') with a temperature shift that ranges between 5 and 16 °C (Huber et al., 2006). DO events were first recognized in the $\delta^{18}O$ record of Greenland ice (Johnsen et al., 1992) and in sediment cores (Bond et al., 1993; Cortijo et al., 1995; Porter and An, 1995) and in several trace gases footprint in Greenland Ice Sheet Project 2 (GISP2) (Chappellaz et al., 1993), Greenland Ice Core Project (GRIP) (Brook et al., 1996) and North Greenland Ice Core Project (NGRIP) (Fluckinger et al., 2004). Evidence for similar climate variability has been found also in terrestrial and marine records at different latitudes (Voelker et al., 2002), demonstrating that DO events happened at least on a hemispheric scale (Clement & Peterson, 2008). Clear examples include sea surface temperatures from sediments off Portugal (Shackleton et al., 2000), from sediments in the Alboran sea (Cacho et al., 1999), in bioturbations from the sediments in the Santa Barbara basin off California (Behl and Kennet, 1996) and in oxygen isotope record from speleothems in the Wulu cave in China (Duan et al., 2014), and in the Austrian Alps (Spötl and Mangini, 2002). Starting from cold stadial conditions, the pattern of a DO event is always marked by a sudden increase in temperature which can happen in only a few years (Steffensen et al., 2008), and a following gentler decrease that can last several hundreds of years

before more abruptly going back to stadial conditions with a rapid jump towards lower temperatures (Schulz 2002; Barker et al., 2015). Stadial conditions are then maintained for hundreds to thousands of years (Andersen et al., 2006; Vallelonga et al., 2012). During these cold phases, the deposition of dust in Greenland ice increases significantly together with the sea salt content, due to a reorganization of the atmospheric circulation and a change in source areas which intensifies the transport of aerosol particles and dust towards the polar regions (De Angelis et al., 1997; Fuhrer et al., 1999; NGRIP members, 2004). Among others, Ca, Al and Fe are useful proxies for dust as well as Na and seasalt-Mg (ssMg) are for sea salt (Thomas et al., 2009). On a short timescale, these elements present an annual peak that corresponds to spring/summer time for dust and wintertime for sea salt, where concentration can increase more than an order of magnitude. On a longer timescale, concentrations of these elements rise during cold period as a result of an increase in the frequency of storms and aridity. In Greenland, geochemical fingerprints of dust show that particles are mostly coming from Asian deserts (Svensson et al., 2000), whereas sea salt proxies derive form bubble bursting over the North Atlantic ocean waters (Abram et al., 2013).

DO events also have clear counterparts in Antarctic ice (Antarctic Istopic Maxima), even if the records of the two hemispheres are phase-shifted by a few millennia (Jouzel et al., 1995; Blunier et al., 1998; Blunier and Brook, 2001). In fact, while Greenland experiences a stadial phase, in Antarctica temperatures slowly rise and subsequently decrease when Greenland enters abruptly into an interstadial phase. Although the shape of Antarctic and Greenland events is considerably different, recent studies (EPICA Community Members, 2006) show that (almost) all of the 25 DO events in Greenland possess a counterpart in the Antarctic record.

This antiphase relationship is commonly explained with changes in the Thermohaline Circulation (THC) and in particular with a weakening or a change of location of convection of the Atlantic Meridional Overturning Circulation (AMOC), which is responsible for the transport of heat polewards (Gong et al., 2013). In order to explain the DO event evolution in the two

hemispheres, Stocker and Johnsen (2003) developed the theory of the 'thermal bipolar seesaw', based on a model firstly proposed by Broecker (1998), which hypothesized that the Atlantic functioned as a seesaw: while the North was warming the South had to cool. In their model, Stocker and Johnsen (2003) add a heat reservoir (Southern Ocean) that, due to thermal inertia, introduces a lagged response between the two hemispheres during warming/cooling events.

Although some data and simulations show that the AMOC was likely altered during the last glaciation (Lynch-Stieglitz et al., 2007; Sarnthein et al., 2000; Thornalley et al., 2013), there is still limited evidence that the thermohaline circulation was responsible for the causing of all the DO events (Gherardi et al., 2005). Moreover, recent studies demonstrated that a strong and deep AMOC persisted through the entire glacial cycle with only few reductions that seem to coincide more with Heinrich events than DO events (Böhm et al., 2015).

It is therefore clear that high resolution temporal data are required to unravel the ocean-atmosphere interaction that drives climatic changes within the last glacial period. Greenland ice core contain several proxies that represent different inputs from the North Atlantic ocean-atmosphere system at extremely high resolution. The phasing of these different signals is thus important to determine the dynamics and mechanisms during the very first part of the onset and the termination of abrupt climate changes. Thomas et al. (2009) demonstrated that, during DO event 8 (38.22-35.48 ka), Ca^{2+} and Na^{+} lead the temperature changes, as was previously observed in Greenland ice cores during the Bølling-Allerød (Steffensen et al., 2008). However, it is not clear if dust proxies complete their transition to pre-warming values in phase with $\delta^{18}O$, since evidence suggests that the phasing may be variable between different DO events, in particular between the recent DO cycles and the older ones (Steffensen et al., 2008).

To answer such questions, we investigated the transitions between GI22 and GS22 (87.60 ± 0.06 ka) and GS22 to GI21 (84.76 ± 0.02 ka), analysing simultaneously Na, Mg, Al, Ca, and Fe via UV-LA-ICPMS (Ultraviolet laser

ablation Inductively Coupled Plasma Mass Spectrometry) at a spatial resolution of <200 µm (i.e. bimonthly resolution at this depth), compared to existing high-resolution data for $\delta^{18}O$ (5 cm) and insoluble dust (1 mm) for the same ice core (Vallelonga et al., 2012). GS22 shows an oscillation of about 5.5 ‰ $\delta^{18}O$ (Fig. 1), which corresponds to a temperature shift of approximately 5 °C over Greenland, according to the recently established $\delta^{18}O$-ΔT direct relationship of 1.1‰ /°C (Masson-Delmotte et al., 2015). The need of a high resolution dataset is also related to the fact that the uncertainty in annual layer counting for ice cores at this depth leads to a different chronology for GS22 in different records (Wolff et al., 2010; Capron et al., 2010; Boch et al., 2011). Based on high resolution CFA analysis Vallelonga et al., (2012) propose a duration of 2894±198 yrs, which was also adopted in Rasmussen et al. (2014), where the GS22 age has been established between 87.60 and 84.76 ka. To further clarify the depth (and therefore age) interval of GS22 our data aim to pinpoint GS22 start and termination, the relationship between different atmospheric proxies (dust and sea salt) at sub-annual resolution, possible source variation, their sensitivity to warming/cooling events, their periodicity on short time-scales and their suitability for inter DO-events comparison.

Methodology

We analysed NGRIP samples directly in frozen state with cryo-cell UV-LA-ICPMS at Royal Holloway University of London. The setup and instrumentation is extensively described in Della Lunga et al. (2014 and 2015, in preparation), as well as sample cutting and location of sub-samples within the ice core cross-section. Thus, only a brief summary is given herein. Figure 1 shows in light orange the depth range of the ice core samples we analysed in the present study compared with $\delta^{18}O$ profile. Two sections have been sampled and analysed:

1. GI22-GS22 transition, 340 cm from depth 2716.80 m to 2120.20 m.
2. GS22-GI21 transition, 355 cm from depth 2685.00 to 2688.55 m.

Sample preparation included smoothing of the surface by a 'metal-free' Y-doped ZrO_2 blade to remove 0.5 mm of ice which reduced contamination from cutting and surface roughness, facilitating the homogeneity of the ablation process. Data acquisition was performed using a series of longitudinal laser tracks with 212 µm spot size, 20 Hz repetition rate at 3 mm/min speed. All the acquisition tracks were pre-cleaned using a series of three consecutive laser passages at 280 µm spot size, 25 Hz repetition rate and 8 mm/min speed to further reduce contamination from ambient air and sample handling/loading. Data were subsequently corrected for instrumental drift and sea salt contribution and calibrated as in Della Lunga et al. (2015, in preparation).

We used an Agilent 7500cs ICPMS in reaction mode to acquire several isotopic mass/charge ratios including: 23(Na), 24(Mg), 27(Al), 34(S), 39(K), 40(Ca), 44(Ca), 55(Mn), 56(Fe), 65(Cu), 85(Rb), 88(Sr), 89(Y), 138(Ba), 139(La), 140(Ce), 141(Pr), 147(Sm), 153(Eu), 157(Gd), 172(Yb), 208(Pb), with dwell times ranging from 5 to 40 ms (see Della Lunga et al., 2014). We monitored Yttrium (mass: 89) and higher masses to assess possible contamination from the surface smoothing process (which utilizes a Y-doped zirconia blade) and other handling procedures. Among the masses acquired, only the following usually show resolvable signal/background ratio and will be displayed as results: 23(Na), 24(Mg), 27(Al), 40(Ca), 55 (Mn), 56(Fe). Mass 39(K) presents resolvable signal/background ratio but has a possible significant interference of ^{38}ArH and therefore it will not be displayed either. Limit of detection are specified in Della Lunga et al (2015, in preparation). All the isotopes acquired have been converted to elements according to their isotopic abundance following Berglund and Wieser (2011). Conversion from net-counts per second (cps) to concentrations (ppb) follows the calibration strategy described in Della Lunga et al. (2015, in preparation).

Results

Not-sea-salt-Ca (nssCa) and Al are usually considered the best proxies for continental dust, followed by Fe. Na and sea-salt-Mg (ssMg; for conversion

from Ca to nssCa and from Mg to ssMg see Della Lunga et al., 2015) are instead good proxies for sea salt input into glacial ice. All results are shown in Fig. 2-10. Figure 2 and 3 show LA-ICPMS elemental concentrations across GI22-GS22 cooling transition compared to CFA insoluble dust (size >1 μm) at 1 mm resolution and $\delta^{18}O$ at 5 cm resolution from Vallelonga et al. (2012). Similarly, the same comparison for GS22-GI21 warming transition is illustrated in Fig. 4. Figure 5 shows a zoom over 10 and 20 centimetres of ice core where most of the jump in concentrations is observed for GS22-GI21 and GI22-GS22 respectively. Furthermore, Fig. 5 shows an example of annual layer counting performed using both elemental concentration from UV-LA-ICPMS analysis and CFA insoluble dust profile, while Fig. 6 shows the anatomy of a single annual peak in LA-ICPMS dust proxies compared to CFA insoluble dust record. Corresponding Ca/Al, Fe/Al and Mg/Al ratios for each transition (Fig. 7 and 8) have been used to track possible sources of dust among Asian deserts (e.g. Zhang et al., 2014). In this case Ca and Mg data are total-Mg and total-Ca respectively.

Finally we present Fast Fourier Transform data (Fig. 9 and Fig. 10) performed on both transitions for Mg and Ca, to unravel possible periodicity hidden in the dataset. Data for Na have been down-sampled by a factor of 10 since the record was more sporadic, with several gaps where no data was acquired due to the unavoidably high ICPMS background. In sections were Na was below our LOD (see Della Lunga et al., 2015, in preparation), we modelled Na level based on ssMg record and ssMg/Na ratio inferred from other section where Na was resolvable.

Elemental Concentrations

The cooling transition between interstadial 22 and stadial 22 is well represented in dust and sea salt proxies (Fig.2). All elements show, from higher to lower depths, a noticeable increase in concentrations, which is on average around an order of magnitude. Al and nssCa present the highest intensities up to few hundreds of ppb, whereas the lowest concentrations are shown by ssMg. Although the record clearly shows a pronounced increase, it is hard to pinpoint exactly at what depth stadial conditions begin. We observed that the record shift between complete ‘interstadial’ values, i.e. tens

of ppb for most elements, to ‘stadial’ values, i.e. hundreds of ppb for most elements (similar to what published for GS22, see Vallelonga et al., 2012) within depths 2718.15 and 2717.30 m. The beginning of this section is marked by a noticeable spike in all element profiles (especially Fe, nssCa and ssMg) where concentrations increase of approximately two orders of magnitude. The record then seems to show several consecutive oscillations modulated over a general increasing trend towards lower depths. Figure 3 illustrates a zoom of 110 cm across these oscillations for Al, ssMg, nssCa and Fe, clearly showing very pronounced jumps in concentrations of about one order of magnitude up and down across few centimetres, maintaining an increasing trend. We distinguish two major abrupt rises in concentrations for all the elements at 2717.70 and 2717.32 m. The amplitude of each oscillation is similar to the amplitude of stadial/interstadial concentration drop. CFA dust profile shows a similar pattern, having two major jumps in concentrations going towards lower depths, respectively 2717.60 and 2717.30 m. Furthermore, we observe that the point that marks a change in the frequency of dusty layers in the CFA dust profile can be located at a depth of 2718.10, in good agreement with LA-ICPMS profiles. From this point towards shallower depths, the amplitude of the oscillations in concentration between adjacent layers increases in both CFA and LA-ICPMS profiles.

$\delta^{18}O$ profile shows a decreasing trend from the depth of 2718.60 m, having, however, oscillations of ± 2 ‰ on the scale of 15 cm. A direct comparison of this proxy to LA-ICPMS data is difficult, since the two dataset have considerably different resolution (5 cm and <200 µm respectively). Therefore, it is hard to establish whether $\delta^{18}O$ or dust proxies show the earliest prodromes of stadial conditions.

Similarly, the warming transition between GS22 and GI21 presents a drop in concentration of about one order of magnitude in all elements (Fig. 4). It is a sharp and abrupt variation that seems to happen over the space of less than a single cm (<1 yr). Defining an exact depth is in this case more straightforward, as concentrations clearly drop within depths of 2687.44 and 2687.42 m. The variations also have slightly stronger amplitude if we compare interstadial 22 and interstadial 21 values, which usually are in the

range of few ppb up to few tens of ppb, whereas in this case they can reach several tens of ppb. The onset of the warming phase is preceded by a peak in concentration just before the drop, especially visible in Al, nssCa and Fe, in good agreement with CFA dust profile, which also clearly shows a major peak. This is observable also in Fig. 5, which shows a comparison of two different zooms of 10 and 20 cm across GS22-GI21 and GI22-GS22 transitions respectively. In the left panel we can observe in detail the abruptness of the change in concentrations and the variation in frequency of dusty layers starting at 2687.43 m. Annual layer counting based on both CFA dust and nssCa profiles results in both cases in 9 annual layers of various thickness (7-18 mm). A similar thickness range is also observed in annual layering counting for a short section of ice core across GI22-GS22 transition (Fig. 5, right panel). In this 20 cm section we identified 15 annual layers based on CFA dust profile and 19 based on LA-ICPMS Al, for an average thickness of 11.5 ±1.5 mm. Overall, CFA dust profile and LA-ICPMS elemental profiles show a good agreement at both small and large scale (Fig 3, 4 and 5). The structure of a single annual peak is illustrated in Figure 6, which shows a zoom on a section of just 2 cm. Elemental profiles clearly show that, in this case, a single annual peak can be divided in at least three major peaks which contribute to most of the seasonal signal.

Elemental ratios

Ratios of Ca/Al, Fe/Al and Mg/Al across the GI22-GS22 transition present a record that is divided in two parts: from depth 2716.80 to 2717.96 m the average value are 1.05 ± 0.2 for Ca/Al, 0.30 ± 0.08 for Fe/Al and 0.25 ± 0.07 for Mg/Al, whereas from depth 2717.96 to 2720.20 m average values are 1.64 ± 0.25, 0.48 ± 0.1 and 0.45 ±0.09 for Ca/Al, Fe/Al and Mg/Al respectively (Fig. 7) representing an increase of 60-90 %. However, the ratios are very variable also at smaller scale showing abrupt variations in as short as three cm (Fig. 7). We observe that the major shift in ratio takes place within the depth range where the increase in CFA dust and LA-ICPMS profiles occurs (cfr Fig 2 and 7).

GS22-GI21 transition (Fig. 8) shows a similar pattern: at greater depths (2688.55-2687.60 m) Ca/Al, Fe/Al and Mg/Al values are low as averages are 1.15 ± 0.21, 0.30 ± 0.08 and 0.18 ± 0.04 respectively. Towards lower depths (2687.60- 2685.00 m) the values suddenly increase of 90-120 %, showing average values of 1.90 ± 0.31, 0.75 ± 0.19 and 0.45 ± 0.15 for Ca/Al, Fe/Al and Mg/Al respectively. The major shift in this case occurs at a depth of 2687.60 ± 0.2 m and is fairly synchronous with the drop in concentration we observe at the onset of GI21 in CFA and LA-ICPMS data (Fig. 4).

Spectral analysis

We applied FFT (Fast Fourier Transform) analysis to Ca and Mg concentration profiles for both GI22-GS22 and GS22-GI21 transitions, as these two proxies represent 'dust' and 'sea salt' input respectively, and show the most complete dataset with very few gaps in the record. The power spectra (Fig. 9 and 10) are placed on a floating time scale as the record was converted from depth domain to time domain based on the layer thickness (λ) data by Vallelonga et al. (2012). Solid grey lines represent the 95% confidence level of simulated power spectra of random noise with analogous amplitude.

Both Mg and Ca spectra for GI22-GS22 transition present three major cycles (Fig. 9). One approximately coincides with a yearly frequency while another one seems to indicate a frequency between two and three times per year. The longer cycle coincides with multi-decadal period of about 25 years. Similar periodicities are found in the power spectra for the GS22-GI21 transition. The yearly cycle is still represented, as well as two major cycles at low frequency, coinciding with periods of about five and ten years. In this case, the spectra do not anymore show resolvable peaks at high frequencies, representing the 4-5 months periodicity.

Discussion

All element concentrations record a major shift from low to high concentrations between interstadial and stadial phase, and vice versa. For

319 the cold GS22-GI21 event we established a transition interval between
320 2687.44 and 2687.43 m, over the space of just 1 cm. Since the layer
321 thickness at this depth is between 11 and 12 mm (Vallelonga et al., 2012),
322 this range corresponds to a time interval of a single year, during which we
323 observed a complete and sustained switch between stadial to interstadial
324 conditions. This confirms previous high-resolution observations in younger
325 and more shallow NGRIP ice which showed that abrupt climate change
326 (ACC) can happen as rapid as a few years (Steffensen et al., 2008;
327 Fluckinger, 2008, Thomas et al., 2009) and extends this finding to deeper ice
328 at NGRIP (~ 85 ka), in agreement with previous findings at GRIP for DO
329 event transitions at various depths (Fuhrer et al., 1999). Our GS22-GI21
330 transition depth agrees fairly well with the starting point of GI-21 (GI-21e) in
331 Rasmussen et al. (2014), which has been established at a depth of 2687.29
332 m, based on $\delta^{18}O$ and other proxies.

333 On the other hand, it is more difficult to establish if the GI22-GS22 transition
334 presents a clear shift in concentrations that can be pinpointed as the start of
335 GS22. This is because all the elements present a rather smooth and gradual
336 increase in concentration which mirrors the $\delta^{18}O$ record. We established,
337 however, an interval between depths 2718.10 and 2717.20 where most of the
338 shift occurs. This is compatible with previous findings about GSS starting
339 point, which was located at 2718.00 m (Vallelonga et al., 2012) and suggests
340 that continental ions (Ca, Al, Fe) precede the change in Greenland
341 temperature by five-ten years, since the start of stadial 22, as defined by
342 Rasmussen et al. (2014) based on $\delta^{18}O$, is at 2717.11 m.

343 These findings confirm that DO event 22 starts with a rapid warming followed
344 by a more gradual cooling, as it has generally been observed in most
345 Greenland DO events (Alley, 2000).

346 ***Phasing in the impurity record***

347 Our data suggest that dust and sea salt proxies appear to complete the
348 stadial-interstadial switch (and vice versa) earlier and more clearly than $\delta^{18}O$,
349 similarly to what was observed in other high resolution analysis of DO events
350 (Steffensen et al., 2008; Thomas et al., 2009). Although it is difficult to

quantify the lag between dust and oxygen response to warming/cooling transitions, we notice that maxima in dust proxies precede $\delta^{18}O$ minima of about 5-10 years, given the layer thickness at this depth. This may indicate that alteration of the atmospheric circulation preceded also the temperature change and therefore it was not caused by it, despite the trigger of these two variations seems to be synchronous. This agrees with previous investigations about interstadial-stadial transitions where it was observed that, for instance in the GS4-GI3 transition (around 27.78 ka), the Ca change occurred in two discrete steps lasting overall less than 10 cm (2-3 yrs) while the $\delta^{18}O$ rise was completed over approximately a meter of ice (40 yrs), even if the beginning of the shift of the two proxies was synchronous (Fuhrer et al., 1999). The discrepancy in these two proxies could have been enhanced by isotope diffusion which tends to dampen oxygen signal, especially in deep ice where layer thickness is below 6 cm (Rasmussen et al., 2006). However, this effect is partially compensated by high accumulation rates as in the case of NGRIP (Vallelonga et al., 2012).

Fuhrer et al. (1999) also demonstrate that coolings occur more gradually: in the GI5-GS5 transition for example (around 32.04 ka), the Ca increase takes a total of 4 m (150 yrs) to complete the transition, similarly to what we can observe for $\delta^{18}O$ for GI22-GS22. However, also in this transition, two distinct steps where most of the rise occurs can be identified, each one lasting between 10 and 15 years. These considerations can be extended to our dataset for GI22-GS22 transition where we observe two different steps: taking nssCa as reference in this case, we pinpoint these two steps at 2718.10 and 2717.70 m (Fig. 2 and 3), each one occurring over few cm (2-8 years). This suggests that nssCa is actually a more distinct indicator of switches in the climate states than $\delta^{18}O$, as proposed earlier (Marsh and Ditlevsen, 1997). In fact, it has been established that Ca and $\delta^{18}O$ are correlated so that 10% shift in Ca corresponds to 1‰ change in $\delta^{18}O$, making Ca a more suitable piece of evidence for abrupt climate changes, especially because it shows much less intra-stadial variability and especially much lower diffusion than $\delta^{18}O$, making easier to establish the exact moment of the warming/cooling events (Fuhrer et al., 1999). However, considering the GI22-

GS22 transition in detail (Fig. 3) we can observe that the magnitude of the oscillations of nssCa, Al, ssMg and Fe immediately before and after the transition point remain similar for a few decades, even if average values change significantly by about one order of magnitude. This may reflect a transient stage where the mechanism that governs dust and sea salt supply switches from one state to another, producing abrupt jumps in concentration before full stadial conditions are established. This pattern has been previously observed in Electrical Conductivity Measurements (ECM) across interstadial/stadial transitions at GISP2, where frequent, brief (10-20 yrs) and abruptly terminating periods (less than 5 yrs), during which values return to pre-transition level, were identified (Taylor et al., 1993). However, this 'flickering switch' may be an artefact due to non-linear responses of ECM as ice approaches acid/base neutrality (Barker et al., 2005). Nevertheless, a flickering behaviour has been observed at the onset of Holocene in several proxies from sediment cores (Lehman et al., 1992; Bakke et al., 2009) and speleothems (Baldini et al., 2015). In particular, Baldini et al. (2015) measured annually-resolved sea-spray-Mg from a speleothem located on the west coast of Spain, identifying a flickering of the signal across YD and Holocene likely related to a variation in strength of the westerlies at mid-latitudes.

For the GS22-GI21 transition, this pattern is less pronounced (Fig. 4 and 5). In fact, with the drop of elemental concentrations to interstadial conditions, the amplitude of annual and multi-annual oscillations decreases proportionally.

Annual layer counting (Fig. 5) derived from UV-La-ICPMS data show that average thickness of yearly layers is around 11.5 ± 1.5 mm, which is compatible with values presented in other studies for GS22 at NGRIP (Vallelonga et al., 2012). In our data, however, sub-annual variability (Fig. 6) is often observed, with period and amplitude of the oscillations that are similar to the annual pattern. This may represent the contribution of particularly intense events within the storm season.

Sources

Ca/Al, Fe/Al and Mg/Al ratios (Fig 7 and 8) show a significant shift across both transitions, decreasing from interstadial to stadial conditions and vice versa. These proxies can be used to distinguish sources of Greenland dust, which usually are identified within an area that comprises mid-Asian deserts and in particular Chinese deserts (Biscaye et al., 1997, Svensson et al., 2000). Within these regions, Zhang et al. (1996; 2014) and Cao et al. (2008) distinguish three different sources: northwestern (Ca/Al: 1.90, Fe/Al: 0.74, Mg/Al: 0.38) northern (Fe/Al: 0.39, Mg/Al: 0.17) and northeastern (Ca/Al: 1.17, Fe/Al: 0.44, Mg/Al: 0.20). In this view, our data (Fig. 7 and 8) are compatible with a change in source from interstadial to stadial conditions, from north/northwest dominated to more northeastern dominated sources. It has been observed that the most prominent reservoir of dust deposited on the Greenland ice sheet is the Taklamakan desert (Prospero et al., 2002; Bory et al., 2014) which lies in the westernmost part of China, and is comprised within a large topographical depression called the Tarim basin. Owing to the elevated mountain ranges surrounding the basin (Pamir, Tian Shan), the Taklamakan dust must be uplifted to elevations >5000 m to escape the basin, whereas dust from the Gobi and Northern Chinese deserts is generally transported below 3000 m (Bory et al., 2014). This is consistent with models that show an intensification of the northwesterly winds over Greenland during stadials, with a jet stream divided in two branches by the effect of a blocking anticyclone over the Laurentide ice sheet (Bromwich et al., 2004). Moreover, studies of particle size distribution in Chinese loess deposits (Ruth et al., 2003) estimated that the transit time of particles during stadials was 25 % shorter than during interstadials, implying a strengthening of the atmospheric circulation. Therefore, during stadial conditions, an intensification of atmospheric circulation would allow the uplift of more, larger, particles, with significant contribution also from other sources such as Gobi or Eastern Asian deserts, resulting in a relative decrease of Ca/Al, Fe/Al and Mg/Al values (Fig. 7 and 8). Conversely, during interstadials, the westerlies reduce their strength following a northward shift of the polar front. Indeed, this mechanism has been recently proposed to explain the reduction of

concentration of dust deposited in Tibetan ice cores during the second half of the 20th century (Grigholm et al., 2015).

Furthermore, it has been observed that sizes of particles in Greenland dust are 25% larger in GS22 than in the adjacent interstadial periods (Steffensen 1997; Ruth et al., 2003), suggesting that the transporting wind speed during cold periods was 20-50% higher than in interstadials. These findings also agree with GCMs (Global Circulation Models; e.g Fawcett et al., 1997), which demonstrate that size and quantity of long-range transported particles can significantly increase when wind speed overtake a threshold value for dust mobilization and uplift (Gillette and Passi, 1988).

Comparing the stalagmite $\delta^{18}O$ record from Wulu cave with NGRIP $\delta^{18}O$ record, Wang et al (2001) and Duan et al. (2014) observed pronounced East Asian Monsoons (EAMs) during Greenland Interstadials. The rapid drop of concentrations of continental ions across GS22-GI22 transition could be therefore related to an intensification of the EAM which would reduce the dust mobility at the source as conditions shift from dry to wet at a speed that is consistent with speleothems records from the Indian Ocean during DO 12 (Burns et al., 2003). On the other hand, the transition from interstadial to stadial (as GI22-GS22) would correspond to a weakening of EAM and therefore drier conditions which would favour dust mobility and uplift and result in higher concentration in ice cores (Fig. 2 and 3). The EAM variability can also account for the possible source differentiation we observed from stadial to interstadial conditions and vice versa, as it would lead to a periodic jump of the main wind paths across the Himalayan-Tibetan-plateau which would favour or reduce the uplift from the Tarim basin in stadial and interstadial conditions respectively (Nagashima et al., 2011; Grigholm et al., 2015).

Thomas et al. (2009) also observed that the drop in marine species in Greenland ice cores (Cl^- and SO_4^{2-}) from stadial to interstadial levels occurs slightly after the decrease in continental ions concentrations, which supports the thesis that source changes rather than circulation changes in the first place cause the drop of dust and sea salt proxies, otherwise dust and sea

salt decrease should be synchronous. This is also confirmed by high resolution measurements of deuterium excess (d= δD- 8δ^{18}O; Dansgaard 1964) in NGRIP ice cores (Steffensen et al., 2008; Thomas et al., 2009), which represents sea surface temperatures (SSTs) and sea surface humidity at the initial evaporation site (Petit et al., 1991). In fact, during the warming phase of DO events 8 and 1, deuterium excess presents a rapid decrease (in antiphase with δD and δ^{18}O), most of which occurs in a single step that lasts approximately one year and usually precedes the δ^{18}O rise (Thomas et al., 2009).

This is compatible with a shift in the NGRIP moisture source. Generally, it is thought that stadial-interstadial changes are driven by a modification of the strength or location of formation of the Atlantic Meridional Overturning Circulation (AMOC) (Lynch-Stieglitz et al., 2007). In fact, during interstadials, the circulation in the North Atlantic is considered to be similar to the present one (Van Meerbeeck et al., 2011), with warm surface water flowing north into the Nordic Sea and sinking as deep water (NADW). This flow is then reduced when stadial conditions start to take over, and the site of NADW formation migrates south (Sarnthein et al., 2000; Ganopolski & Rahmstorf, 2001; Shin et al., 2003). As a consequence, sea ice expands over a greater area of the North Atlantic ocean, and causes the polar front to migrate south, together with the NGRIP moisture source, while evaporation site still remains within warmer and subtropical areas (Masson-Delmotte et al., 2005).

Although evidence of a weakening of the AMOC coinciding with stadial periods in the North Hemisphere is strong and numerous (Dokken & Jansen, 1999; Kissel et al., 2008; Barker et al., 2009; Thornalley et al., 2011, 2013, Van Meerbeeck et al., 2011; Zhang et al., 2014), it is not clear whether a considerable reduction of the overturning rate characterized all Greenland DO events, as it seems to be related more to Heinrich events (Bradtmiller et al., 2014; Bohm et al., 2015). Furthermore, recently, Landais et al., (2015) suggested that for long stadials, as GS22, the conceptual bipolar seesaw model does not account for the timing and pattern of proxies' variations in several Greenland ice cores, concluding that Greenland climate might have been partially decoupled from the North Atlantic climate system.

513 ***Cyclicity***

514 Our data for both transitions seem to be dominated by few components that
515 correspond approximately to 4-5 months, 1, 5, 10 and 25 years (Fig 9 and
516 10). The yearly cycle is expected as annual layer counting is usually based
517 on ions spring/summer peak (e.g. for Ca^{2+}) or winter peak (Na^{+}) (Svensson et
518 al., 2011). This component has been identified before in Holocene and
519 Eemian ice in similar power spectra performed over few meters of ice cores
520 (Svensson et al., 2011). Our data for layer counting also show that these
521 peaks can be identified at annual and sub-annual level (Fig. 6) and represent
522 a component that is ascribable to storm seasons transporting dust to the
523 Greenland ice caps once per year.

524 On the other hand, it is very hard to clearly link the seasonal variations we
525 observed at a pace of 4-5 months to a single phenomenon, as many possible
526 mechanisms exist. The fact that our 4-5 months periodicity is conserved in
527 both Ca and Mg for warm/cool transition and vice versa, suggests that these
528 oscillations represent a climatic signal possibly related to rainfall oscillations
529 that can affect the dust mobilization and uplift in source regions, possibly
530 triggered by changes in atmospheric patterns within a year as in the North
531 Atlantic Oscillation (NAO) index which has often been associated with
532 temperature oscillations recorded in Greenland ice cores or sediments
533 (Appenzeller et al., 1998; Olsen et al., 2012). NAO index oscillations show
534 also strong peaks in the power spectra at multi-annual frequencies of 2, 5,
535 10, 25, 41 years (Olsen et al., 2012). Interestingly, this is compatible with the
536 low frequency peaks we observe for Ca and Mg across GS22-GI21 and
537 GS22-GI21 transitions, which correspond to 5, 10 and 25 years.

538 Another possible mechanism that could account for the observed variability is
539 again the oscillation in the East Asian Monsoon (EAM) , which has been
540 associated to many decadal to multi-decadal variability observed in several
541 palaeo-environmental archives such as speleothems (Wang et al., 2001;
542 Fleitmann et al., 2003), and ice cores (Joswiak et al., 2010, Grigholm et al.,
543 2015). Evidence suggests that oscillations of the EAM recorded in
544 speleothems are related to tropical rainfall variability which acts at an annual

to sub-annual level (Fairchild et al., 2001; Treble et al., 2003). Nevertheless, our records cover approximately 300 years each, therefore caution must be applied in the interpretation of these periodicities, which would need further confirmations, especially regarding the low frequency cycles given that our two records possibly include a small number of them (<15).

However, we can observe that NGRIP deep ice seems to conserve annual and sub-annual periodicity even at great depth (2685-2720 m, ~360 m above bedrock at NGRIP), meaning that diffusion of the signal or rotation and recrystallization of the ice grains do not affect the palaeo-climatic signal at this depth even if they might play a role in dampening some of the signal at high frequencies in both transitions (see Chapter 6; Svensson et al., 2011).

Conclusions

We successfully applied UV-LA-ICPMS to NGRIP ice cores to evaluate the speed and the extent of dust and sea salt proxies changes across interstadial to stadial 22 transition and vice versa, producing the highest-resolution record of continental (nssCa, Al, Fe) and marine (Na, ssMg) ions ever acquired for DO events in an ice core. Our major findings include:

- Elemental profiles support the thesis that dust and sea salt proxies react to interstadial/stadial transitions more rapidly than $\delta^{18}O$ and result in a drop/rise of about an order of magnitude in concentrations. For warming events the transition is abrupt, taking place over the space of 1 cm, which represents less than 1 yr of accumulation.
  For cooling events, the transition is smoother, even if most of the variation is provided by few small jumps in concentrations that occur within the interval where we observe a complete $\delta^{18}O$ switch from interstadial to stadial conditions.
- Ca/Al, Fe/Al and Mg/Al ratios confirm that an abrupt change of source for Greenland dust is observed across DO events transitions, although the region of provenance is it still likely to be located within the Asian deserts. We suggest that this change is probably related to a strengthening of the atmospheric circulation during stadials due to a

southward shift of the polar front and a long-term weakening of monsoon circulation patterns.

- Power spectra for Ca and Mg shows that NGRIP deep ice preserves an annual to sub-annual cyclicity in the dust input, opening the possibility to further investigate the short-term dynamics of atmosphere reorganization during the oldest DO events.

Acknowledgments

This work has been supported by RHUL studentship granted to Damiano Della Lunga and a Resolution/Laurin Technic grant by Wolfgang Müller. The Authors would like to thank Jerry Morris (RHUL) for technical support and Michael Kriews and Dorothee Wilhelms-Dick for helpful advice.

References

Abram, N. J., Wolff, E. W., and Curran, M. A. (2013). A review of sea ice proxy information from polar ice cores. *Quaternary Science Reviews*, **79**, 168-183.

Andersen, K. K., Svensson, A., Johnsen, S. J., Rasmussen, S. O., Bigler, M., Rothlisberger, R., Ruth U., Siggard-Andersen M. L., Steffensen J. P., Dahl-Jensen D., Vinther B. M., Clausen H. B. (2006). The Greenland ice core chronology 2005, 15-42 ka. part 1: Constructing the time scale. *Quaternary Science Reviews*, **25**(23-24), 3246-3257.

Alley, R. B. (2000). Ice-core evidence of abrupt climate changes. *Proceedings of the National Academy of Sciences*, **97**(4), 1331-1334.

Appenzeller, C., Stocker, T. F., and Anklin, M. (1998). North Atlantic oscillation dynamics recorded in Greenland ice cores. *Science*, **282**(5388), 446-449.

Bakke, J., Lie, Ø., Heegaard, E., Dokken, T., Haug, G. H., Birks, H. H., Dulski P., and Nilsen, T. (2009). Rapid oceanic and atmospheric changes

606 during the Younger Dryas cold period. *Nature Geoscience*, **2**(3), 202-
607 205.

608 Baldini, L. M., McDermott, F., Baldini, J. U., Arias, P., Cueto, M., Fairchild, I.
609 J.,. Hoffmannf D. L, Mattey D.P., Müller W., Nitaf D.C., Ontañónd R.,
610 Garciá-Moncód C. & Richards, D. A. (2015). Regional temperature,
611 atmospheric circulation, and sea-ice variability within the Younger
612 Dryas Event constrained using a speleothem from northern Iberia.
613 *Earth and Planetary Science Letters*, **419**, 101-110.

614 Barker, S. (2005). The 'flickering switch'of late Pleistocene climate change
615 revisited. *Geophysical research letters*, **32**(24).

616 Barker, S., Diz, P., Vautravers, M. J., Pike, J., Knorr, G., Hall, I. R., and
617 Broecker, W. S. (2009). Interhemispheric Atlantic seesaw response
618 during the last deglaciation. *Nature*, **457**(7233), 1097-1102.

619 Barker, S., Chen, J., Gong, X., Jonkers, L., Knorr, G., & Thornalley, D.
620 (2015). Icebergs not the trigger for North Atlantic cold events. *Nature*,
621 **520**(7547), 333-336.

622 Behl, R. J., and Kennett, J. P. (1996). Brief interstadial events in the Santa
623 Barbara basin, NE Pacific, during the past 60 kyr. *Nature*, **379**(6562),
624 243-246.

625 Berglund, M., and Wieser, M. E. (2011). Isotopic compositions of the
626 elements 2009 (IUPAC technical report). *Pure and Applied Chemistry*,
627 **83**(2), 397-410.

628 Biscaye, P. E., Grousset, F. E., Revel, M., VanderGaast, S., Zielinski, G. A.,
629 Vaars, A., and Kukla, G. (1997). Asian provenance of glacial dust
630 (stage 2) in the Greenland ice sheet project 2 ice core, summit,
631 Greenland. *Journal of Geophysical Research-Oceans*, **102**(C12),
632 26765-26781.

633 Blunier, T., & Brook, E. J. (2001). Timing of millennial-scale climate change in
634 Antarctica and Greenland during the last glacial period. *Science*,
635 **291**(5501), 109-112.

636 Blunier, T., Chappellaz, J., Schwander, J., Dallenbach, A., Stauffer, B.,
637 Stocker, T. F., Raynaud D., Jouzel J., Clausen H. B., Hammer C. U.,
638 Johnsen, S. J. (1998). Asynchrony of Antarctic and Greenland climate
639 change during the last glacial period. *Nature*, **394**(6695), 739-743.

640 Boch, R., Cheng, H., Spoetl, C., Edwards, R. L., Wang, X., and
641 Haeuselmann, P. (2011). NALPS: A precisely dated European climate
642 record 120-60 ka. *Climate of the Past*, **7**(4), 1247-1259.

643 Böhm, E., Lippold, J., Gutjahr, M., Frank, M., Blaser, P., Antz, B., Fohlmeister
644 J., Frank N., Andersen M. B. and Deininger, M. (2015). Strong and
645 deep Atlantic meridional overturning circulation during the last glacial
646 cycle. *Nature*, **517**(7532), 73-76.

647 Bond, G., Broecker, W., Johnsen, S., Mcmanus, J., Labeyrie, L., Jouzel, J.,
648 and Bonani, G. (1993). Correlations between climate records from
649 north-Atlantic sediments and Greenland ice. *Nature*, **365**(6442), 143-
650 147.

651 Bory, A. J., Abouchami, W., Galer, S. J. G., Svensson, A., Christensen, J. N.,
652 and Biscaye, P. E. (2014). A Chinese imprint in insoluble pollutants
653 recently deposited in central Greenland as indicated by lead isotopes.
654 *Environmental Science and Technology*, **48**(3), 1451-1457.

655 Bradtmiller, L. I., McManus, J. F., and Robinson, L. F. (2014). $^{231}Pa/^{230}Th$
656 evidence for a weakened but persistent Atlantic meridional overturning
657 circulation during Heinrich Stadial 1. *Nature communications*, **5**. 5817.

658 Broecker, W. S. (1998). Paleocean circulation during the last deglaciation: A
659 bipolar seesaw? *Paleoceanography*, **13**(2), 119-121.

660 Bromwich, D. H., Toracinta, E. R., Wei, H. L., Oglesby, R. J., Fastook, J. L.
661 and Hughes, T. J. (2004). Polar MM5 simulations of the winter climate
662 of the Laurentide ice sheet at the LGM. *Journal of Climate*, **17**(17),
663 3415-3433.

664 Brook, E. J., Sowers, T., and Orchardo, J. (1996). Rapid variations in
665 atmospheric methane concentration during the past 110,000 years.
666 *Science*, **273**(5278), 1087-1091.

667 Burns, S. J., Fleitmann, D., Matter, A., Kramers, J., and Al-Subbary, A. A.
668 (2003). Indian Ocean climate and an absolute chronology over
669 Dansgaard/Oeschger events 9 to 13. *Science*, **301**(5638), 1365-1367.

670 Cacho, I., Grimalt, J. O., Pelejero, C., Canals, M., Sierro, F. J., Flores, J. A.,
671 and Shackleton, N. (1999). Dansgaard-Oeschger and Heinrich event
672 imprints in Alboran sea paleotemperatures. *Paleoceanography*, **14**(6),
673 698-705.

674 Cao, J. J., Chow, J. C., Watson, J. G., Wu, F., Han, Y. M., Jin, Z. D., Shen Z.
675 S. and An, Z. S. (2008). Size-differentiated source profiles for fugitive
676 dust in the Chinese Loess Plateau. *Atmospheric Environment*, **42**(10),
677 2261-2275.

678 Capron, E., Landais, A., Chappellaz, J., Schilt, A., Buiron, D., Dahl-Jensen,
679 D., Johnsen S. J., Jouzel J., Lemiex-Dudon B., Loulergue L.,
680 Leuenberger M., Masson-Delmotte V., Meyer H., Oerter H., Stenni, B.
681 (2010). Millennial and sub-millennial scale climatic variations recorded
682 in polar ice cores over the last glacial period. *Climate of the Past*, **6**(3),
683 345-365.

684 Chappellaz, J., Blunier, T., Raynaud, D., Barnola, J. M., Schwander, J., and
685 Stauffer, B. (1993). Synchronous changes in atmospheric Ch4 and
686 Greenland climate between 40-kyr and 8-kyr bp. *Nature*, **366**(6454),
687 443-445.

688 Clement, A. C., & Peterson, L. C. (2008). Mechanisms of abrupt climate
689 change of the last glacial period. *Reviews of Geophysics*, **46**(4).

690 Cortijo, E., Yiou, P., Labeyrie, L., and Cremer, M. (1995). Sedimentary record
691 of rapid climatic variability in the north-atlantic ocean during the last
692 glacial cycle. *Paleoceanography*, **10**(5), 911-926.

693 Dansgaard, W. (1964). Stable isotopes in precipitation. *Tellus*, **16**(4), 436-
694 468.

695 Dansgaard, W., Johnsen, S. J., Clausen, H. B., Dahljensen, D., Gundestrup,
696 N. S., Hammer, C. U., Hvidberg C. S., Steffensen J. P.,
697 Sveinbjornsdottir A.E., Jouzel J., Bond, G. (1993). Evidence for
698 general instability of past climate from a 250-kyr ice-core record.
699 *Nature*, **364**(6434), 218-220.

700 DeAngelis, M., Steffensen, J. P., Legrand, M., Clausen, H., and Hammer, C.
701 (1997). Primary aerosol (sea salt and soil dust) deposited in
702 Greenland ice during the last climatic cycle: Comparison with east
703 Antarctic records. *Journal of Geophysical Research-Oceans*,
704 **102**(C12), 26681-26698.

705 Della Lunga, D., Mueller, W., Rasmussen, S. O., and Svensson, A. (2014).
706 Location of cation impurities in NGRIP deep ice revealed by cryo-cell
707 UV-laser-ablation ICPMS. *Journal of Glaciology*, **60**(223), 970-988.

708 Della Lunga, D., Müller W., Rasmussen, S. O., Svensson, A., Steffensen,
709 J.P., (2015). Calibrated cryo-cell UV-LA-ICPMS elemental
710 concentrations in NGRIP ice reveal abrupt, sub-annual shift in dust
711 across glacial stadial precursor event GI-21.2. Planned submission to
712 *Journal of Quaternary Science*.

713 Dokken, T. M., & Jansen, E. (1999). Rapid changes in the mechanism of
714 ocean convection during the last glacial period. *Nature*, **401**(6752),
715 458-461.

716 Duan, F., Liu, D., Cheng, H., Wang, X., Wang, Y., Kong, X., and Chen, S.
717 (2014). A high-resolution monsoon record of millennial-scale
718 oscillations during late MIS 3 from Wulu cave, south-west china.
719 *Journal of Quaternary Science*, **29**(1), 83-90.

720 EPICA Community Members. (2006). One-to-one coupling of glacial climate
721 variability in Greenland and Antarctica. *Nature*, **444**(7116), 195-198.

722 Fairchild, I. J., Baker, A., Borsato, A., Frisia, S., Hinton, R. W., McDermott,
723 F., and Tooth, A. F. (2001). Annual to sub-annual resolution of multiple
724 trace-element trends in speleothems. *Journal of the Geological*
725 *Society*, **158**, 831-841.

726 Fleitmann, D., Burns, S. J., Mudelsee, M., Neff, U., Kramers, J., Mangini, A.,
727 and Matter, A. (2003). Holocene forcing of the Indian monsoon
728 recorded in a stalagmite from southern Oman. *Science*, **300**(5626),
729 1737-1739.

730 Fluckiger, J., Blunier, T., Stauffer, B., Chappellaz, J., Spahni, R., Kawamura,
731 K., Schwander J., Stocker T. F., DahlJensen, D. (2004). N2O and CH4
732 variations during the last glacial epoch: Insight into global processes.
733 *Global Biogeochemical Cycles*, **18**(1), GB1020.

734 Fluckiger, J. (2008). Climate change - did you say "fast"? *Science*,
735 **321**(5889), 650-651.

736 Fuhrer, K., Wolff, E. W., and Johnsen, S. J. (1999). Timescales for dust
737 variability in the Greenland ice core project (GRIP) ice core in the last
738 100,000 years. *Journal of Geophysical Research-Atmospheres*,
739 **104**(D24), 31043-31052.

740 Ganopolski, A., & Rahmstorf, S. (2001). Rapid changes of glacial climate
741 simulated in a coupled climate model. *Nature*, **409**(6817), 153-158.

742 Gherardi, J. M., Labeyrie, L., McManus, J. F., Francois, R., Skinner, L. C.,
743 and Cortijo, E. (2005). Evidence from the north-eastern Atlantic basin
744 for variability in the rate of the meridional overturning circulation
745 through the last deglaciation. *Earth and Planetary Science Letters*,
746 **240**(3-4), 710-723.

747 Gillette, D. A., and Passi, R. (1988). Modeling dust emission caused by wind
748 erosion. *Journal of Geophysical Research-Atmospheres*, **93**(D11),
749 14233-14242.

750 Gong, X., Knorr, G., Lohmann, G., & Zhang, X. (2013). Dependence of
751 abrupt Atlantic meridional ocean circulation changes on climate
752 background states. *Geophysical Research Letters*, **40**(14), 3698-3704.

753 Grigholm, B., Mayewski, P. A., Kang, S., Zhang, Y., Morgenstern, U.,
754 Schwikowski, M., Kaspari S., Aizen V., Aizen E., Takeuchi N., Maasch
755 K.A., Birkel S., Handley M. & Sneed, S. (2015). 20th Century Dust
756 Lows and the Weakening of the Westerly Winds over the Tibetan
757 Plateau. *Geophysical Research Letters*. In press.

758 Huber, C., Leuenberger, M., Spahni, R., Fluckiger, J., Schwander, J.,
759 Stocker, T. F., Johnsen S. J., Landais A., Jouzel, J. (2006). Isotope
760 calibrated Greenland temperature record over marine isotope stage 3
761 and its relation to CH4. *Earth and Planetary Science Letters*, **243**(3-4),
762 504-519.

763 Johnsen, S. J., Clausen, H. B., Dansgaard, W., Fuhrer, K., Gundestrup, N.,
764 Hammer, C. U., Iversen P., Jouzel J., Stauffer B., Steffensen, J. P.
765 (1992). Irregular glacial interstadials recorded in a new Greenland ice
766 core. *Nature*, **359**(6393), 311-313.

767 Joswiak, D. R., Yao, T., Wu, G., Xu, B., and Zheng, W. (2010). A 70-yr
768 record of oxygen-18 variability in an ice core from the Tanggula
769 mountains, central Tibetan plateau. *Climate of the Past*, **6**(2), 219-227.

770 Jouzel, J., Vaikmae, R., Petit, J. R., Martin, M., Duclos, Y., Stievenard, M.,
771 Lorius C., Melieres M. A., Burckle L. H., Barkov N. I., Kotlyakov, V. M.
772 (1995). The 2-step shape and timing of the last deglaciation in
773 Antarctica. *Climate Dynamics*, **11**(3), 151-161.

774 Kissel, C., Laj, C., Piotrowski, A. M., Goldstein, S. L., & Hemming, S. R.
775 (2008). Millennial-scale propagation of Atlantic deep waters to the
776 glacial Southern Ocean. *Paleoceanography*, **23**(2).

777 Landais, A., Masson-Delmotte, V., Stenni, B., Selmo, E., Roche, D. M.,
778 Jouzel, J., Lambert F., Guillevic M., Bazin L., Arzel O., Vinther B.,
779 Gkinis V. & Popp, T. (2015). A review of the bipolar see–saw from

780 synchronized and high resolution ice core water stable isotope records
781 from Greenland and East Antarctica. Quaternary Science Reviews,
782 114, 18-32.

783 Lehman, S. I., and Keigwin, L. D. (1992). Sudden changes in North Atlantic
784 circulation during the last deglaciation. *Nature*, **356**, 757.

785 Lippold, J., Luo, Y., Francois, R., Allen, S. E., Gherardi, J., Pichat, S., Hickey
786 B., Schulz, H. (2012). Strength and geometry of the glacial Atlantic
787 meridional overturning circulation. *Nature Geoscience*, **5**(11), 813-816.

788 Lynch-Stieglitz J, Adkins JF, Curry WB, Dokken T, Hall IR,Herguera JC,
789 Hirschi JJ-M, Ivanova EV, Kissel C, Marchal O,Marchitto TM, McCave
790 IN, McManus JF, Mulitza S, Ninnemann, U, Peeters F, Yu E-F, Zahn
791 R (2007) Atlantic meridionaloverturning circulation during the Last
792 Glacial Maximum.*Science* **316**:66–69.

793 Marsh, N. D., and Ditlevsen, P. D. (1997). Observation of atmospheric and
794 climate dynamics from a high resolution ice core record of a passive
795 tracer over the last glaciation. *Journal of Geophysical Research-*
796 *Atmospheres*, **102**(D10), 11219-11224.

797 Masson-Delmotte, V., Jouzel, J., Landais, A., Stievenard, M., Johnsen, S. J.,
798 White, J. W. C., Werner M., Sveinbjorndottir A., Fuhrer, K. (2005).
799 GRIP deuterium excess reveals rapid and orbital-scale changes in
800 Greenland moisture origin. *Science*, **309**(5731), 118-121.

801 Masson-Delmotte, V., Steen-Larsen, H. C., Ortega, P., Swingedouw, D.,
802 Popp, T., Vinther, B. M., Oerter H., Sveinbjornsdottir A. E.,
803 Gudlaugsdottir H., Box J.E., Falourd S., Fettweiss X., Gallée H.,
804 Garnier E., Jouzel J., Landais A., Minster B., Paradis N., Orsi A., Risi
805 C., Werner M., White, J. W. C. (2015). Recent changes in north-west
806 Greenland climate documented by NEEM shallow ice core data and
807 simulations, and implications for past temperature reconstructions.
808 *The Cryosphere Discussions*, **9**(1), 655-717.

809 Nagashima, K., Tada, R., Tani, A., Sun, Y., Isozaki, Y., Toyoda, S., and
810 Hasegawa, H. (2011). Millennial-scale oscillations of the westerly jet
811 path during the last glacial period. *Journal of Asian Earth Sciences*,
812 **40**(6), 1214-1220.

813 NGRIP community members. (2004). High-resolution record of northern
814 hemisphere climate extending into the last interglacial period. *Nature*,
815 **431**(7005), 147-151.

816 Olsen, J., Anderson, N. J., and Knudsen, M. F. (2012). Variability of the north
817 Atlantic oscillation over the past 5,200 years. *Nature Geoscience*,
818 **5**(11), 808-812.

819 Petit, J. R., White, J. W. C., Young, N. W., Jouzel, J., and Korotkevich, Y. S.
820 (1991). Deuterium excess in recent Antarctic snow. *Journal of*
821 *Geophysical Research-Atmospheres*, **96**(D3), 5113-5122.

822 Porter, S. C., and An, Z. S. (1995). Correlation between climate events in the
823 north-Atlantic and China during last glaciation. *Nature*, **375**(6529),
824 305-308.

825 Prospero, J. M., Ginoux, P., Torres, O., Nicholson, S. E., and Gill, T. E.
826 (2002). Environmental characterization of global sources of
827 atmospheric soil dust identified with the nimbus 7 total ozone mapping
828 spectrometer (TOMS) absorbing aerosol product. *Reviews of*
829 *Geophysics*, **40**(1), 1002.

830 Rahmstorf, S. (2003). Timing of abrupt climate change: A precise clock.
831 *Geophysical Research Letters*, **30**(10), 1510.

832 Rasmussen, S. O., Andersen, K. K., Svensson, A. M., Steffensen, J. P.,
833 Vinther, B. M., Clausen, H. B., Siggaard-Andersen M.-L,. Johnsen S.
834 J, Larsen L. B, Dahl-Jensen D., Bigler M., Röthlisberger R., Fischer
835 H., Goto-Azuma K., Hansson M. E. and Ruth, U. (2006). A new
836 Greenland ice core chronology for the last glacial termination. *Journal*
837 *of Geophysical Research: Atmospheres* (1984–2012), **111**(D6).

838 Rasmussen, S. O., Bigler, M., Blockley, S. P., Blunier, T., Buchardt, S. L.,
839 Clausen, H. B., Cvijanovic I., Dahl-Jensen D., Johnsen S.J., Fischer
840 H., Gkinis V., Guillevic M., Hoel W. Z., Lowe J. J., Pedro J. B., Popp
841 T., Seierstad I. K>, Steffensen J. P., Svensson A. M., Vallelonga P.,
842 Vinther M., Walker J. C., Whetley J.J., Winstrup, M. (2014). A
843 stratigraphic framework for abrupt climatic changes during the last
844 glacial period based on three synchronized Greenland ice-core
845 records: Refining and extending the INTIMATE event stratigraphy.
846 *Quaternary Science Reviews*, **106**, 14-28.

847 Ruth, U., Wagenbach, D., Steffensen, J. P., and Bigler, M. (2003).
848 Continuous record of microparticle concentration and size distribution
849 in the central Greenland NGRIP ice core during the last glacial period.
850 *Journal of Geophysical Research-Atmospheres*, **108**(D3), 4098.

851 Sarnthein M, Stattegger K, Dreger D, Erlenkeuser H, Grootes P,Haupt BJ,
852 Jung S, Kiefer T, Kuhnt W, Pflaumann U, Scha¨fer-Neth C, Schulz H,
853 Schulz M, Seidov D, Simstich J, van KreveldS, Vogelsang E, Volker A,
854 Weinelt M (2000) Fundamental modes and abrupt changes in North
855 Atlantic circulation and climate over the last 60 k years—concepts,
856 reconstruction andnumerical modeling. In: Schafer P, Ritzrau W,
857 Schlu¨ter M, Thiede J (eds) *The northern North Atlantic: a changing*
858 *environment*. *Springer*, Berlin, pp 365–410.

859 Schulz, M. (2002). The tempo of climate change during Dansgaard-Oeschger
860 interstadials and its potential to affect the manifestation of the 1470-
861 year climate cycle. *Geophysical Research Letters*, **29**(1), 2-1.

862 Shackleton, N. J., Hall, M. A., and Vincent, E. (2000). Phase relationships
863 between millennial-scale events 64,000-24,000 years ago.
864 *Paleoceanography*, **15**(6), 565-569.

865 Shin, S. I., Liu, Z., Otto-Bliesner, B. L., Kutzbach, J. E., and Vavrus, S. J.
866 (2003). Southern Ocean sea-ice control of the glacial North Atlantic
867 thermohaline circulation. *Geophysical Research Letters*, **30**(2).

868 Spotl, C., and Mangini, A. (2002). Stalagmite from the Austrian Alps reveals
869 Dansgaard-Oeschger events during isotope stage 3: Implications for
870 the absolute chronology of Greenland ice cores. *Earth and Planetary*
871 *Science Letters*, **203**(1), 507-518.

872 Steffensen, J. P. (1997). The size distribution of microparticles from selected
873 segments of the Greenland ice core project ice core representing
874 different climatic periods. *Journal of Geophysical Research-Oceans*,
875 **102**(C12), 26755-26763.

876 Steffensen, J. P., Andersen, K. K., Bigler, M., Clausen, H. B., Dahl-Jensen,
877 D., Fischer, H., Goto-Azuma K., Hansson M., Johnsen S.J., Jouzel J.,
878 Masson-Delmotte V., Popp T., Rasmussen S. O., Röthlisberger R.,
879 Ruth U., Stauffer B., Siggard-Andersen M. L., Sveinbjörndottir A. E.,
880 Svensson A., White, J. W. C. (2008). High-resolution Greenland ice
881 core data show abrupt climate change happens in few years. *Science*,
882 **321**(5889), 680-684.

883 Stocker, T. F., and Johnsen, S. J. (2003). A minimum thermodynamic model
884 for the bipolar seesaw*. Paleoceanography*, **18**(4), 1087.

885 Stouffer, R. J., Yin, J., Gregory, J. M., Dixon, K. W., Spelman, M. J., Hurlin,
886 W., Weaver, A. J., Eby, M., Flato, G. M., Hasumi, H., Hu, A.,
887 Jungclaus, J. H., Kamenkovich, I. V., Levermann, A., Montoya, M.,
888 Murakami, S., Nawrath, S., Oka, A., Peltier, W. R., Robitaille, D. Y.,
889 Sokolov, A., Vettoretti, G. and Weber, S. L (2006). Investigating the
890 causes of the response of the thermohaline circulation to past and
891 future climate changes. *Journal of Climate*, **19**(8), 1365-1387.

892 Svensson, A., Biscaye, P. E., and Grousset, F. E. (2000). Characterization of
893 late glacial continental dust in the Greenland ice core project ice core.
894 *Journal of Geophysical Research-Atmospheres*, **105**(D4), 4637-4656.

895 Svensson, A., Bigler, M., Kettner, E., Dahl-Jensen, D., Johnsen, S., Kipfstuhl,
896 S., Nielsen M., Steffensen, J. P. (2011). Annual layering in the NGRIP
897 ice core during the Eemian. *Climate of the Past*, **7**(4), 1427-1437.

898 Taylor, K. C., Lamorey, G. W., Doyle, G. A., Alley, R. B., Grootes, P. M.,
899 Mayewski, P. A., White J.W.C., and Barlow, L. K. (1993). The
900 'flickering switch'of late Pleistocene climate change. *Nature* **361**, 432-
901 436.

902 Thomas, E. R., Wolff, E. W., Mulvaney, R., Johnsen, S. J., Steffensen, J. P.,
903 and Arrowsmith, C. (2009). Anatomy of a Dansgaard-Oeschger
904 warming transition: High-resolution analysis of the north Greenland ice
905 core project ice core. *Journal of Geophysical Research-Atmospheres*,
906 **114**, D08102.

907 Thornalley, D.J.R., Barker, S., Broecker, W.S., Elderfield, H. and McCave,
908 I.N., (2011). The deglacial evolution of North Atlantic deep convection.
909 *Science*, **331**, 202-205.

910 Thornalley, D. J. R., Barker, S., Becker, J., Hall, I. R., and Knorr, G. (2013).
911 Abrupt changes in deep Atlantic circulation during the transition to full
912 glacial conditions. *Paleoceanography*, **28**(2), 253-262.

913 Thouveny, N., Debeaulieu, J. L., Bonifay, E., Creer, K. M., Guiot, J., Icole, M.,
914 Johnsen S. J., Jouzel J., Reille M., Williams T., Williamson, D. (1994).
915 Climate variations in Europe over the past 140-kyr deduced from rock
916 magnetism. *Nature*, **371**(6497), 503-506.

917 Treble, P., Shelley, J. M. G., and Chappell, J. (2003). Comparison of high
918 resolution sub-annual records of trace elements in a modern (1911-
919 1992) speleothem with instrumental climate data from southwest
920 Australia. *Earth and Planetary Science Letters*, **216**(1-2), 141-153.

921 Vallelonga, P., Bertagna, G., Blunier, T., Kjaer, H. A., Popp, T. J.,
922 Rasmussen, S. O., Steffensen J.P., Stowasser C., Svensson A. S.,
923 Warming E., Winstrup M., Bigler M., Kipfstuhl, S. (2012). Duration of
924 Greenland stadial 22 and ice-gas delta age from counting of annual
925 layers in Greenland NGRIP ice core. *Climate of the Past*, **8**(6), 1839-
926 1847.

927 Van Meerbeeck, C. J., Renssen, H., Roche, D. M., Wohlfarth, B., Bohncke,
928 S. J. P., Bos, J. A. A., Engels S., Helmens K.F., Sánchez-Goñi M.F.,
929 Svensson A..S., and Vandenberghe, J. (2011). The nature of MIS 3
930 stadial–interstadial transitions in Europe: new insights from model–
931 data comparisons. *Quaternary Science Reviews*, **3025**, 3618-3637.

932 Voelker, A. H. L. (2002). Global distribution of centennial-scale records for
933 marine isotope stage (MIS) 3: A database. *Quaternary Science*
934 *Reviews*, **21**(10), 1185-1212.

935 Wang, Y. J., Cheng, H., Edwards, R. L., An, Z. S., Wu, J. Y., Shen, C. C.,
936 and Dorale, J. A. (2001). A high-resolution absolute-dated late
937 Pleistocene monsoon record from Wulu cave, china. *Science*,
938 **294**(5550), 2345-2348.

939 Wolff, E. W., Chappellaz, J., Blunier, T., Rasmussen, S. O., and Svensson,
940 A. (2010). Millennial-scale variability during the last glacial: The ice
941 core record. *Quaternary Science Reviews*, **29**(21-22), 2828-2838.

942 Zhang, X. Y., Zhang, G. Y., Zhu, G. H., Zhang, D., An, Z. S., Chen, T., and
943 Huang, X. P. (1996). Elemental tracers for chinese source dust.
944 *Science in China Series D-Earth Sciences*, **39**(5), 512-521.

945 Zhang, R., Cao, J., Tang, Y., Arimoto, R., Shen, Z., Wu, F., Han Y., Wang G.,
946 Zhang J., Li G., (2014). Elemental profiles and signatures of fugitive
947 dusts from chinese deserts. *Science of the Total Environment*, **472**,
948 1121-1129.

949 Zhang, X., Prange, M., Merkel, U., and Schulz, M. (2014). Instability of the
950 Atlantic overturning circulation during Marine Isotope Stage 3.
951 *Geophysical Research Letters*, **41**(12), 4285-4293.

952

953

954

955

Figures

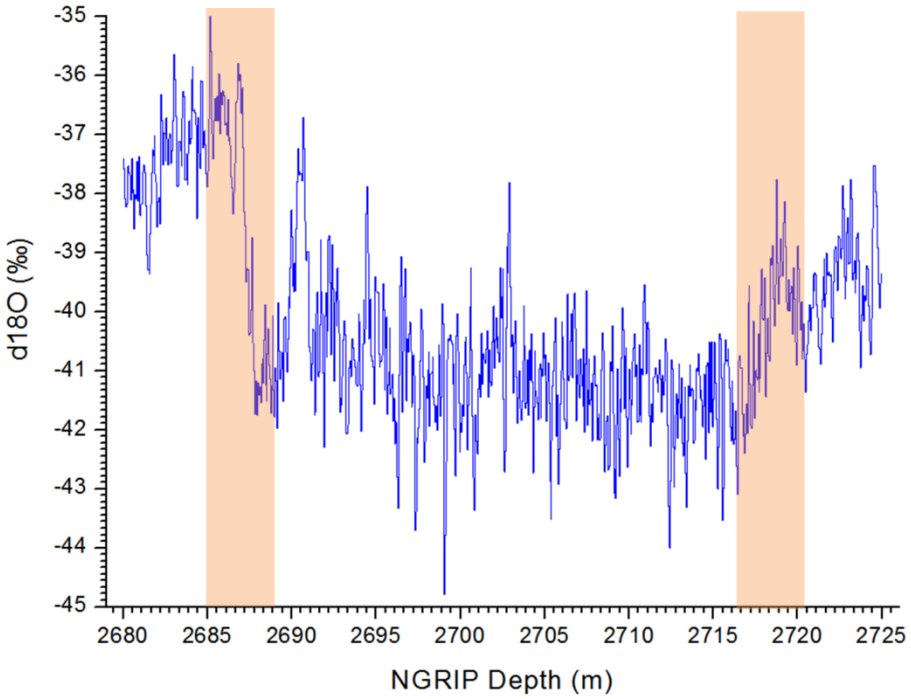

Figure 1: NGRIP $\delta^{18}O$ profile across the GS22 stadial at 5 cm resolution. In light orange we highlighted the ice core section analysed in the present study, which include the transition from GI22 to GS22 and between GS22 and GI21. See text for details.

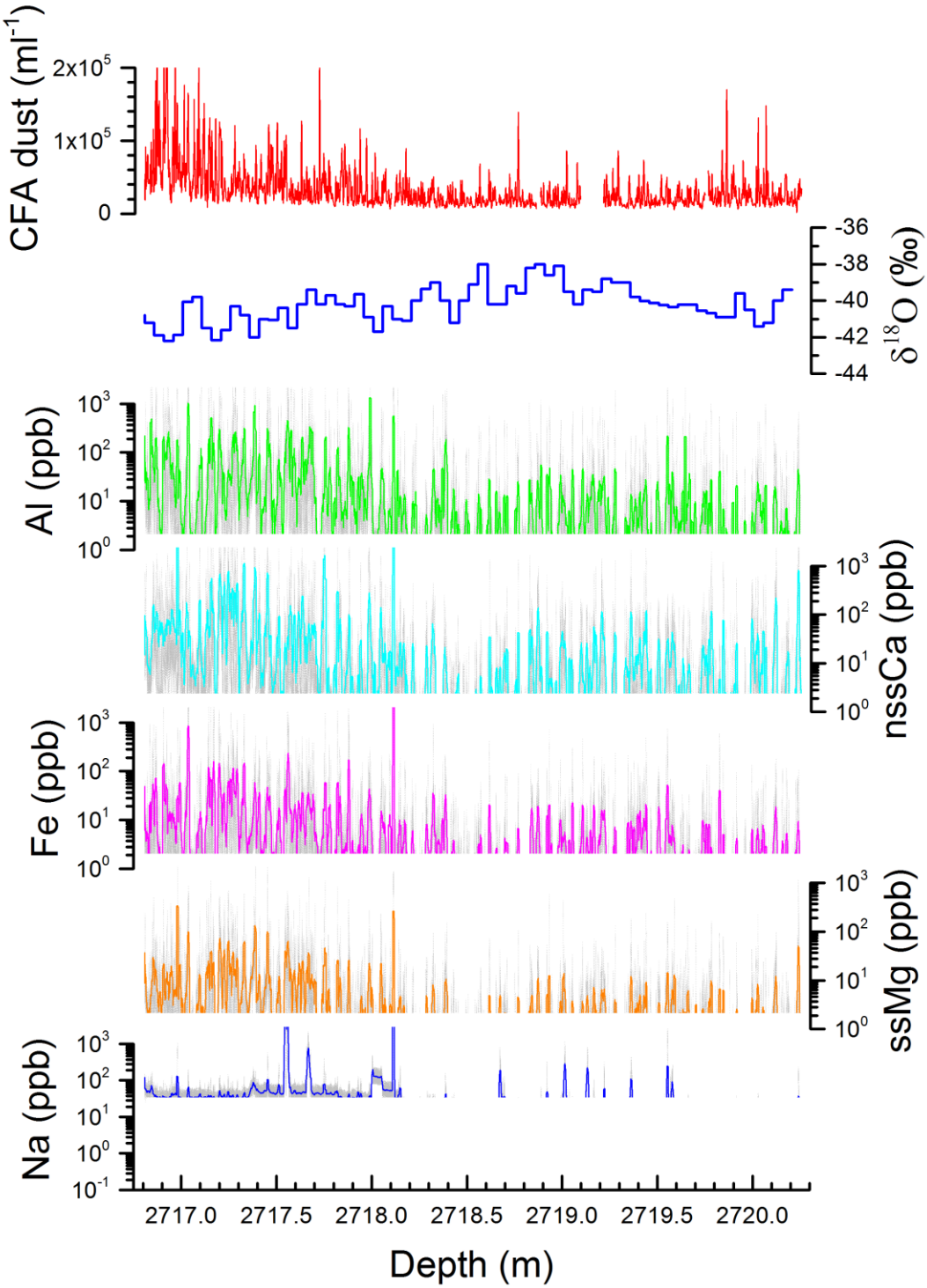

Figure 2: Elemental concentration across GI22-GS22 transition. Grey dotted lines represent UV-LA-ICPMS original data; moving average (period 100) is indicated by the solid coloured line. The data have been cut off at their respective LODs (see table 1 in Della Lunga et al., 2015a *in preparation*). Oxygen at 5 cm sampling resolution and dust profile (resolution: 1mm) are from Vallelonga et al. (2012).

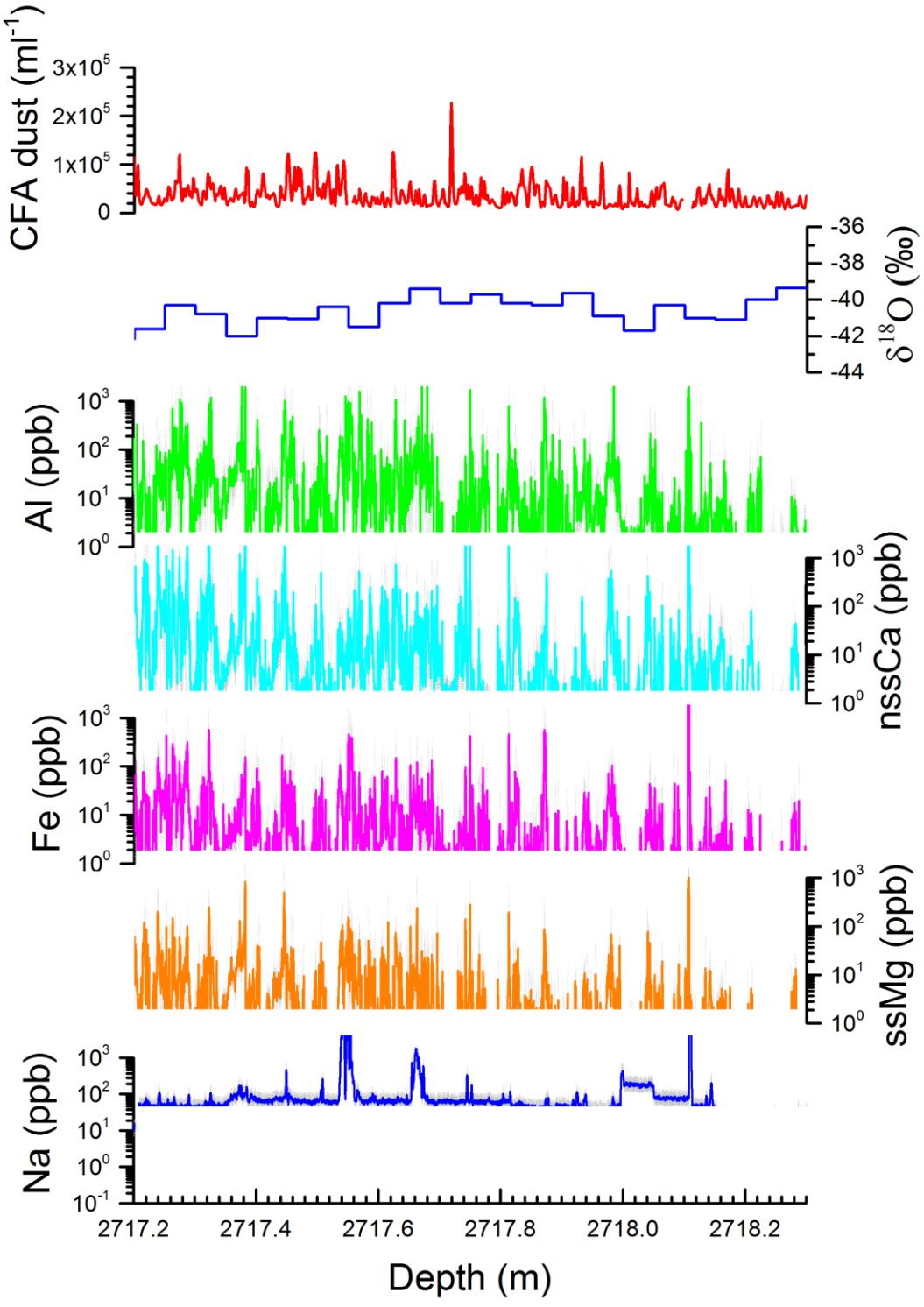

969

970 **Figure 3: Elemental concentration across 110 cm of ice core where most of the increase in**
971 **concentration appears as stadial conditions take over (GS22). Grey dotted lines represent UV-**
972 **LA-ICPMS original data; moving average (period 100) is indicated by the solid coloured line.**
973 **The data have been cut off at their respective LODs (see table 1 in Della Lunga et al., 2015a *in***
974 ***preparation*). Oxygen at 5 cm sampling resolution and dust profile (resolution: 1mm) are from**
975 **Vallelonga et al. (2012).**

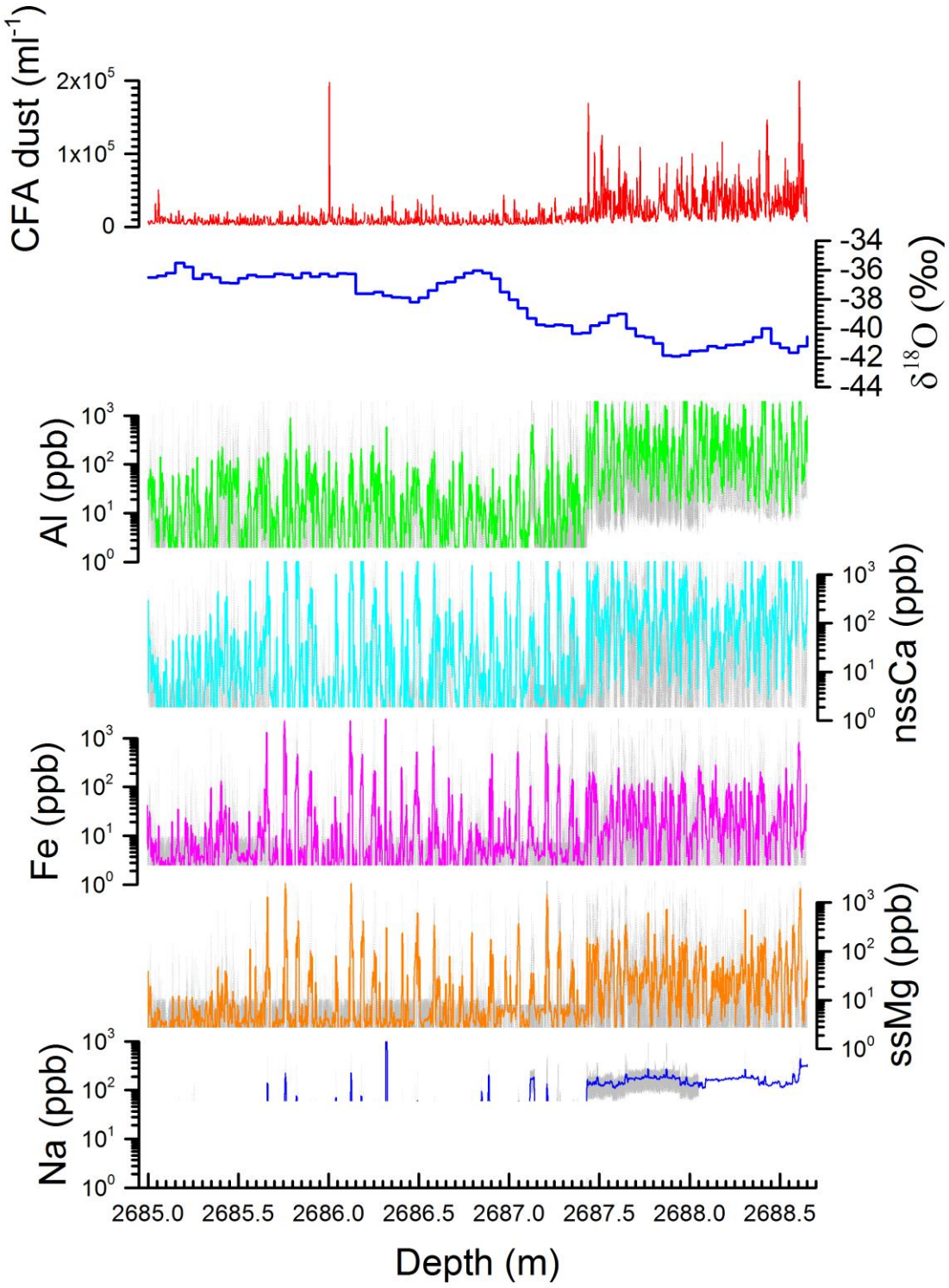

976

977 **Figure 4: Elemental concentration across GS22-GI21 transition. Dotted lines represent UV-LA-**
978 **ICPMS original data; moving average (period 100) is indicated by the solid coloured line. The**
979 **data have been cut off at their respective LODs (see table 1). $\delta^{18}O$ and CFA data after Vallelonga**
980 **et al. (2012), the resolution is 5 and 0.1 cm respectively.**

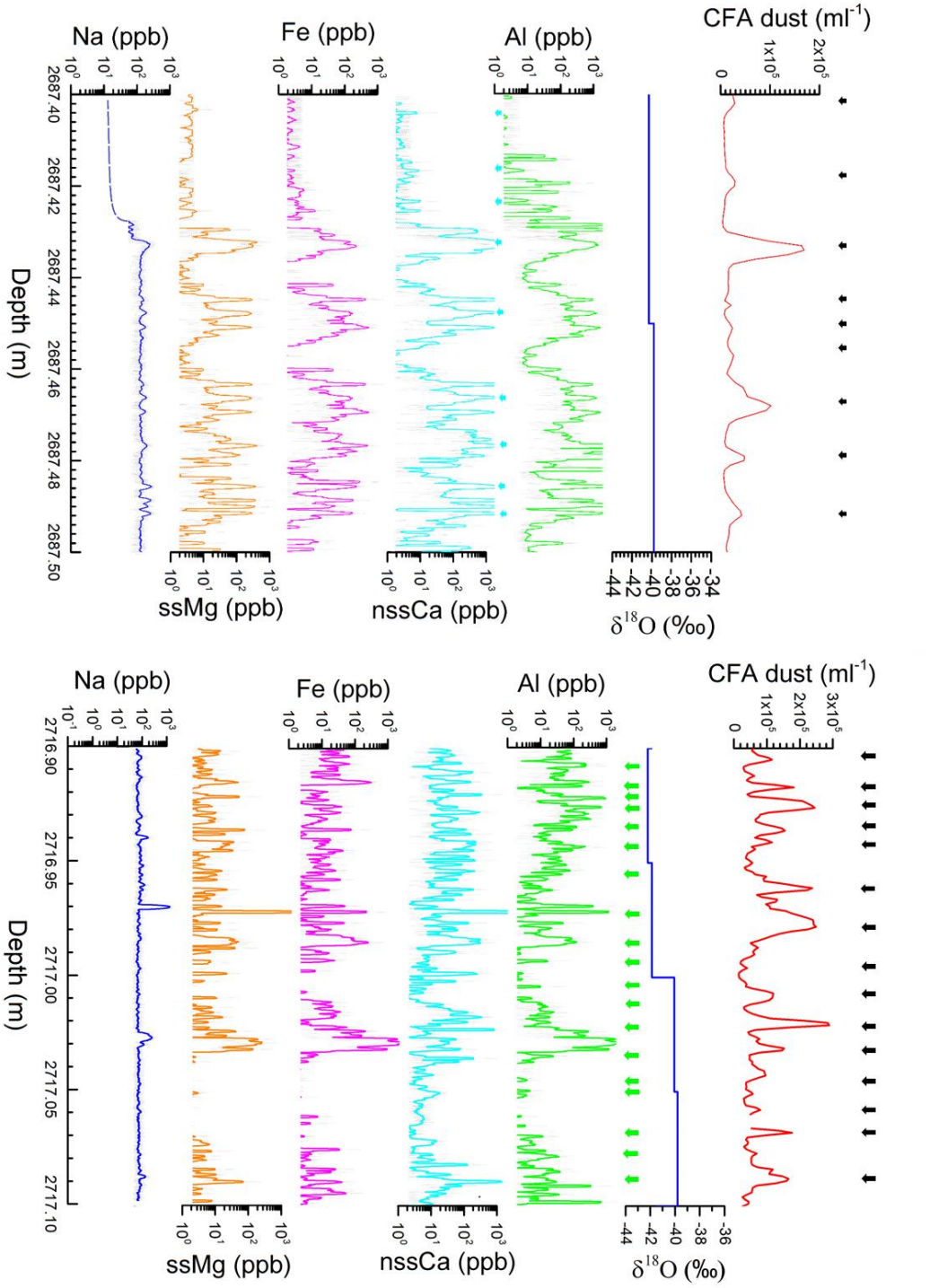

Figure 5: Zoom over 10 and 20 cm of GS22-GI21 and GI22-GS22 transition respectively. Na, Al, ssMg, nssCa and Fe are shown. Data have been cut off at their corresponding LODs (see table 1). Blue dashed line in Na record is extrapolated based on ssMg/Na ratio on the deeper section. Grey dotted lines are original LA-ICPMS data; coloured lines represent moving average (period 100). CFA dust data (resolution: 1mm) and $\delta^{18}O$ profile (resolution 5 cm), are from Vallelonga et al. (2012). For GS22-GI21 transition we observe a sharp decrease in dustiness around a depth of 2687.43 m, marking the start of GI21. Black arrows indicate annual layers identified by CFA dust profile, while coloured arrows indicate annual layers identified based on nssCa and Al respectively. LA-ICPMS data show more potential annual layers in the 20 cm section (19 compared to 15), whereas in the shallower section both counting agree (9 layers identified each). Average annual layer thickness is 11.5±1.5 mm.

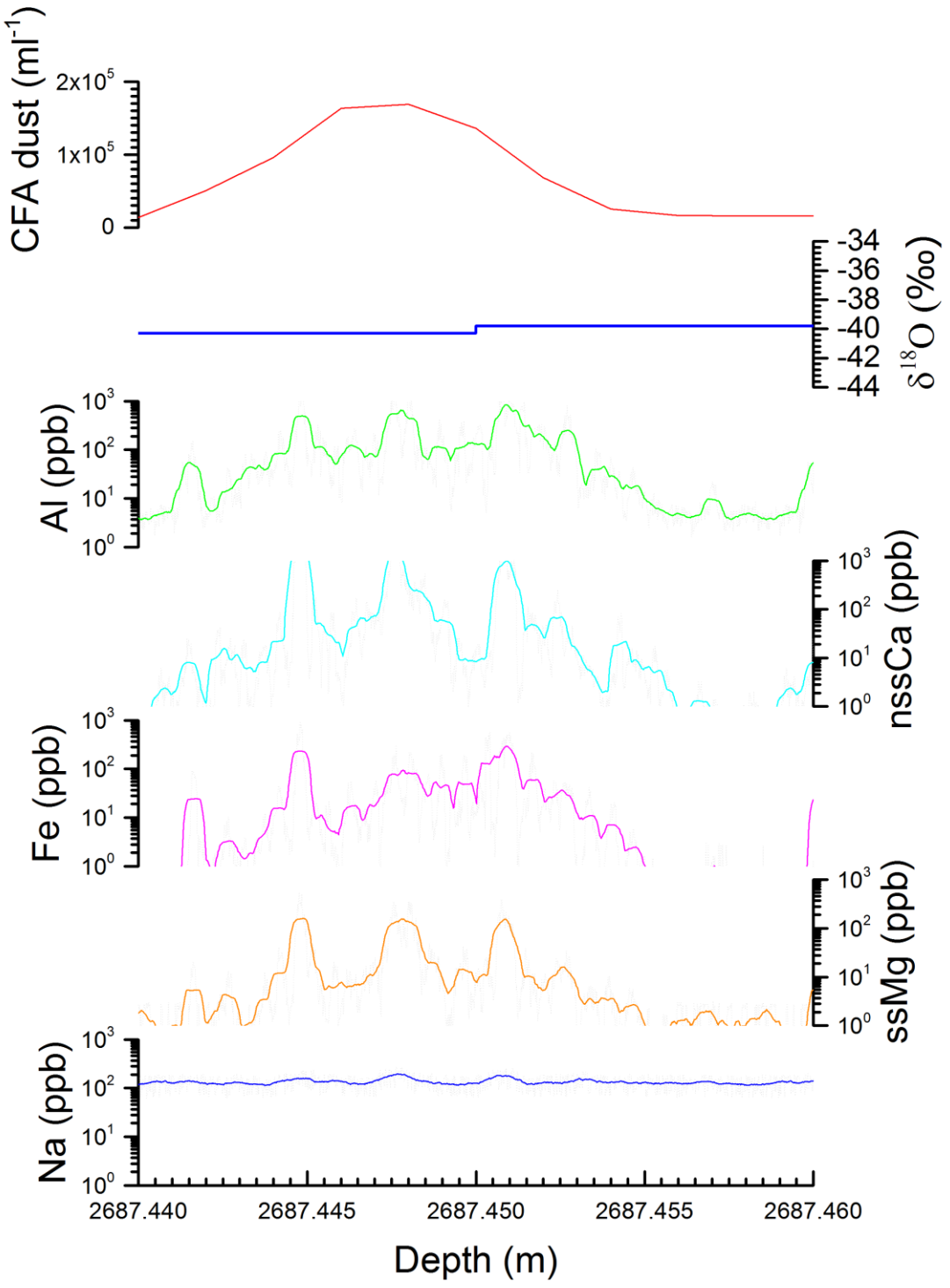

994

995 **Figure 6: Structure of a single annual peak in GS22-GI21 transition. CFA and $\delta^{18}O$ profile have 1**
996 **mm and 5 cm resolution respectively (from Vallelonga et al., 2012). Coloured lines are**
997 **unsmoothed LA-ICPMS data. LA-ICPMS data suggest that the broad annual peak observable in**
998 **CFA dust profile may present internal variability, with 3-5 different peaks contributing to the**
999 **dust signal. These peaks may represent single intense events during storm season.**

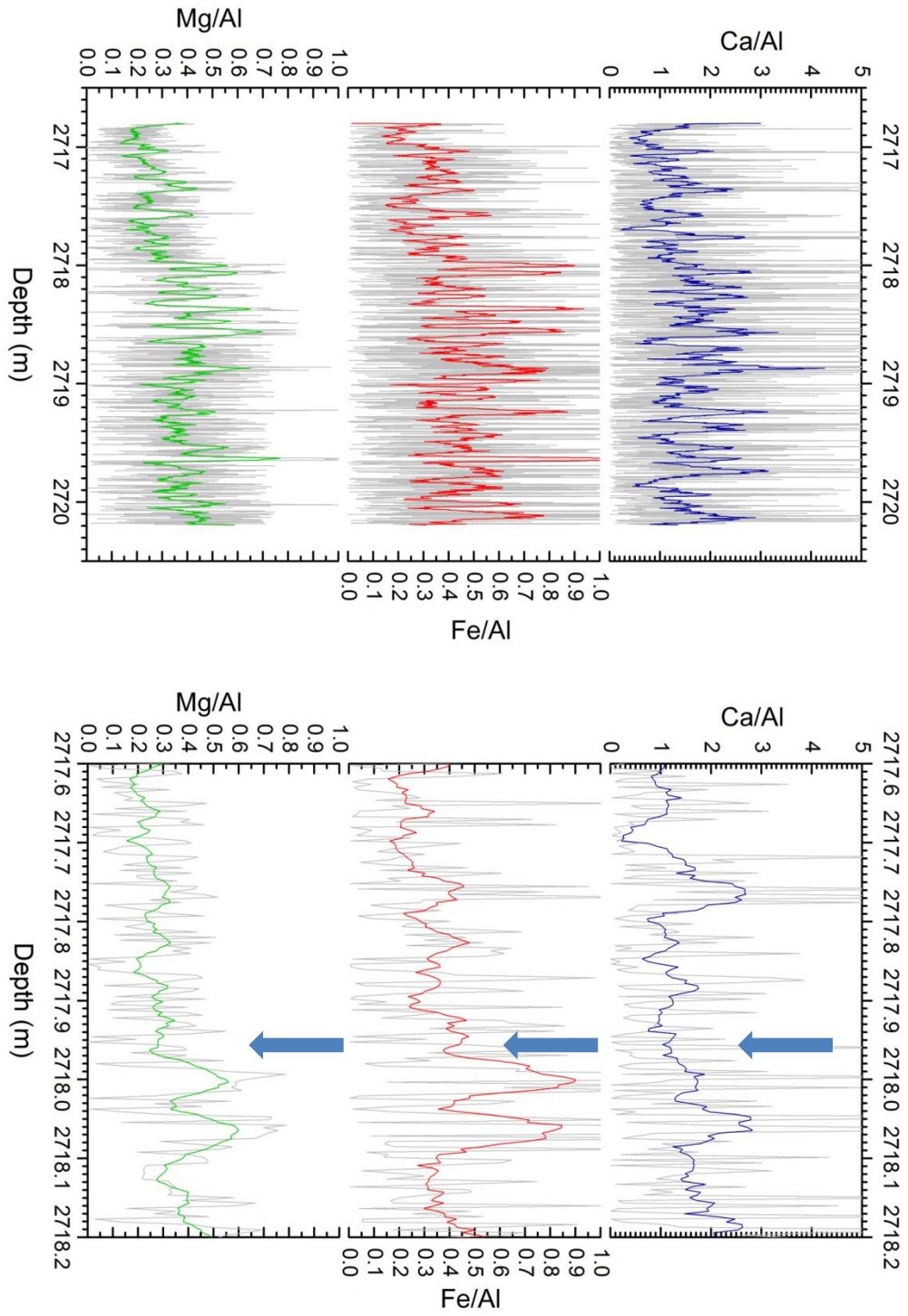

Figure 7: Above: Ca/Al, Fe/Al and Mg/Al ratios across GI22-GS22 transition. Below: zoom over 60 cm of Ca/Al, Fe/Al and Mg/Al record across GI22-GS22 transition A significant shift in ratios is observed at a depth of 2717.96 m (blue arrows), where values rise from an average of 0.25, 0.30 and 1.05 to 0.45 0.48 and 1.64 for Mg/Al, Fe/Al and Ca/Al respectively. This may be related to a change in source of dust at the onset of GS22.

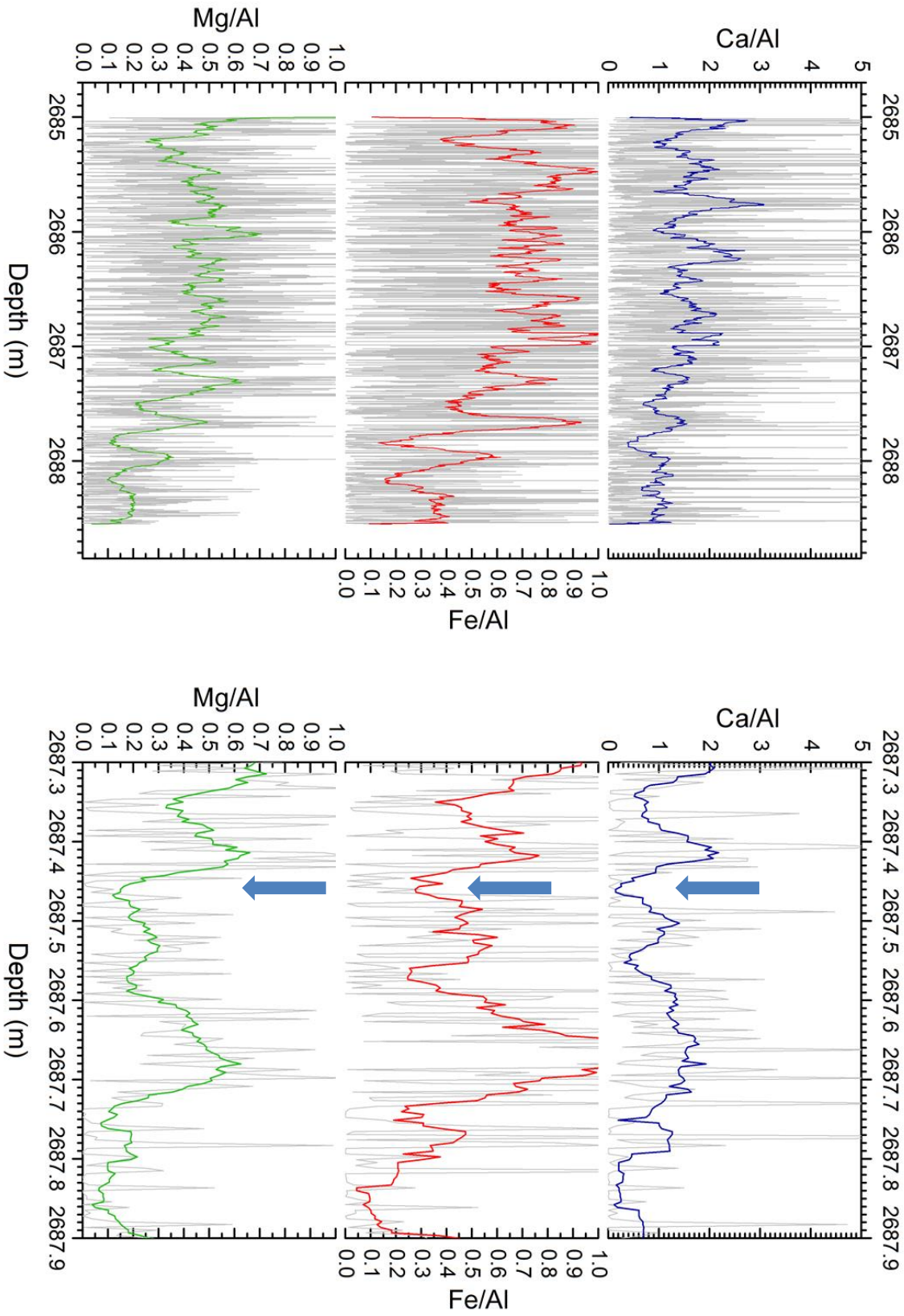

1009

1010 **Figure 8: Above: Ca/Al, Fe/Al and Mg/Al ratios across GS22-GI2I transition. Below: zoom over**
1011 **60 cm of Ca/Al, Fe/Al and Mg/Al record across GS22-GI2I transition. A significant shift in ratios**
1012 **is observed at a depth of 2687.43 m (blue arrow), where values rise from an average of 0.18,**
1013 **0.30 and 1.15 to 0.45 0.75 and 1.90 for Mg/Al, Fe/Al and Ca/Al respectively. This may be related**
1014 **to a change in source of dust at the onset of GI21.**

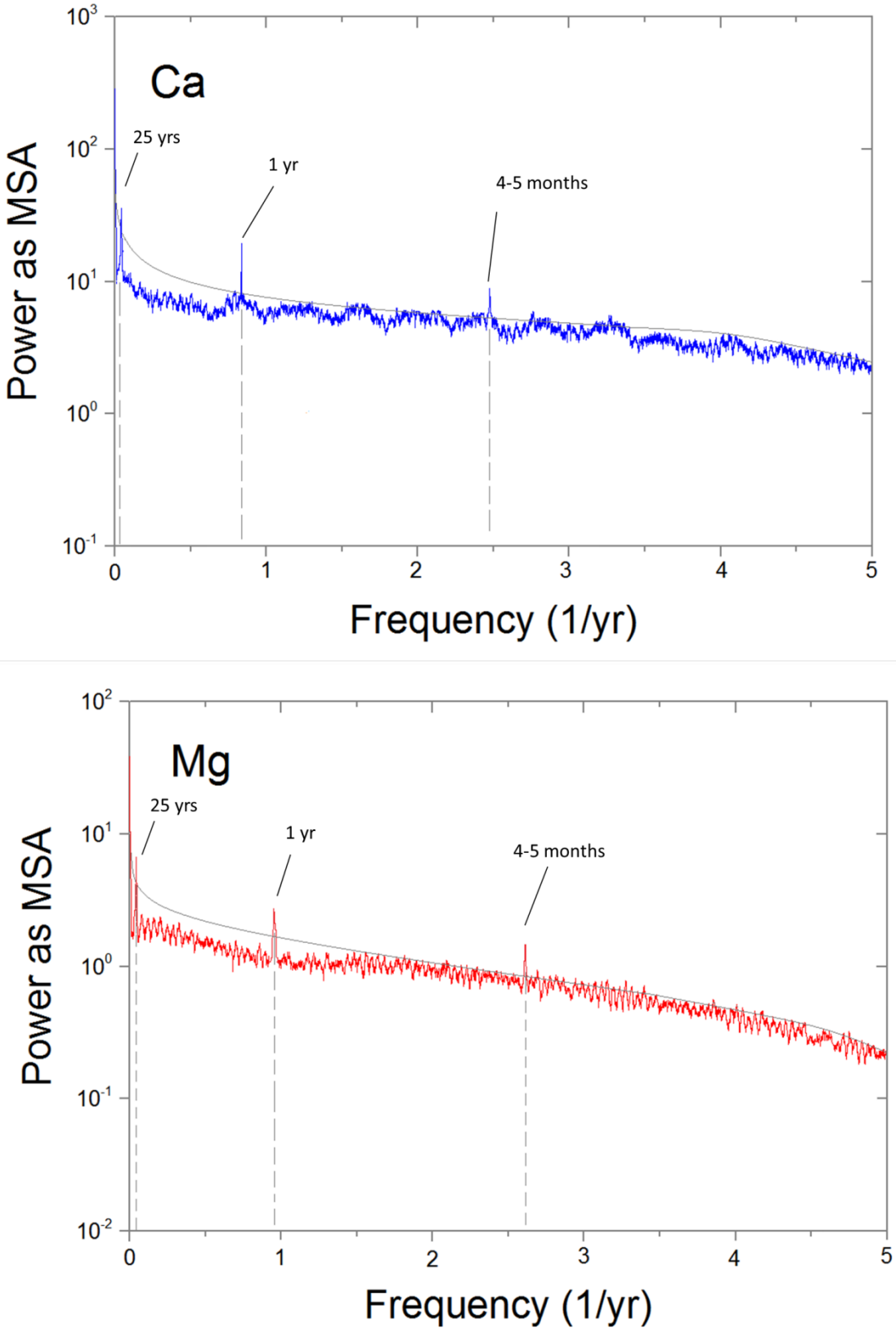

Figure 9: Power spectra as 'mean square amplitude' (MSA) for Ca and Mg across GI22-GS22 transition. Data are displayed on a floating time scale obtained converting from depth domain to time domain using layer thickness (λ) data (from Vallelonga et al., 2012).

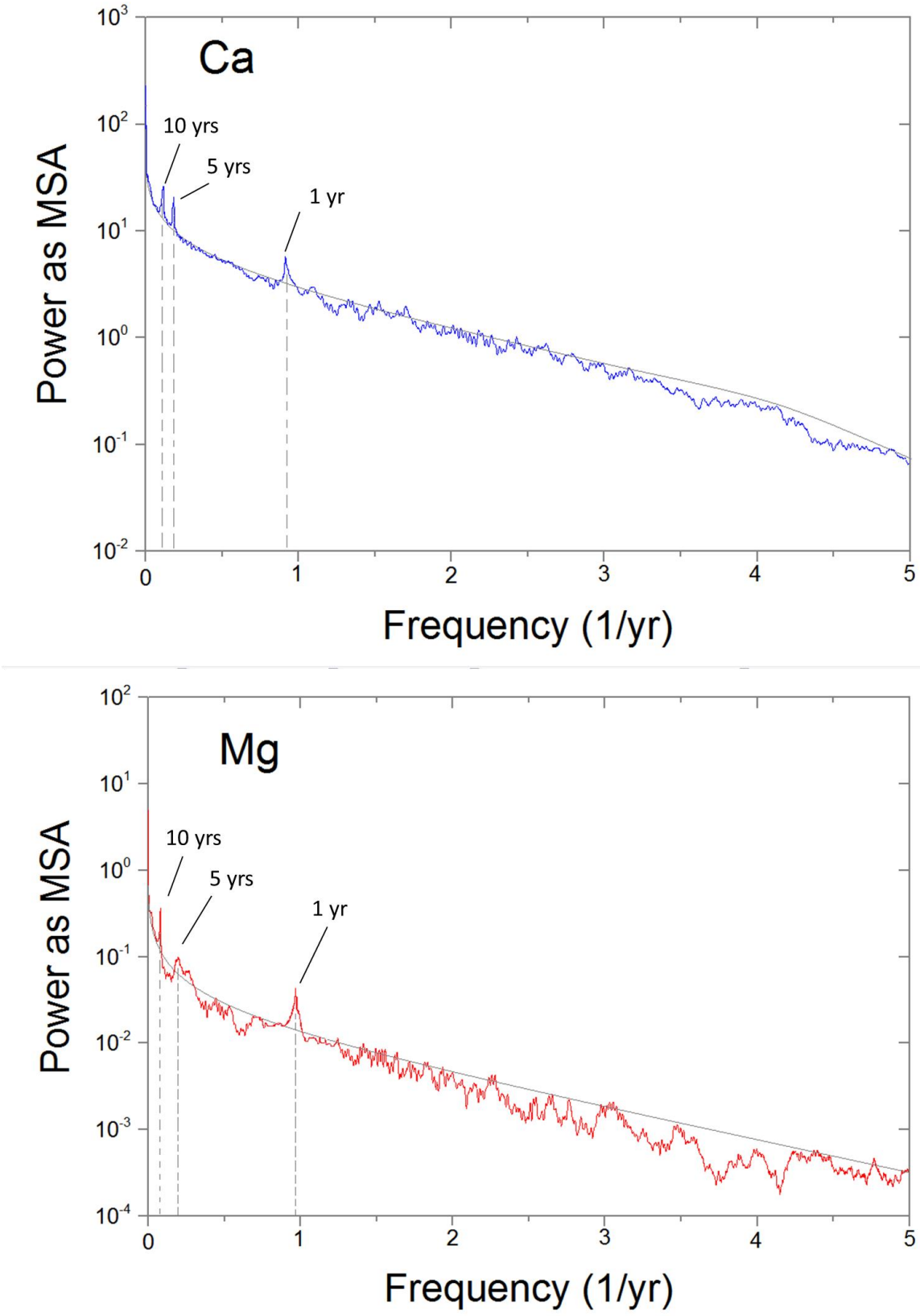

Figure 10: Power spectra as 'mean square amplitude' (MSA) for Ca and Mg across GS22-GI21 transition. Data are displayed on a floating time scale obtained converting from depth domain to time domain using layer thickness (λ) data. (from Vallelonga et al., 2012).

8) Critical evaluation

8.1 - Rationale and Research Synthesis

The present work aimed to refine and apply the pilot study established earlier at RHUL (Müller et al., 2011) to routinely perform UV laser ablation ICPMS analysis of frozen ice cores at sub-millimetre resolution. The improved methodology and instrumentation is mainly described in chapter 4) along with strategies to remove possible contamination from cutting and sample handling with some details also in chapter 1) and the calibration strategies in chapter 5). The instrumentation at RHUL (Müller et al., 2011) was further developed to allow routine sample handling, smoothing and storing at sub-zero temperatures and clean-room conditions. The equipment has been entirely designed and built at RHUL and allows analysis of several meters of ice cores during many continuous days without losing overall performance, as it was initially outlined in our Research Hypothesis (RH) 1 and 2. In particular, the use of a two-volume cryo-cell represents a key improvement over previous LA-ICPMS studies of ice cores which used infrared wavelength at 1064 nm (Reinhardt et al., 2001, 2003) and most recently ultraviolet wavelength at 213 nm (Sneed et al., 2015) and large volume LA cells. The actual volume of our 'two-volume' cell of 1-2 cm^3 allows a much faster signal washout of about 1.5 s compared to ~7 min (cell volume: 660 cm^3) in Reinhardt et al. (2003) and ~8 s (cell volume: 20 cm^3) in Sneed et al. (2015), thus enabling depth-profiling and track analysis without significant signal mixing. UV light absorption in ice show an optimal balance at wavelength at 193 nm between sufficient material removal and ablation uniformity, creating craters and tracks of more symmetric shape (RH 1) (Muller et al., 2011, Della Lunga et al, 2014) compared to 1064 nm and 213 nm wavelengths (Reinhardt et al., 2003, Sneed et al., 2015) and still maintaining low-ppb limit of detection (LODs) for major elements, similar to Sneed et al. (2015). Finally, our maximal resolution, while maintaining acceptable LODs, is around 100 µm, similar to Sneed et al (2015) and 3 to 10 higher than Reinhardt et al. (2003).

A complete calibration method for converting net ICPMS count rates into elemental concentrations is described in chapter 5), together with an ice standard preparation technique (Della Lunga et al., 2015a, planned submission). Quantification of major elements in ice cores takes place directly in frozen state, producing a robust and reproducible calibration technique that is here presented for the first time in cryo-cell UV-LA-ICPMS studies (RH 3). I succeeded in preparing ice standards with signal fluctuations <15% RSD, which guarantee sufficient homogeneity of reference values in ice to allow quantification, and represents an improvement to other UV-LA-ICPMS ice core works (RH 3)(Reinhardt et al., 2003; Mayewski et al., 2014, Sneed et al., 2015), which showed typical RSD values on signals from artificial ice standards of 23-24 % (Sneed et al., 2015) and 16-35 % (Wilhelms-Dick, 2008) on the same concentration range in the reference materials.

The need for high resolution studies of climatic proxies in ice cores has been growing significantly since millennial to centennial climate variations have been observed in Greenland and Antarctic ice cores (Dansgaard et al., 1993; Jouzel et al., 2007). Among these, the most relevant ones are the so-called 'Dansgaard-Oeschger' (DO) events, a series of at least 25 temperature oscillations of 5-16 °C over Greenland lasting between one and three thousand years each one, and extending back to the previous interglacial (120 kyrs). The data regarding the younger DO events (1 to 17, from 11.70 to 59.44 ka) are relatively abundant and well constrained in terms of chronology (Landais et al., 2015), because they benefit from correlation of several ice core records where yearly accumulation is high enough to resolve sub-annual cycles with routine continuous flow analysis (CFA), allowing establishing a chronology simply by layer counting. However, for older DO events ice compaction produces a thinning of the annual layer below the resolution limit of CFA (~10 mm, Bigler et al., 2011), so that sub-annual cycles of climate proxies are not resolvable. Furthermore, it has been demonstrated that the warming events starting a DO cycle take place extremely fast, in as short as few years (Steffensen et al., 2008). Our main contribution was to resolve deep ice sub-annual variability across DO 22

transition to confirm that from stadial to interstadial (warming phase) dust and also sea salt elemental proxies (nssCa, Al, Fe, ssMg and Na) show a sudden drop in concentrations over only one cm of ice, which, considering the depth, possibly represent a bit less than one year (RH 6 & 7) (chapter 4, 6). For the interstadial to stadial transition we could confirm previous studies (Fuhrer et al., 1999, Wolff et al., 2010) which observed that the rise in concentrations of dust proxies is not abrupt but takes place in more than one step that gradually brings the total content of dust to values that are one order of magnitude higher than before (chapter 6). We could observe also that this particular time period is characterized by a very high degree of variability, the amplitude of these oscillations being similar to the one that characterizes interstadial-stadial transition itself. I suggest that this phenomenon represents a “flickering of climate signals” (chapter 2, 5 and 7), similarly to what has been defined by previous authors (Taylor et al., 1993; Baldini et al., 2015; Bakke et al., 2009).

In many cases, the onset of stadial conditions is also marked by a sharp grain size decrease. This has been observed for Termination II and I in the EPICA Dome C core from Antarctica (Durand et al., 2006), the GISP 2 ice core (Gow et al., 1997), the GRIP ice core (Thorsteinsson et al., 1995, 1997) and the NGRIP ice core (Wang et al., 2002). On a smaller scale, seasonal dusty layers, called “cloudy bands”, that are related to spring/summer dust peaks induced by storms, present smaller grains compared to clear ice representing autumn/winter layers. This phenomenon has been related in various ways to the influence of soluble and insoluble particles on grain growth and recrystallization (Faria et al., 2014).

I investigated the difference between clear and cloudy ice using 1D profiles, 2D mapping and 3D interpolation of impurities, with particular emphasis on the relationship between grain boundaries and impurity content. Using UV-LA-ICPMS, we were able to reveal a different distribution of impurities between clear and dusty ice: When ice is clean, impurities are preferentially concentrated along boundaries, whereas when ice is dusty impurities lie equally in boundaries and interiors (RH 4) . This confirms but also refines previous observations (Mulvaney et al., 1988; Iizuka et al., 2004; Barnes and

Wolf 2004). In the following section these findings are discussed in more detail.

8.1 - Soluble and insoluble impurities in ice

Concentrations and microstructural locations of soluble and insoluble impurities in ice cores influence significantly mechanical properties, recrystallization and grain growth of the ice itself (Faria et al., 2014). In particular, several studies have investigated the partitioning of soluble and insoluble impurities between grain boundaries and grain interiors.

The data (chapter 4 and 6) suggest that impurities preferentially lie on grain boundaries when their concentrations are relatively low (tens of ppb), whereas they are equally distributed between boundaries and interiors when concentrations are higher (RH 4) (hundreds of ppb). This observation can be explained by taking into account that impurity-enriched layers contain insoluble particles from dust, whose size is significantly bigger (Svensson et al., 2000). These findings are compatible with a number of previous works. In fact, using X-ray microanalysis (EDS) on a cryo-scanning electron microscope (SEM), Mulvaney et al. (1988) detected high concentrations of H_2SO_4 at triple junctions in Antarctic ice, which was confirmed by Mulvaney and Peel (1988) and Wolff et al. (1988). They also showed that other impurities were concentrating at triple junctions, although the total content on particles in natural ice was low. Fukuzawa et al. (1998) confirmed that impurities preferentially lie on boundaries and junction using Raman spectroscopy. These findings are also supported by several other studies performed mainly by EDS-SEM from different ice cores (Cullen and Baker, 2002; Baker and Cullen, 2002; Barnes et al., 2002a,b, 2003; Baker et al., 2003, 2005; Iliescu and Baker, 2008; Obbard et al., 2003a,b, 2006a,b; Obbard and Baker, 2007).

However, many other studies highlighted that impurities are distributed in a wide range of location including triple junctions, two-grain boundaries and grain interiors (Barnes and Wolff, 2004; Cullen and Baker 2000, 2001; Baker and Cullen 2003; Ohno et al., 2005; Iizuka et al., 2008), with small

differentiations dictated by impurity chemistry (Iizuka et al., 2004) or random clustering (Sakurai et al., 2009, 2010).

I suggest that in relatively clear ice, soluble impurities are harvested by moving boundaries and therefore align along them. When particles are bigger, as in dusty ice (cloudy bands), the drag effect of micro-particles is reduced (see eq. 3, Della Lunga et al., 2014), as well as the mobility of the boundaries and thus the grain size. Therefore, boundaries are not capable anymore to harvest micro-particles which then are equally distributed between junctions and interiors. However, we observed that this pattern does not occur in 100% of the cases (cfr. chapter 4 and 6), suggesting that this significant reduction of the drag effect might be the result of the interplay between particle size and volume fraction of particles which both influence the dragging force (see eq. 3, Della Lunga et al., 2014). Further studies are needed to unravel this relationship and to explain how the impurities become concentrated in the grain boundaries and the triple junctions since, in snow, they are randomly distributed throughout the snowflake and possibly concentrated in the centre of nucleation (Faria et al., 2014).

Diffusion to both grain boundaries and junctions in the deep ice could represent one of the mechanisms involved, possibly enhanced by heat released from the bedrock (RH 5)(Johnsen et al., 2001). Taking an alternative approach based on the assumption that soluble and insoluble impurities follow the same depositional patterns, we estimated diffusion length of soluble impurities in deep NGRIP ice (chapter 6), resulting in a value of <1 cm (RH 5). This agrees well with previous estimation and model (Gkinis et al., 2014; Van der Wel et al., 2015), showing that the integrity of paleoclimatic signals at this depth is reasonably well preserved. An indirect confirmation of this consistency is given by our dataset for GI21.2 and GI22-GS22-GI21, where I identify abrupt changes of more than one order of magnitude in concentrations over the space of a single centimetre. Therefore, if micro-particles have been influenced by diffusion, this phenomenon has not resulted in a smoothing of the signal due to soluble impurities diffusing according to a concentration gradient and thus can be considered negligible.

8.2 - Anatomy of Dansgaard-Oeschger event 22

Both duration, start and end dates of Dansgaard-Oeschger stadial 22 (i.e. GS22) have recently been constrained in the context of the INTIMATE project (INTegration of Ice-core, MArine and TErrestrial records) within the age range of 87.600 - 84.760 ka and a depth range at NGRIP of 2717.11-2687.29 m (Rasmussen et al., 2014). For the interstadial 22 – stadial 22 transition (GI22-GS22), the uncertainty has been estimated to be ±40-60 a (1σ) and ±40-70 cm of ice core depth range, using a multiproxy approach. For stadial 22 – interstadial 21 transition (GS22-GI21), the sharp change recorded in several proxies reduces the uncertainty to ± 20 a (1σ) and ± 20-30 cm (Rasmussen et al., 2014). GS22 transitions are also recorded in other palaeoclimatic archives such as speleothems from the Northern rim of the Alps (NALPS). It has to be noted that, for GS22, NGRIP and NALPS datasets present the highest discrepancy. In fact, in the NALPS record the onset of GS22 and GI21 is occurring at 88.69 and 85.03 ka respectively, preceding NGRIP transition by 1000 and 300 yrs respectively, resulting in a difference in duration of about 700 yrs: 3660 years in NALPS and 2840 in NGRIP (Boch et al., 2011, Rasmussen et al., 2014).

The high resolution dataset provide further insights into the spatial limits of the DO 22 transitions. I pinpoint the GS22-GI21 transition, the warming phase, at a depth of 2687.43 ± 0.005 m, while GI22-GS22, the cooling phase, can be collocated at 2717.38 ± 0.18 m. It is important to notice that, in both cases, the dust proxy-related ‘jumps’ occur at greater depths compared to what has been established by Rasmussen et al. (2014), thus possibly preceding temperature shifts (based on $\delta^{18}O$) by at least 5-10 years, suggesting that atmospheric transport of dust is not caused primarily by temperature changes, but preceded it.

This represents one of the major finding of the present work. The difference in uncertainty of the depth we assigned for the two transitions is simply related to the nature of these switches. In the first case, the dust proxies react abruptly to the warming phase and it is straightforward to establish where the starting point is located. This refines previous studies that showed

that climate can switch from DO stadial to interstadial in only three-five years (RH 7) (Fuhrer et al., 1999; Steffensen et al., 2008; Thomas et al., 2009). During the GS22-GI21 transition, proxies increase gradually and no clear mark can be unequivocally identified as a starting point of the cooling phase. Furthermore, immediately before and after the onset of GI21 we observe a high variability of the dust-related concentrations, which show several 'troughs' where the signal drops and rises very rapidly and with similar amplitude of GS22-GI21 transition itself. This has been previously observed in ice cores using electrical conductivity measurements (ECM) at GISP2 for the onset and termination of the Younger dryas (YD) (Taylor et al., 1993). These authors observed frequent brief and abruptly terminating (less than 5 yrs) periods during which the ECM returns to pre-transition values and therefore concluded that, instead of being rapid and smooth, Bolling-Allerod (B-A)/YD and YD/Holocene transitions are characterized by 'flickering' between preferred states. However, these features are possibly related to non-linear response of ice as it approaches acid/base neutrality and the possibility that they represent an artefact cannot be ruled out (Barker 2005).

Nevertheless, the same 'climate flickering' has been observed in proxies from annually-laminated lake sediment cores such as Lake Kråkenes in western Norway and from the Nordic seas (Bakke et al., 2009). These authors show that at the end of YD the climate shifted repeatedly from cold and dry to wet and less cold, from decade to decade, before interglacial conditions were finally reached and the climate system became more stable.

This phenomenon has been related to a re-ordering of the atmospheric circulation that could rapidly change the surface moisture, wind speeds and air-mass routing and, hence, change the quantity of airborne particles (Taylor et al., 1993). Bakke et al. (2009) suggests that the westerly wind system could drift northward, i.e. closer to their present-day positions, as a result of an influx of warm water. The winds thus brought relatively warm maritime air to Northern Europe, resulting in rising temperatures and melting of glaciers. However, the resulting input of fresh meltwater into the ocean caused the renewed formation of sea ice, which forced the westerly winds back to the south, cooling Northern Europe again. Further evidence of 'climate flickering'

has been found in sea-spray aerosol proxies such as Mg measured in stalagmite retrieved from a cave along the south coast of Spain (Baldini et al., 2015). The authors found considerable interannual-decadal variability of Mg anomaly in the Allerød, Holocene and half-way through the Early YD sections, reflecting the strength and position of the westerlies that reached their southernmost extent during the coldest part of the YD at 12.15 ka in agreement with evidence from more northerly sites (Bakke et al., 2009; Martin-Puertas et al., 2012). Baldini et al. (2015) also suggest that the northward shift of the polar front following a strengthening of the AMOC (Pearce et al., 2013) resulted in gradual northward migration of the ITCZ and a spatially heterogeneous change of the associated atmospheric circulation, including westerlies over Europe which therefore showed possible spatial and temporal 'flickering' of the their strength.

Similar features have been identified also in stalagmites from NALPS (Boch et al. 2011) for GS22-24 and GI-21-23 where $\delta^{18}O_{VPDB}$ profiles show intermittent climate swings consisting of short and abrupt warmings before GI 21 and 23 and of rapid warmings at the end of GI 21 and 25 at multidecadal to multiannual timescales.

The data confirm these observations, showing that the flickering switch for the GS22-GI21 transition completes an entire cycle from high to low and high concentrations again in less than three years (chapter 7), a timing that is comparable with the interstadial/stadial abrupt jump. I observe this pattern in most of the elements, and especially nssCa, not only across the DO22 transitions but also across the GI21 precursor event (or GI21.2) (chapter 5).

This evidence suggests that a flickering mechanism could characterize not only YD and DO22 but also other DO events, and possibly all of their transitions. The similarity in timing and magnitude of the flickering variability and the abrupt GI22-GS22 jump suggest that the mechanisms responsible of both phenomena is the same. This must include a change in atmospheric patterns from the sources of Greenland dust such as the Asian deserts (Svensson et al., 2000) to the North Pole as deduced from elemental ratios we obtained for DO22 (chapter 7). The patterns observed in our Ca/Al, Fe/Al

and Mg/Al ratios again show an abrupt change, indicating a switch in dust source for DO warming phases and a more gradual change for DO cooling phases (RH 8). The values are compatible with a range of source areas within the Asian deserts, and specifically a change from north/northwest dominating to more northeastern dominating sources from interstadial to stadial conditions (chapter 7). A modification of the Atlantic Meridional Overturning Circulation (AMOC) has been often suggested as one the most influencing driver of DO events in more than one way (Clark et al., 2002; Zickfield et al., 2007, Thornalley et al., 2013). However, there is still limited evidence that an AMOC collapse or weakening triggered all the 25 DO events (Böhm et al., 2015), perhaps suggesting that ocean circulation changes have less influence on Greenland climate than previously thought, especially during long stadials such as GS22 (Landais et al., 2015).

I propose here a simple model to describe our observation (Fig 8.1). During an interstadial period I suggest that the polar front shifts from ~60° to ~50 °N from summer to spring, similarly to the present day (Nagashima et al., 2011). In this situation (Fig. 8.1a), the only active source of Greenland dust is represented by the Taklamakan desert, which, due to its particular topography (Fig 8.1b), allows the uplifting of dust to high altitudes, where it can be transported north for thousands of km (Bory et al., 2003b). In stadial conditions (Fig 8.1c), the polar front moves south as well as the jet stream, possibly even southward of the Tibetan Plateau (Nagashima et al., 2011; Grigholm et al., 2015). Atmospheric circulation is strengthened over Asian deserts and the conditions shift to dry. As a result, more large particles are mobilized and transported to the Greenland ice cap (Fig 8.1d). This also explains the shift from north/northwest dominating to more northeastern dominating sources from interstadials to stadials. The variability we observe in the dataset can be assigned to few periodic components of 4-5 months, 1, 5, 10 and 25 years (chapter 7) and is compatible with previous studies on NGRIP ice cores (Svensson et al., 2011) and speleothems (Wang et al., 2001; Fleitmann et al., 2003, Baldini et al., 2015).

The shift of the polar front likely represents a consequence of a general cooling of the Northern Hemisphere entering the cold phase of a DO event.

Again, the strength of the East Asian Monsoon has been related to the AMOC (Sun et al., 2012). A brief review of the possible mechanisms responsible of these change is given in chapter 2.2.

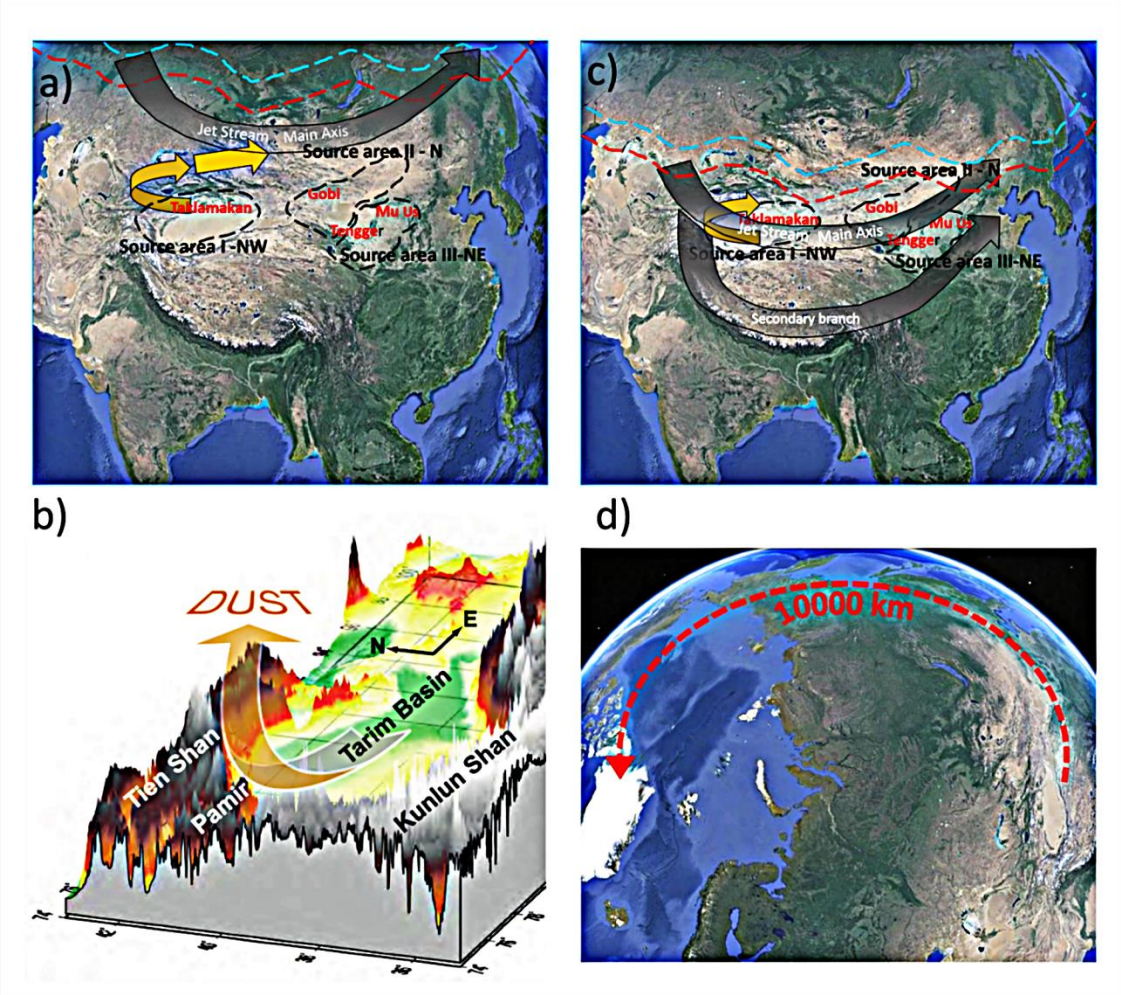

Figure 8.1: Dust transport to Greenland during Interstadial and stadial mode. a) *Interstadial* conditions: The Polar front is located north of the major Asian desert both during summer (blue dashed line) and spring (red dashed line), as well as the area of air advection, storm and jet stream formation. In this case only the dust coming from the Taklamakan desert reaches altitudes of more than 5000 m, where it can be carried by high-altitude winds (Bory et al. 2003b). (b) The characteristic topography of the Tarim basin, surrounded by high mountain belts which border the Taklamakan desert, facilitates the uplift of dust to high altitude [from Bory et al., 2014]. c) *Stadial* mode: Polar front moves south together with the area of storm and jet stream formation. The increase in strength of atmospheric circulation over the area of Asians deserts allow uplifting and transport of particles in greater number from different sources and of greater dimension. A possible secondary branch of jet stream is formed south of the Tibetan plateau. d) Pathway of dust from Asian deserts to Greenland.

The rapidity of the change in concentrations of LA-ICPMS dust and sea salt proxies, together with the evidence that the switch from full interstadial to full stadial conditions occurs earlier than $\delta^{18}O$ and therefore temperature, suggests that atmospheric transport presents possibly one of the fastest teleconnection with climate change triggering factors in the whole climate system and therefore is a pivotal parameter to unravel abrupt climate changes.

8.3 - Conclusions and Outlook

Development and application of cryo-cell UV-laser ablation mass spectrometry to Greenland ice cores for both ice physics and paleoclimatology has been the main objective of this work. Analysis of major element proxies for dust (Al, nssCa, Fe) and sea salt (Na, ssMg), which are present in the ice as impurities, has been successfully performed at the spatial resolution of 150-200 µm for a total of ~13 m of ice core from NGRIP, improving resolution of previous studies by a factor of more than 10. The project included the development of equipment to allow routine analysis of ice cores in frozen state via UV-laser ablation and to allow a safe handling, smoothing and cleaning of the ice samples as well as contamination removal. Calibration of the data was carried out using a set of external ice standards specifically created for this project from international aqueous solution using a custom-built ice-making mould. Ice standards show satisfactory homogeneity (<15 % RSD) compared to previous LA-ICPMS works (Reinhardt et al., 2001, 2003) providing an acceptable total uncertainty range between 15 and 20 % for UV-LA-ICPMS works on ice.

The main findings of the present work are here summarized:

1. A different pattern of distribution of impurities between clean and dusty ice has been highlighted, showing that impurities tend to lie preferentially on grain boundaries and junctions in clean ice layers but not in dusty ice.
2. Dust and sea salt proxies present abrupt variation in concentrations at the onset of DO warm and cold phases and also during minor warming

event as DO 21 precursor (GI21.2). For cold stadial to warm interstadial transitions the corresponding drop in dust and sea salt concentration takes place over the space of only 1 cm of ice, representing a single year of accumulation at this depth, and usually precedes temperature shifts, inferred by $\delta^{18}O$, by 5-10 years.

3. Warm to cold transitions show a greater variability in concentration of dust and sea salt proxies, which frequently flicker from cold-like to warm-like relative concentrations in as short as a single year ('climate flickering').
4. A change in source from stadial to interstadial conditions has been detected measuring Ca/Al, Fe/Al and Mg/Al ratios. We suggest that a southern shift of the polar front could account for this change and also for the observed variability in concentrations, as the atmospheric circulation strengthens over the main sources of Greenland dust (Asian deserts) during cold period, allowing uplifting and transport of more particles from mixed sources. The oscillatory nature of the data seems to confirm that periodic cycles are present with multidecadal, annual and sub-annual components.

For a better assessment of the nature of DO events at transitions further high-resolution work is required. Future work should include:

1. Obtaining $\delta^{18}O$ and δD profiles at a resolution of 2 mm to better assess the relative phasing of temperature/moisture proxies and dust/sea salt proxies.
2. Investigating DO event 20 in NGRIP ice core, with particular emphasis on detection of volcanogenic sulphur across the Toba eruption marker (74 ka).
3. Investigating DO 21-20 Antarctic counterparts (AIM 20-21), to better assess the relative phasing of these events between the two hemispheres.

References

Abram, N. J., Wolff, E. W., & Curran, M. A. (2013). A review of sea ice proxy information from polar ice cores. *Quaternary Science Reviews*, **79**, 168-183.

Adkins, J. F., Boyle, E. A., Keigwin, L., & Cortijo, E. (1997). Variability of the north atlantic thermohaline circulation during the last interglacial period. *Nature*, **390**(6656), 154-156.

Agassiz, L., & Bettannier, J. (1840). Etudes sur les glaciers. Jent et Gassmann.

Ahlmann H. W., Å.,Anders, & Fjeldstad, J. E. (1933). Scientific results of the swedish-norwegian arctic expedition in the summer of 1931, part IX-X. *Geografiska Annaler*, **15**, pp. 261-348.

Ahlmann H. W., Kulling, O., Håkon Mosby, & Scholander, P. F. (1936). Scientific results of the swedish-norwegian arctic expedition in the summer of 1931. part XII-XIV. *Geografiska Annaler*, **18**, pp. 1-33.

Ahlmann, H. W. (1934). The stratification of the snow and firn on Isachsen's plateau. Scientific Results of the Norwegian and Swedish Spitzbergen Expedition.

Ahn, J., & Brook, E. J. (2008). Atmospheric CO(2) and climate on millennial time scales during the last glacial period. *Science*, **322**(5898), 83-85.

Allen, J. R. M., & Huntley, B. (2000). Weichselian palynological records from southern europe: Correlation and chronology. *Quaternary International*, **73-4**, 111-125.

Alley, R. B., Meese, D. A., Shuman, C. A., Gow, A. J., Taylor, K. C., Grootes, P. M., White J.W.C., Ram M., Waddington E.M., Mayewski P.A. & Zielinski, G. A. (1993). Abrupt increase in Greenland snow accumulation at the end of the Younger Dryas event. *Nature – London* --, **362**, 527-527.

Alley, R. B., Perepezko, J. H., & Bentley, C. R. (1986). Grain-growth in polar ice .1. theory. *Journal of Glaciology*, **32**(112), 413-424.

Alley, R. B. (2000). Ice-core evidence of abrupt climate changes. *Proceedings of the National Academy of Sciences*, **97**(4), 1331-1334.

Alley, R. B. (2000b). The Younger Dryas cold interval as viewed from central Greenland. *Quaternary Science Reviews*, **19**(1), 213-226.

Alley, R. B., Anandakrishnan, S., & Jung, P. (2001). Stochastic resonance in the north atlantic. *Paleoceanography*, **16**(2), 190-198.

Alley, R. B., Clark, P. U., Huybrechts, P., & Joughin, I. (2005). Ice-sheet and sea-level changes. *Science*, **310**(5747), 456-460.

Alvarez-Solas, J., Charbit, S., Ritz, C., Paillard, D., Ramstein, G., & Dumas, C. (2010). Links between ocean temperature and iceberg discharge during heinrich events. *Nature Geoscience*, **3**(2), 122-126. doi:10.1038/NGEO752

Andersen, K.K., et al., (2004) High-resolution record of Northern Hemisphere climate extending into the last interglacial period. *Nature*,. **431**(7005): p. 147-151.

Andrews, J. T., & Barber, D. C. (2002). Dansgaard-oeschger events: Is there a signal off the hudson strait ice stream? *Quaternary Science Reviews*, **21**(1-3), 443-454.

Arnold, E., Merrill, J., Leinen, M., & King, J. (1998). The effect of source area and atmospheric transport on mineral aerosol collected over the north pacific ocean. *Global and Planetary Change*, **18**(3-4), 137-159.

Aubry, M. P., Van Couvering, J. A., Christie-Blick, N., Landing, E., Pratt, B. R., Owen, D. E., & Ferrusquía-Villafranca, I. (2009). Terminology of geological time: Establishment of a community standard. *Stratigraphy*, **6**(2), 100-105.

Baker, I., & Cullen, D. (2002). The structure and chemistry of 94 m greenland ice sheet project 2 ice. *Annals of Glaciology*, Vol 35, 35, 224-230.

Baker, I., & Cullen, D. (2003). SEM/EDS observations of impurities in polar ice: Artifacts or not? *Journal of Glaciology*, **49**(165), 184-190.

Baker, I., Cullen, D., & Iliescu, D. (2003). The microstructural location of impurities in ice. *Canadian Journal of Physics*, **81**(1-2), 1-9.

Baker, I., Iliescu, D., Obbard, R., Chang, H., Bostick, B., & Daghlian, C. P. (2005). Microstructural characterization of ice cores. *Annals of Glaciology*, Vol **42**, 2005, 42, 441-444.

Bakke, J., Lie, Ø., Heegaard, E., Dokken, T., Haug, G. H., Birks, H. H., Dulski P., and Nilsen, T. (2009). Rapid oceanic and atmospheric changes during the Younger Dryas cold period. *Nature Geoscience*, **2**(3), 202-205.

Baldini, L. M., McDermott, F., Baldini, J. U., Arias, P., Cueto, M., Fairchild, I. J.,. Hoffmannf D. L, Mattey D.P., Müller W., Nitaf D.C., Ontañónd R., Garciá-Moncód C. & Richards, D. A. (2015). Regional temperature, atmospheric circulation, and sea-ice variability within the Younger Dryas Event constrained using a speleothem from northern Iberia. *Earth and Planetary Science Letters*, **419**, 101-110.

Baldwin, M. P., Rhines, P. B., Huang, H., & McIntyre, M. E. (2007). The jet-stream conundrum. *Science*, **315**(5811), 467-468.

Bamber, J. L., Layberry, R. L., & Gogineni, S. P. (2001). A new ice thickness and bed data set for the Greenland ice sheet: 1. Measurement, data reduction, and errors. *Journal of Geophysical Research: Atmospheres* (1984–2012), **106**(D24), 33773-33780.

Barker, S. (2005). The 'flickering switch'of late Pleistocene climate change revisited. *Geophysical research letters*, **32**(24).

Barker, S., Diz, P., Vautravers, M. J., Pike, J., Knorr, G., Hall, I. R., & Broecker, W. S. (2009). Interhemispheric Atlantic seesaw response during the last deglaciation. *Nature*, **457**(7233), 1097-1102.

Barker, S., Knorr, G., Edwards, R. L., Parrenin, F., Putnam, A. E., Skinner, L. C., Wolff E. & Ziegler, M. (2011). 800,000 years of abrupt climate variability. *Science*, **334**(6054), 347-351.

Barker, S., Chen, J., Gong, X., Jonkers, L., Knorr, G., & Thornalley, D. (2015). Icebergs not the trigger for North Atlantic cold events. *Nature*, **520**(7547), 333-336.

Barnes, P. R. F., & Wolff, E. W. (2004). Distribution of soluble impurities in cold glacial ice. *Journal of Glaciology*, **50**(170), 311-324.

Barnes, P. R. F., Mulvaney, R., Robinson, K., & Wolff, E. W. (2002). Observations of polar ice from the holocene and the glacial period using the scanning electron microscope. *Annals of Glaciology*, **35**, 559-566.

Barnes, P. R. F., Mulvaney, R., Wolff, E. W., & Robinson, K. (2002). A technique for the examination of polar ice using the scanning electron microscope. *Journal of Microscopy-Oxford*, **205**, 118-124.

Barnes, P. R. F., Wolff, E. W., Mallard, D. C., & Mader, H. M. (2003). SEM studies of the morphology and chemistry of polar ice. *Microscopy Research and Technique*, **62**(1), 62-69.

Beer, J., Bonani, G., Hofmann, H. J., Suter, M., Synal, A., Wölfli, W., Oeschger H., Siegenthaler U. & Finkel, R. C. (1987). 10Be measurements on polar ice: Comparison of arctic and antarctic records. *Nuclear Instruments and Methods in Physics Research Section B: Beam Interactions with Materials and Atoms*, **29**(1–2), 203-206.

Belkin, I. M., Levitus, S., Antonov, J., & Malmberg, S. (1998). "Great salinity anomalies" in the North Atlantic. *Progress in Oceanography*, **41**(1), 1-68.

Benson, C. S. (1962). Stratigraphic studies in the snow and firn of the Greenland ice sheet. *Research Report*, **70** (Hanover, NH: USA Cold Regions Research and Engineering Laboratory)

Benzi, R., Sutera, A., & Vulpiani, A. (1981). The mechanism of stochastic resonance. *Journal of Physics A-Mathematical and General*, **14**(11), L453-L457.

Bernal, J. D., & Fowler, H. R. (1933). Cod id: 1011023. Crystallography Open Database,

Bestmann, M., & Prior, D. J. (2003). Intragranular dynamic recrystallization in naturally deformed calcite marble: Diffusion accommodated grain boundary sliding as a result of subgrain rotation recrystallization. *Journal of Structural Geology*, **25**(10), 1597-1613.

Bigler, M., Svensson, A., Kettner, E., Vallelonga, P., Nielsen, M. E., & Steffensen, J. P. (2011). Optimization of high-resolution continuous flow analysis for transient climate signals in ice cores. *Environmental science & technology*, **45**(10), 4483-4489.

Bjorck, S., Walker, M. J. C., Cwynar, L. C., Johnsen, S., Knudsen, K. L., Lowe, J. J. & Wohlfarth B. (1998). An event stratigraphy for the last termination in the north atlantic region based on the greenland ice-core record: A proposal by the INTIMATE group. *Journal of Quaternary Science*, **13**(4), 283-292.

Blake, W., Leuschen, C., Laird, C., & Dahl-Jensen, D. (2009). Ground based SAR survey of basal interface at NEEM drill site. *Geoscience and Remote Sensing Symposium,2009 IEEE International,IGARSS*, 2 II-594-II-597.

Blunier, T., & Brook, E. J. (2001). Timing of millennial-scale climate change in Antarctica and Greenland during the last glacial period. *Science*, 291(5501),

Blunier, T., Chappellaz, J., Schwander, J., Dallenbach, A., Stauffer, B., Stocker, T. F., Raynaud D., Jouzel J., Clausen H.B., Hammer C.U. & Johnsen, S. J. (1998). Asynchrony of Antarctic and Greenland climate change during the last glacial period. *Nature*, **394**(6695), 739-743.

Böhm, E., Lippold, J., Gutjahr, M., Frank, M., Blaser, P., Antz, B., Fohlmeister J., Frank N., Andersen M. B. & Deininger, M. (2015). Strong and deep Atlantic meridional overturning circulation during the last glacial cycle. *Nature*, **517**(7532), 73-76.

Bond, G., Broecker, W., Johnsen, S., McManus, J., Labeyrie, L., Jouzel, J., & Bonani, G. (1993). Correlations between climate records from North Atlantic sediments and Greenland ice. *Nature*, **365**, 143-147.

Bond, G. C., & Lotti, R. (1995). Iceberg discharges into the north-atlantic on millennial time scales during the last glaciation. *Science*, **267**(5200), 1005-1010.

Bond, G., Heinrich, H., Broecker, W., Labeyrie, L., Mcmanus, J., Andrews, J., Huon S., Jantschik R., Clasen S., Simet C., Tedesco K., Klas M., Bonani G., & Ivy, S. (1992). Evidence for massive discharges of icebergs into the North-Atlantic ocean during the last glacial period. *Nature*, **360**(6401), 245-249.

Bond, G., Kromer, B., Beer, J., Muscheler, R., Evans, M. N., Showers, W., Hoffmann S., Lotti-Bond R., Hajdas I. & Bonani, G. (2001). Persistent solar influence on north atlantic climate during the holocene. *Science*, **294**(5549), 2130-2136.

Bory, A. J. M., Abouchami, W., Galer, S. J., Svensson, A., Christensen, J. N., & Biscaye, P. E. (2014). A Chinese imprint in insoluble pollutants recently deposited in central Greenland as indicated by lead isotopes. *Environmental science & technology*, **48**(3), 1451-1457.

Bory, A. J. M., Biscaye, P. E., & Grousset, F. E. (2003a). Two distinct seasonal Asian source regions for mineral dust deposited in Greenland (NorthGRIP). *Geophysical Research Letters*, **30** (4)1167.

Bory, A. J. M., Biscaye, P. E., Piotrowski, A. M., & Steffensen, J. P. (2003b). Regional variability of ice core dust composition and provenance in Greenland. *Geochemistry Geophysics Geosystems*, **4**, 1107.

Boyle, E. A. (2000). Is ocean thermohaline circulation linked to abrupt stadial/interstadial transitions? *Quaternary Science Reviews*, **19**(1-5), 255-272.

Braun, H., Christl, M., Rahmstorf, S., Ganopolski, A., Mangini, A., Kubatzki, C., Roth K., Kromer, B. (2005). Possible solar origin of the 1,470-year glacial climate cycle demonstrated in a coupled model. *Nature*, **438**(7065), 208-211.

Broecker, W. (Ed.). (2009). The great ocean conveyor (*Princeton University Press ed*.). Princeton, New Jersey:

Broecker, W. S. (1991). Global change and oceanography programs. *Science*, **254**(5038), 1566-1566.

Broecker, W. S. (1994). Massive iceberg discharges as triggers for global climate-change. *Nature*, **372**(6505), 421-424.

Broecker, W. S. (1997). Thermohaline circulation, the achilles heel of our climate system: Will man-made CO2 upset the current balance? *Science*, **278**(5343), 1582-1588.

Broecker, W. S., & Hemming, S. (2001). Paleoclimate - climate swings come into focus. *Science*, **294**(5550), 2308-2309.

Broecker, W., Andree, M., Klas, M., Bonani, G., Wolfli, W., & Oeschger, H. (1988). New evidence from the south china sea for an abrupt termination of the last glacial period. *Nature*, **333**(6169),

Bromwich, D. H., Toracinta, E. R., Wei, H. L., Oglesby, R. J., Fastook, J. L., & Hughes, T. J. (2004). Polar MM5 simulations of the winter climate of the laurentide ice sheet at the LGM. *Journal of Climate*, **17**(17), 3415-3433.

Buchardt, S. L., & Dahl-Jensen, D. (2008). At what depth is the Eemian layer expected to be found at NEEM?. *Annals of Glaciology*, **48**(1), 100-102.

Burns, S. J., Fleitmann, D., Matter, A., Kramers, J., & Al-Subbary, A. A. (2003). Indian ocean climate and an absolute chronology over Dansgaard/Oeschger events 9 to 13. *Science*, **301**(5638), 1365-1367.

Calvo, E., Villanueva, J., Grimalt, J. O., Boelaert, A., & Labeyrie, L. (2001). New insights into the glacial latitudinal temperature gradients in the North Atlantic. results from U-37(K ') sea surface temperatures and terrigenous inputs. *Earth and Planetary Science Letters*, **188**(3-4), 509-519.

Capron, E., Landais, A., Lemieux-Dudon, B., Schilt, A., Masson-Delmotte, V., Buiron, D., Chappellaz J., Dahl-Jensens D., Johnsen S., Leuenberger M., , Loulergue L. & Oerter, H. (2010). Synchronising EDML and NorthGRIP ice cores using δ 18 O of atmospheric oxygen (δ 18 O atm) and CH 4 measurements over MIS5 (80–123 kyr). *Quaternary Science Reviews*, **29**(1), 222-234.

Clark, E. F. (1965). Camp Century evolution of concept and history of design construction and performance (No. TR-174). *COLD REGIONS RESEARCH AND ENGINEERING LAB HANOVER NH*, 1965.

Clark, P. U., Pisias, N. G., Stocker, T. F., & Weaver, A. J. (2002). The role of the thermohaline circulation in abrupt climate change. *Nature*, **415**(6874), 863-869.

COHMAP MEMBERS. (1988). Climatic changes of the last 18,000 years: Observations and model simulations. *Science*, **241**(4869), 1043-52.

Crowley T. J. (1992). North atlantic deep water cools the southern hemisphere. *Paleoceanography*, **7**, 489-497.

Cullen, D., & Baker, I. (2000). The chemistry of grain boundaries in greenland ice. *Journal of Glaciology*, **46**(155), 703-706.

Cullen, D., & Baker, I. (2001). Observation of impurities in ice. *Microscopy Research and Technique*, **55**(3), 198-207.

Cullen, D., & Baker, I. (2002). Observation of sulfate crystallites in Vostok accretion ice. *Materials Characterization*, **48**(4), 263-269.

Dahl-Jensen, D., Mosegaard, K., Gundestrup, N., Clow, G. D., Johnsen, S. J., Hansen, A. W., & Balling, N. (1998). Past temperatures directly from the Greenland ice sheet. *Science*, **282**(5387), 268-271.

Dahl-Jensen, D., et al. (2013). Eemian interglacial reconstructed from a Greenland folded ice core. *Nature*, **493**(7433), 489-494.

Dansgaard, W. (1952). Use of stable isotopes in biological research. [Stabile isotopers anvendelse i biologisk forskning.] *Ugeskrift for Laeger*, **114**(36), 1209-13.

Dansgaard, W., Nief, G., & Roth, E. (1960). Isotopic distribution in a Greenland iceberg. *Nature*, **185**, 232.

Dansgaard, W. (Ed.). (2004). Frozen annals. greenland ice cap research (The Department of Geophysics of The Niels Bohr Institute for Astronomy, Physics and Geophysics at The University of Copenhagen, Denmark. ed*.) Narayana Press*, Odder, Denmark.

Dansgaard, W., Clausen, H. B., & Aarkroga, A. (1966). The Si32 fallout in scandinavia. *Tellus*, **18**(2-3), 187-191.

Dansgaard, W., Johnsen, S. J., Clausen, H. B., Dahl-Jensen, D., Gundestrup, N., Hammer, C. U., & Oeschger, H. (1984). North atlantic climatic oscillations revealed by deep greenland ice cores. *Climate processes and climate sensitivity* (pp. 288-298) American Geophysical Union.

Dansgaard, W., Johnsen, S. J., Clausen, H. B., Dahl-Jensen, D., Gundestrup, N. S., Hammer, C. U., Hvidberg C. S., Steffensen J. P., Sveinbjörnsdottir, A. E., Jouzel, J., & Bond, G. (1993). Evidence for general instability of past climate from a 250-kyr ice-core record. *Nature*, **364**(6434), 218-220.

Dansgaard, W., Johnsen, S. J., Moller, J., & Langway, C. C. J. (1969). 1000 centuries of climatic record from camp century on the greenland ice sheet. *Science* (Washington D C), **166**(3903), 377-380.

Dansgaard, W., White, J. W. C., & Johnsen, S. J. (1989). The abrupt termination of the younger dryas climate event. *Nature*, **339**(6225), 532-534.

Dansgaard, W., (1954). The O18-abundance in fresh water. *Geochimica Et Cosmochimica Acta*, **6**(5-6), 241-260.

De Angelis, M., Steffensen, J. P., Legrand, M., Clausen, H., & Hammer, C. (1997). Primary aerosol (sea salt and soil dust) deposited in Greenland ice during the last climatic cycle: Comparison with east antarctic records. *Journal of Geophysical Research: Oceans*, **102**(C12), 26681-26698.

Deangelis, M., Barkov, N. I., & Petrov, V. N. (1992). Sources of continental dust over antarctica during the last glacial cycle. *Journal of Atmospheric Chemistry*, **14**(1-4), 233-244.

Della Lunga, D., Müller, W., Rasmussen, S. O., & Svensson, A. (2014). Location of cation impurities in NGRIP deep ice revealed by cryo-cell UV-laser-ablation ICPMS. Journal of Glaciology, 60(223), 970-988.

Della Lunga, D., Müller W., Rasmussen S. O., Svensson A. S., Vallelonga P. T., (2015a). Calibrated cryo-cell UV-LA-ICPMS elemental concentra-tions in NGRIP ice reveal abrupt, sub-annual shift in dust across D-O 21 precursor event. Planned submission to *Journal of Quaternary Science*.

Della Lunga, D., Müller W., Rasmussen S. O., Svensson A. S.(2015b). 3-D mapping of cation impurities in deep NGRIP ice. Planned submission to *The cryosphere*.

Della Lunga, D., Müller W., Rasmussen S. O., Svensson A. S. Vallelonga P. T., Steffensen J.P., (2015c). High resolution UV-LA-ICPMS analysis of dust and sea salt proxies in deep glacial ice: a complete survey of Greenland Stadial 22 transitions. Planned submission to *Nature communications*.

Denton, G. H., Alley, R. B., Comer, G. C., & Broecker, W. S. (2005). The role of seasonality in abrupt climate change. *Quaternary Science Reviews*, **24**(10), 1159-1182.

Derbyshire, E. (2003). Loess, and the dust indicators and records of terrestrial and marine palaeoenvironments (DIRTMAP) database. *Quaternary Science Reviews*, **22**(18–19), 1813-1819.

Dickson, R. R., Meincke, J., Malmberg, S., & Lee, A. J. (1988). The “great salinity anomaly” in the northern North Atlantic 1968–1982. *Progress in Oceanography*, 20(2), 103-151.

Ditlevsen, P. D., Andersen, K. K., & Svensson, A. (2007). The DO-climate events are probably noise induced: Statistical investigation of the claimed 1470 years cycle. *Climate of the Past*, **3**(1), 129-134.

Dokken, T. M., & Jansen, E. (1999). Rapid changes in the mechanism of ocean convection during the last glacial period. *Nature*, **401**(6752), 458-461.

Dokken, T. M., Nisancioglu, K. H., Li, C., Battisti, D. S., & Kissel, C. (2013). Dansgaard-Oeschger cycles: Interactions between ocean and sea ice intrinsic to the Nordic seas. *Paleoceanography*, **28**(3), 491-502.

Durand, G., Weiss, J., Lipenkov, V., Barnola, J. M., Krinner, G., Parrenin, F., Del Monte, B., Ritz, C., Duval, R., Rothlisberger, R., Bigler, M. (2006). Effect of impurities on grain growth in cold ice sheets. *Journal of Geophysical Research-Earth Surface* **111**(F1).

Duval, P., & Castelnau, O. (1995). Dynamic recrystallization of ice in polar ice sheets. *Journal De Physique IV*, **5**(C3), 197-205.

Dwyer, G. S., & Chandler, M. A. (2009). Mid-pliocene sea level and continental ice volume based on coupled benthic Mg/Ca palaeotemperatures and oxygen isotopes. *Philosophical Transactions of the Royal Society A-Mathematical Physical and Engineering Sciences*, **367**(1886), 157-168.

Dykoski, C. A., Edwards, R. L., Cheng, H., Yuan, D., Cai, Y., Zhang, M., Lin Y., Qing J., An Z. & Revenaugh, J. (2005). A high-resolution, absolute-dated Holocene and deglacial Asian monsoon record from Dongge Cave, China. *Earth and Planetary Science Letters*, **233**(1), 71-86.

Ehlers, J., & Gibbard, P. L. (2003). Extent and chronology of glaciations. *Quaternary Science Reviews*, **22**(15), 1561-1568.

Ehlers, J., & Gibbard, P. L. (2004). Quaternary glaciations: extent and chronology. 475 pp.

Ehlers, J., & Gibbard, P. L. (2007). The extent and chronology of Cenozoic global glaciation. *Quaternary International*, **164**, 6-20.

EPICA community members (2004). "Eight glacial cycles from an Antarctic ice core." *Nature* **429**.6992: 623-628.

EPICA community members (2006). One-to-one coupling of glacial climate variability in Greenland and Antarctica. *Nature*, **444**(7116), 195-198.

Evans, D., & Müller, W. (2012). Deep time foraminifera Mg/Ca paleothermometry: Nonlinear correction for secular change in seawater Mg/Ca. *Paleoceanography*, **27**(4).

Faria, S. H., Weikusat, I., & Azuma, N. (2014). The microstructure of polar ice. Part II: state of the art. *Journal of Structural Geology*, **61**, 21-49.

Felzer, B. (2001). Climate impacts of an ice sheet in east siberia during the last glacial maximum. *Quaternary Science Reviews*, **20**(1–3), 437-447.

Fenger, M., Sørensen, L. L., Kristensen, K., Jensen, B., Nguyen, Q. T., Nøjgaard, J. K., Massling, A., Skov, H., Becker, T., and Glasius, M. (2013). Sources of

anions in aerosols in northeast Greenland during late winter. *Atmos. Chem. Phys*., **13**, 1569-1578,

Field, J. P., Belnap, J., Breshears, D. D., Neff, J. C., Okin, G. S., Whicker, J. J., .Painter T.H., Ravi S., Reheis M.C. & Reynolds, R. L. (2010). The ecology of dust. *Frontiers in Ecology and the Environment*, **8**(8), 423-430.

Fischer, H., Siggaard-Andersen, M., Ruth, U., Rothlisberger, R., & Wolff, E. (2007). Glacial/interglacial changes in mineral dust and sea-salt records in polar ice cores: Sources, transport, and deposition. *Reviews of Geophysics*, **45**(1), RG1002.

Fleitmann, D., Burns, S. J., Mangini, A., Mudelsee, M., Kramers, J., Villa, I., Neff U., Al-Subbary A.A., Buettner A., Hippler D. & Matter, A. (2007). Holocene ITCZ and indian monsoon dynamics recorded in stalagmites from oman and Yemen (Socotra). *Quaternary Science Reviews*, **26**(1-2), 170-188.

Fluckiger, J., Dallenbach, A., Blunier, T., Stauffer, B., Stocker, T. F., Raynaud, D., & Barnola, J. M. (1999). Variations in atmospheric N2O concentration during abrupt climatic changes. *Science*, **285**(5425), 227-230.

Frey, D. G. (1962). Cladocera from the Eemian interglacial of Denmark. *Journal of Paleontology*, 1133-1154.

Fronval, T., Jansen, E., Bloemendal, J., & Johnsen, S. (1995). Oceanic evidence for coherent fluctuations in fennoscandian and Laurentide ice sheets on millennium timescales. *Nature*, **374**(6521), 443-446.

Fuhrer, K., Wolff, E. W., & Johnsen, S. J. (1999). Timescales for dust variability in the greenland ice core project (GRIP) ice core in the last 100,000 years. *Journal of Geophysical Research-Atmospheres*, **104**(D24), 31043-31052.

Ganopolski, A., & Rahmstorf, S. (2001). Rapid changes of glacial climate simulated in a coupled climate model. *Nature*, **409**(6817), 153-158.

Ganopolski, A., & Rahmstorf, S. (2002). Abrupt glacial climate changes due to stochastic resonance. *Physical Review Letters*, **88**(3), 038501.

Genthon, C. (1992). Simulations of the long-range transport of desert dust and sea-salt in a general-circulation model. In *SCHWARTZ S. S.,WGN* (Ed.).

Gkinis, V., Simonsen, S. B., Buchardt, S. L., White, J. W. C., & Vinther, B. M. (2014). Water isotope diffusion rates from the NorthGRIP ice core for the last 16,000 years - glaciological and paleoclimatic implications. *Earth and Planetary Science Letters*, **405**, 132-141.

Gong, X., Zhang, X., Lohmann, G., Wei, W., Zhang, X., & Pfeiffer, M. (2015). Higher Laurentide and Greenland ice sheets strengthen the North Atlantic ocean circulation. *Climate Dynamics*, 1-12.

Goñi, M. F. S., Turon, J. L., Eynaud, F., & Gendreau, S. (2000). European climatic response to millennial-scale changes in the atmosphere–ocean system during the last glacial period. *Quaternary Research*, **54**(3), 394-403.

Gow, A. J., & Williamson, T. (1976). Rheological implications of internal structure and crystal fabrics of west antarctic ice sheet as revealed by deep core drilling at Byrd-station. *Geological Society of America Bulletin*, **87**(12), 1665-1677.

Gow, A. J., Meese, D. A., Alley, R. B., Fitzpatrick, J. J., Anandakrishnan, S., Woods, G. A., & Elder, B. C. (1997). Physical and structural properties of the Greenland ice sheet project 2 ice core: A review. *Journal of Geophysical Research-Oceans*, **102**(C12), 26559-26575.

Grigholm, B., Mayewski, P. A., Kang, S., Zhang, Y., Morgenstern, U., Schwikowski, M., Kaspari S., Aizen V., Aizen E., Takeuchi N., Maasch K.A., Birkel S., Handley M. & Sneed, S. (2015). 20th Century Dust Lows and the Weakening of the Westerly Winds over the Tibetan Plateau. *Geophysical Research Letters*. In press.

Grootes, P. M., Stuiver, M., White, J. W. C., Johnsen, S., & Jouzel, J. (1993). Comparison of oxygen-isotope records from the gisp2 and grip Greenland ice cores. *Nature*, **366**(6455), 552-554.

Grousset, F. E., Rognon, P., Coudegaussen, G., & Pedemay, P. (1992). Origins of peri-saharan dust deposits traced by their nd and sr isotopic composition. *Palaeogeography Palaeoclimatology Palaeoecology*, **93**(3-4), 203-212.

Grover, S. N., & Beard, K. V. (1974). Numerical computation of collision efficiency of raindrops colliding with aerosol-particles and cloud drops. *Bulletin of the American Meteorological Society*, **55**(6), 677-677.

Guillope, M., & Poirier, J. P. (1979). Dynamic recrystallization during creep of single-crystalline halite: An experimental study. *Journal of Geophysical Research: Solid Earth*, **84**(B10), 5557-5567.

Gwiazda, R. H., Hemming, S. R., & Broecker, W. S. (1996). Provenance of icebergs during Heinrich event 3 and the contrast to their sources during other Heinrich episodes. *Paleoceanography*, **11**(4), 371-378.

Hanna, E., Fettweis, X., Mernild, S. H., Cappelen, J., Ribergaard, M. H., Shuman, C. A., Steffen K., Wood L. & Mote, T. L. (2014). Atmospheric and oceanic

climate forcing of the exceptional greenland ice sheet surface melt in summer 2012. *International Journal of Climatology*, **34**(4), 1022-1037.

Hawkins, E., Smith, R. S., Allison, L. C., Gregory, J. M., Woollings, T. J., Pohlmann, H., & De Cuevas, B. (2011). Bistability of the Atlantic overturning circulation in a global climate model and links to ocean freshwater transport. *Geophysical Research Letters*, **38**(10).

He, Y. D., & Price, P. B. (1998). Remote sensing of dust in deep ice at the south pole. *Journal of Geophysical Research-Atmospheres*, **103**(D14), 17041-17056.

Heinrich, H. (1988). Origin and consequences of cyclic ice rafting in the northeast atlantic-ocean during the past 130,000 years. *Quaternary Research*, **29**(2), 142-152.

Hemming, S. R. (2004). Heinrich events: Massive late Pleistocene detritus layers of the North Atlantic and their global climate imprint. *Reviews of Geophysics*, **42**(1).

Hendy, I. L., & Kennett, J. P. (2000). Dansgaard-Oeschger cycles and the California current system: Planktonic foraminiferal response to rapid climate change in Santa Barbara basin, ocean drilling program hole 893A. *Paleoceanography*, **15**(1), 30-42.

Hewitt, C. D., Stouffer, R. J., Broccoli, A. J., Mitchell, J. F. B., & Valdes, P. J. (2003). The effect of ocean dynamics in a coupled GCM simulation of the last glacial maximum. *Climate Dynamics*, **20**(2-3), 203-218.

Hillamo, R. E., Kerminen, V. -., Maenhaut, W., Jaffrezo, J. -., Balachandran, S., & Davidson, C. I. (1993). Size distributions of atmospheric trace elements at dye 3, Greenland — I. distribution characteristics and dry deposition velocities. *Atmospheric Environment.Part A.General Topics*, **27**(17–18), 2787-2802.

Hillert, M. (1965). On the theory of normal and abnormal grain growth. *Acta Metallurgica*, **13**(3), 227-238.

Hobbs P.V., . (1974). Ice physics. *Oxford Univeristy Press*, N.Y, 874 p.

Huber, C., Leuenberger, M., Spahni, R., Flückiger, J., Schwander, J., Stocker, T. F., Johnsen S. J., Landais A. & Jouzel, J. (2006). Isotope calibrated Greenland temperature record over Marine Isotope Stage 3 and its relation to CH 4. *Earth and Planetary Science Letters*, **243**(3), 504-519.

Huon, S., & Jantschik, R. (1993). Detrital silicates in northeast Atlantic deep-sea sediments during the late quaternary - major-element, ree and rb-sr isotopic data. *Eclogae Geologicae Helvetiae*, **86**(1), 195-218.

Husar, R. B., Tratt, D. M., Schichtel, B. A., Falke, S. R., Li, F., Jaffe, D., Gassó S., Gill T., Laulainen N. S., Lu F., Reheis M. C.,. Chun Y, Westphal D., Holben B. N., Gueymard C., McKendry I., Kuring N.,. Feldman G. C, McClain C., Frouin R. J., Merrill J., DuBois D., Vignola F., Murayama T., Nickovic S., Wilson W. E,. Sassen K., Sugimoto N. & Malm W. C. (2001). Asian dust events of april 1998. *Journal of Geophysical Research: Atmospheres*, **106**(D16), 18317-18330.

Iizuka, Y., Horikawa, S., Sakurai, T., Johnson, S., Dahl-Jensen, D., Steffensen, J. P., & Hondoh, T. (2008). A relationship between ion balance and the chemical compounds of salt inclusions found in the Greenland Ice Core Project and Dome Fuji ice cores. *Journal of Geophysical Research: Atmospheres*, **113**(D7).

Iizuka, Y., Takata, M., Hondoh, T., & Fujii, Y. (2004). High-time-resolution profiles of soluble ions in the last glacial period of a Dome Fuji (Antarctica) deep ice core. *Annals of Glaciology*, **39**(1), 452-456.

Iliescu, D., & Baker, I. (2008). Effects of impurities and their redistribution during recrystallization of ice crystals. *Journal of Glaciology*, **54**(185), 362-370.

Itambi, A. C., von Dobeneck, T., Mulitza, S., Bickert, T., & Heslop, D. (2009). Millennial-scale northwest african droughts related to heinrich events and dansgaard-oeschger cycles: Evidence in marine sediments from offshore senegal. *Paleoceanography*, **24**, PA1205.

Jantschik, R., & Huon, S. (1992). Detrital silicates in northeast Atlantic deep-sea sediments during the late quaternary - mineralogical and K-ar isotopic data. *Eclogae Geologicae Helvetiae*, **85**(1), 195-212.

Jennings, A. E., Hald, M., Smith, M., & Andrews, J. T. (2006). Freshwater forcing from the greenland ice sheet during the younger dryas: Evidence from southeastern greenland shelf cores. *Quaternary Science Reviews*, **25**(3-4), 282-298.

Johnsen, S. J., Clausen, H. B., Dansgaard, W., Fuhrer, K., Gundestrup, N., Hammer, C. U., Iversen P., Jouzel J., Stauffer B., Steffensen, J. P. (1992). Irregular glacial interstadials recorded in a new greenland ice core. *Nature*, **359**(6393), 311-313.

Johnsen, S. J., Clausen, H. B., Dansgaard, W., Gundestrup, N. S., Hammer, C. U., & Tauber, H. (1995). The Eem stable isotope record along the GRIP ice core and its interpretation. *Quaternary Research*, **43**(2), 117-124.

Johnsen, S. J., DahlJensen, D., Gundestrup, N., Steffensen, J. P., Clausen, H. B., Miller, H., Masson-Delmotte V., Sveinbjörnsdottir A.E. & White, J. (2001). Oxygen isotope and palaeotemperature records from six Greenland ice-core

stations: Camp century, dye-3, GRIP, GISP2, Renland and NorthGRIP. *Journal of Quaternary Science*, **16**(4), 299-307.

Johnson, R. G., & Lauritzen, S. E. (1995). Hudson bay-Hudson strait jokulhlaups and Heinrich events - a hypothesis. *Palaeogeography Palaeoclimatology Palaeoecology*, **117**(1-2), 123-137.

Jouzel J., V. Masson-Delmotte, O. Cattani, G. Dreyfus, S. Falourd, G. Hoffmann, B. Minster, J. Nouet, J. M. Barnola, J. Chappellaz, H. Fischer, J. C. Gallet, S. Johnsen, M. Leuenberger, L. Loulergue, D. Luethi, H. Oerter, F. Parrenin, G. Raisbeck, D. Raynaud, A. Schilt, J. Schwander, E. Selmo, R. Souchez, R. Spahni, B. Stauffer, J. P. Steffensen, B. Stenni, T. F. Stocker, J. L. Tison, M. Werner, and E. W. Wolff, (2007). Orbital and millennial Antarctic climate variability over the past 800,000 years. *Science*, **317**(5839), 793-796.

Jouzel, J. (2011). Willi Dansgaard: From isotopes to ice. *Nature Geoscience*, **4**(3), 138-138.

Kageyama, M., & Paillard, D. (2005). Dansgaard-Oeschger events: An oscillation of the climate-ice-sheet system? *Comptes Rendus Geoscience*, **337**(10-11), 993-1000.

Kageyama, M., Valdes, P. J., Ramstein, G., Hewitt, C., & Wyputta, U. (1999). Northern hemisphere storm tracks in present day and last glacial maximum climate simulations: A comparison of the european PMIP models. *Journal of Climate*, **12**(3), 742-760.

Kim, J. H., Romero, O. E., Lohmann, G., Donner, B., Laepple, T., Haam, E., & Damste, J. S. S. (2012). Pronounced subsurface cooling of North Atlantic waters off Northwest Africa during Dansgaard–Oeschger interstadials. *Earth and Planetary Science Letters*, **339**, 95-102.

Kissel, C., Laj, C., Piotrowski, A. M., Goldstein, S. L., & Hemming, S. R. (2008). Millennial-scale propagation of Atlantic deep waters to the glacial Southern Ocean. *Paleoceanography*, **23**(2).

Kohfeld, K. E., & Harrison, S. P. (2001). DIRTMAP: The geological record of dust. *Earth-Science Reviews*, **54**(1–3), 81-114.

Kutzbach, J. E., & Guetter, P. J. (1986). The influence of changing orbital parameters and surface boundary-conditions on climate simulations for the past 18000 years. *Journal of the Atmospheric Sciences*, **43**(16), 1726-1759.

Lachniet, M. S. (2009). Climatic and environmental controls on speleothem oxygen-isotope values. *Quaternary Science Reviews*, **28**(5-6), 412-432.

Landais, A., Masson-Delmotte, V., Stenni, B., Selmo, E., Roche, D. M., Jouzel, J., Lambert F., Guillevic M., Bazin L., Arzel O., Vinther B., Gkinis V. & Popp, T.

(2015). A review of the bipolar see–saw from synchronized and high resolution ice core water stable isotope records from Greenland and East Antarctica. *Quaternary Science Reviews*, **114**, 18-32.

Langway, C. C., & Shoji, H. (1985). Comparison of mechanical tests on the dye-3, Greenland ice core and artificial laboratory ice. *Annals of Glaciology*, **6**, 305-305.

Lenton, T. M., Held, H., Kriegler, E., Hall, J. W., Lucht, W., Rahmstorf, S., & Schellnhuber, H. J. (2008). Tipping elements in the Earth's climate system. *Proceedings of the National Academy of Sciences*, **105**(6), 1786-1793.

Li, C., Battisti, D. S., & Bitz, C. M. (2010). Can North Atlantic Sea Ice Anomalies Account for Dansgaard-Oeschger Climate Signals? *Journal of Climate*, **23**(20), 5457-5475.

Li, C., Battisti, D. S., Schrag, D. P., & Tziperman, E. (2005). Abrupt climate shifts in Greenland due to displacements of the sea ice edge. *Geophysical Research Letters*, **32**(19).

Löfverström, M., Caballero, R., Nilsson, J., & Kleman, J. (2014). Evolution of the large-scale atmospheric circulation in response to changing ice sheets over the last glacial cycle. *Climate of the Past*, **10**(4), 1453-1471.

Lücke, K., and Stüwe, H. P. (1971.). On the theory of impurity controlled grain boundary motion. *Acta Met*., **19**(1087-1099)

Macayeal, D. R. (1993). A low-order model of the heinrich event cycle. *Paleoceanography*, **8**(6), 767-773.

Madureira, L. A. S., vanKreveld, S. A., Eglinton, G., Conte, M., Ganssen, G., vanHinte, J. E., & Ottens, J. J. (1997). Late quaternary high-resolution biomarker and other sedimentary climate proxies in a northeast atlantic core. *Paleoceanography*, **12**(2), 255-269.

Manabe, S., & Broccoli, A. J. (1985). The influence of continental ice sheets on the climate of an ice age. *Journal of Geophysical Research: Atmospheres* (1984–2012), **90(**D1), 2167-2190.

Manabe, S., & Stouffer, R. J. (1997). Climate variability of a coupled ocean-atmosphere-land surface model: Implication for the detection of global warming - the walter orr roberts lecture. *Bulletin of the American Meteorological Society*, **78**(6), 1177-1185.

Martin-Puertas, C., Brauer, A., Dulski, P., & Brademann, B. (2012). Testing climate–proxy stationarity throughout the Holocene: an example from the varved sediments of Lake Meerfelder Maar (Germany). *Quaternary Science Reviews*, **58**, 56-65.

Mayewski, P. A., Sneed, S. B., Birkel, S. D., Kurbatov, A. V., & Maasch, K. A. (2014). Holocene warming marked by abrupt onset of longer summers and reduced storm frequency around Greenland. *Journal of Quaternary Science*, **29**(1), 99-104.

McGee, W. D. (2010). Reconstructing and interpreting the dust record and probing the plumbing of Mono Lake. *Nature*, **383**, 705-707.

Mcmanus, J. F., Bond, G. C., Broecker, W. S., Johnsen, S., Labeyrie, L., & Higgins, S. (1994). High-resolution climate records from the north-Atlantic during the last interglacial. *Nature*, **371**(6495), 326-329.

Meeker, L. D., Mayewski, P. A., Twickler, M. S., Whitlow, S. I., & Meese, D. (1997). A 110,000-year history of change in continental biogenic emissions and related atmospheric circulation inferred from the greenland ice sheet project ice core. *Journal of Geophysical Research-Oceans*, **102**(C12), 26489-26504.

Menviel, L., Timmermann, A., Friedrich, T., & England, M. H. (2014). Hindcasting the continuum of Dansgaard–Oeschger variability: mechanisms, patterns and timing. *Climate of the Past*, **10**(1), 63-77.

Muhs, D. R., Budahn, J. R., McGeehin, J. P., Bettis, E. A., Skipp, G., Paces, J. B., & Wheeler, E. A. (2013). Loess origin, transport, and deposition over the past 10,000 years, Wrangell-St. Elias National Park, Alaska. *Aeolian Research*, **11**, 85-99.

Müller, W., Shelley, M., Miller, P., & Broude, S. (2009). Initial performance metrics of a new custom-designed ArF excimer LA-ICPMS system coupled to a two-volume laser-ablation cell. *Journal of Analytical Atomic Spectrometry*, **24**(2), 209-214.

Müller, W., Shelley, J. M. G., & Rasmussen, S. O. (2011). Direct chemical analysis of frozen ice cores by UV-laser ablation ICPMS. *Journal of Analytical Atomic Spectrometry*, **26**(12), 2391-2395.

Mulvaney, R., Alemany, O., & Possenti, P. (2007). The Berkner island (Antarctica) ice-core drilling project. *Annals of Glaciology*, **47**, 115-124.

Mulvaney, R., Wolff, E. W., & Oates, K. (1988). Sulfuric-acid at grain-boundaries in antarctic ice. *Nature*, **331**(6153), 247-249.

Nagashima, K., Tada, R., Tani, A., Sun, Y., Isozaki, Y., Toyoda, S., & Hasegawa, H. (2011). Millennial-scale oscillations of the westerly jet path during the last glacial period. *Journal of Asian Earth Sciences*, **40**(6), 1214-1220.

National Research Council. Geoscience Data and Collections: National Resources in Peril. Washington, DC: *The National Academies Press*, 2002.

Obbard, R., & Baker, I. (2007). The microstructure of meteoric ice from Vostok, antarctica. *Journal of Glaciology*, **53**(180), 41-62.

Obbard, R., Baker, I., & Iliescu, D. (2006). Grain boundary grooving in ice in a scanning electron microscope. *Journal of Glaciology*, **52**(176), 169-172.

Obbard, R., Baker, I., & Sieg, K. (2006). Using electron backscatter diffraction patterns to examine recrystallization in polar ice sheets. *Journal of Glaciology*, **52**(179), 546-557.

Obbard, R., Iliescu, D., Baker, I., & Cullen, D. (2003). In Weertman, JR Fine, M Faber, K King, W Liaw,P. (Ed.), A technique for the scanning electron microscopy and microanalysis of uncoated ice crystals

Obbard, R., Iliescu, D., Cullen, D., Chang, J., & Baker, I. (2003). SEM/EDS comparison of polar and seasonal temperate ice. *Microscopy Research and Technique*, **62**(1), 49-61.

Ohno, H., Igarashi, M., & Hondoh, T. (2005). Salt inclusions in polar ice core: Location and chemical form of water-soluble impurities. *Earth and Planetary Science Letters*, **232**(1-2), 171-178.

Pasteur, E. C., & Mulvaney, R. (2000). Migration of methane sulphonate in antarctic firn and ice. *Journal of Geophysical Research-Atmospheres*, 105(D9), 11525-11534.

Paterson W.S.B. (1994). THE PHYSICS OF GLACIERS, third edition. elsevier, oxford, new york and tokyo, 1994. *Earth Surface Processes and Landforms*, **21**(10), 980-981.

Pearce, C., Seidenkrantz, M. S., Kuijpers, A., Massé, G., Reynisson, N. F., & Kristiansen, S. M. (2013). Ocean lead at the termination of the Younger Dryas cold spell. *Nature communications*, **4**, 1664.

Peel, D. A., & Mulvaney, R. (1992). Time-trends in the pattern of ocean-atmosphere exchange in an ice core from the weddell sea sector of antarctica. *Tellus Series B-Chemical and Physical Meteorology*, **44**(4), 430-442.

Péguy, C. (1951). Les premiers enseignements morphologiques des expéditions polaires françaises (d'après M. boye). *Revue De Géographie Alpine*, **39**(3), 595-598.

Peltier, W. R., & Vettoretti, G. (2014). Dansgaard-Oeschger oscillations predicted in a comprehensive model of glacial climate: A “kicked” salt oscillator in the Atlantic. *Geophysical Research Letters*, **41**(20), 7306-7313.

Petersen, S. V., Schrag, D. P., & Clark, P. U. (2013). A new mechanism for Dansgaard-Oeschger cycles. *Paleoceanography*, **28**(1), 24-30.

Petit, J. R., Mounier, L., Jouzel, J., Korotkevich, Y. S., Kotlyakov, V. I., & Lorius, C. (1990). Palaeoclimatological and chronological implications of the vostok core dust record. *Nature*, **343**(6253), 56-58.

Pfahl, S., & Sodemann, H. (2014). What controls deuterium excess in global precipitation?. *Climate of the Past*, **10**(2), 771-781.

Pollard, D. (2010). A retrospective look at coupled ice sheet-climate modeling. *Climatic Change*, **100**(1), 173-194.

Porter, S. C. (2001). Chinese loess record of monsoon climate during the last glacial-interglacial cycle. *Earth-Science Reviews*, 54(1-3), 115-128.

Prospero, J. M. (1990). Mineral-aerosol transport to the north-Atlantic and north Pacific - the impact of african and asian sources. In *KNAP A. K.,MS* (Ed.),

Prospero, J. M., Charlson, R. J., Mohnen, V., Jaenicke, R., Delany, A. C., Moyers, J., Zoller W. & Rahn, K. (1983). The atmospheric aerosol system - an overview. *Reviews of Geophysics*, 21(7), 1607-1629.

Prospero, J. M., Ginoux, P., Torres, O., Nicholson, S. E., & Gill, T. E. (2002). Environmental characterization of global sources of atmospheric soil dust identified with the nimbus 7 total ozone mapping spectrometer (TOMS) absorbing aerosol product. *Reviews of Geophysics*, **40**(1), 1002.

Pye, K. (1995). The nature, origin and accumulation of loess. *Quaternary Science Reviews*, 14(7-8), 653-667.

Rahmstorf, S. (2002). Ocean circulation and climate during the past 120,000 years. *Nature*, **419**(6903), 207-214.

Rahmstorf, S. (2003). The current climate. *Nature*, **421**(6924), 699-699.

Rahmstorf, S. (2003). Timing of abrupt climate change: A precise clock. *Geophysical Research Letters*, **30**(10), 1510.

Rankin, A. M., Wolff, E. W., & Martin, S. (2002). Frost flowers: Implications for tropospheric chemistry and ice core interpretation. *Journal of Geophysical Research-Atmospheres*, **107**(D23), 4683.

Rankin, A. M., Wolff, E. W., & Mulvaney, R. (2004). A reinterpretation of sea-salt records in Greenland and Antarctic ice cores?. *Annals of Glaciology*, Volume **39**.(1), pp. 276-282(7).

Rasmussen, S. O., Abbott, P. M., Blunier, T., Bourne, A. J., Brook, E., Buchardt, S. L., Buizert, C., Chappellaz, J., Clausen, H. B., Cook, E., Dahl-Jensen, D.,

Davies, S. M., Guillevic, M., Kipfstuhl, S., Laepple, T., Seierstad, I. K., Severinghaus, J. P., Steffensen, J. P., Stowasser, C., Svensson, A., Vallelonga, P., Vinther, B. M., Wilhelms, F., and Winstrup, M.: A first chronology for the North Greenland Eemian Ice Drilling (NEEM) ice core, *Clim. Past*, **9**, 2713-2730

Rasmussen, S. O., Bigler, M., Blockley, S. P., Blunier, T., Buchardt, S. L., Clausen, H. B., Cvijanovic I., Dahl-Jensen D., Johnsen S.J., Fischer H., Gkinis V., Guillevic M., Hoel W. Z., Lowe J. J., Pedro J. B., Popp T., Seierstad I. K>, Steffensen J. P., Svensson A. M., Vallelonga P., Vinther M., Walker J. C., Whetley J.J., Winstrup, M. (2014). A stratigraphic framework for abrupt climatic changes during the last glacial period based on three synchronized greenland ice-core records: Refining and extending the INTIMATE event stratigraphy. *Quaternary Science Reviews*, **106**, 14-28.

Raynaud, D., Chappellaz, J., Ritz, C., & Martinerie, P. (1997). Air content along the Greenland Ice Core Project core: A record of surface climatic parameters and elevation in central Greenland. *Journal of Geophysical Research: Oceans* **102**(C12), 26607-26613.

Reader, M. C., & McFarlane, N. (2003). Sea-salt aerosol distribution during the last glacial maximum and its implications for mineral dust. *Journal of Geophysical Research-Atmospheres*, **108**(D8), 4253.

Reinhardt, H., Kriews, M., Miller, H., Lüdke, C., Hoffmann, E., & Skole, J. (2003). Application of LA–ICP–MS in polar ice core studies. *Analytical and bioanalytical chemistry*, **375**(8), 1265-1275.

Reinhardt, H., Kriews, M., Miller, H., Schrems, O., Lüdke, C., Hoffmann, E., & Skole, J. (2001). Laser ablation inductively coupled plasma mass spectrometry: a new tool for trace element analysis in ice cores. *Fresenius' journal of analytical chemistry*, **370**(5), 629-636.

Rind, D. (1987). Components of the ice-age circulation. *Journal of Geophysical Research-Atmospheres*, **92**(D4), 4241-4281.

Rind, D., Lerner, J., & McLinden, C. (2001). Changes of tracer distributions in the doubled CO2 climate. *Journal of Geophysical Research: Atmospheres* (1984–2012), **106**(D22), 28061-28079.

Rintoul, S. R. (1991). South-atlantic interbasin exchange. *Journal of Geophysical Research-Oceans*, **96**(C2), 2675-2692.

Risien, C. M., & Chelton, D. B. (2006). A satellite-derived climatology of global ocean winds. *Remote sensing of environment*, **105**(3), 221-236.

Roberts, W. H., Valdes, P. J., & Payne, A. J. (2014). Topography's crucial role in Heinrich Events. *Proceedings of the National Academy of Sciences*, **111**(47), 16688-16693.

Ruijgrok, W., Davidson, C. I., & Nicholson, K. W. (1996). Dry deposition of particles - implications and recommendations for mapping of deposition over europe (vol 47B, pg 587, 1995). *Tellus Series B-Chemical and Physical Meteorology*, **48**(5), 710-710.

Ruth, U., Wagenbach, D., Bigler, M., Steffensen, P., Rothlisberger, R., & Millar, H. (2002). High-resolution microparticle profiles at NorthGRIP, Greenland: Case studies of the calcium-dust relationship. *Annals of Glaciology*, Vol 35, 35, 237-242.

Ruth, U., Wagenbach, D., Mulvaney, R., Oerter, H., Graf, W., Pulz, H., & Littot, G. (2004). Comprehensive 1000 year climatic history from an intermediate-depth ice core from the south dome of berkner island, antarctica: Methods, dating and first results. *Annals of Glaciology*, **39**, 146-154.

Ruth, U., Wagenbach, D., Steffensen, J. P., & Bigler, M. (2003). Continuous record of microparticle concentration and size distribution in the central greenland NGRIP ice core during the last glacial period. *Journal of Geophysical Research-Atmospheres*, **108**(D3), 4098.

Sakurai, T., Iizuka, Y., Horikawa, S., Johnsen, S., Dahl-Jensen, D., Steffensen, J. P., & Hondoh, T. (2009). Direct observation of salts as micro-inclusions in the Greenland GRIP ice core. *Journal of Glaciology*, **55**(193), 777-783.

Sakurai, T., Ohno, H., Horikawa, S., Iizuka, Y., Uchida, T., & Hondoh, T. (2010). A technique for measuring microparticles in polar ice using micro-Raman spectroscopy. *International Journal of Spectroscopy*, **2010**.

Schiemann, R., Lüthi, D., & Schär, C. (2009). Seasonality and Interannual Variability of the Westerly Jet in the Tibetan Plateau Region*. *Journal of Climate*, **22**(11), 2940-2957.

Schiller, A., Mikolajewicz, U., & Voss, R. (1997). The stability of the north Atlantic thermohaline circulation in a coupled ocean-atmosphere general circulation model. *Climate Dynamics*, **13**(5), 325-347.

Schmidt, M. W., Vautravers, M. J., & Spero, H. J. (2006). Rapid subtropical north Atlantic salinity oscillations across Dansgaard-Oeschger cycles. *Nature*, **443**(7111), 561-564.

Schmittner, A., Yoshimori, M., & Weaver, A. J. (2002). Instability of glacial climate in a model of the ocean-atmosphere-cryosphere system. *Science*, **295**(5559), 1489-1493.

Schneider, B., & Schmittner, A. (2006). Simulating the impact of the Panamanian seaway closure on ocean circulation, marine productivity and nutrient cycling. *Earth and Planetary Science Letters*, **246**(3), 367-380.

Scholander, P. F., Hemmingsen, E. A., Coachman, L. K., & Nutt, D. C. (1961). Composition of gas bubbles in Greenland icebergs. *Journal of Glaciology*, **3**(29), 813-822.

Schulte, S., & Muller, P. J. (2001). Variations of sea surface temperature and primary productivity during heinrich and dansgaard-oeschger events in the northeastern arabian sea. *Geo-Marine Letters*, **21**(3), 168-175.

Schwarzbach, M. (1986). Alfred wegener the father of continental drift. *Science Tech*, Madison, Wisconsin, , 241 p.

Seidov, D., & Maslin, M. (2001). Atlantic ocean heat piracy and the bipolar climate see-saw during Heinrich and Dansgaard-Oeschger events. *Journal of Quaternary Science*, **16**(4), 321-328.

Seidov, D., Stouffer, R. J., & Haupt, B. J. (2005). Is there a simple bi-polar ocean seesaw? *Global and Planetary Change*, **49**(1–2), 19-27.

Shackleton, N. J., Hall, M. A., & Vincent, E. (2000). Phase relationships between millennial-scale events 64,000–24,000 years ago. *Paleoceanography*, **15**(6), 565-569.

Shoji, H., & Langway, C. C. (1985). Comparison of mechanical tests on the dye-3, Greenland ice core and artificial laboratory ice. *Annals of Glaciology*, **6**, 305-305.

Sicre, M. A., Labeyrie, L., Ezat, U., Duprat, J., Turon, J. L., Schmidt, S., Michael E. &. Mazaud, A. (2005). Mid-latitude southern indian ocean response to Northern hemisphere Heinrich events. *Earth and Planetary Science Letters*, **240**(3-4), 724-731.

Singer, C., Shulmeister, J., & McLea, B. (1998). Evidence against a significant younger dryas cooling event in New Zealand. *Science*, **281**(5378), 812-814.

Sneed, S. B., Mayewki, P. A., Sayre, W., Handley, M. J., Kurbatov, A. V., Taylor, K. C., Bohleber P., Wagenbach D., Erhardt T., Spaulding, N. E. (2015). Instruments and Methods New LA-ICP-MS cryocell and calibration technique for sub-millimeter analysis of ice cores. *Journal of Glaciology*, **61**(226), 233.

Snoeckx, H., Grousset, F., Revel, M., & Boelaert, A. (1999). European contribution of ice-rafted sand to Heinrich layers H3 and H4. *Marine Geology*, **158**(1-4), 197-208.

Sorge, E. (1933). The scientific results of the Wegener expeditions to Greenland. *The Geographical Journal*, **81**(4), pp. 333-344.

Sorge, E. (1935).Glaciological research at Eismitte [Glaziologische Untersuchungen in Eismitte] *Wissenschaftliche Ergebnisse Der Deutschen Groenland Expedition Alfred Wegener 1929 Und 1930-31*, Leipzig, Germany: F. A. Brokaus, **3**, 270.

Spötl, C., & Mangini, A. (2002). Stalagmite from the austrian alps reveals Dansgaard–Oeschger events during isotope stage 3:: Implications for the absolute chronology of Greenland ice cores. *Earth and Planetary Science Letters*, **203**(1), 507-518.

Steffensen, J. P. (1997). The size distribution of microparticles from selected segments of the Greenland ice core project ice core representing different climatic periods. *Journal of Geophysical Research-Oceans*, **102**(C12), 26755-26763.

Steffensen, J. P., Andersen, K. K., Bigler, M., Clausen, H. B., Dahl-Jensen, D., Fischer, H., Goto-Azuma K., Hansson M., Johnsen S. J., Jouzel J., Masson-Delmotte V., Popp T.,. Rasmussen S. O, R. Röthlisberger R., Ruth U., Stauffer B., Siggaard-Andersen M. L., Sveinbjörnsdóttir Á. E., Svensson A.,. White, J. W. C. (2008). High-resolution greenland ice core data show abrupt climate change happens in few years. *Science*, **321**(5889), 680-684.

Steig, E. J., & Alley, R. B. (2002). Phase relationships between Antarctic and Greenland climate records. *Annals of Glaciology*, **35**, 451-456.

Steig, E. J., Brook, E. J., White, J. W. C., Sucher, C. M., Bender, M. L., Lehman, S. J., Morse D.L., Waddington E.D. & Clow, G. D. (1998). Synchronous climate changes in Antarctica and the north Atlantic. *Science*, **282**(5386), 92-95.

Stirling, C. H., Esat, T. M., Lambeck, K., & McCulloch, M. T. (1998). Timing and duration of the Last Interglacial: evidence for a restricted interval of widespread coral reef growth. *Earth and Planetary Science Letters*, **160**(3), 745-762.

Stocker, T. F., & Johnsen, S. J. (2003). A minimum thermodynamic model for the bipolar seesaw. *Paleoceanography*, **18**(4), 1087.

Stocker, T. F., & Mysak, L. A. (1992). Climatic fluctuations on the century time scale - a review of high-resolution proxy data and possible mechanisms. *Climatic Change*, **20**(3), 227-250.

Sun, J. M., Zhang, M. Y., & Liu, T. S. (2001). Spatial and temporal characteristics of dust storms in China and its surrounding regions, 1960-1999: Relations to

source area and climate. *Journal of Geophysical Research-Atmospheres*, **106**(D10), 10325-10333.

Sun, Y., Clemens, S. C., Morrill, C., Lin, X., Wang, X., & An, Z. (2012). Influence of Atlantic meridional overturning circulation on the East Asian winter monsoon. *Nature Geoscience*, **5**(1), 46-49.

Svensson, A., Biscaye, P. E., & Grousset, F. E. (2000). Characterization of late glacial continental dust in the greenland ice core project ice core. *Journal of Geophysical Research-Atmospheres*, **105**(D4), 4637-4656.

Svensson, A., Biscaye, P. E., & Grousset, F. E. (2000). Characterization of late glacial continental dust in the Greenland Ice Core Project ice core. *Journal of Geophysical Research: Atmospheres*.**105**, 4637-4656.

Sverdrup, H. U., & Hans W:son Ahlmann. (1935). Scientific results of the norwegian-swedish spitsbergen expedition in 1934. part IV-V. *Geografiska Annaler*, **17**, pp. 145-218.

Taylor, K. C., Lamorey, G. W., Doyle, G. A., Alley, R. B., Grootes, P. M., Mayewski, P. A., White J.W.C., and Barlow, L. K. (1993). The 'flickering switch'of late Pleistocene climate change. *Nature* **361**, 432 - 436

Tegen, I. (2003). Modeling the mineral dust aerosol cycle in the climate system. *Quaternary Science Reviews*, **22**(18–19), 1821-1834.

Thomas, E. R., Wolff, E. W., Mulvaney, R., Steffensen, J. P., Johnsen, S. J., Arrowsmith, C., White J.W.C., Vaughn B. & Popp, T. (2007). The 8.2 ka event from Greenland ice cores. *Quaternary Science Reviews*, **26**(1), 70-81.

Thomas, E. R., Wolff, E. W., Mulvaney, R., Johnsen, S. J., Steffensen, J. P., & Arrowsmith, C. (2009). Anatomy of a Dansgaard-Oeschger warming transition: High-resolution analysis of the north greenland ice core project ice core. *Journal of Geophysical Research-Atmospheres*, **114**, D08102.

Thornalley, D. J., Barker, S., Becker, J., Hall, I. R., & Knorr, G. (2013). Abrupt changes in deep Atlantic circulation during the transition to full glacial conditions. *Paleoceanography*, **28**(2), 253-262.

Thornalley, D.J.R., Barker, S., Broecker, W.S., Elderfield, H. & McCave, I.N., (2011). The deglacial evolution of North Atlantic deep convection. *Science*, **331**, 202-205.

Thorsteinsson, T., Kipfstuhl, J., & Miller, H. (1997). Textures and fabrics in the GRIP ice core. *Journal of Geophysical Research-Oceans*, **102**(C12), 26583-26599.

Thorsteinsson, T., Kipfstuhl, J., Eicken, H., Johnsen, S. J., & Fuhrer, K. (1995). Crystal size variations in eemian-age ice from the grip ice core, central greenland. *Earth and Planetary Science Letters*, **131**(3-4), 381-394.

Thouveny, N., Debeaulieu, J. L., Bonifay, E., Creer, K. M., Guiot, J., Icole, M., Johnsen S., Jouzel J., Reille M., Williams T. & Williamson, D. (1994). Climate variations in europe over the past 140-kyr deduced from rock magnetism. *Nature*, **371**(6497), 503-506.

Van der Wel, G., Fischer H., Oerter H., Meyer H. and Meijer H.A., (2015). Estimating the differential diffusion length of the stable water isotope signals obtained from ice core records. *The Cryosphere*, **9**, 927-973.

Voelker, A. H. L. (2002). Global distribution of centennial-scale records for marine isotope stage (MIS) 3: A database. *Quaternary Science Reviews*, **21**(10), 1185-1212.

WAIS Divide Project Members. (2015). Precise interpolar phasing of abrupt climate change during the last ice age. *Nature*, **520**(7549), 661-665.

Walin, G. (1985). The thermohaline circulation and the control of ice ages. *Palaeogeography, Palaeoclimatology, Palaeoecology*, **50**(2–3), 323-332.

Wang, Y., Thorsteinsson, T., Kipfstuhl, J., Miller, H., DahlJensen, D., & Shoji, H. (2002). A vertical girdle fabric in the NorthGRIP deep ice core, north Greenland. *Annals of Glaciology*, **35**, 515-520.

Warren, S. G., & Brandt, R. E. (2008). Optical constants of ice from the ultraviolet to the microwave: A revised compilation. *Journal of Geophysical Research: Atmospheres* (1984–2012), **113**(D14).

Werner, M., Tegen, I., Harrison, S. P., Kohfeld, K. E., Prentice, I. C., Balkanski, Y., Rodhe H. & Roelandt, C. (2002). Seasonal and interannual variability of the mineral dust cycle under present and glacial climate conditions. *Journal of Geophysical Research: Atmospheres*, **107**(D24), - 4744.

Wilhelms-Dick, D. (2008) Enhanced analysis of stratified climate archives through upgrade of Laser Ablation Inductively Coupled Plasma Quadrupole to Time of Flight Mass Spectrometry?. Phd Thesis.

Winton, M. (1993). Deep decoupling oscillations of the oceanic thermohaline circulation. In *Ice in the climate system* (pp. 417-432). Springer Berlin Heidelberg.

Wolff, E. W., Mulvaney, R., & Oates, K. (1988). The location of impurities in Antarctic ice. *Ann. Glaciol*, **11**, 194-197.

Wolff, E. W., Rankin, A. M., & Rothlisberger, R. (2003). An ice core indicator of antarctic sea ice production? *Geophysical Research Letters*, **30**(22), 2158.

Woodhead, J. D., Hellstrom, J., Hergt, J. M., Greig, A., & Maas, R. (2007). Isotopic and elemental imaging of geological materials by laser ablation inductively coupled plasma-mass spectrometry. *Geostandards and Geoanalytical Research*, **31**(4), 331-343.

Wunsch, C. (2003). Greenland—Antarctic phase relations and millennial time-scale climate fluctuations in the greenland ice-cores. *Quaternary Science Reviews*, **22**(15–17), 1631-1646.

Xue, B., & Yu, G. (2000). Changes of atmospheric circulation since the last interstadial as indicated by the lake-status record in China. *Acta Geologica Sinica-English Edition*, **74**(4), 836-845.

Yanase, W., & Abe-Ouchi, A. (2010). A numerical study on the atmospheric circulation over the midlatitude north Pacific during the last glacial maximum. *Journal of Climate*, **23**(1), 135-151.

Yokoyama, Y., Lambeck, K., De Deckker, P., Johnston, P., & Fifield, L. K. (2000). Timing of the Last Glacial Maximum from observed sea-level minima. *Nature*, **406**(6797), 713-716.

Yung, Y. L., Lee, T., Wang, C. H., & Shieh, Y. T. (1996). Dust: A diagnostic of the hydrologic cycle during the last glacial maximum. *Science*, **271**(5251), 962-963.

Zhang, X. Y., Lu, H. Y., Arimoto, R., & Gong, S. L. (2002). Atmospheric dust loadings and their relationship to rapid oscillations of the asian winter monsoon climate: Two 250-kyr loess records. *Earth and Planetary Science Letters*, **202**(3-4), 637-643.

Zhang, X., Lohmann, G., Knorr, G., & Purcell, C. (2014). Abrupt glacial climate shifts controlled by ice sheet changes. *Nature*. **512**, 290–294

Zickfeld, K., Levermann, A., Morgan, M. G., Kuhlbrodt, T., Rahmstorf, S., & Keith, D. W. (2007). Expert judgements on the response of the Atlantic meridional overturning circulation to climate change. *Climatic Change*, **82**(3-4), 235-265.

Appendix – Samples

Two different depth intervals were sampled from the NGRIP ice core:

- 2684.55-2695.00 m
- 2715.90-2720.30 m

Cutting and labelling was done by DDL at the ice repository of NBI, Copenhagen, as illustrated in the figure below (Fig. A.1).

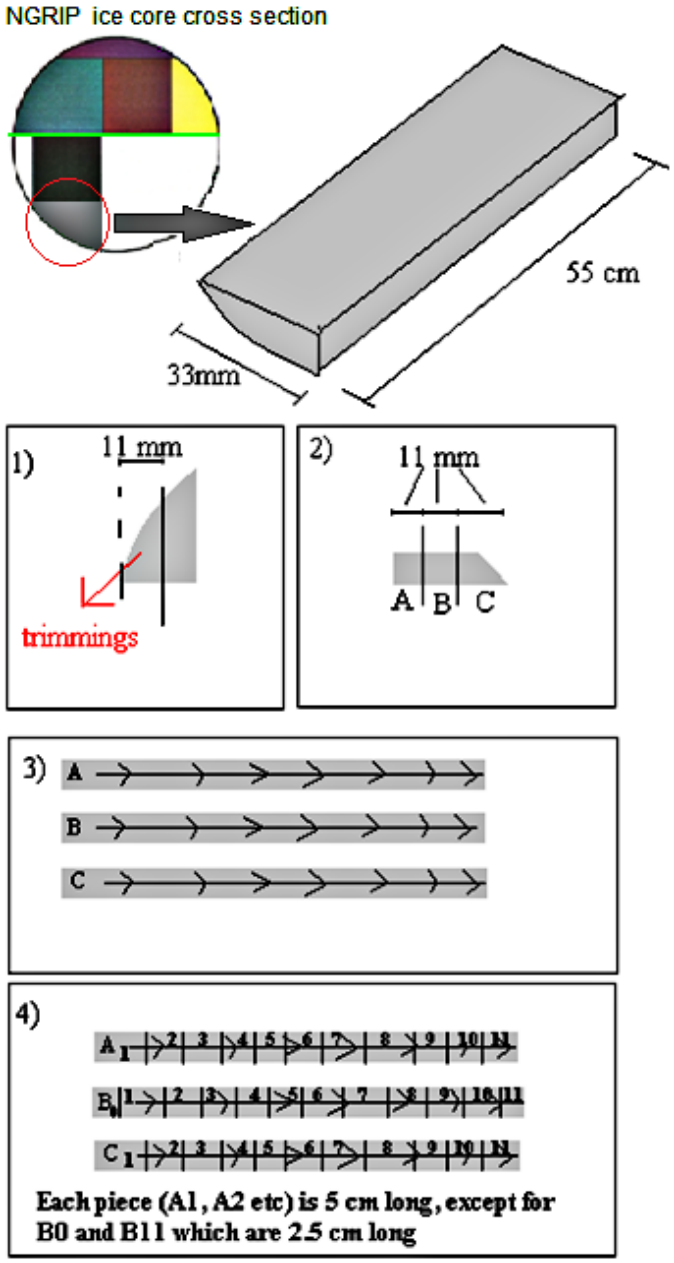

Figure A.1: Cutting procedure performed at the ice repository of Niels Bohr Institute, Centre for Ice and Climate, Copenhagen. The section utilized for LA-ICPMS ice core analysis is section A.

List of samples

NGRIP bag	Depth of the top (m)	Depth of the bottom (m)		
4882	2684.55	2685.1	84424	84477
4883	2685.1	2685.65	84477	84530
4884	2685.65	2686.2	84530	84583
4885	2686.2	2686.75	84583	84636
4886	2686.75	2687.3	84636	84689
4887	2687.3	2687.85	84689	84742
4888	2687.85	2688.4	84742	84795
4889	2688.4	2688.95	84795	84848
4890	2688.95	2689.5	84848	84901
4891	2689.5	2690.05	84901	84954
4892	2690.05	2690.6	84954	85007
4893	2690.6	2691.15	85007	85060
4894	2691.15	2691.7	85060	85113
4895	2691.7	2692.25	85113	85166
4896	2692.25	2692.8	85166	85219
4897	2692.8	2693.35	85219	85272
4898	2693.35	2693.9	85272	85325
4899	2693.9	2694.45	85325	85378
4900	2694.45	2695	85378	85431
4939	2715.9	2716.45	87468	87521
4940	2716.45	2717	87521	87574
4941	2717	2717.55	87574	87627
4942	2717.55	2718.1	87627	87680
4943	2718.1	2718.65	87680	87733
4944	2718.65	2719.2	87733	87786
4945	2719.2	2719.75	87786	87839
4946	2719.75	2720.3	87839	87892

NGRIP bag	Label	Label	Depth top	Depth bottom	Label	Depth top	Depth bottom
4882	A1	C1	2685.05	2685.1	B0	2685.075	2685.1
	A2	C2	2685	2685.05	B1	2685.025	2685.075
	A3	C3	2684.95	2685	B2	2684.975	2685.025
	A4	C4	2684.9	2684.95	B3	2684.925	2684.975
	A5	C5	2684.85	2684.9	B4	2684.875	2684.925
	A6	C6	2684.8	2684.85	B5	2684.825	2684.875
	A7	C7	2684.75	2684.8	B6	2684.775	2684.825
	A8	C8	2684.7	2684.75	B7	2684.725	2684.775
	A9	C9	2684.65	2684.7	B8	2684.675	2684.725
	A10	C10	2684.6	2684.65	B9	2684.625	2684.675
	A11	C11	2684.55	2684.6	B10	2684.575	2684.625
					B11	2684.55	2684.575

NGRIP bag	Label	Label	Depth top	Depth bottom	Label	Depth top	Depth bottom
4883	A1	C1	2685.6	2685.65	B0	2685.625	2685.65
	A2	C2	2685.55	2685.6	B1	2685.575	2685.625
	A3	C3	2685.5	2685.55	B2	2685.525	2685.6
	A4	C4	2685.45	2685.5	B3	2685.475	2685.575
	A5	C5	2685.4	2685.45	B4	2685.425	2685.55
	A6	C6	2685.35	2685.4	B5	2685.375	2685.525
	A7	C7	2685.3	2685.35	B6	2685.325	2685.5
	A8	C8	2685.25	2685.3	B7	2685.275	2685.475
	A9	C9	2685.2	2685.25	B8	2685.225	2685.45
	A10	C10	2685.15	2685.2	B9	2685.175	2685.425
	A11	C11	2685.1	2685.15	B10	2685.125	2685.375
					B11	2685.1	2685.125

NGRIP bag	Label	Label	Depth top	Depth bottom	Label	Depth top	Depth bottom
4884	A1	C1	2686.15	2686.2	B0	2686.175	2686.2

	A2	C2	2686.1	2686.15	B1	2686.125	2686.175
	A3	C3	2686.05	2686.1	B2	2686.075	2686.125
	A4	C4	2686	2686.05	B3	2686.025	2686.075
	A5	C5	2685.95	2686	B4	2685.975	2686.025
	A6	C6	2685.9	2685.95	B5	2685.925	2685.975
	A7	C7	2685.85	2685.9	B6	2685.875	2685.925
	A8	C8	2685.8	2685.85	B7	2685.825	2685.875
	A9	C9	2685.75	2685.8	B8	2685.775	2685.825
	A10	C10	2685.7	2685.75	B9	2685.725	2685.775
	A11	C11	2685.65	2685.7	B10	2685.675	2685.725
					B11	2685.65	2685.675
NGRIP bag	Label	Label	Depth top	Depth bottom	Label	Depth top	Depth bottom
4885	A1	C1	2686.7	2686.75	B0	2686.725	2686.75
	A2	C2	2686.65	2686.7	B1	2686.675	2686.725
	A3	C3	2686.6	2686.65	B2	2686.625	2686.675
	A4	C4	2686.55	2686.6	B3	2686.575	2686.625
	A5	C5	2686.5	2686.55	B4	2686.525	2686.575
	A6	C6	2686.45	2686.5	B5	2686.475	2686.525
	A7	C7	2686.4	2686.45	B6	2686.425	2686.475
	A8	C8	2686.35	2686.4	B7	2686.375	2686.425
	A9	C9	2686.3	2686.35	B8	2686.325	2686.375
	A10	C10	2686.25	2686.3	B9	2686.275	2686.325
	A11	C11	2686.2	2686.25	B10	2686.225	2686.275
					B11	2686.2	2686.225
NGRIP bag	Label	Label	Depth top	Depth bottom	Label	Depth top	Depth bottom
4886	A1	C1	2687.25	2687.3	B0	2687.275	2687.3
	A2	C2	2687.2	2687.25	B1	2687.225	2687.275
	A3	C3	2687.15	2687.2	B2	2687.175	2687.225
	A4	C4	2687.1	2687.15	B3	2687.125	2687.175
	A5	C5	2687.05	2687.1	B4	2687.075	2687.125
	A6	C6	2687	2687.05	B5	2687.025	2687.075
	A7	C7	2686.95	2687	B6	2686.975	2687.025
	A8	C8	2686.9	2686.95	B7	2686.925	2686.975
	A9	C9	2686.85	2686.9	B8	2686.875	2686.925
	A10	C10	2686.8	2686.85	B9	2686.825	2686.875
	A11	C11	2686.75	2686.8	B10	2686.775	2686.825
					B11	2686.75	2686.775
NGRIP bag	Label	Label	Depth top	Depth bottom	Label	Depth top	Depth bottom
4887	A1	C1	2687.8	2687.85	B0	2687.825	2687.85
	A2	C2	2687.75	2687.8	B1	2687.775	2687.825
	A3	C3	2687.7	2687.75	B2	2687.725	2687.775
	A4	C4	2687.65	2687.7	B3	2687.675	2687.725
	A5	C5	2687.6	2687.65	B4	2687.625	2687.675
	A6	C6	2687.55	2687.6	B5	2687.575	2687.625
	A7	C7	2687.5	2687.55	B6	2687.525	2687.575
	A8	C8	2687.45	2687.5	B7	2687.475	2687.525
	A9	C9	2687.4	2687.45	B8	2687.425	2687.475
	A10	C10	2687.35	2687.4	B9	2687.375	2687.425
	A11	C11	2687.3	2687.35	B10	2687.325	2687.375
					B11	2687.3	2687.325
NGRIP bag	Label	Label	Depth top	Depth bottom	Label	Depth top	Depth bottom
4888	A1	C1	2688.35	2688.4	B0	2688.375	2688.4
	A2	C2	2688.3	2688.35	B1	2688.325	2688.375
	A3	C3	2688.25	2688.3	B2	2688.275	2688.325
	A4	C4	2688.2	2688.25	B3	2688.225	2688.275
	A5	C5	2688.15	2688.2	B4	2688.175	2688.225
	A6	C6	2688.1	2688.15	B5	2688.125	2688.175
	A7	C7	2688.05	2688.1	B6	2688.075	2688.125
	A8	C8	2688	2688.05	B7	2688.025	2688.075

	A9	C9	2687.95	2688	B8	2687.975	2688.025
	A10	C10	2687.9	2687.95	B9	2687.925	2687.975
	A11	C11	2687.85	2687.9	B10	2687.875	2687.925
					B11	2687.85	2687.875
NGRIP bag	Label	Label	Depth top	Depth bottom	Label	Depth top	Depth bottom
4889	A1	C1	2688.9	2688.95	B0	2688.925	2688.95
	A2	C2	2688.85	2688.9	B1	2688.875	2688.925
	A3	C3	2688.8	2688.85	B2	2688.825	2688.875
	A4	C4	2688.75	2688.8	B3	2688.775	2688.825
	A5	C5	2688.7	2688.75	B4	2688.725	2688.775
	A6	C6	2688.65	2688.7	B5	2688.675	2688.725
	A7	C7	2688.6	2688.65	B6	2688.625	2688.675
	A8	C8	2688.55	2688.6	B7	2688.575	2688.625
	A9	C9	2688.5	2688.55	B8	2688.525	2688.575
	A10	C10	2688.45	2688.5	B9	2688.475	2688.525
	A11	C11	2688.4	2688.45	B10	2688.425	2688.475
					B11	2688.4	2688.425
NGRIP bag	Label	Label	Depth top	Depth bottom	Label	Depth top	Depth bottom
4890	A1	C1	2689.45	2689.5	B0	2689.475	2689.5
	A2	C2	2689.4	2689.45	B1	2689.425	2689.475
	A3	C3	2689.35	2689.4	B2	2689.375	2689.425
	A4	C4	2689.3	2689.35	B3	2689.325	2689.375
	A5	C5	2689.25	2689.3	B4	2689.275	2689.325
	A6	C6	2689.2	2689.25	B5	2689.225	2689.275
	A7	C7	2689.15	2689.2	B6	2689.175	2689.225
	A8	C8	2689.1	2689.15	B7	2689.125	2689.175
	A9	C9	2689.05	2689.1	B8	2689.075	2689.125
	A10	C10	2689	2689.05	B9	2689.025	2689.075
	A11	C11	2688.95	2689	B10	2688.975	2689.025
					B11	2688.95	2688.975
NGRIP bag	Label	Label	Depth top	Depth bottom	Label	Depth top	Depth bottom
4891	A1	C1	2690	2690.05	B0	2690.025	2690.05
	A2	C2	2689.95	2690	B1	2689.975	2690.025
	A3	C3	2689.9	2689.95	B2	2689.925	2689.975
	A4	C4	2689.85	2689.9	B3	2689.875	2689.925
	A5	C5	2689.8	2689.85	B4	2689.825	2689.875
	A6	C6	2689.75	2689.8	B5	2689.775	2689.825
	A7	C7	2689.7	2689.75	B6	2689.725	2689.775
	A8	C8	2689.65	2689.7	B7	2689.675	2689.725
	A9	C9	2689.6	2689.65	B8	2689.625	2689.675
	A10	C10	2689.55	2689.6	B9	2689.575	2689.625
	A11	C11	2689.5	2689.55	B10	2689.525	2689.575
					B11	2689.5	2689.525
NGRIP bag	Label	Label	Depth top	Depth bottom	Label	Depth top	Depth bottom
4892	A1	C1	2690.55	2690.6	B0	2690.575	2690.6
	A2	C2	2690.5	2690.55	B1	2690.525	2690.575
	A3	C3	2690.45	2690.5	B2	2690.475	2690.525
	A4	C4	2690.4	2690.45	B3	2690.425	2690.475
	A5	C5	2690.35	2690.4	B4	2690.375	2690.425
	A6	C6	2690.3	2690.35	B5	2690.325	2690.375
	A7	C7	2690.25	2690.3	B6	2690.275	2690.325
	A8	C8	2690.2	2690.25	B7	2690.225	2690.275
	A9	C9	2690.15	2690.2	B8	2690.175	2690.225
	A10	C10	2690.1	2690.15	B9	2690.125	2690.175
	A11	C11	2690.05	2690.1	B10	2690.075	2690.125
					B11	2690.05	2690.075
NGRIP bag	Label	Label	Depth top	Depth bottom	Label	Depth top	Depth bottom
4893	A1	C1	2691.1	2691.15	B0	2691.125	2691.15

	A2	C2	2691.05	2691.1	B1	2691.075	2691.125
	A3	C3	2691	2691.05	B2	2691.025	2691.075
	A4	C4	2690.95	2691	B3	2690.975	2691.025
	A5	C5	2690.9	2690.95	B4	2690.925	2690.975
	A6	C6	2690.85	2690.9	B5	2690.875	2690.925
	A7	C7	2690.8	2690.85	B6	2690.825	2690.875
	A8	C8	2690.75	2690.8	B7	2690.775	2690.825
	A9	C9	2690.7	2690.75	B8	2690.725	2690.775
	A10	C10	2690.65	2690.7	B9	2690.675	2690.725
	A11	C11	2690.6	2690.65	B10	2690.625	2690.675
					B11	2690.6	2690.625
NGRIP bag	Label	Label	Depth top	Depth bottom	Label	Depth top	Depth bottom
4894	A1	C1	2691.65	2691.7	B0	2691.675	2691.7
	A2	C2	2691.6	2691.65	B1	2691.625	2691.675
	A3	C3	2691.55	2691.6	B2	2691.575	2691.625
	A4	C4	2691.5	2691.55	B3	2691.525	2691.575
	A5	C5	2691.45	2691.5	B4	2691.475	2691.525
	A6	C6	2691.4	2691.45	B5	2691.425	2691.475
	A7	C7	2691.35	2691.4	B6	2691.375	2691.425
	A8	C8	2691.3	2691.35	B7	2691.325	2691.375
	A9	C9	2691.25	2691.3	B8	2691.275	2691.325
	A10	C10	2691.2	2691.25	B9	2691.225	2691.275
	A11	C11	2691.15	2691.2	B10	2691.175	2691.225
					B11	2691.15	2691.175
NGRIP bag	Label	Label	Depth top	Depth bottom	Label	Depth top	Depth bottom
4895	A1	C1	2692.2	2692.25	B0	2692.225	2692.25
	A2	C2	2692.15	2692.2	B1	2692.175	2692.225
	A3	C3	2692.1	2692.15	B2	2692.125	2692.175
	A4	C4	2692.05	2692.1	B3	2692.075	2692.125
	A5	C5	2692	2692.05	B4	2692.025	2692.075
	A6	C6	2691.95	2692	B5	2691.975	2692.025
	A7	C7	2691.9	2691.95	B6	2691.925	2691.975
	A8	C8	2691.85	2691.9	B7	2691.875	2691.925
	A9	C9	2691.8	2691.85	B8	2691.825	2691.875
	A10	C10	2691.75	2691.8	B9	2691.775	2691.825
	A11	C11	2691.7	2691.75	B10	2691.725	2691.775
					B11	2691.7	2691.725
NGRIP bag	Label	Label	Depth top	Depth bottom	Label	Depth top	Depth bottom
4896	A1	C1	2692.75	2692.8	B0	2692.775	2692.8
	A2	C2	2692.7	2692.75	B1	2692.725	2692.775
	A3	C3	2692.65	2692.7	B2	2692.675	2692.725
	A4	C4	2692.6	2692.65	B3	2692.625	2692.675
	A5	C5	2692.55	2692.6	B4	2692.575	2692.625
	A6	C6	2692.5	2692.55	B5	2692.525	2692.575
	A7	C7	2692.45	2692.5	B6	2692.475	2692.525
	A8	C8	2692.4	2692.45	B7	2692.425	2692.475
	A9	C9	2692.35	2692.4	B8	2692.375	2692.425
	A10	C10	2692.3	2692.35	B9	2692.325	2692.375
	A11	C11	2692.25	2692.3	B10	2692.275	2692.325
					B11	2692.25	2692.275
NGRIP bag	Label	Label	Depth top	Depth bottom	Label	Depth top	Depth bottom
4897	A1	C1	2693.3	2693.35	B0	2693.325	2693.35
	A2	C2	2693.25	2693.3	B1	2693.275	2693.325
	A3	C3	2693.2	2693.25	B2	2693.225	2693.275
	A4	C4	2693.15	2693.2	B3	2693.175	2693.225
	A5	C5	2693.1	2693.15	B4	2693.125	2693.175
	A6	C6	2693.05	2693.1	B5	2693.075	2693.125
	A7	C7	2693	2693.05	B6	2693.025	2693.075
	A8	C8	2692.95	2693	B7	2692.975	2693.025

	A9	C9	2692.9	2692.95	B8	2692.925	2692.975
	A10	C10	2692.85	2692.9	B9	2692.875	2692.925
	A11	C11	2692.8	2692.85	B10	2692.825	2692.875
					B11	2692.8	2692.825
NGRIP bag	Label	Label	Depth top	Depth bottom	Label	Depth top	Depth bottom
4898	A1	C1	2693.85	2693.9	B0	2693.875	2693.9
	A2	C2	2693.8	2693.85	B1	2693.825	2693.875
	A3	C3	2693.75	2693.8	B2	2693.775	2693.825
	A4	C4	2693.7	2693.75	B3	2693.725	2693.775
	A5	C5	2693.65	2693.7	B4	2693.675	2693.725
	A6	C6	2693.6	2693.65	B5	2693.625	2693.675
	A7	C7	2693.55	2693.6	B6	2693.575	2693.625
	A8	C8	2693.5	2693.55	B7	2693.525	2693.575
	A9	C9	2693.45	2693.5	B8	2693.475	2693.525
	A10	C10	2693.4	2693.45	B9	2693.425	2693.475
	A11	C11	2693.35	2693.4	B10	2693.375	2693.425
					B11	2693.35	2693.375
NGRIP bag	Label	Label	Depth top	Depth bottom	Label	Depth top	Depth bottom
4899	A1	C1	2694.4	2694.45	B0	2694.425	2694.45
	A2	C2	2694.35	2694.4	B1	2694.375	2694.425
	A3	C3	2694.3	2694.35	B2	2694.325	2694.375
	A4	C4	2694.25	2694.3	B3	2694.275	2694.325
	A5	C5	2694.2	2694.25	B4	2694.225	2694.275
	A6	C6	2694.15	2694.2	B5	2694.175	2694.225
	A7	C7	2694.1	2694.15	B6	2694.125	2694.175
	A8	C8	2694.05	2694.1	B7	2694.075	2694.125
	A9	C9	2694	2694.05	B8	2694.025	2694.075
	A10	C10	2693.95	2694	B9	2693.975	2694.025
	A11	C11	2693.9	2693.95	B10	2693.925	2693.975
					B11	2693.9	2693.925
NGRIP bag	Label	Label	Depth top	Depth bottom	Label	Depth top	Depth bottom
4900	A1	C1	2694.95	2695	B0	2694.975	2695
	A2	C2	2694.9	2694.95	B1	2694.925	2694.975
	A3	C3	2694.85	2694.9	B2	2694.875	2694.925
	A4	C4	2694.8	2694.85	B3	2694.825	2694.875
	A5	C5	2694.75	2694.8	B4	2694.775	2694.825
	A6	C6	2694.7	2694.75	B5	2694.725	2694.775
	A7	C7	2694.65	2694.7	B6	2694.675	2694.725
	A8	C8	2694.6	2694.65	B7	2694.625	2694.675
	A9	C9	2694.55	2694.6	B8	2694.575	2694.625
	A10	C10	2694.5	2694.55	B9	2694.525	2694.575
	A11	C11	2694.45	2694.5	B10	2694.475	2694.525
					B11	2694.45	2694.475
NGRIP bag	Label	Label	Depth top	Depth bottom	Label	Depth top	Depth bottom
4939	A1	C1	2716.4	2716.45	B0	2716.425	2716.45
	A2	C2	2716.35	2716.4	B1	2716.375	2716.425
	A3	C3	2716.3	2716.35	B2	2716.325	2716.375
	A4	C4	2716.25	2716.3	B3	2716.275	2716.325
	A5	C5	2716.2	2716.25	B4	2716.225	2716.275
	A6	C6	2716.15	2716.2	B5	2716.175	2716.225
	A7	C7	2716.1	2716.15	B6	2716.125	2716.175
	A8	C8	2716.05	2716.1	B7	2716.075	2716.125
	A9	C9	2716	2716.05	B8	2716.025	2716.075
	A10	C10	2715.95	2716	B9	2715.975	2716.025
	A11	C11	2715.9	2715.95	B10	2715.925	2715.975
					B11	2715.9	2715.925
NGRIP bag	Label	Label	Depth top	Depth bottom	Label	Depth top	Depth bottom
4940	A1	C1	2716.95	2717	B0	2716.975	2717

	A2	C2	2716.9	2716.95	B1	2716.925	2716.975
	A3	C3	2716.85	2716.9	B2	2716.875	2716.925
	A4	C4	2716.8	2716.85	B3	2716.825	2716.875
	A5	C5	2716.75	2716.8	B4	2716.775	2716.825
	A6	C6	2716.7	2716.75	B5	2716.725	2716.775
	A7	C7	2716.65	2716.7	B6	2716.675	2716.725
	A8	C8	2716.6	2716.65	B7	2716.625	2716.675
	A9	C9	2716.55	2716.6	B8	2716.575	2716.625
	A10	C10	2716.5	2716.55	B9	2716.525	2716.575
	A11	C11	2716.45	2716.5	B10	2716.475	2716.525
					B11	2716.45	2716.475
NGRIP bag	Label	Label	Depth top	Depth bottom	Label	Depth top	Depth bottom
4941	A1	C1	2717.5	2717.55	B0	2717.525	2717.55
	A2	C2	2717.45	2717.5	B1	2717.475	2717.525
	A3	C3	2717.4	2717.45	B2	2717.425	2717.475
	A4	C4	2717.35	2717.4	B3	2717.375	2717.425
	A5	C5	2717.3	2717.35	B4	2717.325	2717.375
	A6	C6	2717.25	2717.3	B5	2717.275	2717.325
	A7	C7	2717.2	2717.25	B6	2717.225	2717.275
	A8	C8	2717.15	2717.2	B7	2717.175	2717.225
	A9	C9	2717.1	2717.15	B8	2717.125	2717.175
	A10	C10	2717.05	2717.1	B9	2717.075	2717.125
	A11	C11	2717	2717.05	B10	2717.025	2717.075
					B11	2717	2717.025
NGRIP bag	Label	Label	Depth top	Depth bottom	Label	Depth top	Depth bottom
4942	A1	C1	2718.05	2718.1	B0	2718.075	2718.1
	A2	C2	2718	2718.05	B1	2718.025	2718.075
	A3	C3	2717.95	2718	B2	2717.975	2718.025
	A4	C4	2717.9	2717.95	B3	2717.925	2717.975
	A5	C5	2717.85	2717.9	B4	2717.875	2717.925
	A6	C6	2717.8	2717.85	B5	2717.825	2717.875
	A7	C7	2717.75	2717.8	B6	2717.775	2717.825
	A8	C8	2717.7	2717.75	B7	2717.725	2717.775
	A9	C9	2717.65	2717.7	B8	2717.675	2717.725
	A10	C10	2717.6	2717.65	B9	2717.625	2717.675
	A11	C11	2717.55	2717.6	B10	2717.575	2717.625
					B11	2717.55	2717.575
NGRIP bag	Label	Label	Depth top	Depth bottom	Label	Depth top	Depth bottom
4943	A1	C1	2718.6	2718.65	B0	2718.625	2718.65
	A2	C2	2718.55	2718.6	B1	2718.575	2718.625
	A3	C3	2718.5	2718.55	B2	2718.525	2718.575
	A4	C4	2718.45	2718.5	B3	2718.475	2718.525
	A5	C5	2718.4	2718.45	B4	2718.425	2718.475
	A6	C6	2718.35	2718.4	B5	2718.375	2718.425
	A7	C7	2718.3	2718.35	B6	2718.325	2718.375
	A8	C8	2718.25	2718.3	B7	2718.275	2718.325
	A9	C9	2718.2	2718.25	B8	2718.225	2718.275
	A10	C10	2718.15	2718.2	B9	2718.175	2718.225
	A11	C11	2718.1	2718.15	B10	2718.125	2718.175
					B11	2718.1	2718.125
NGRIP bag	Label	Label	Depth top	Depth bottom	Label	Depth top	Depth bottom
4944	A1	C1	2719.15	2719.2	B0	2719.175	2719.2
	A2	C2	2719.1	2719.15	B1	2719.125	2719.175
	A3	C3	2719.05	2719.1	B2	2719.075	2719.125
	A4	C4	2719	2719.05	B3	2719.025	2719.075
	A5	C5	2718.95	2719	B4	2718.975	2719.025
	A6	C6	2718.9	2718.95	B5	2718.925	2718.975
	A7	C7	2718.85	2718.9	B6	2718.875	2718.925
	A8	C8	2718.8	2718.85	B7	2718.825	2718.875

	A9	C9	2718.75	2718.8	B8	2718.775	2718.825
	A10	C10	2718.7	2718.75	B9	2718.725	2718.775
	A11	C11	2718.65	2718.7	B10	2718.675	2718.725
					B11	2718.65	2718.675

NGRIP bag	Label	Label	Depth top	Depth bottom	Label	Depth top	Depth bottom
4945	A1	C1	2719.7	2719.75	B0	2719.725	2719.75
	A2	C2	2719.65	2719.7	B1	2719.675	2719.725
	A3	C3	2719.6	2719.65	B2	2719.625	2719.675
	A4	C4	2719.55	2719.6	B3	2719.575	2719.625
	A5	C5	2719.5	2719.55	B4	2719.525	2719.575
	A6	C6	2719.45	2719.5	B5	2719.475	2719.525
	A7	C7	2719.4	2719.45	B6	2719.425	2719.475
	A8	C8	2719.35	2719.4	B7	2719.375	2719.425
	A9	C9	2719.3	2719.35	B8	2719.325	2719.375
	A10	C10	2719.25	2719.3	B9	2719.275	2719.325
	A11	C11	2719.2	2719.25	B10	2719.225	2719.275
					B11	2719.2	2719.225

NGRIP bag	Label	Label	Depth top	Depth bottom	Label	Depth top	Depth bottom
4946	A1	C1	2720.25	2720.3	B0	2720.275	2720.3
	A2	C2	2720.2	2720.25	B1	2720.225	2720.275
	A3	C3	2720.15	2720.2	B2	2720.175	2720.225
	A4	C4	2720.1	2720.15	B3	2720.125	2720.175
	A5	C5	2720.05	2720.1	B4	2720.075	2720.125
	A6	C6	2720	2720.05	B5	2720.025	2720.075
	A7	C7	2719.95	2720	B6	2719.975	2720.025
	A8	C8	2719.9	2719.95	B7	2719.925	2719.975
	A9	C9	2719.85	2719.9	B8	2719.875	2719.925
	A10	C10	2719.8	2719.85	B9	2719.825	2719.875
	A11	C11	2719.75	2719.8	B10	2719.775	2719.825
					B11	2719.75	2719.775